



Department of Material Science and Engineering

University of Sheffield

Electrical Properties of Rare Earth-Doped Barium Titanate

A thesis submitted for the degree of

Doctor of Philosophy by

Adil Alshoaibi

Supervisor:

Prof. A. R. West

May 2017

Acknowledgements

“In the name of Allah, the Most Gracious, the Most Merciful”

First of all, I express my humble thanks to God. I would like to express my profound thankfulness to my Ph.D. research supervisor, Prof. Anthony R. West for his crucial support, patience, encouragement and words of wisdom during the course of my work. I benefitted greatly from his guidance, and I would have not been able to complete this work without his experience and his thorough insight and scientific thinking. It has been a great honour and privilege for me to work under the supervision of Prof. Anthony R. West.

I would also like to convey my deep gratitude to my advisor Dr Nahum Masó for his continuous support and academic suggestions throughout the course of this research. The great deal of support, direction and insightful advice he offered to my study and experimentation were vital in the completion of this work.

I was very fortunate to have the opportunity to work with many brilliant individuals throughout the course of this work. I would like to offer special thanks to Dr Abtsam, Dr Amir, Bo, Dr Fadhlina, Dr Fayaz, Griffin, John, Dr Le Ma, Luran, Mouldy, Dr Nik, Dr Nouf, Dr Rouzbeh, Dr Shine, Wan, Dr Yang and Yun for their significant advice, guidance and support. Additionally, I would like to thank all the members of our group for working together and making my time enjoyable. Most of all, I would like to show my appreciation to the people who took care of me and patiently gave me the greatest support, my parents Ahmed and Aziza. I would never have finished this study without their encouragement and backing. I owe everything I have and everything I have become to my family whose love and support cannot be overstated.

Additionally, special thanks go to my lovely children, Shaden, Ahmed and Hassan, who are a source of unending joy, happiness and smiles.

Last but not the least, this thesis would not have been possible without the guidance and support of my wife, Khawla, who made me happy to develop my career and always encouraged me and never doubted that I could do it. Thanks for standing beside me through thick and thin.

I would like to thank the Saudi Government, King Faisal University, the Royal Embassy, Saudi Cultural Bureau and Ministry of Higher Education for my scholarship and for supporting my study.

Thanks be to Allah Almighty

Sheffield, UK

Adil Alshoabi

Dedication

To The Glory of God

This thesis is dedication to my wife, *Khawla Almulla*, for her continuous support and significant encouragement.

Abstract

Samples of undoped BaTiO_3 , BT were prepared by three mixed oxide routes; hand mixing, *HM* using a pestle and mortar, ball milling, *BM* using Y_2O_3 -stabilised zirconia balls and planetary ball milling, *PBM* using tungsten carbide balls.

The electrical properties of slow cooled (SC) and quenched (Q) BT material for *HM*, *BM* and *PBM* samples were studied by impedance spectroscopy, IS after heat treatments in air at different temperatures. IS measurements with application of applied voltage and in atmospheres of different oxygen partial pressure were used to determine the conduction mechanism.

The application of bias voltage was used during IS measurements to separate Schottky barrier interfacial impedances from sample impedances. In general, two types of Schottky barrier can be detected: (i) barriers at electrode-sample interfaces due to Fermi level mismatch and (ii) barriers between grains associated with partial oxidation of sample surfaces. In-Ga electrodes were considered to yield ohmic contacts and associated with partial oxidation that also produced the positive temperature coefficient of resistance, PTCR effect.

A methodology has been developed to understand the effect of an applied voltage and changing oxygen partial pressure on electrical properties and possible explanations.

Rare earth dopants can occupy either Ba or Ti sites or a mixture of Ba and Ti sites depending on their size. This requires charge compensation mechanisms which can be ionic or electronic. The ionic mechanism can involve either cation or oxygen vacancies. A survey has been carried out of the charge compensation mechanism for different rare earth ions (Gd, Dy, Ho, Y, Er and Yb). It was found that Y^{3+} preferentially occupied the Ti^{4+} site with charge compensation by oxygen vacancies and therefore, Y behaved as an acceptor with solid solubility limit of $\sim 15\%$. Y^{3+} can also simultaneously occupy both Ba and Ti sites with a solubility limit of $\sim 7.5\%$, but exclusive occupancy of Ba sites is limited to $\sim 1.5\%$.

A partial phase diagram $\text{BaO-TiO}_2\text{-Y}_2\text{O}_3$ can be presented showing the different solid solutions and the polymorphism of doped BaTiO_3 .

Several parameters affected the electrical properties of pure and doped BT ceramics: the charge compensation mechanism, whether ionic or electronic; the sample preparation methods; the cooling rate at the end of sample heat treatment because many samples lost a small amount of oxygen at high temperature and showed n-type semiconductivity. A common observation was that many slow cooled samples showed weak p-type behaviour attributed to uptake of oxygen on cooling. The holes may be associated with either underbonded oxide (O^-) ions or unavoidable impurities such as Fe^{3+} .

Leaky dielectric properties were observed for extrinsic n-type region whereas, normal dielectric properties were observed for extrinsic p-type region.

The electrical properties of $BaTi_{1-x}Y_xO_{3-x/2}$ samples fired and cooled in air were ferroelectric insulators at $x \leq 0.05$ and relaxor ferroelectrics at higher x with no evidence of semiconductivity in any of the samples, whether they were cooled slowly or quenched from high temperatures (1200-1600 °C).

The possible occurrence of a resistivity minimum in rare earth doped BT was investigated. Three possible mechanisms for semiconductivity were considered for generating Ti^{3+} ions: direct donor doping, oxygen loss at high temperatures and a more complex double doping mechanism involving Y^{3+} and Ti^{3+} ions to charge-balance the oxygen vacancies.

No semiconductivity and resistivity minimum were observed for Yb-BT for all three joins and Er-BT. Semiconductivity was observed for other RE dopants and the total resistivity passed through a minimum at 0.1% RE substitution then increased generally for > 1% Y, Ho, Dy and Gd substitution on all three joins.

Contents

Acknowledgements	II
Dedication	IV
Abstract	V
Contents.....	VII
Chapter 1: Literature Review	- 1 -
1.1 Introduction	- 1 -
1.2 Dielectrics	- 2 -
1.3 Perovskite Structure (ABX ₃)	- 3 -
1.4 Ferroelectrics	- 5 -
1.5 Barium Titanate (BaTiO ₃)	- 6 -
1.5.1 Doped BaTiO ₃	- 9 -
1.5.1.1 Isovalent doping	- 10 -
1.5.1.2 Aliovalent doping.....	- 11 -
1.5.1.2.1 RE ³⁺ -doped BT.....	- 12 -
1.6 Effect of application of dc bias and pO ₂ on undoped BT and RE ³⁺ -doped BT..	- 31 -
1.6.1 pO ₂ effect.....	- 31 -
1.6.2 Dc bias effect.....	- 33 -
1.6.3 Schottky barrier effect.....	- 35 -
1.7 Motivation and aim of this study	- 40 -
1.8 References	- 41 -
2. Experimental Procedure	- 55 -
2.1 Sample Preparation.....	- 55 -
2.1.1 Hand Mixing (<i>HM</i>) of Reagents.....	- 55 -
2.1.2 Ball Milling (<i>BM</i>) Route	- 55 -
2.1.3 Planetary Ball Milling (<i>PBM</i>) Route.....	- 56 -

2.2 Structural Characterisation	- 58 -
2.2.1 X-Ray Powder Diffraction	- 58 -
2.2.2 Density Measurement.....	- 58 -
2.2.3 Differential Scanning Calorimetry (DSC).....	- 59 -
2.2.4 Scanning Electron Microscopy (SEM)	- 59 -
2.2.5 Raman Spectroscopy	- 60 -
2.3 Electrical Property Characterisation	- 60 -
2.3.1 Sample Preparation	- 60 -
2.3.2 Polarisation-Electric Field Measurements	- 61 -
2.3.3 Impedance Spectroscopy (IS).....	- 62 -
2.3.3.1 Basic electrical and impedance spectroscopy theory:	- 62 -
2.3.3.2 Arrhenius plot:.....	- 72 -
2.3.4 Fixed frequency capacitance measurement: LCR (L= Inductance, C= Capacitance and R= Resistance) measurements	- 73 -
2.4 References	- 74 -
Chapter 3: Effect of dc bias and pO_2 on the conductivity of undoped-BaTiO ₃	- 77 -
3.1 Introduction	- 77 -
3.2 Experimental Procedure	- 82 -
3.3 Results	- 83 -
3.3.1 XRD study of undoped BaTiO ₃	- 83 -
3.3.2 Electrical and structural characteristics of undoped BaTiO ₃	- 83 -
3.3.2.1 LCR results.....	- 83 -
3.3.2.2 Differential Scanning Calorimetry (DSC).....	- 84 -
3.3.2.3 Raman Spectroscopy Results	- 87 -
3.3.2.4 SEM Results	- 88 -
3.3.2.5 Impedance Spectroscopy Results	- 89 -
3.3.2.5.1 Slow-cooled samples.....	- 90 -

(1) Typical impedance data	- 90 -
(2) Effect of oxygen partial pressure	- 94 -
(3) Effect of sintering temperature	- 96 -
(4) Effect of application of a small dc bias voltage	- 97 -
3.3.2.5.2 Quenched samples	- 99 -
(1) P-type conductivity samples	- 99 -
(A) Typical impedance data	- 99 -
(B) Effect of oxygen partial pressure	- 100 -
(C) Effect of application of a small dc bias voltage	- 104 -
(2) N-type conductivity or Schottky barrier samples	- 107 -
(A) Typical impedance data	- 107 -
(B) Effect of electrode material	- 109 -
(C) Effect of oxygen partial pressure	- 111 -
(D) Effect of application of a small dc bias voltage	- 112 -
3.4 Discussion	- 115 -
3.5 Conclusions	- 128 -
3.6 References	- 129 -
Chapter 4: Phase assemblages, polymorphism and solid solutions of Y-doped BaTiO ₃	- 140 -
4.1 Introduction	- 140 -
4.1.1 Effect of yttrium (Y) as a dopant in barium titanate	- 141 -
4.2 Experimental Procedure	- 144 -
4.3 Results	- 145 -
4.3.1 Crystal structure and phase diagram study of Y-doped BaTiO ₃	- 145 -
1. Self-compensation mechanism, Ba _{1-y} Ti _{1-y} Y _{2y} O ₃	- 146 -
2. Donor doping mechanism, Ba _{1-y} TiY _y O ₃	- 147 -
3. Acceptor doping mechanism, BaTi _{1-x} Y _x O _{3-x/2}	- 149 -

4.3.2 Electrical and structural characteristics	157 -
4.3.2.1 LCR results	157 -
4.3.2.2 Hysteresis Loop Results	163 -
4.3.2.3 Raman Spectroscopy Results	165 -
4.3.2.4 SEM Results	167 -
4.3.2.5 IS Results	170 -
(A) Y-B samples:	170 -
(1) Typical impedance data	170 -
(2) Effect of oxygen partial pressure	176 -
(3) Effect of application of a small dc bias voltage	177 -
(B) Y-AB samples:	178 -
(1) Typical impedance data	178 -
(2) Effect of cooling rate	179 -
(3) Effect of oxygen partial pressure	184 -
(4) Effect of application of a small dc bias voltage	187 -
(C) Y-A sample:	188 -
(1) Typical impedance data	188 -
(2) Effect of cooling rate	190 -
(3) Effect of oxygen partial pressure	194 -
(4) Effect of application of a small dc bias voltage	195 -
4.4 Discussion	199 -
Phase diagram study of Y-doped BaTiO ₃	199 -
4.5 Conclusions	210 -
4.6 References	211 -
Chapter 5: Electrical properties of RE ³⁺ -doped BaTiO ₃ at low concentrations ..	219 -
5.1 Introduction	219 -
5.2 Experimental procedure	222 -

5.3 Results	- 223 -
5.3.1 XRD Results.....	- 223 -
5.3.2 Electrical properties of Yb-doped BT	- 223 -
5.3.3 Electrical properties of Er-doped BT	- 230 -
5.3.4 Electrical properties of Y-doped BT	- 247 -
5.4 Discussion.....	- 270 -
5.5 Conclusions	- 280 -
5.6 References	- 281 -
Chapter 6: Conclusions and Further Work.....	- 285 -
6.1 Conclusions	- 285 -
6.1.1 Electrical properties of BT	- 285 -
6.1.1.1 Electrical properties of SC BT	- 285 -
6.1.1.2 Electrical properties of Q BT	- 286 -
6.1.2 Phase diagram study and crystal chemistry of Y-doped BT	- 288 -
6.1.3 Electrical properties of Y-doped BT at high concentrations.....	- 289 -
6.1.4 Electrical properties of RE-doped BT with low dopant concentrations-	290
-	
6.1.5 Resistivity minimum of RE-doped BT.....	- 293 -
6.1.6 Effect of preparation routes	- 293 -
6.2 Further Work	- 293 -
6.3 References	- 295 -

Chapter 1: Literature Review

1.1 Introduction

Ferroelectric ceramics are considered as one of the major classes of functional materials [1] due to their ability to show spontaneous electric polarization below a certain temperature known as the Curie temperature (T_C) [2]. Since the discovery of the ferroelectric property in Rochelle Salt [3] in 1921 and the later discovery of ferroelectricity in polycrystalline barium titanate, $BaTiO_3$, huge efforts have been exerted by scientists in order to study and utilise this phenomenon. As a result, whole new technological applications have emerged. Major applications of ferroelectric materials can be seen in high dielectric constant capacitors such as multilayer ceramic capacitors (MLCCs), piezoelectrics, transducers, electronic and communication filters and biomedical sensors [3-6].

$BaTiO_3$ (BT) is one of the most important and interesting ferroelectric materials that is used in various technical applications [7, 8]. The reason for such importance is due to its high relative permittivity (dielectric constant) that increases with temperature and reaches its maximum value at T_C (130 °C) and then decreases with increasing temperature according to the Curie-Weiss law [9]. At T_C , the crystal structure transforms from tetragonal to cubic [10]. When BT is doped with a rare earth metal (such as La^{3+} , Y^{3+} , or Nd^{3+}), n-type semiconducting material is often obtained. With such doped materials, large increases in the specific resistivity are found as the temperature increases above T_C . This behaviour is known as the Positive Temperature Coefficient of Resistivity (PTCR) [11].

On the other hand, when BT, in its dielectric form, is doped with ions such as Sr^{+2} or Pb^{+2} to occupy the Ba-site, or doped with ions such as Hf^{+4} or Sn^{+4} to occupy the Ti^{+4} -site, changes in lattice constants, electrical properties, microscopic properties and T_C position take place due to differences in the ionic radii [12]. Additionally, if semiconducting BT structure is doped with the aforementioned ions (amongst others), changes in the PTCR properties are expected to occur [13]. The PTCR phenomenon, which has been explained by the Heywang and Jonker model [14], can be attributed to the existence of a potential barrier (ϕ_0) at the grain boundary (gb) as

a result of the interface acceptor states. The potential barrier height is inversely proportional to the relative permittivity [15, 16].

The first section of this chapter discusses basic theory and concepts related to ferroelectrics. In the second section, a literature review on BT and rare earth RE doped-BT is given.

1.2 Dielectrics

Materials which do not allow passage of electric current are known as dielectrics. A dielectric material is characterised by its dielectric constant, which arises from the polarisation induced by an applied electric field. The macroscopic polarisation is a combination of polarisations at the microscopic levels. A dielectric material can have more than one of the following microscopic polarizations.

1. Electronic polarisation: This type of polarisation arises when the symmetric distribution of electrons is disturbed by the application of an external electric field.
2. Ionic polarisation: The polarisation which arises due to the relative motion of ions with respect to each other as the external electric field is applied.
3. Orientational polarisation: This type of polarisation exists in materials with permanent dipole moments. Application of an electric field can orient these dipoles in a specific direction, which gives rise to a net polarisation known as orientational polarisation.
4. Spontaneous polarisation: This type of polarisation exists in ferroelectric materials and is associated with off-centre ion displacements leading to dipole creation.
5. Interfacial polarisation: This type of polarisation arises due separation of mobile charges under application of an electric field.

Based on the type of polarisation, dielectric materials can be classified into non-polar and polar dielectrics, dipolar dielectrics and ferroelectrics. Non-polar materials possess only electronic polarisation, polar materials can have both electronic and ionic polarisations, while dipolar materials possess electronic, ionic and orientational polarisation.

On the basis of symmetry, dielectrics can be classified into 32 point groups. Amongst the 32 groups, 21 are noncentrosymmetric, 20 of which show piezoelectricity. Amongst the 20 piezoelectric groups, 10 groups have spontaneous polarisation known as pyroelectrics. A sub-group of pyroelectrics is ferroelectrics which is defined as the materials having switchable polarisation with applied electric fields. Ferroelectric materials can be subdivided into four major groups: Tungsten Bronze, Oxygen Octahedral, Pyrochlore and layer structure. Oxygen octahedral (perovskite) is by far the most important structure in terms of applications and is discussed in the coming section. A schematic of dielectric classification based on symmetry is shown in Figure 1-1, [17].

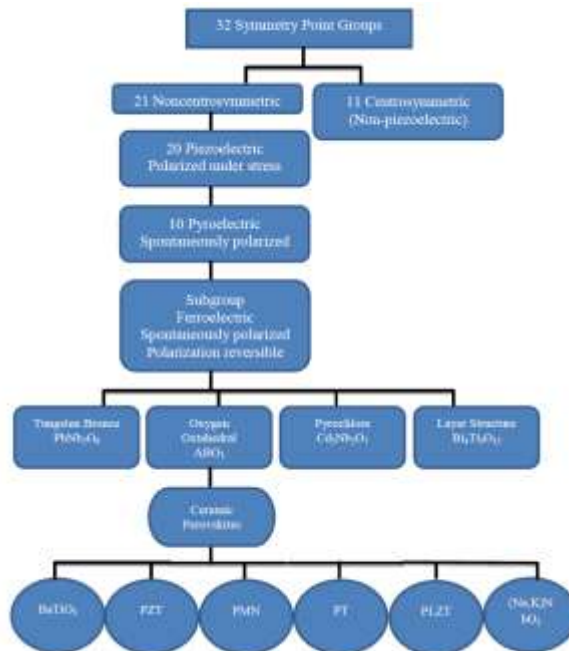


Figure 1-1: A classification scheme for the crystallographic symmetry groups. Graph also shows the classification position of BaTiO₃.

1.3 Perovskite Structure (ABX₃)

The perovskite structure was discovered in 1839 by Gustav Rose, a Russian mineralogist. He discovered the mineral calcium titanate CaTiO₃, named after the Russian Mineralogist, C. L. A. Von Perovski. It has been observed that CaTiO₃ is obtained as orthorhombic crystals [18]. The most general formula is ABX₃, where A and B are metallic cations and X is a non-metallic anion. In most cases, the non metallic anion is oxygen forming the ABO₃ structure, which is relevant to this study.

The perovskite structure is flexible and can be exploited to alter its structural details and physical properties [19, 20]. Perovskites have different structural variants, such as tetragonal, orthorhombic, rhombohedral, monoclinic and triclinic, but the cubic form is the ideal, undistorted structure [21]. The structure of perovskite is shown in Figure 1-2(a) and is described by a cubic unit cell. (A) represents large cations such as Na^{1+} , K^{1+} , Ca^{2+} , Sr^{2+} , Ba^{2+} , Y^{3+} which are surrounded by twelve anions in cubo-octahedral coordination in the centre of the unit cell, (b). (B) represents small cations such as Ga^{3+} , In^{3+} , Ti^{4+} , Nb^{5+} , Mn^{4+} , Sn^{4+} , Zr^{4+} which are surrounded by six anions in octahedral coordination, located at the corners of the unit cell, (c). (X) represents non-metallic anions such as O^{-2} , F^{-1} and Cl^{-1} which are coordinated by two B-site cations and four A-site cations. The most common atoms in position X are oxygen, but they can be any member of the halogen family [22].

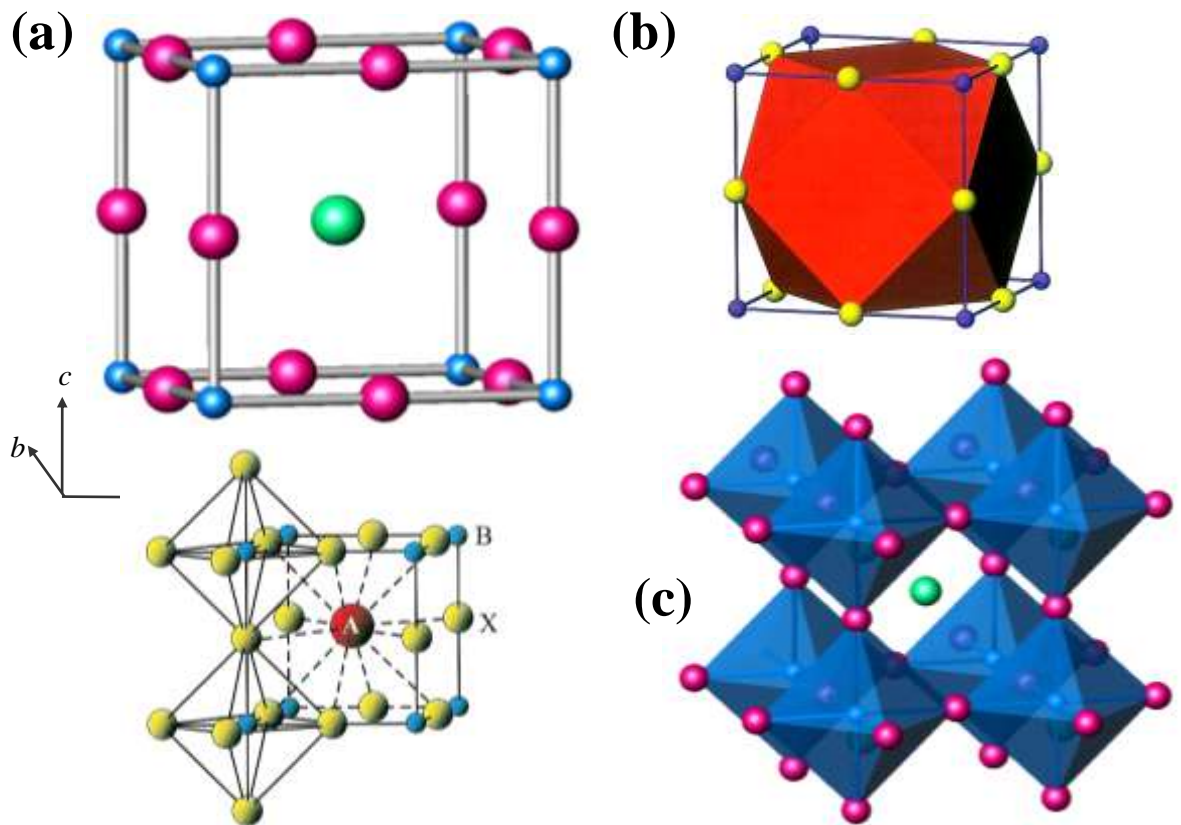


Figure 1-2: (a) Simple perovskite structure (b) Unit cell for cubo-octahedral polyhedron structure, AX_{12} (c) Perovskite projection depicting 8 X anion octahedra enclosing the A-site cation [20].

The tolerance factor “t” given in equation 1-1 is used to describe deviations from ideal perovskite structures.

$$t = \frac{R_A + R_O}{\sqrt{2} (R_B + R_O)} \quad (1-1)$$

In the ideal case, $t = 1$; however the atomic radii seldom satisfy ideal conditions and generally $t \neq 1$, which usually results in a deviation from cubic symmetry. The distortions may arise from ionic displacement, chemical ordering or tilting of octahedra and can have different symmetries such as tetragonal, rhombohedral etc.

Perovskites are very heavily studied because of their diverse properties which can be easily tailored by altering structure and have therefore numerous technological applications.

1.4 Ferroelectrics

Ferroelectrics are defined as materials having spontaneous polarisation which can be switched by applied electric fields. The temperature at which these materials lose their spontaneous polarisation is the Curie temperature, T_C beyond which, the material becomes paraelectric and obeys the Curie-Weiss law, equation 1-2:

$$\epsilon_r - 1 = \frac{C}{T - T_0} \quad (1-2)$$

where ϵ_r is relative permittivity, C is Curie constant and T_0 is Curie-Weiss temperature.

Rochelle salt ($\text{NaKC}_4\text{H}_4\text{O}_6 \cdot 4\text{H}_2\text{O}$) is the first ferroelectric material, discovered by Valasek in 1920. However, the instability in the ferroelectric properties of Rochelle salt do not make it suitable for industrial applications. In 1945, A Von Hippel discovered barium titanate, BT, which has become one of the most important materials in ferroelectric ceramics. Later, Gray investigated the role of domains within grains of BT in producing a behaviour similar to the behaviour of a single crystal [3], with piezoelectric and ferroelectric properties when these domains are influenced by an electric field. Huge interest in the phenomenon was triggered by discovery of ferroelectricity in polycrystalline BT. Since then, huge efforts have been exerted by scientists in order to study and utilise this phenomenon. As a result, whole new technological applications have emerged. Major applications of

ferroelectric materials can be seen in high dielectric constant capacitors such as multilayer ceramic capacitors (MLCCs), piezoelectric, transducers, electronic and communication filters and biomedical sensors. Ferroelectric materials have shown reversibility in their spontaneous polarization under an applied external electric field [3].

In BT, the tetragonal-cubic phase transition is first order. Therefore, several properties such as ϵ_r , lattice constant and the polarization show discontinuity at the transition temperature [23], Figure 1-3. The lattice parameters changes [24] are shown in (a). The spontaneous polarization (in the absence of an electric field) decreases to zero at T_C , (b). The relative permittivity changes clearly at the phase transitions. (c). Figure 1-4 shows the P-E loop where the domains align in the positive direction, with a rise in the field strength even when the polarization reaches a saturation value after applying a certain field. However, when removing the external field, some domains are no longer oriented, resulting in a decrease in polarization; some of the domains remain oriented and hence maintain a level of polarization known as remanent polarization. A hysteresis loop can be observed after applying a coercive field (E_c) [25-27]. At T_C , the hysteresis loop disappears, and above it the phase is usually nonpolar [5, 28].

1.5 Barium Titanate ($BaTiO_3$)

BT was discovered in the 1940s, and is the first famous ferroelectric ceramic material that has been studied in different forms such as thin and thick films, powder and bulk [25]. BT is known for its high permittivity and stable ferroelectric properties that allow it to be used in technological applications. It has a perovskite structure with Ba^{+2} on A-site and Ti^{+4} on B-site as shown in Figure 1-5. It can be seen that 8 Ba^{+2} atoms on corners at (0 0 0), one Ti^{+4} atom is in the centre at $(\frac{1}{2}, \frac{1}{2}, \frac{1}{2})$ and 6 oxygen atoms are located at the centre of all faces at $(0, \frac{1}{2}, \frac{1}{2})$; $(\frac{1}{2}, 0, \frac{1}{2})$; $(\frac{1}{2}, \frac{1}{2}, 0)$ [25].

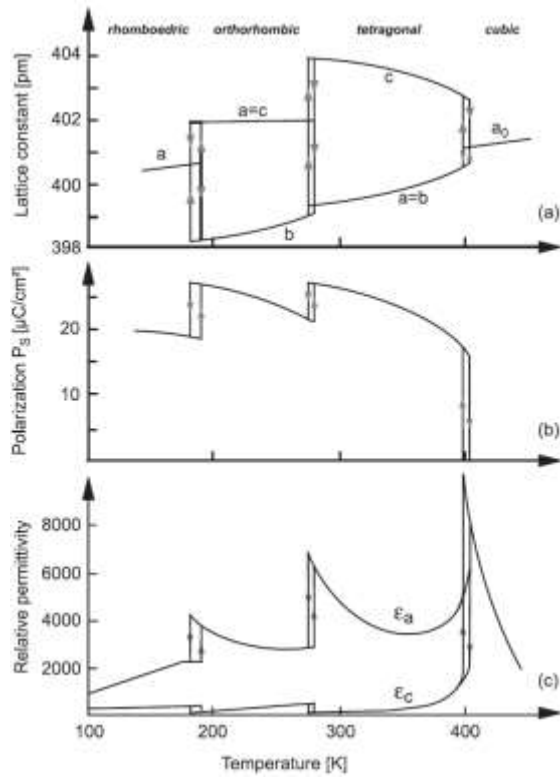


Figure 1-3: Variations with temperature of (a) lattice parameters, (b) the spontaneous polarization P_s (c) relative permittivity [23].

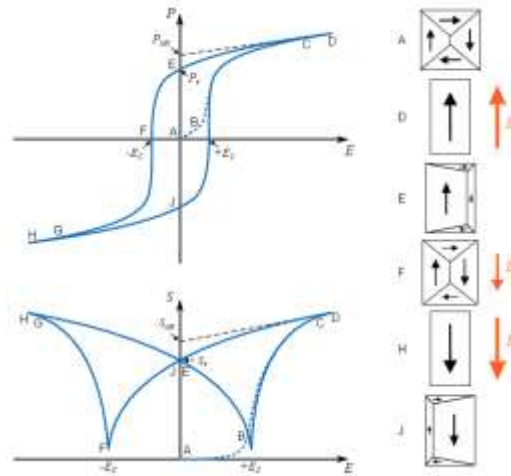


Figure 1-4 Polarization versus the applied Electric Field (P-E) hysteresis loop parameters and strain (S-E) for a typical ferroelectric material [29].

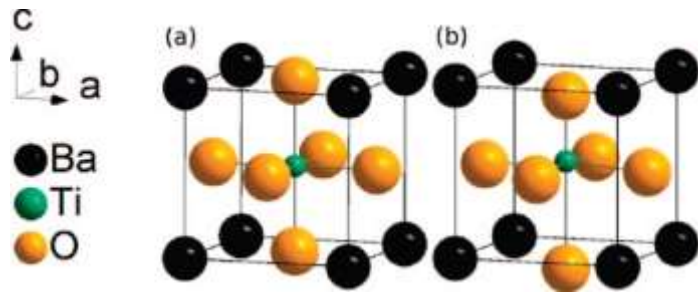


Figure 1-5: Crystal structure of the ferroelectric perovskite BaTiO₃ (a) cubic structure (space group: Pm-3m); (b) tetragonal structure (space group: P4mm) [30].

BT goes through a series of phase transitions from rhombohedral (below -90 °C) to orthorhombic (0° C and -90° C), tetragonal (130° C to 0° C) and cubic (above 130° C) [31, 32]. All symmetries lower than cubic are ferroelectric [5]. BT has $t > 1$ and the coordination environment is optimised by off-centring the Ti⁴⁺ ion, which gives rise to spontaneous polarisation. All structures along with their spontaneous polarisation vectors are shown in Figure 1-6.

At T_C , the spontaneous polarisation falls to zero with a maximum value of permittivity. Below T_C , BT is ferroelectric, non-centrosymmetric and polar. Above T_C , BT is paraelectric, centrosymmetric and non-polar. The ferroelectric state in BT is a result of displacement of the Ti ion away from the position of centrosymmetry within the oxygen octahedra, Figure 1-7.

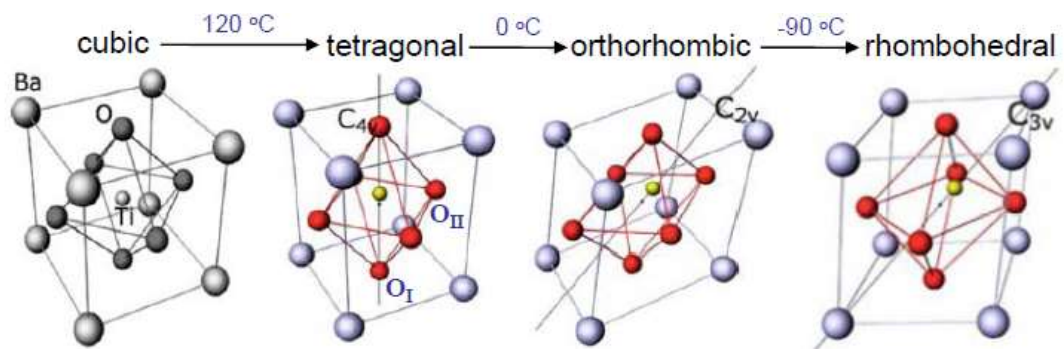


Figure 1-6: Conventional unit cell of BT in polymorphs [33].

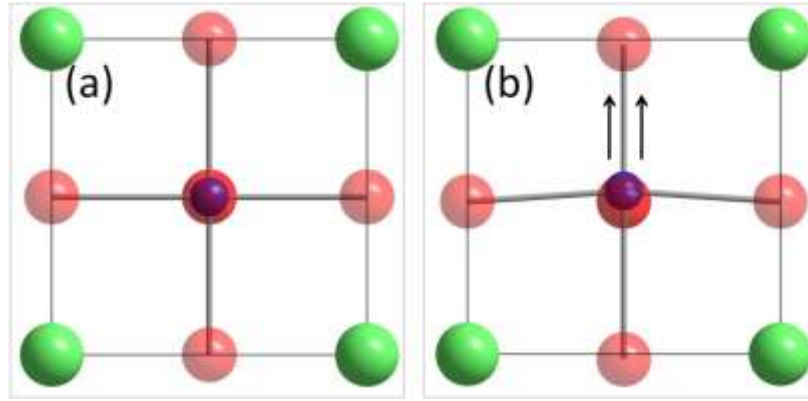


Figure 1-7: Crystal structure of BT, a) High temperature cubic phase and b) RT tetragonal phase with cation displacement. The green spheres are Ba, blue is Ti and red is O [34].

BT also forms a hexagonal structure at very high temperature (above 1460 °C), which is paraelectric in nature. A detailed BaO-TiO₂ phase diagram along with structural phase transitions is given in Figure 1-8.

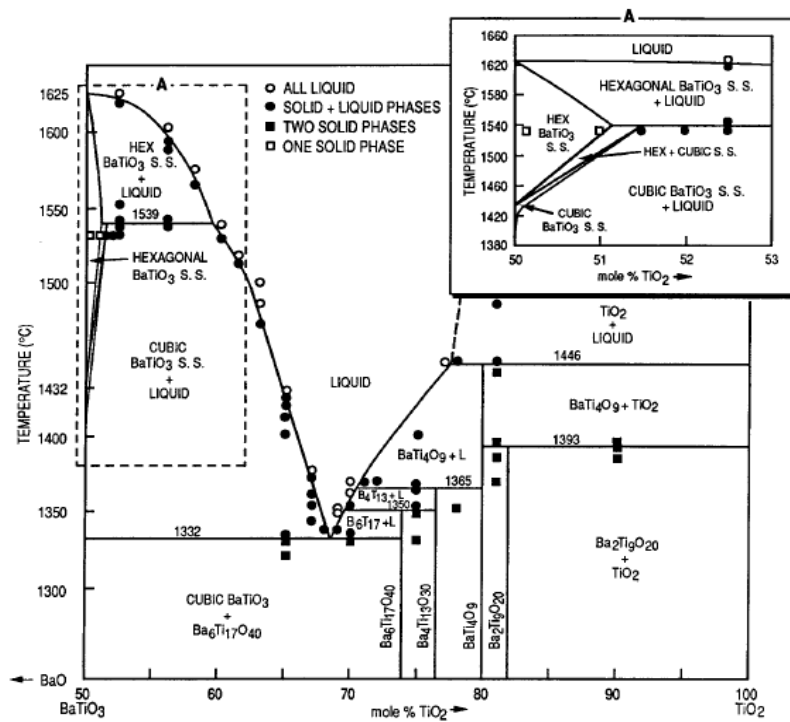


Figure 1-8: Representation of the phase relationships in the BaTiO₃-TiO₂ phase diagram [35].

1.5.1 Doped BaTiO₃

The effects of doping on the crystal structure, defect structure, and electrical properties of BT depend on the kinds of impurity, ionic radius, and valence state [36-

41]. There are three types of cation site occupation possibility in doped BT: the Ba site, the Ti site, or both. On the basis of their charges, dopants are classified into two categories, isovalent and aliovalent. Large A^{2+} impurities occupy the Ba-site [42, 43], small A^{4+} impurities occupy the Ti-site [44] and A^{3+} or A^{5+} impurities occupy either the Ba or Ti-site depending on their size [45-51]. These additions play an important role in changing the properties of BT such as T_C , ϵ_r , density, lattice parameters, grain size and conductivity.

1.5.1.1 Isovalent doping

Isovalent doping means replacement of a host ion by another ion of the same charge. In BT this corresponds to doping of A^{2+} impurities on Ba-site and A^{4+} impurities on the Ti-site.

The usual effect of isovalent doping is that T_C is lowered towards room temperature, while other phase transitions move towards higher temperature, Figure 1-9. All dopants decrease T_C with the exception of Pb^{2+} which behaves in the opposite way. Partial isovalent substitution of Ti^{4+} by Sn^{4+} [52] and Zr^{4+} [53] or Ba^{2+} by Sr^{2+} [54], Ca^{2+} [55] and Pb^{2+} [56] shift T_C to lower or higher temperatures. On substitution of isovalent ions for Ba, the rate of decrease/increase in the Curie temperature is 5 °C/mol% for Sr^{2+}/Pb^{2+} respectively. Ca^{2+} did not show significant shift of T_C . On substitution of isovalent ions for Ti the rate of decrease in T_C is 5 °C/mol% of Hf^{4+} and Zr^{4+} and 10 °C/mol% of Sn^{4+} [57].

The height and sharpness of the permittivity maximum peak are observed more clearly often with the low dopant concentrations whereas a diffuse phase transition accompanied by a broadened permittivity peak often occurs at high dopant concentrations, such as Sn^{4+} at ≥ 10 mol% [58] and Zr^{4+} at ≥ 15 mol% [59].

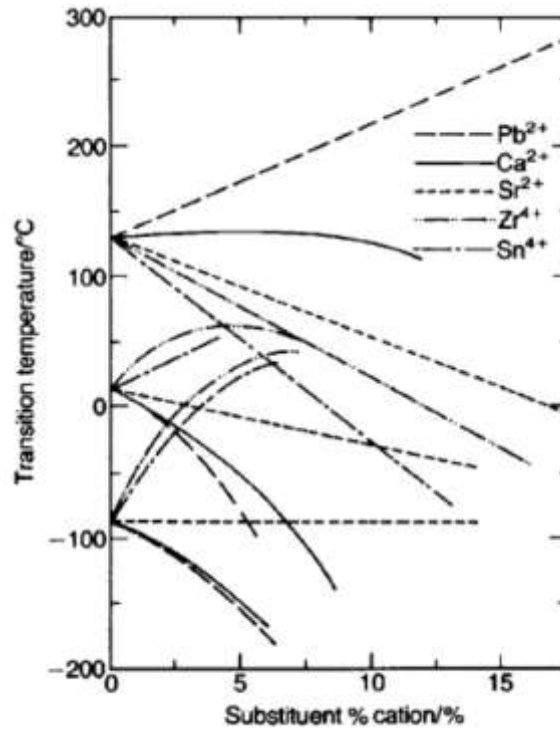


Figure 1-9: Transition temperature vs. concentration of isovalent substitution in BT [42].

1.5.1.2 Aliovalent doping

Aliovalent doping refers to the substitution of host ion with an ion of different charge. If the valence state of the dopant is greater than that of the host ion, it is known as a donor dopant. If the valence state of dopant is less than that of host ion, then it is known as an acceptor dopant. e.g. A^{3+} and A^{+1} ion on A-site of BT are termed as donor and acceptor respectively.

These two kinds of dopant are schematically presented for a cubic perovskite structure in Figure 1-10, which shows that the generation of vacancies in the lattice are generally required for aliovalent doping in order to maintain the charge neutrality with an ionic compensation mechanism. However, electronic compensation mechanisms are also possible.

Aliovalent dopants such as RE^{3+} ions show significant effect on lowering of the ferroelectric phase transition temperature T_C and may also change the character of the phase transition and temperature-dependence of the permittivity which may be associated with differences in ionic radii [12].

On substitution of aliovalent ions for Ba, the rate of decrease in T_C is 25 °C/mol% of La^{3+} [60] and Nd^{3+} [61]. Substitution of aliovalent ions for Ti ions shows that the rate of decrease in T_C is 20 °C/mol% of Ho^{3+} [62].

The character of the diffuse phase transition, accompanied by a broad permittivity peak and relaxor character was separated at high dopant concentration either on Ba-site such as La^{3+} at ≥ 10 mol% [60] or Ti-site such as Ho^{3+} at ≥ 7 mol% [62].

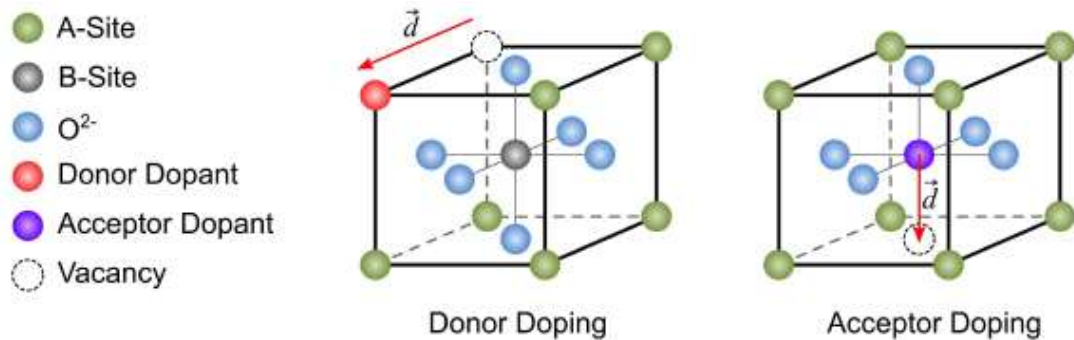


Figure 1-10: Perovskite structure: effect of aliovalent doping. Creation of A- or B-site vacancies is a result of donor doping, whereas creation of oxygen vacancies is a result of acceptor doping. Red arrows represent the resulting electrical dipoles [29].

Examples of donor doping are rare-earths doped on the A-site or Nb^{5+} doped on the B-site. Donor doping with electronic charge compensation results in injection of extra electrons, and semiconducting behaviour. By contrast, ionic compensation results in insulating ceramics. Though there are no clearly defined conditions which favour the choice of compensation mechanism, electronic compensation appears to be dominant at low concentrations of dopant and ionic compensation to be dominant at higher concentrations.

1.5.1.2.1 RE^{3+} -doped BT

Rare-earth (RE^{3+}) ions at low dopant levels in solid state materials are often used for obtaining the commercial formulations of BT-based devices. Performance can be improved by doping RE^{3+} , such as the reliability in capacitors operating under high voltages [63]. The role of ionic radius of RE^{3+} is obviously important to control the substitution mechanism and resulting properties [64]. Small ions occupy the six-coordinated Ti-site whereas, large ions occupy the 12-coordinated Ba-site [65]. All RE^{3+} elements are larger than Ti^{4+} and smaller than Ba^{2+} . Therefore, the

incorporation of RE into BT leads to the expansion the lattice on the B-site and shrinkage on the A-site [66].

The ionic radii of several rare earth elements are listed in Table 1-1, which are categorized into three groups [67, 68].

In order to discuss/review the literature and present the results of this thesis, RE doping is separated into three main groups, B-site doping (acceptor join), (A, B)-site double doping (self-compensation join) and A-site doping (donor join). These are referred to as RE-B, RE-AB and RE-A respectively. Compositions in the three groups are given in terms of variables x , y and v, z, ω which specify the fractional substitution of RE for B, AB and A with the following general formulae:



In this thesis, solid solutions of Yb, Er, Y, Ho, Gd and Dy-doped BT on acceptor, self-compensation and donor joins are discussed which were prepared using a variety of methods and different conditions. Some results seem to contradict other results, depending on the reaction conditions. A summary of reported solid solution limits in the literature is shown in Table 1-2.

Table 1-1: Ionic radii of rare earth elements [68].

	Coordination number	
	6	12
Light rare earth ions (large ionic radius)		
La³⁺	1.032	1.360
Ce³⁺	1.01	1.340
Nd³⁺	0.983	1.270

Middle weight rare earth ion (intermediate ionic radius)

Sm³⁺	0.958	1.240
Eu³⁺	0.947	1.266
Gd³⁺	0.938	1.253
Dy³⁺	0.912	1.229
Ho³⁺	0.901	1.218
Y³⁺	0.90	1.234
Er³⁺	0.89	1.208

Heavy rare earth ions (small ionic radius)

Yb³⁺	0.868	1.188
Lu³⁺	0.861	1.178

Table 1-2: The solid solubility of some RE³⁺ ions in the BaTiO₃ perovskite structure.

	Acceptor (RE-B)	Self (RE-AB)	Donor (RE-A)
Yb	0.15*[57]	$y < 0.01$ *[57]	$\nu < 0.01$ *[57]
Er	$x < 0.03^{\beta}$ [69] or 0.10*[70]	$y < 0.03^{\$}$ [69]	$\nu < 0.01^{\$}$ [69, 70]
Y	$x < 0.03^{\beta\$}$ [71] or 0.122*[72] or 0.15 [@] [36]	$y \leq 0.01$ *[73] or 0.03*[74]	$\nu < 0.015$ *[72]
Ho	$x < 0.03^{\$}$ [75]0.175*[76] or 0.16 [@] [36]	0.03*[76] or $y <$ 0.03*[77] or 0.044*[77]	0.014 [@] [36, 76]
Gd	0.0375*[57]	0.20*[57]	0.05*[57]
Dy	$x < 0.03^{*\$}$ [78] or 0.09*[79] or 0.15 [@] [36]	$y < 0.03$ *[77]	0.025*[79] or $< 0.03^{*\$}$ [78] or 0.015 [@] [36]

* by XRD, β by SEM, [@] by WDS (wavelength-dispersive spectroscopy), ^{\\$} σ , x at RE-B, y at RE-AB, ν at RE-A

Different factors are reported to affect the substitution site such as dopant content, sintering atmosphere and Ba/Ti molar ratio [80, 81].

In donor doping, semiconductivity with a resistivity minimum and PTCR effect has been observed at low RE dopant levels (0.001-0.01) as indicated in Figure 1-23. Increasing RE^{3+} concentration > 0.01 leads to insulating behaviour [80]. The resistivity minimum was linked to an influence of grain size which is associated with either kinetic processes during heating and cooling [47] or switching of the substitution mechanism from electronic charge compensation to cation vacancy creation [65]. Cation vacancy creation may lead to the decrease of grain size and formation of an insulating layer of barium vacancies during cooling [82]. It was attributed also to segregation of dopants at grain boundaries [83].

Many theoretical reports were considered to study BT based on ab initio methods. Density Functional Theory (DFT) provides good structural and energetic agreement with the available experimental data [84].

For RE^{3+} -doped BT, Lewis and Catlow provided a classical simulation model of possible defects in BT. This model was used to describe the perovskite crystal structure and lattice, with the suggestion that electron compensation mechanism of A-site donor doping is unfavourable because the reduction of the RE ion size as the self-compensation mechanism is more favourable.

Another model was provided by Buscaglia et al. [85] which showed that the Ti vacancy compensation with A-site donor doping was energetically unfavourable.

The BT perovskite structure was modelled recently by Freeman and Sinclair using a new set of interatomic potentials. Multiple parameters were used to fit the potential model over the range of experimental and ab initio data through lattice parameters and the cohesive energy of rutile TiO_2 , BT and BaO. Rare-earth doped-BT of five possible compensation mechanisms was investigated to study the energetics of the BT defect chemistry. Both simulations and experimental data confirmed that small rare-earth ions substitute only on the B-site; medium sized rare-earth ions substitute on both the A and B sites and large rare-earth ions substitute only on the A-site. The simulations for donor doping showed that electron compensation mechanism was energetically unfavourable, whereas, Ti vacancy mechanism was favourable [86].

It was believed that the origin of semiconducting grains is direct donor doping for rare earth elements on the Ba-site [87]. Sinclair et al. reported that this is incorrect, depending on the calculations and some experimental data. The origin of the semiconductivity was indicated when oxygen anions are removed from the lattice which is associated with titanium vacancies formation and the arrangement of the rare-earth elements on the Ba-sites [87].

The energetics of La-doped BT were observed for electronic and ionic compensation mechanisms with the creation of Ti^{3+} cations and Ti vacancies respectively. Ionic doping mechanism was favourable experimentally and simulations for all dopant levels of La-doping. The favourability of oxygen loss in the ionic doped mechanism compared to undoped BT was indicated by simulations of the local structure created around the defect site [87].

In acceptor doping, insulator behaviour was observed at room temperature (RT). The first series of transition metals (Ni, Co, Fe, Cr) can be incorporated as acceptor dopants in BT as part of the procedure to fabricate multilayer ceramic capacitors (MLCCs). This can be used to produce cheaper metal electrodes (such as Ni) [80].

Both PTCR and MLCC BT ceramics usually are obtained with RE-doped BT to control conductivity and electrical degradation, respectively [66].

RE ions are well-known to display the valuable functions of stabilizing the temperature dependence of permittivity and lowering the dissipation factor for different kinds of dielectric ceramic [67, 88]. The dielectric performance of capacitors is affected by the amount and kind of RE ions. Many factors influence the substitutional chemistry such as: strain, ionic size, charge and charge distribution [66] but many authors mentioned that ionic size is the main factor [89].

RE^{3+} occupation on Ba or Ti sites causes a charge mismatch in the lattice (an aliovalent dopant). These charges have to be compensated to maintain electrical neutrality [90]. This doping may also lead to the abnormal grain growth and can form a shallow and deep traps at grain boundaries [91].

Dopant site location was found to play a very important role in electrical properties of RE^{3+} -doped BT [92]. Dopants can occupy both A- and B-sites simultaneously to various extents, showing amphoteric behaviour. They were proved to be effective in

improving the lifetime of certain formulations and heat treatments, showing insulating resistance improvement in Ni-electrode MLCCs [64, 66, 93].

A full understanding of the factors leading to property improvement is still not clear [64, 94]. The Ba-site doping model proposes that rare earth elements act as donors where reliability can be improved as a result of the reduction of oxygen vacancy concentration [95] whereas, the Ti-site doping model proposes that rare earth elements act as acceptors and improved reliability attributed to reduction in bulk diffusivity of oxygen vacancies during interactions is between strain and electric field [96].

The lifetime of MLCCs is associated with substitution sites and charge compensation mechanisms. The larger rare-earth ions: La, Ce and Sm, predominantly substitute in A-sites, and act as donors with charge compensation via titanium vacancies. Intermediate ionic size ($0.87 < r < 0.94 \text{ \AA}$) rare-earth ions (Y, Gd, Dy, Ho, Er) [97] dissolve in both A and B- sites. Excess Ba ($\text{Ba/Ti} > 1$) favours substitution at the B-site whereas, excess Ti ($\text{Ba/Ti} < 1$) favours substitution at the A-site. The smaller rare-earth ions: Yb and Lu substitute in the B-site and act as acceptors with charge compensation via oxygen vacancies [98]. A core-shell structure may form with some RE ions [89].

Yb-doped BT:

Yb^{3+} (0.87 \AA) is well-known to act as an acceptor at the Ti^{4+} site where charge deficiency leads to formation of ionized oxygen vacancies ($V_{\text{O}}^{\bullet\bullet}$) [67, 99]. Yb can only be substituted on the Ti site [36, 92, 99, 100]. Secondary phases on the donor and self-compensation joins have been detected for all compositions at $v, y \geq 0.01$ [57].

Yb_2O_3 is used to suppress capacitance degradation in response to a dc bias [36, 100]. The published research regarding the electrical properties of Yb-doped barium titanate are inconclusive [100].

B-site doping of Yb may be represented as follows:



The solubility limit appears to be $> 3\%$ Yb [100]. Yb-doped BT is p-type and becomes n-type with decreasing pO_2 , Figure 1-11 [101-103]. At low pO_2 , there was reduction with creation of oxygen vacancies and electrons as the main carriers whereas, at high pO_2 , there was oxidation reaction for the removal of oxygen vacancies and creation of holes [104]. p-type and n-type mechanisms are discussed later in section 1.6.1.

On the acceptor join, $Yb_2Ti_2O_7$ appears if the Yb content exceeds 3 mol% [105] but some researchers have claimed the solubility limit is 15 mol %. The tetragonality reduced with increasing Yb [100] and cubic BT-Yb was obtained up to $x = 0.05$. Hexagonal $BaTiO_3$ was obtained for $0.05 \leq x \leq 0.15$, $Ba_{12}Yb_{4.67}Ti_8O_{35}$ appears for $x > 0.15$ [57]. With increasing x , the unit cell volume increased dramatically. It increased slightly for the self-compensation and donor joins which might indicate limiting ranges of solid solution on these joins [57].

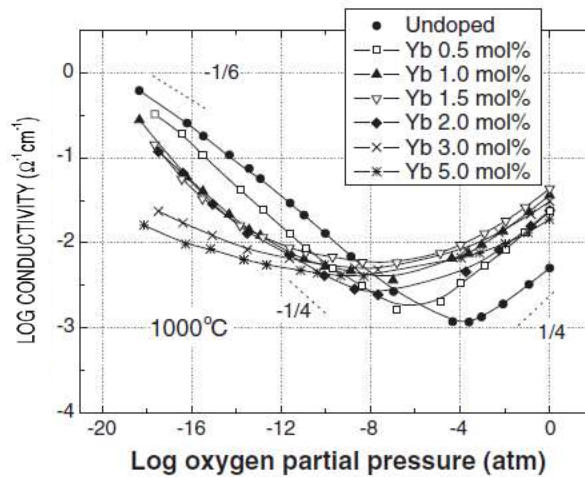


Figure 1-11: σ of BT and acceptor-doped BT vs. $\log pO_2$ at 1000 °C [100].

Er-doped BT:

Er-doped BT was studied on acceptor, self and donor joins. The resulting properties for samples at $x,y,v \leq 0.01$ were significantly independent of the Ba/Ti molar ratio [70].

Semiconducting materials were observed at $x,y,v \leq 0.01$ with resistivity $\sim 10^3-10^4$ Ωcm and resistivity minimum was observed at $x,y,v = 0.002$. Lattice parameter slightly decreased until $x,y,v = 0.0025$ then increased. This behaviour was

interpreted to show that both cation sites incorporated Er with preferential substitution at Ba^{2+} sites at ≤ 0.01 [70].

At 0.02, the resulting properties for samples were significantly dependent on stoichiometry. For example, the pyrochlore $\text{Er}_2\text{Ti}_2\text{O}_7$ phase was detected for Ba/Ti molar ratio < 1 and the material changed from a slight semiconducting behaviour at $x, y, v = 0.02$ to insulating at $x, y, v = 0.08$. The solid solution limit is at $v \leq 0.01$ on the Ba-site. After achieving this level, extra Er dopants can incorporate on the Ti-site until $[\text{Er}'_{\text{Ba}}] \approx [\text{Er}^{\bullet}_{\text{Ti}}]$. Above this limit, the pyrochlore phase forms [70].

For Ba/Ti molar ratio > 1 , a single phase with insulating behaviour was observed at ≥ 0.02 . The solid solution limit for Er^{3+} substituted on the Ti-site is at $x = 0.10$ and is associated with creation of oxygen vacancy and decreasing tetragonality [106] until $x = 0.08$; as the cubic phase was observed at $x \geq 0.08$; accompanied with unit cell expansion and grain size reduction ($\sim 1\mu\text{m}$). A high concentration of oxygen vacancies was obtained at high x and at high temperature, the solid solution may be anionic conductors and potential ceramics for oxygen transport [70].

For Ba/Ti molar ratio = 1, no full incorporation was observed and a secondary phase of pyrochlore phase was detected at $y \geq 0.01$ [70].

It was established that doping of Er^{3+} ions in low content with sintering at < 1400 °C for short times favoured substitution at the Ba site whereas, sintering at > 1400 °C with long times (until 100h) was necessary to obtain a homogeneous dopant distribution on the Ti-sites for high Er content [70]. Moreover, the substitution at low Er content was influenced by a slight variation of the Ba/Ti ratio from the nominal value and the existence of impurity in raw materials [70].

The conductivity was studied with changing $p\text{O}_2$ [69]. The incorporation of Er^{3+} into the Ti-site on the acceptor join, Figure 1-12 (a) showed that the conductivity minimum significantly shifted to lower $p\text{O}_2$. No discernible difference was observed between BT and Er-doped BT on the self-compensation join (b). Acceptor-doped behaviour was observed for both cases (a) and (b). The solid solution limit on Ti-site was determined to be at $x < 0.03$, depending on conductivity data. As no clear change was shown for incorporation of Er into stoichiometric BT, it was assumed that Er substitutes both sites simultaneously. As the transition from electron- to

cation vacancy-compensation occurs usually above $y = 0.005$, the donor behaviour was not observed due to low solid solution limit on Ba-site, at $v < 0.01$.

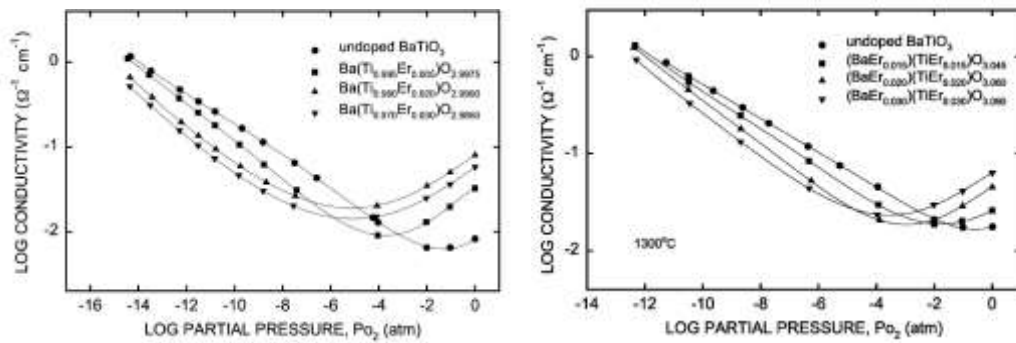


Figure 1-12: σ of BT and (a) ER-B (b) ER-AB vs. $\log pO_2$ at 1200 °C [69].

The conductivity was studied also with changing pO_2 for BT, acceptor (BE), self (BTE) and donor (TE) at 0.01, Figure 1-13 [106]. BE and BTE show similar behaviour. It was suggested that Er substitutes on Ba-site as donor dopant, whereas, the conductivity minimum of TE shifted to lower pO_2 as Er substitutes on Ti-site as acceptor dopant.

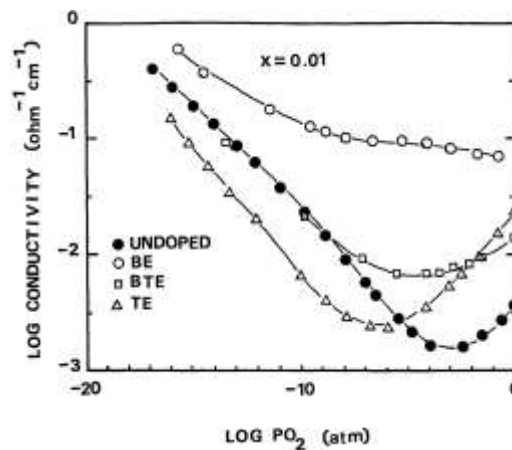


Figure 1-13: σ of BT, acceptor (BE), self (BTE) and donor (TE) vs. $\log pO_2$ at 0.01 at 1000 °C [106].

Y-doped BT:

Numerous studies of the conductivity of Y-doped BT have been reported. The conductivity of doping low level of Y^{3+} to Ti-excess BT ($(Ba+Y)/Ti = 1$) [107] and Ba-excess BT ($Ba/(Ti + Y) = 1$) [108] is shown in Figure 1-14. In both cases, the

preferential substitution site of Y^{3+} ions was Ba-site. The grain size was large at low concentrations ≤ 0.005 whereas, at ≥ 0.01 the grain size was small with uniform grain size distribution. The lattice parameters a and c decreased with increasing Y at ≤ 0.01 , which indicates that Y prefers to substitute on the Ba-site [107, 108] whereas, they increased at ≥ 0.01 for Ba-excess with incorporation into Ti-site [108]. In both cases, at ≤ 0.01 , donor-doped behaviour was observed whereas, at ≥ 0.01 , it was acceptor-doped.

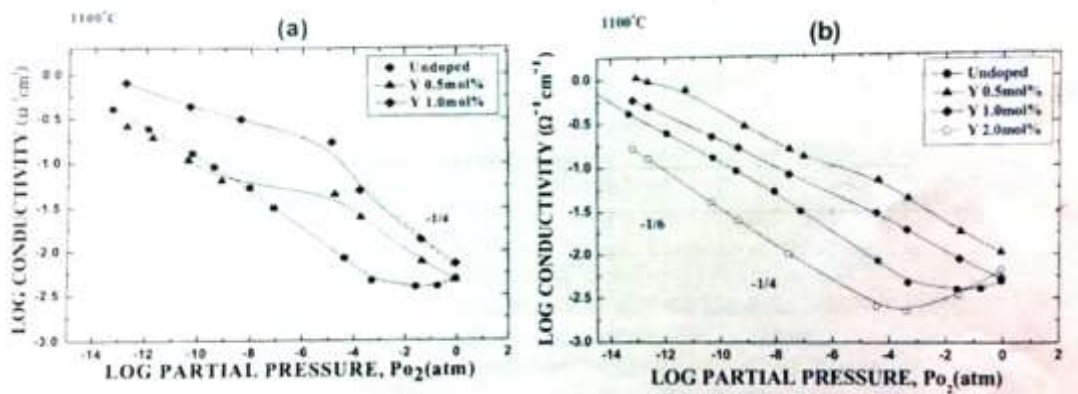


Figure 1-14: σ of (a) $BaTiO_3 + x(0.5Y_2O_3+TiO_2)$ and (b) $BaTiO_3 + y(BaO + 0.5Y_2O_3)$ vs. $\log pO_2$ at $1100\text{ }^\circ\text{C}$ [107].

In contrast, other reports [71, 101] showed that the conductivity minimum of doping Y into Ti-site shifted to lower pO_2 with increasing the oxygen vacancy concentration, showing acceptor-doped behaviour. It was suggested that the solid solution limit is ≤ 0.03 since no change in conductivity was observed with increasing Y which is associated with general suppression of the entire curve, Figure 1-15. At concentrations > 0.02 , SEM showed poor densification with a large amount of residual porosity [101].

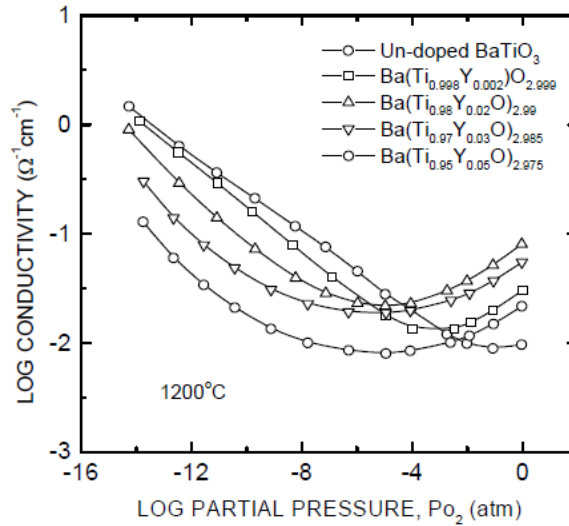


Figure 1-15: σ of BT and acceptor doping of BT vs. $\log pO_2$ at 1200 °C [71].

The equilibrium electrical conductivity was studied as well for self and donor joins, Figure 1-16 [101]. At the high oxygen activity region, the conductivity of $(Ba_{1-y}Y_y)TiO_{3+0.5y}$ shows a power law dependence on pO_2 with an exponent close to $-1/4$. Donor-doped behaviour was observed for stoichiometric BT doped with 0.01 of Y whereas, acceptor-doped behaviour was observed for 0.02 indicated by the shift of conductivity minimum towards a lower pO_2 .

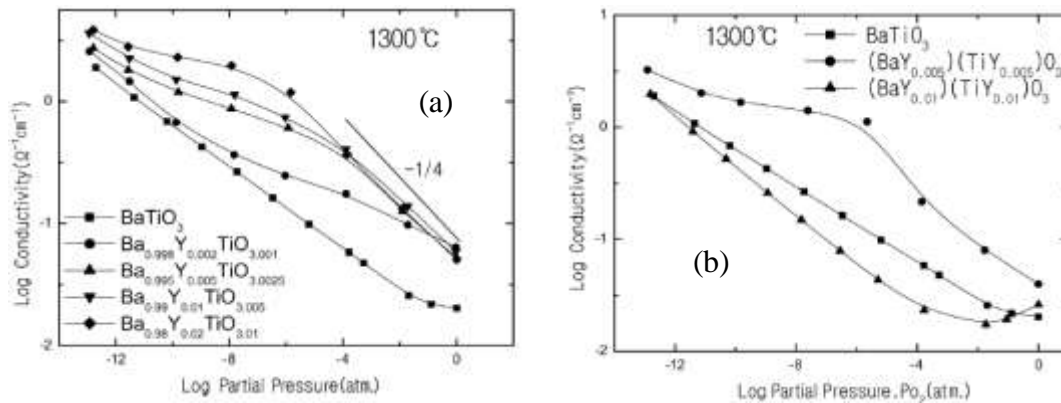


Figure 1-16: σ of (a) $(Ba_{1-y}Y_y)TiO_{3+0.5y}$ and (b) $(BaY_y)(TiY_y)O_3$ vs. $\log pO_2$ at 1300 °C [101].

The resistivity of Y-A for low concentrations for samples sintered at 1300-1350 °C; passed through a minimum between 0.003 and 0.006, Figure 1-17 [109].

The effect of preparation method was studied for BT with 0.01 excess titania doped with Y^{3+} , Figure 1-18 [110]. Conventionally milled samples of barium carbonate,

(A) and an alkoxide-hydroxide route (B) were sintered at 1350 °C for 2h, SC. U-shape curve was observed for both bulk and grain boundary, (a). Figure 1-18 (b) showed the influence of preparation method on bulk resistivity. Semiconducting materials were observed only between 0.001 and 0.004.

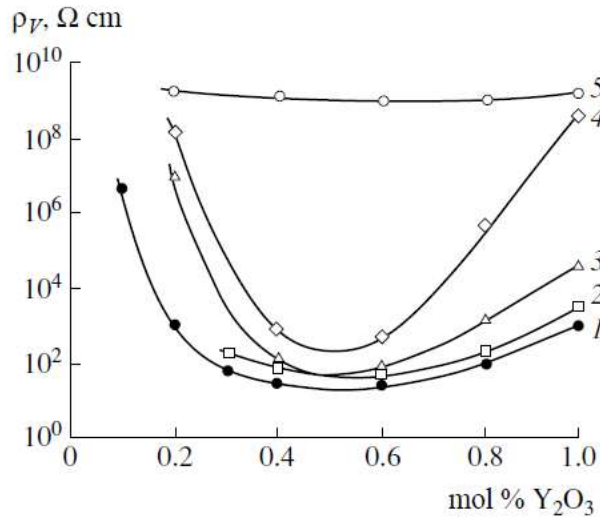


Figure 17: Resistivity vs. Y-A containing (1) 0, (2) 0.004, (3) 0.002, (4) 0.01, and (5) 0.05 mol % Fe₂O₃ [109].

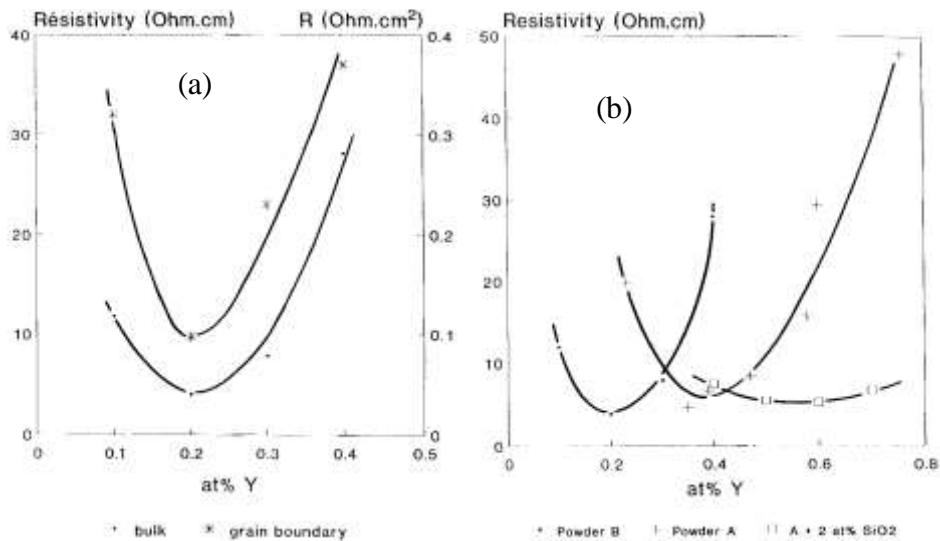


Figure 1-18: Resistivity vs. Y-A for (a) the bulk and the grain boundary of a sample prepared by an alkoxide-hydroxide route, sintered at 1350 °C, SC and (b) the bulk for samples prepared by conventional milling (A), an alkoxide-hydroxide route (B), and a sample containing silica [110].

Y was added to commercial BaO-excess (Ba/Ti=1.013) BT powder, Figure 1-19 [111]. The colour changed from bluish at 0.0015 to a darker hue at 0.0065. At > 0.0065, insulating behaviour was observed with brown to buff colour. A rapid decrease in conductivity was seen for samples sintered at < 1450 °C at 0.0065. σ of RT was in the range 10^{-2} to 10^{-4} (Ωmm)⁻¹ at < 0.005. Conductivity reduction was shown for samples sintered at 1450 °C but without showing the discontinuity compared to those sintered at < 1450 °C. The rapid decrease in semiconductivity was between 0.0050 and 0.0065.

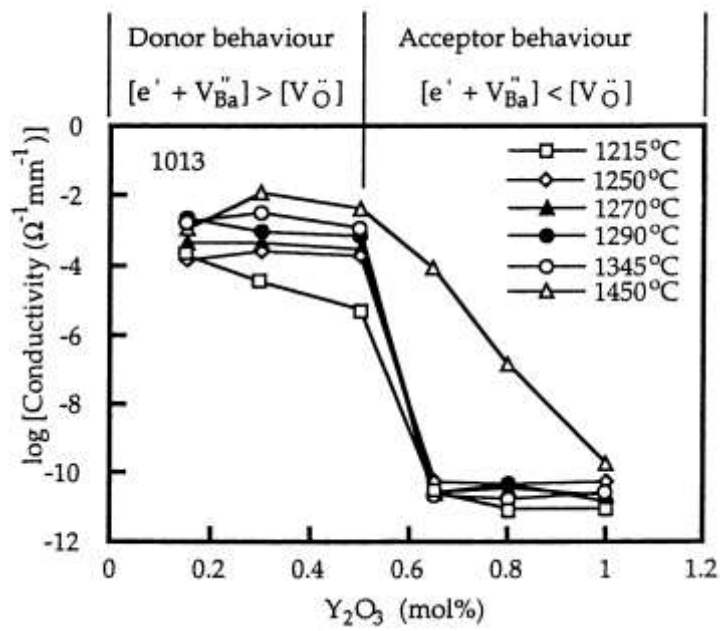


Figure 1-19: Conductivity vs. Y content for samples sintered at 1215–1450 °C [111].

Y-A samples of 0.001, 0.003, 0.005, 0.01 and 0.03 were sintered at 1350 °C in different atmospheres. Grain resistance with increasing Y content increased for samples heated in O₂ whereas, the increase stopped for samples heated in N₂, Figure 1-20 [82].

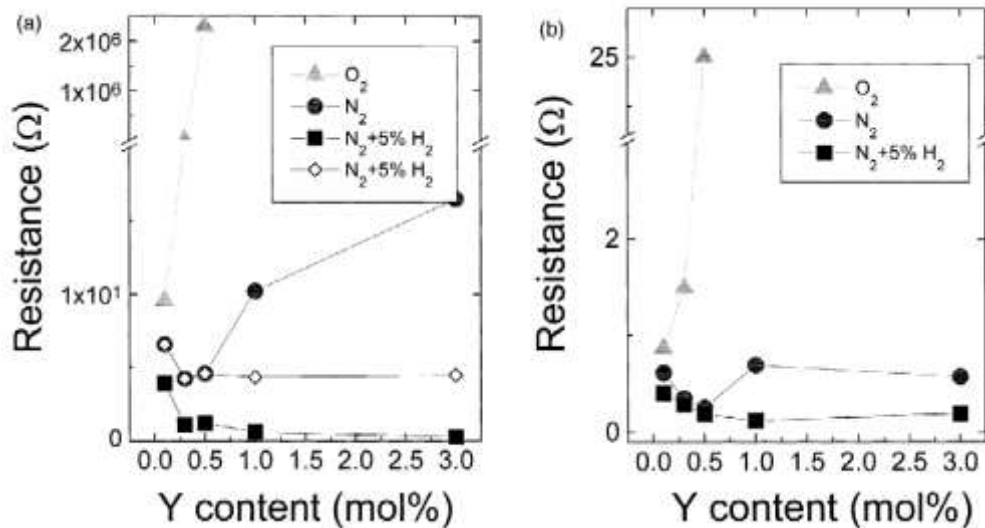


Figure 1-20: Influence of Y content and heating atmosphere on resistance of Y-A samples for (a) grain boundary (gb) and (b) grain (g) [82].

Ho-doped BT:

For Ho-B, the solid solution limit was 0.175 at 1550 °C [62]. Transformation from the hexagonal to the cubic phase at high concentrations can be explained by Ostwald's rule of successive reaction [112]. T_C moved to lower temperatures by ~ 20 °C/at% Ho [62]. Insulation behaviour was observed for samples sintered at 1400-1500 °C, SC. At high temperatures, both bulk and grain boundary components were observed. No systematic trend was observed for conductivity data with increasing Ho content whereas, ϵ_r was very Ho content-dependent showing a decrease in T_C frequency-dependent relaxor behaviour at $x \geq 0.07$. Semiconductivity was observed for samples sintered at 1350 °C in air or nitrogen for $x = 0.001$. A PTCR effect was observed for SC in air whereas, a weak one was shown with SC in nitrogen by a Schottky barrier effect [76].

BT ceramics with low Ho contents show abnormal grain growth with average grain size 20-40 μm [113]. For Ho-AB, lattice parameter increased and showed that Ho dissolved in the B-site until $y = 0.028$ and then in the A-site with a decrease in lattice parameter up to 0.044. The solubility limit was determined at ~ 0.044 as secondary phases were observed [77].

Resistivity minimum behaviour was studied for Ho-B for SC and Q samples, Figure 1-21 [114]. Resistivity generally did not show much dependence on cooling rate,

especially at $x < 0.03$. The resistivity minimum was observed over the range 0.001-0.01. Both 0.001 and 0.01 showed resistivity values for RT and 300 °C that were similar, whereas others were too resistive at RT. It was assumed that one Ho^{3+} occupies a Ti^{4+} site which is accompanied by reduction of a second Ti^{4+} to Ti^{3+} for each oxygen vacancy. A different report for the same compositions showed the conductivity minimum for Ho-B shifted to lower $p\text{O}_2$ as the incorporation Ho^{3+} for Ti-sites is increased to 0.03, Figure 1-22 [75].

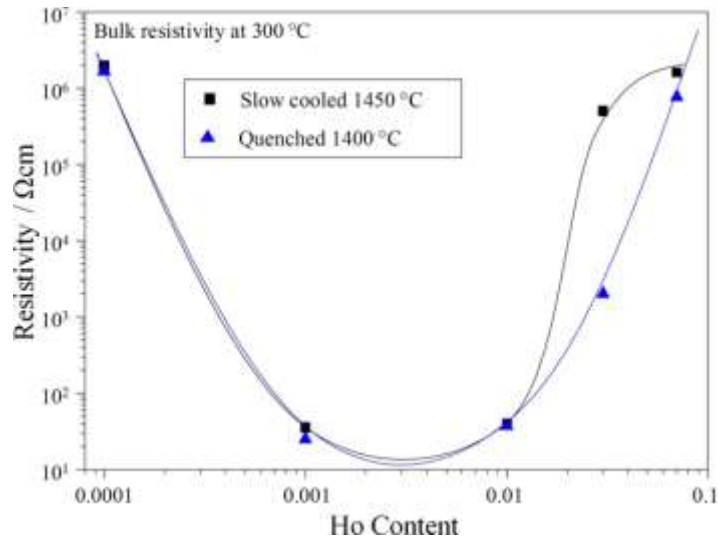


Figure 1-21: Resistivity vs. Ho content for Ho-B at 300 °C [114].

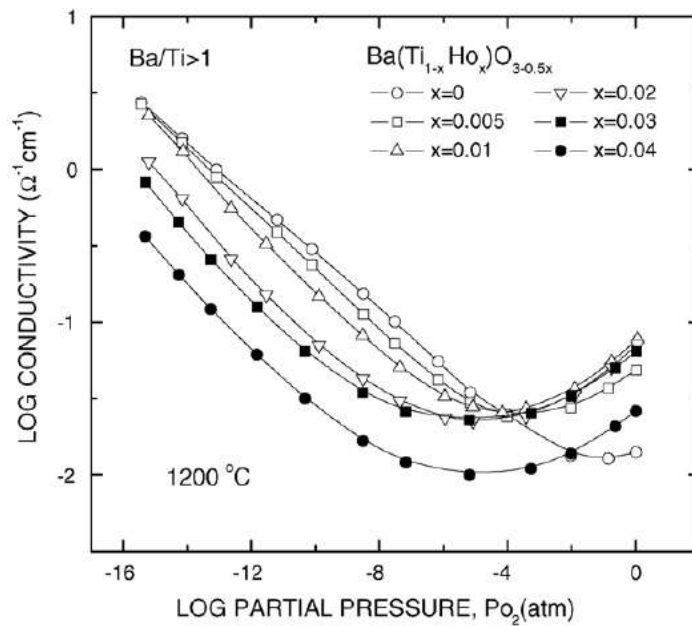


Figure 1-22: Equilibrium electrical conductivity of Ho-B at 1200 °C [75].

Gd-doped BT:

The solubility limits of Gd-B, Gd-AB and Gd-A were reported to be ~ 0.0375 , 0.20 and 0.05 respectively [57] and at 0.025 for Gd-A [115]. The hexagonal polymorph of BT was observed for Gd-B, $0.06 \leq x \leq 0.125$ [116]. An increase in unit cell volume was observed for Gd-B whereas, a decrease was observed for Gd-A, attributed to occupancy of Ti and Ba-sites respectively [57, 117]. For Gd-AB, unit cell volume was between Gd-B and Gd-A as self-compensation. Increasing Ba/Ti ratio resulted an increase in unit cell volume [57]. T_C decreased depending on the substitution mechanism [57, 117, 118]. It decreased at ~ 11 , 5 and 8 °C per mol% x, y and v for Gd-B, Gd-AB and Gd-A respectively.

Leaky dielectric behaviour was observed for Gd-A samples sintered in air with high $\epsilon_{r \text{ max}}$ at T_C and high $\tan \delta$ near RT. This was attributed to loss of oxygen, giving rise to semiconducting grains and insulating grain boundaries with generation of internal space polarisation between grains [57]. Non-leaky dielectric behaviour was observed for Gd-A sintered in O_2 and Gd-B and Gd-AB sintered in air. $\epsilon_{r \text{ max}}$ decreased dramatically with increasing x for Gd-B [57] and Gd-A [105]. Relaxor-type behaviour was shown over the range 0.10 - 0.20 for Gd-A [57].

The phase transition of Gd^{3+} -doped BT ceramics was studied by Raman spectroscopy. The intensity of the Raman bands for Gd-A at 205 cm^{-1} , 265 cm^{-1} , and 304 cm^{-1} decreased with increasing Gd. The decrease in intensity was attributed to the decrease in tetragonality. As a result, an extra band was obtained at 833 cm^{-1} . This extra band was observed with $0.01 \leq z \leq 0.35$, which was accompanied by the secondary phase $Gd_2Ti_2O_7$ [119].

Oxygen vacancies for Gd-B and Gd-AB at concentrations < 0.10 were created with similar bulk conductivity and activation energy. Oxygen vacancies were attributed to compensation of the acceptor doping for Gd-B and compensation of accidental acceptor impurities for Gd-AB. For Gd-AB at $0.10 \leq y \leq 0.20$, oxygen vacancies were excluded as a result of extra slight substitution of Gd on A-site more than B-site. Inhomogeneous materials with core-shell structure were observed at $y < 0.10$ whereas, homogenous materials were observed at $0.10 \leq y \leq 0.20$. The charge compensation mechanism was associated with Ti vacancy creation showing semiconducting bulk for Gd-A as a result of loss of oxygen [57].

The relationship between resistivity and concentration of Gd ions incorporated into BT under different conditions is shown in Figure 1-23. A sharp minimum or reduction of resistivity was observed generally [120]. For samples sintered at 1300 to 1400 °C in air or in N₂, electrical resistivity decreased with increasing Gd content and shows a minimum at a specific content. The semiconductivity was observed between 0.0005 and 0.003, but between 0.005 and 0.01 for samples sintered in N₂ and 0.001 and 0.006 for samples reheated in air [121]. For samples sintered at 1375 °C, semiconductivity was observed at 0.002 and insulating behaviour was shown at 0.006 for SC samples. Similar behaviour was observed for samples sintered in N₂ or quenched in air at 0.002 but the resistivity continues at the same level and independent of Gd concentrations until 0.01 [122]. Another study shows that a deep minimum was over the range from 0.0015 to 0.0025 [123].

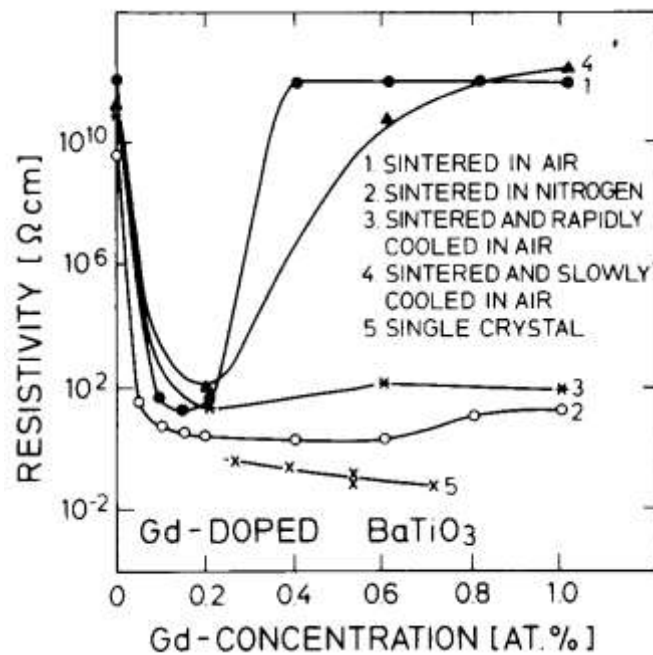


Figure 1-23: Resistivity vs. Gd content for Gd-A at different conditions [120].

Dy-doped BT:

The solubilities of Dy-B, Dy-AB and Dy-A were ~ 0.15, 0.044 and 0.012 respectively [36, 77]. Dy-doped BT may form a second phase, Ba₁₂Dy_{4.67}Ti₈O₃₅ for Dy-B and Dy₂Ti₂O₇ for Dy-A [79].

The hexagonal phase of BT was stabilized by preferential substitution of Dy³⁺ at the Ti⁴⁺ lattice sites [36].

For Dy-B, T_C decreased and $\tan \delta$ moved to higher frequencies with increasing Dy content by $-13.2 \text{ }^\circ\text{C/mol\%}$ which was associated with increase in unit cell volume and decrease in tetragonality (c/a ratio) [124]. The substitution of Ba^{+2} by smaller Dy^{+3} ions causes reduction of Ti^{4+} to Ti^{3+} . Consequently, a sharp decrease in resistivity was observed, Figure 1-24. A high resistivity anomaly was observed at 0.04 [125]. Inhibition of abnormal grain growth was observed at 0.0075 [125].

Equilibrium conductivities of Dy-B and Dy-A samples as functions of $p\text{O}_2$ are shown in Figure 1-25. For Dy-B, the conductivity minimum shifted significantly, showing acceptor-doped behaviour, (a) which indicates that the solid solution limit was < 0.03 .

Switching of the compensating mechanism from electronic to ionic was observed at 0.003 for Dy-A (b) in an oxidizing atmosphere, giving rise to insulating behaviour. At high oxygen activity, the equilibrium conductivity follows the $-1/4$ power $p\text{O}_2$ dependence.

The effect of substitution of Dy at Ba site is shown in Figure 1-26 at RT. The resistivity minimum was observed at very small range of Dy contents. The resistivity increased significantly above 0.005 showing insulator behaviour attributed to inward diffusion of Ba vacancies from the grain surfaces [126] or cation vacancy compensation of donors which act as acceptors [127] as there is a switch in the doping mechanism from semiconducting to insulating behaviour with increasing doping level [87].

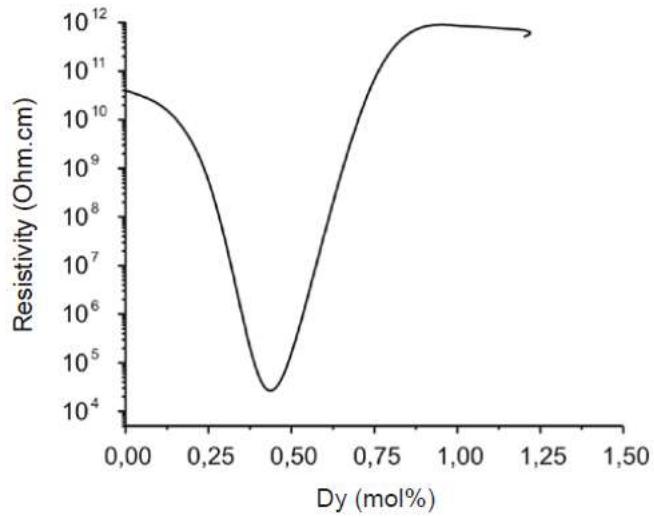


Figure 1-24: Resistivity vs. Dy content for Dy-A sintered at 1275 °C [125].

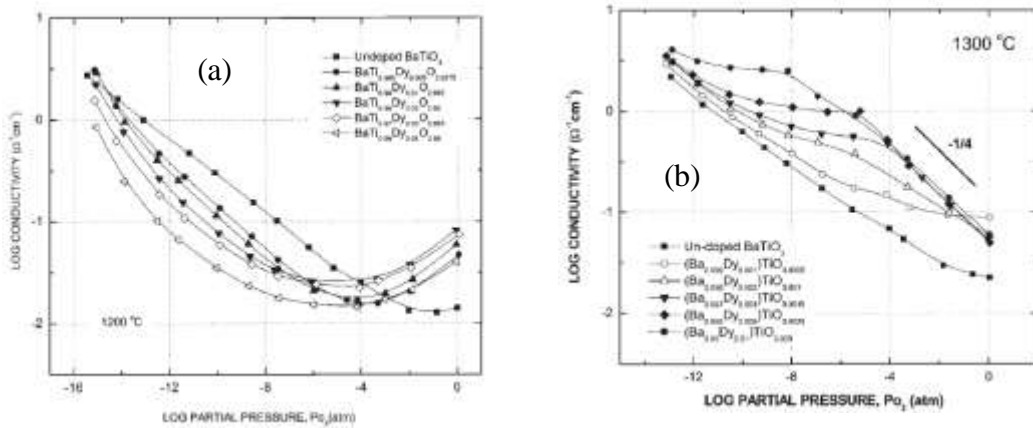


Figure 1-25: Equilibrium electrical conductivity of (a) Dy-B at 1200 °C and (b) Dy-A at 1300 °C [78].

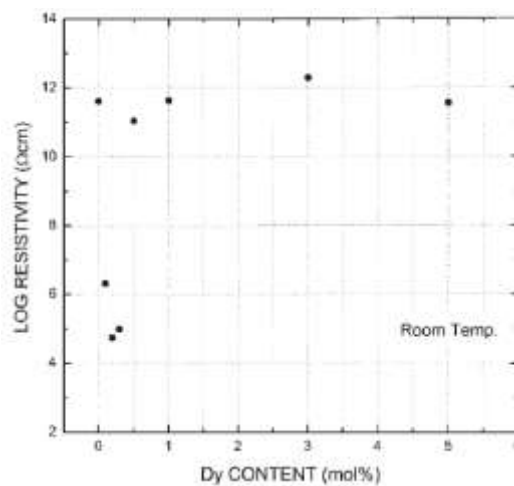


Figure 1-26: RT resistivity of Dy-A samples vs. Dy content for samples sintered at 1320 °C [78].

Ln-doped BT:

The substitution of BT materials by various Ln (rare-earth ions) produced semiconducting behaviour as the electrical resistivity decreased by several orders of magnitude, with increasing Ln content, Figure 1-27. The resistivity minimum was obtained at ~ 0.002 for (a) [128] and $0.003 - 0.005$ for (b) [129]. Y content showed the widest range of semiconductivity in both reports.

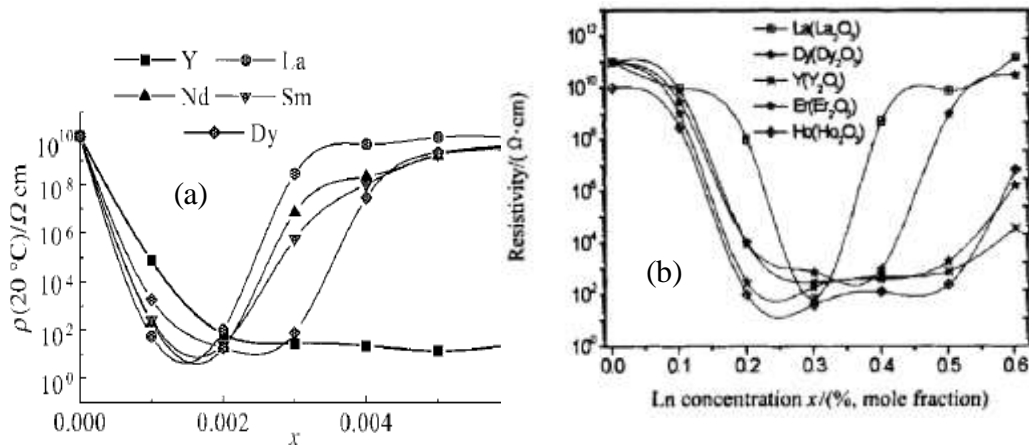


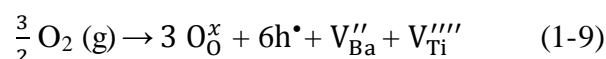
Figure 1-27: RT Resistivity vs. Ln content for (a) $\text{Ba}_{1-x}\text{Ln}_x\text{TiO}_3$ [128] and (b) $\text{BaTiO}_3 + 1/2_x\text{Ln}_2\text{O}_3 + 2\%\text{TiO}_2$ [129].

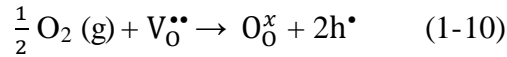
1.6 Effect of application of dc bias and pO_2 on undoped BT and RE^{3+} -doped BT

Application of dc bias and changing the oxygen partial pressure in the atmosphere is a useful strategy to investigate the nature of grain and grain boundary impedances, to separate material-dependent impedances from those associated with Schottky barriers (SB) and to characterise p- and n-type conduction mechanisms. This is because application of dc bias and/or changing pO_2 may show a general shift of impedance data to higher or lower resistances.

1.6.1 pO_2 effect

With increasing pO_2 , oxygen molecules are absorbed at the sample surface and ionized by trapping electrons from the sample interior as follows:

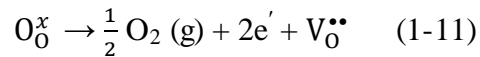




Electrons are clearly withdrawn from the sample. p-type conduction is indicated when the conductivity is increased as a result of an increase in $p\text{O}_2$ which is associated with increasing hole concentration due to withdrawal of electrons. n-type conduction is indicated, when the conductivity is decreased with increasing $p\text{O}_2$ [130].

The occurrence of p-type conductivity is associated with creation of holes. The source and location of the holes is usually attributed to the existence of unavoidable acceptor impurities such as Fe. However, it has been suggested recently that oxygen is the location of holes and O^- ions are the source of p-type semiconductivity. O^- ions are generated as a result of the sample uptaking of ionized oxygen and is associated with electron transformation from lattice oxide ions [131].

As conductivity increases with decreasing $p\text{O}_2$, n-type behaviour results. The variation of $p\text{O}_2$ from N_2 to O_2 changes the conductivity and carrier concentration. The reaction of oxygen at the sample surface is as follows [132]:



n-type semiconductivity behaviour can be observed as result of loss of oxygen from the sample as electrons are the carriers which are created by loss of oxygen [130].

The electrical properties of stoichiometric BT and nonstoichiometric-BT(as BaO-deficient and TiO_2 -deficient BT), prepared by conventional solid state reaction and sol-gel method, sintered at 1400 °C were studied in different $p\text{O}_2$ [133]. Polycrystalline BT prepared by conventional solid-state method, sintered at 1350 °C was also studied similarly [134]. Variation of $p\text{O}_2$ showed that both nonstoichiometric-BT samples, Figure 1-28 [133], Figure 1-29 [135] are p-type.

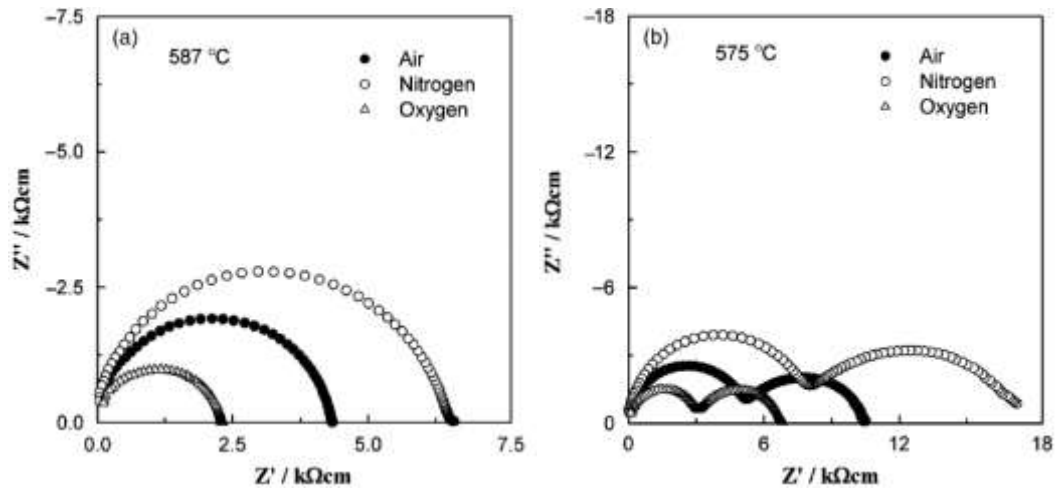


Figure 1-28: Z^* measured in different pO_2 for (a) BaTi_{0.99}O_{2.98} and (b) Ba_{0.99}TiO_{2.99} for solid-state reaction samples [133].

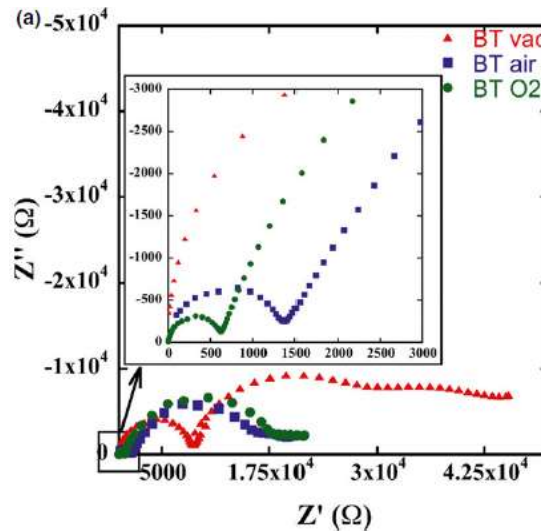


Figure 1-29: Z^* data measured in different pO_2 at 400 °C [135].

1.6.2 Dc bias effect

The increase in resistance with a small dc bias indicates n-type behaviour and vice versa, p-type may be indicated with a decrease in resistance with dc bias. The increase in resistance for n-type is associated with reversible trapping of electrons with dc bias at surface states. Trapped electrons can be released by removing the bias [130]. Ionization of absorbed oxygen molecules at the sample surface with electron withdrawal from sample interiors may be observed when dc bias is applied [136].

The electrical properties of BT, doped BT and some other materials are modified by application of a small dc bias [130, 131, 133, 134, 136-146]. n-type behaviour was indicated for Mn-doped BT and donor-doped rutile [145] and is associated with a decrease in conductivity. p-type behaviour was indicated for acceptor-BT such as Zn [142], Mg [143], and Ca [139] and was associated with increase in conductivity. In general, the ceramic conductivity increased by $\sim 1-2$ orders of magnitude under a small dc bias, which was recovered on removal of the bias. No effect was observed for an isovalent dopant such as Ba-site substitution by Ca [139] and other donor-doped materials such as Nb^{5+} for Ti^{4+} and La^{3+} for Ba^{2+} [139].

The source of this effect for the composition $\text{Ba}(\text{Ti}_{1-x}\text{Mg}_x)\text{O}_{3-x}$ is ascribed to a two-level electronic structure in a defect complex which includes Mg substituted on a Ti-site as acceptor dopant, leading to ionization of underbonded oxide ions in the crystal structure with application of a dc bias. O^- ions are considered as holes on oxygen and the source of p-type conductivity. The holes may be mobile rather than electrons trapped at the surface and oxygen vacancies [143].

The electrical properties of stoichiometric BT and nonstoichiometric-BT (as BaO-deficient and TiO_2 -deficient BT), prepared by conventional solid state reaction and sol-gel method, sintered at 1400°C were studied under a dc bias [133], Figure 1-30. No significant sensitivity to dc bias was observed for stoichiometric-BT whereas, dc bias decreased the resistance of nonstoichiometric-BT samples. For stoichiometric-BT, R_1 and R_2 of sol-gel sample mostly unchanged with very little decrease for R_2 whereas, R_1 and R_2 of solid-state sample reduced slightly.

Polycrystalline BT prepared by conventional solid-state method and sintered at 1350°C was studied by dc bias [134], Figure 1-31. Both bulk and grain boundary showed significant reduction of resistance with application of dc bias.

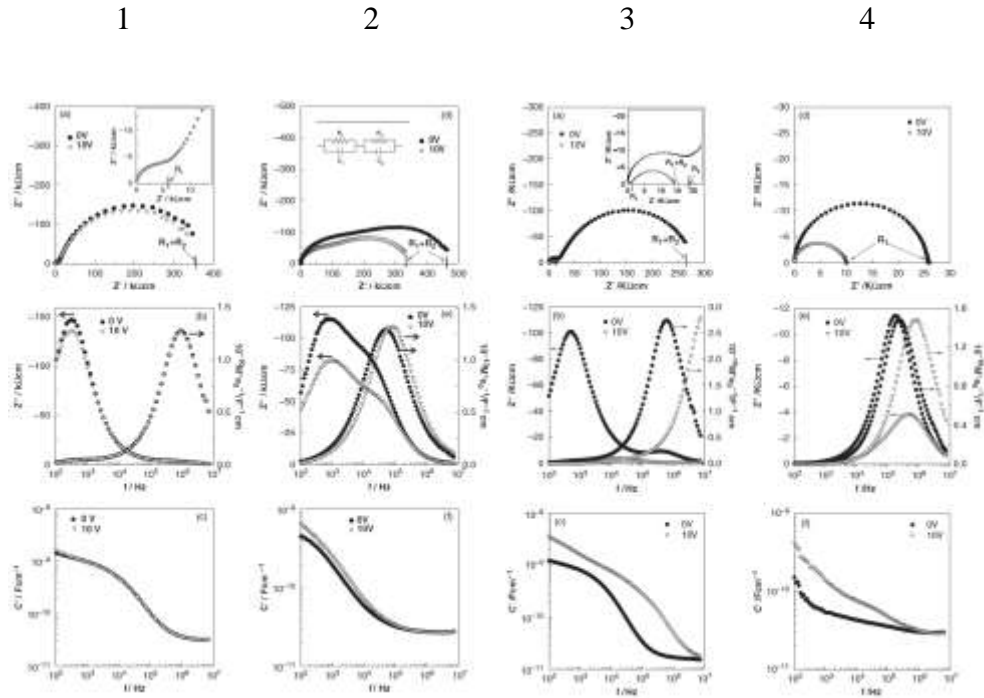


Figure 1-30: IS data at 472 °C for stoichiometric BT for sol-gel samples (a-c) (1) and solid-state reaction samples (d-f) (2), and at 485 and 477 °C for BaTi_{0.99}O_{2.98} for sol-gel samples (a-c) (3) and solid-state reaction samples (d-f) (4), with application and removing of 10 V [133].

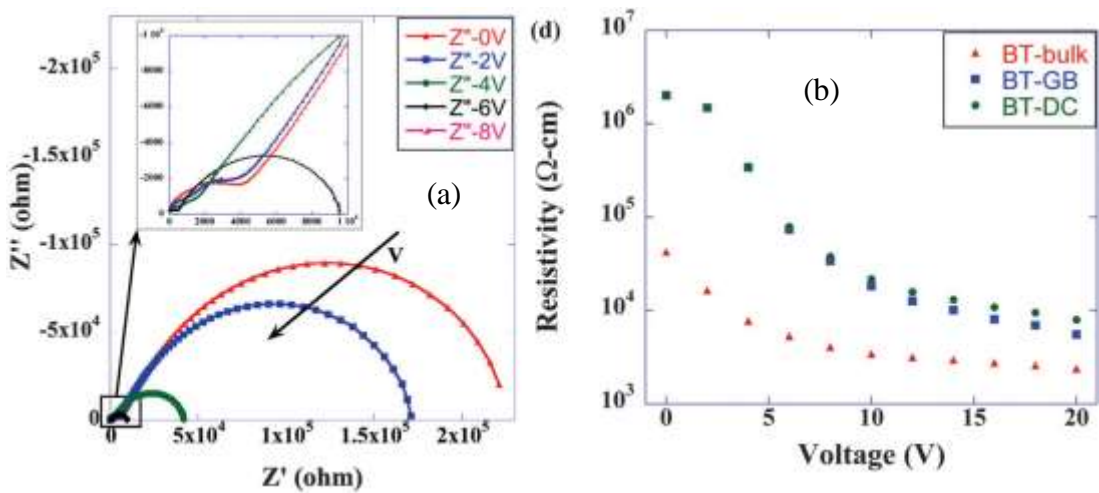


Figure 1-31: (a) Z^* data at 300 °C for stoichiometric BT with different dc bias and (b) resistivity of Bulk, GB and DC as a function of dc bias [134].

1.6.3 Schottky barrier effect

A Schottky barrier, SB, is a voltage barrier produced by charge transfer across a metal-semiconductor interface [140]. This phenomenon is used in various devices [147] such as: gas sensors, photovoltaics, photocatalysis and electronics [148]. The

formation of Schottky barriers is also associated with inhomogeneous materials at insulating gb separated by semiconducting g and/or at sample surfaces between insulating outer and semiconducting inner surfaces [149-151].

The heterogeneity between grains and grain boundaries is useful for many applications. The formation of SB at grain-grain boundary interfaces is often associated with ceramics that show PTCR effect in which the SB acts as an extrinsic source of electrical impedance [152]. A schematic diagram of a Schottky barrier is shown in Figure 1-32. Double Schottky potential barrier formation at grain-grain interfaces leads to an increase in the resistance which is used in different electrically heterogeneous materials, such as varistors and PTCR thermistors [150]. The potential barrier for conducting electrons between adjacent grains is produced by bending of the conduction band across the grain boundary as a result of the occurrence of charge trapping between adjacent grains [153].

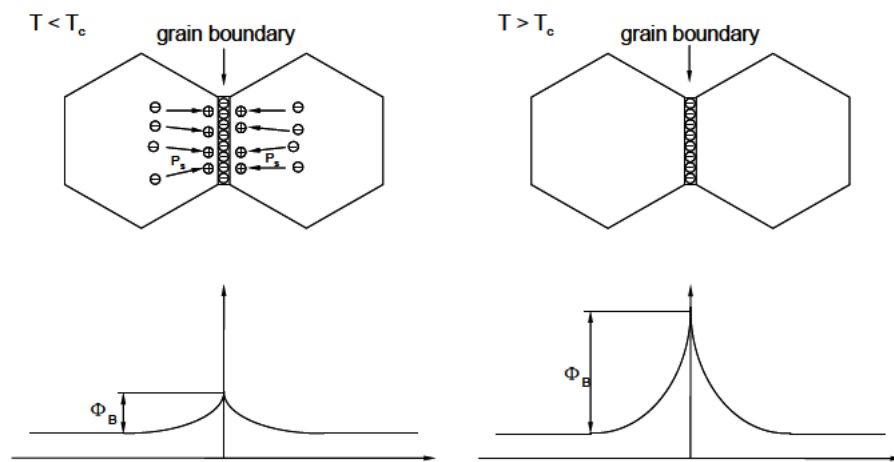


Figure 1-32: A schematic diagram of double Schottky barrier formation at a grain boundary [76].

The Schottky barrier height is associated with the distribution of charge carriers in the surface space charge region. This effect occurs usually between two materials as the result of the difference between their Fermi energies or when a charge is built-up on one side of the interface which induces a polarisation on the other side. Thus, a voltage-dependent resistance can be observed as result of the reduction of Schottky barrier height when dc bias was applied. This behaviour is useful for some applications such as: the operation of varistors (voltage dependent resistor (VDR)) and PTCR devices due to a rapid and reversible of the reduction in barrier height which can be observed on removal of the dc bias (in varistors) or changing

temperature through the paraelectric–ferroelectric transition temperature, T_C in PTCR devices. The rapidly reversible behaviour supports some applications in current- and voltage-overload protection devices [152].

Two contributions may be associated with Schottky barrier impedances:

- 1- Space charge separation generates the barrier height and dc bias can change its resistance as dc bias reduces the barrier height and its resistance.
- 2- A depletion layer can be formed at the surface. This is accompanied by displacement of electrons from the sample surface to the electrode, leading to formation an electron-deficient depletion layer. Its resistivity is greater than that of the grain interior, Figure 1-33 [140].

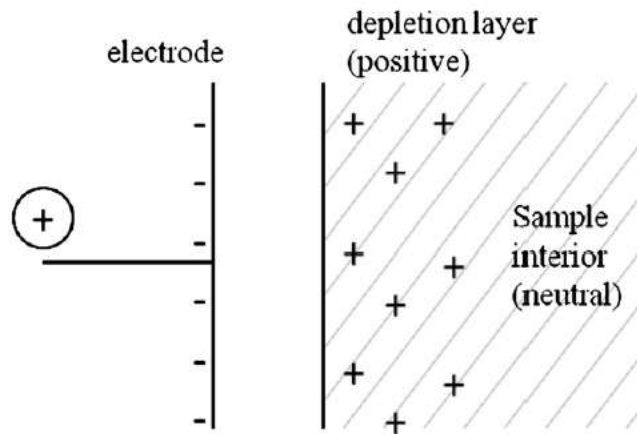


Figure 1-33: Depletion layer formation at the sample surface with dc bias [140].

Under application of a small dc bias voltage for insulating materials, linear bulk V–I behaviour is observed and dielectric breakdown is observed as well. The failure of dielectrics is a complex behaviour of very significant practical importance [152]. In materials that conduct electrically, random walk theory is a good model of the conductivity [154] when the mechanism of conduction involves hopping of electrons or ions.

The V/I behaviour obeys Ohm’s Law because the movement of electrons from one atom to another or the movement of charged negative particles (ions) can not be forced by application of a small dc bias.

A net drift in a specific direction can be obtained by applying a small dc bias voltage to the random hopping motions of the conducting species. This is a useful

test to determine the conduction by electron or ion hopping which should be uninfluenced by small applied voltages.

In contrast to bulk property measurements which obeys Ohm's Law, nonlinear behaviour may be found as interfacial effects between sample and the electrodes, ie Schottky barriers effects.

Nonlinear behaviour was observed for memristor effects [155] as result of a specific coupling of electronic and ionic transport charge through the interface for special state of $\text{TiO}_2/\text{TiO}_{2-\delta}$ interfaces [156]. There is electron injection into TiO_2 which is associated with transition from an insulating Ti^{4+} to semiconducting Ti^{3+} . The resulting conductivity modification, which is reversed by applying different amounts of reverse bias, provides unique applications in different types of memory storage devices.

The V-I characteristic usually obeys Ohm's law at small applied voltages for bulk homogeneous ceramics and non-appearance of a chemical potential gradient. Both structural and electronic changes such as promotion to higher energy levels usually are not influenced by the electric potential gradient.

At high applied voltages, V-I characteristics are more complex and may be associated with different parameters such as concentration, nature of the electrode materials, voltage level, trap energy level, charge carrier mobility, hopping rate, sample thickness, etc [130, 134, 157-159].

The relationship $I \sim V^a$, obeys Ohm's law when $a = 1$ whereas $a > 1$ is associated with high applied voltages.

The typical non-ohmic characteristics of barium titanate are interpreted by using different theories such as (i) Schottky barrier (SB) between metal electrode and semiconductor or between grains, (ii) Fowler-Nordheim (FN) tunneling, and (iii) space charge limited conduction (SCLC) with or without exponential trap distribution [160, 161].

SB usually form between the semiconducting sample-electrode interface. Mismatch of the valence (conduction) and Fermi levels of the electrode causes a SB for holes (electrons) [162]. The existence of this barrier can be avoided or reduced significantly by use of ohmic contact electrodes such as In-Ga.

At high field, the non-linearity in V-I behaviour of single crystals of BaTiO₃, BT and SrTiO₃ was attributed to hole injection from the Au anode. At low field, SrTiO₃ did not show this behaviour [163-167]. Dielectric breakdown was observed as result of charge injection from electrodes into the material's conduction band (CB) [143, 168].

It is considered that all the previous suggested models provide explanations about non-ohmic characteristic only at high fields, whereas at low fields, the non-linear regime is preceded by an ohmic linear region [134].

Under an applied dc bias voltage for stoichiometric, pure BT, the linear bulk V-I behaviour was observed whereas, nonlinear was observed for nonstoichiometric BT which could be BaO-deficient or TiO₂-deficient [133].

Impedance data of acceptor-doped BT showed two components; the voltage dependence of conductivity was detected in both g and gb and was insensitive to different types of electrodes, whereas impedance data of Ba(Ti_{1-x}Fe_x)O_{3-δ} showed that the low frequency component was insensitive to different types of electrode but had the behaviour of a voltage-dependent Schottky barrier at low frequency; the effect of both pO₂ and dc bias showed a charge carrier-rich, p-type layer to either side of the grain-grain contact [137].

1.7 Motivation and aim of this study

The aims of the project can be summarised as follows:

- 1- To clarify the effect of both dc bias and pO_2 on conductivity of BT obtained by different preparation routes, sintering temperatures and cooling rates; determination of the conduction mechanism(s), whether n- or p-type, and their dependence on sample preparation conditions.
- 2- To study the effect of yttrium on the polymorphism of $BaTiO_3$ and to determine the principal mechanisms for substitution of Y into the $BaTiO_3$ lattice.
- 3- To measure the electrical properties of Y-doped $BaTiO_3$ with particular emphasis on establishing the conditions under which either insulating behaviour or semiconductivity occurs, with determination of the conduction mechanism.
- 4- To determine the conditions under which a resistivity minimum occurs with increasing Yb, Er, Y, Ho, Gd and Dy content for BT doped on acceptor, self-compensation and donor joins at doping levels of x,y and $v \leq 0.01$, with determination of the conduction mechanism.
- 5- To investigate Schottky barrier effects and how the associated impedance depends on pO_2 and dc bias.

1.8 References

- [1] L.B. Kong, T. Zhang, J. Ma, F. Boey, Progress in synthesis of ferroelectric ceramic materials via high-energy mechanochemical technique, *Progress in Materials Science*, 53 (2008) 207-322.
- [2] G. Bertotti, I.D. Mayergoyz, *The Science of Hysteresis: Volume 1 of 3-volume set*, Academic Press, 2005.
- [3] G.H. Haertling, Ferroelectric ceramics: history and technology, *Journal of the American Ceramic Society*, 82 (1999) 797-818.
- [4] L. Cross, R. Newnham, History of ferroelectrics, *J Am Ceram*, 11 (1987) 289-305.
- [5] A. Moulson, J. Herbert, *Electroceramics* Chapman and Hall, New York, (1990) 41.
- [6] C. Randall, R. Newnham, L. Cross, History of the First Ferroelectric Oxide, BaTiO₃, Web Source, (2004).
- [7] S. Venigalla, BARIUM TITANATE(BaTiO₃), *American Ceramic Society Bulletin*, 79 (2000) 47-48.
- [8] M. Zenkner, L. Jäger, R. Köferstein, H.P. Abicht, Synthesis and characterization of nanoscaled Ba(Ti_{1-x-y}Sn_xGe_y)O₃ powders and corresponding ceramics, *Solid State Sciences*, 10 (2008) 1556-1562.
- [9] W. Heywang, Resistivity anomaly in doped barium titanate, *Journal of the American Ceramic Society*, 47 (2006) 484-490.
- [10] R. DeVries, J. Burke, Microstructure of barium titanate ceramics, *Journal of the American Ceramic Society*, 40 (1957) 200-206.
- [11] O. Saburi, Properties of semiconductive barium titanates, *Journal of the physical Society of Japan*, 14 (1959) 1159-1174.
- [12] J. Lin, T. Wu, Effects of isovalent substitutions on lattice softening and transition character of BaTiO₃ solid solutions, *Journal of Applied Physics*, 68 (1990) 985-993.
- [13] M. Issa, Electrical properties of polycrystalline PTCR barium titanate, *Journal of materials science*, 27 (1992) 3685-3692.
- [14] M. Kuwabara, K. Hamamoto, Electric field-induced birefringence in single grain boundaries of PTCR barium titanate ceramics above the Curie point, *Ferroelectrics*, 290 (2003) 71-81.

- [15] G. Jonker, Halogen treatment of barium titanate semiconductors, *Materials Research Bulletin*, 2 (1967) 401-407.
- [16] W. Heywang, Semiconducting barium titanate, *Journal of Materials Science*, 6 (1971) 1214-1224.
- [17] H. Gu, Processing of $\text{Pb}(\text{Mg}_{1/3}\text{Nb}_{2/3})\text{O}_3\text{-PbTiO}_3$ by a novel coating approach, in, Drexel University, 2003.
- [18] V. Lemanov, A. Sotnikov, E. Smirnova, M. Weihnacht, R. Kunze, Perovskite CaTiO_3 as an incipient ferroelectric, *Solid State Communications*, 110 (1999) 611-614.
- [19] J. Goodenough, J. Longo, Crystallographic and magnetic properties of perovskite and perovskite-related compounds, in, Springer-Verlag: Berlin, 1970, pp. 126-314.
- [20] R.H. Mitchell, *Perovskites: modern and ancient*, Almaz Press Thunder Bay, Ontario, 2002.
- [21] P.M. Woodward, Octahedral tilting in perovskites. I. Geometrical considerations, *Acta Crystallographica Section B: Structural Science*, 53 (1997) 32-43.
- [22] L. Feng, L. Jiang, M. Zhu, H. Liu, X. Zhou, C. Li, Formability of ABO_3 cubic perovskites, *Journal of Physics and Chemistry of Solids*, 69 (2008) 967-974.
- [23] U. Böttger, Dielectric properties of polar oxides, *Polar Oxides: Properties, Characterization, and Imaging*, (2005) 11-38.
- [24] W.D. Kingery, H. Bowen, D.R. Uhlmann, R. Frieser, Introduction to ceramics, *Journal of The Electrochemical Society*, 124 (1977) 152C-152C.
- [25] S. Swain, Synthesis and characterization of polymer ferroelectric composite material, in, 2011.
- [26] A.R. West, *Basic solid state chemistry*, Wiley New York, 1988.
- [27] A. Safari, R.K. Panda, V.F. Janas, *Ferroelectric Ceramics: Processing, Properties and Applications*, Dept. of Ceramic Science and Engineering, Rutgers University, Piscataway NJ, 8855 (2000).
- [28] D. Taylor, D. Damjanovic, Evidence of domain wall contribution to the dielectric permittivity in PZT thin films at sub-switching fields, *Journal of Applied Physics*, 82 (1997) 1973-1975.

- [29] F.H. Schader, Mechanical Stability of the Electromechanical Properties and Phase Transitions in Lead-Containing and Lead-Free Ferroelectrics, (2016).
- [30] M.B. Smith, K. Page, T. Siegrist, P.L. Redmond, E.C. Walter, R. Seshadri, L.E. Brus, M.L. Steigerwald, Crystal structure and the paraelectric-to-ferroelectric phase transition of nanoscale BaTiO₃, Journal of the American Chemical Society, 130 (2008) 6955-6963.
- [31] K.C. Kao, Dielectric phenomena in solids, Academic Press, 2004.
- [32] A. Mishra, Synthesis and Characterization of La doped BaTiO₃ ceramic by solgel route, in, 2011.
- [33] R. Blinc, Order and disorder in perovskites and relaxor ferroelectrics, in: Ferro- and Antiferroelectricity, Springer, 2007, pp. 51-67.
- [34] M.H. Harunsani, Characterisation of mixed-metal oxides prepared by hydrothermal synthesis, (2013).
- [35] K.W. Kirby, B.A. Wechsler, Phase relations in the Barium Titanate—Titanium Oxide System, Journal of the American Ceramic Society, 74 (2005) 1841-1847.
- [36] D. Makovec, Z. Samardžija, M. Drofènik, Solid solubility of holmium, yttrium, and dysprosium in BaTiO₃, Journal of the American Ceramic Society, 87 (2004) 1324-1329.
- [37] J. Bouwma, K. De Vries, A. Burggraaf, Non-stoichiometry, defect structure, and dielectric relaxation in lanthana-substituted SrTiO₃, physica status solidi (a), 35 (1976) 281-290.
- [38] P.M. Kumar, K.S. Rao, Influence of alkali-rare earth ions on the synthesis dielectric and ferroelectric properties of BaTiO₃ ceramics, Ferroelectrics, 94 (1989) 299-303.
- [39] J. Maier, G. Schwitzgebel, H.J. Hagemann, Electrochemical investigations of conductivity and chemical diffusion in pure and doped cubic SrTiO₃ and BaTiO₃, Journal of Solid State Chemistry, 58 (1985) 1-13.
- [40] K. Uematsu, O. Sakurai, N. Mizutani, M. Kato, Electrical properties of La-doped SrTiO₃ (La: 0.1 to 2.0 at%) single crystals grown by xenon-arc image floating zone method, Journal of materials science, 19 (1984) 3671-3679.
- [41] D. Johnson, L. Cross, F. Hummel, Dielectric Relaxation in Strontium Titanates Containing Rare-Earth Ions, Journal of Applied Physics, 41 (1970) 2828-2833.

- [42] B. Jaffe, W.R. Cook, H. Jaffe, Piezoelectric ceramics, Academic press London, 1971.
- [43] J.Q. Qi, W.P. Chen, Y. Wang, H.L.W. Chan, L.T. Li, Dielectric properties of barium titanate ceramics doped by B_2O_3 vapor, Journal of Applied Physics, 96 (2004) 6937-6939.
- [44] H. Tian, Y. Wang, J. Miao, H. Chan, C. Choy, Preparation and characterization of hafnium doped barium titanate ceramics, Journal of alloys and compounds, 431 (2007) 197-202.
- [45] M. Wegmann, R. Brönnimann, F. Clemens, T. Graule, Barium titanate-based PTCR thermistor fibers: Processing and properties, Sensors and Actuators A: Physical, 135 (2007) 394-404.
- [46] T. Murakami, T. Miyashita, M. Nakahara, E. SEKINE, Effect of Rare-Earth Ions on Electrical Conductivity of $BaTiO_3$ Ceramics, Journal of the American Ceramic Society, 56 (1973) 294-297.
- [47] R. Wernicke, The influence of kinetic processes on the electrical conductivity of donor-doped $BaTiO_3$ ceramics, physica status solidi (a), 47 (1978) 139-144.
- [48] O. Saburi, Semiconducting bodies in the family of barium titanates, Journal of the American Ceramic Society, 44 (1961) 54-63.
- [49] J.G. Kim, W.S. Cho, K. Park, PTCR characteristics in porous $(Ba, Sr)TiO_3$ ceramics produced by adding partially oxidized Ti powders, Materials Science and Engineering: B, 77 (2000) 255-260.
- [50] M. Nasrallah, H. Anderson, A. Agarwal, B. Flandermeyer, Oxygen activity dependence of the defect structure of La-doped $BaTiO_3$, Journal of materials science, 19 (1984) 3159-3165.
- [51] Z. Samardžija, D. Makovec, M. Čeh, EPMA and Microstructural Characterization of Yttrium Doped $BaTiO_3$ Ceramics, Microchimica Acta, 132 (2000) 383-386.
- [52] Z. Lijuan, W. Lihai, L. Jiandang, C. Bin, Z. Minglei, Y. Bangjiao, Dielectric properties and structural defects in $BaTi_{1-x}Sn_xO_3$ ceramics, in, IOP Publishing, pp. 012014.
- [53] S.K. Rout, E. Sinha, S. Panigrahi, Dielectric properties and diffuse phase transition in $Ba_{1-x}Mg_xTi_{0.6}Zr_{0.4}O_3$ solid solutions, Materials chemistry and physics, 101 (2007) 428-432.

- [54] A.M. Slipenyuk, M.D. Glinchuk, I.P. Bykov, L.P. Yurchenko, V.A. Mikheev, O.A. Frenkel, V.D. Tkachenko, E.P. Garmash, Study of BaTiO₃ ceramics doped with Mn and Ce or Nb and Sr, *Confidence Matter Phys*, 6 (2003) 237-244.
- [55] R.K. Zheng, J. Wang, X. Tang, Y. Wang, H.L.W. Chan, C.L. Choy, X.G. Li, Effects of Ca doping on the Curie temperature, structural, dielectric, and elastic properties of Ba_{0.4}Sr_{0.6-x}Ca_xTiO₃ (0 ≤ x ≤ 0.3) perovskites, *Journal of applied physics*, (2005).
- [56] X. Liu, X. Tan, Crystal Structure and Electrical Properties of Lead-Free (1-x) BaTiO_{3-x} (Bi/2A1/2) TiO₃ (A= Ag, Li, Na, K, Rb, Cs) Ceramics, *Journal of the American Ceramic Society*, 96 (2013) 3425-3429.
- [57] L. Ben, Synthesis and Characterisation of Rare-earth and Calcium Doped BaTiO₃ Ceramics, PhD thesis, The University of Sheffield, (2009).
- [58] N. Baskaran, H. Chang, Effect of Sn doping on the phase transformation properties of ferroelectric BaTiO₃, *Journal of Materials Science: Materials in Electronics*, 12 (2001) 527-531.
- [59] Z. Yu, C. Ang, R. Guo, A.S. Bhalla, Dielectric properties of Ba(Ti_{1-x}Zr_x)O₃ solid solutions, *Materials Letters*, 61 (2007) 326-329.
- [60] F.D. Morrison, D.C. Sinclair, A.R. West, Electrical and structural characteristics of lanthanum-doped barium titanate ceramics, *Journal of Applied Physics*, 86 (1999) 6355-6366.
- [61] Z. Yao, H. Liu, Y. Liu, Z. Wu, Z. Shen, Y. Liu, M. Cao, Structure and dielectric behavior of Nd-doped BaTiO₃ perovskites, *Materials Chemistry and Physics*, 109 (2008) 475-481.
- [62] Y. Liu, A.R. West, Ho-doped BaTiO₃: Polymorphism, phase equilibria and dielectric properties of BaTi_{1-x}Ho_xO_{3-x/2}: 0 ≤ x ≤ 0.17, *Journal of the European Ceramic Society*, 29 (2009) 3249-3257.
- [63] H. Kishi, Y. Mizuno, H. Chazono, Base-metal electrode-multilayer ceramic capacitors: past, present and future perspectives, *Japanese journal of applied physics*, 42 (2003) 1-15.
- [64] Y. Tsur, A. Hitomi, I. Scrymgeour, C.A. Randall, Site occupancy of rare-earth cations in BaTiO₃, *Japanese Journal of Applied Physics*, 40 (2001) 255.

- [65] L.A. Xue, Y. Chen, R.J. Brook, The influence of ionic radii on the incorporation of trivalent dopants into BaTiO₃, *Materials Science and Engineering: B*, 1 (1988) 193-201.
- [66] Y. Tsur, T.D. Dunbar, C.A. Randall, Crystal and defect chemistry of rare earth cations in BaTiO₃, *Journal of Electroceramics*, 7 (2001) 25-34.
- [67] Y. Sakabe, Y. Hamaji, H. Sano, N. Wada, Effects of rare-earth oxides on the reliability of X7R dielectrics, *Japanese journal of applied physics*, 41 (2002) 5668.
- [68] Y. Mizuno, H. Kishi, K. Ohnuma, T. Ishikawa, H. Ohsato, Effect of site occupancies of rare earth ions on electrical properties in Ni-MLCC based on BaTiO₃, *Journal of the European Ceramic Society*, 27 (2007) 4017-4020.
- [69] J.H. Hwang, Y.H. Han, Defect chemistry of Er-doped BaTiO₃, *Solid State Ionics*, 140 (2001) 181-186.
- [70] M.T. Buscaglia, M. Viviani, V. Buscaglia, C. Bottino, P. Nanni, Incorporation of Er³⁺ into BaTiO₃, *Journal of the American Ceramic Society*, 85 (2002) 1569-1575.
- [71] J. Jeong, E.J. Lee, Y.H. Han, J.H. Jeong, J.H. Hwang, Electrical Properties of BaTiO₃ Co-Doped with Rare Earth and Mn, (2005).
- [72] J. Zhi, A. Chen, Y. Zhi, P.M. Vilarinho, J.L. Baptista, Incorporation of yttrium in barium titanate ceramics, *Journal of the American Ceramic Society*, 82 (1999) 1345-1348.
- [73] C.M. Huang, C.Y. Lin, J. Shieh, Relationship between the evolutions of the microstructure and semiconductor properties of yttrium-doped barium titanate ceramics, *Journal of Physics D: Applied Physics*, 44 (2011) 345403.
- [74] C. Gómez-Yáñez, H. Balmori-Ramírez, J.A. Romero-Serrano, J.J. Cruz-Rivera, O. Dominguez-Espino, Dissolution of Zr and Y into BaTiO₃ by Milling, in, *Wiley Online Library*, pp. 87-94.
- [75] J. Jeong, E.J. Lee, Y.H. Han, Effects of Ho₂O₃ addition on defects of BaTiO₃, *Materials chemistry and physics*, 100 (2006) 434-437.
- [76] Y. Liu, Synthesis and Characterisation of Ho-doped Barium Titanate, in, *The University of Sheffield*, 2009.
- [77] H. Ohsato, M. Imaeda, Y. Okino, H. Kishi, T. Okuda, Lattice Parameters of BaTiO₃ Solid Solutions Containing Dy and Ho at High Temperature, (1997).

- [78] E.J. Lee, J. Jeong, Y.H. Han, Electrical properties of Dy₂O₃-doped BaTiO₃, Japanese journal of applied physics, 43 (2004) 8126.
- [79] W.-H. Lee, W.A. Groen, H. Schreinemacher, D. Hennings, Dysprosium doped dielectric materials for sintering in reducing atmospheres, Journal of electroceramics, 5 (2000) 31-36.
- [80] M.T. Buscaglia, V. Buscaglia, M. Viviani, P. Nanni, M. Hanuskova, Influence of foreign ions on the crystal structure of BaTiO₃, Journal of the european ceramic society, 20 (2000) 1997-2007.
- [81] K. Takada, E. Chang, D.M. Smyth, Rare earth additions to BaTiO₃, Advances in Ceramics, 19 (1987) 147-152.
- [82] S.H. Hur, J.K. Lee, K.-S. Hong, S.J. Park, Incorporation phenomena of donor dopant in BaTiO₃ systems, Solid state ionics, 108 (1998) 81-84.
- [83] S.B. Desu, D.A. Payne, Interfacial segregation in perovskites: III, microstructure and electrical properties, Journal of the American Ceramic Society, 73 (1990) 3407-3415.
- [84] T.A. Colson, M.J.S. Spencer, I. Yarovsky, A DFT study of the perovskite and hexagonal phases of BaTiO₃, Computational materials science, 34 (2005) 157-165.
- [85] M.T. Buscaglia, V. Buscaglia, M. Viviani, P. Nanni, Atomistic simulation of dopant incorporation in barium titanate, Journal of the American Ceramic Society, 84 (2001) 376-384.
- [86] C.L. Freeman, J.A. Dawson, H.-R. Chen, J.H. Harding, L.-B. Ben, D.C. Sinclair, A new potential model for barium titanate and its implications for rare-earth doping, Journal of Materials Chemistry, 21 (2011) 4861-4868.
- [87] C.L. Freeman, J.A. Dawson, H.R. Chen, L. Ben, J.H. Harding, F.D. Morrison, D.C. Sinclair, A.R. West, Energetics of Donor-Doping, Metal Vacancies, and Oxygen-Loss in A-Site Rare-Earth-Doped BaTiO₃, Advanced Functional Materials, 23 (2013) 3925-3928.
- [88] H. Saito, H. Chazono, H. Kishi, N. Yamaoka, X 7 R Multilayer Ceramic Capacitors with Nickel Electrodes, Japanese journal of applied physics, 30 (1991) 2307-2310.
- [89] K.-J. Park, C.-H. Kim, Y.-J. Yoon, S.-M. Song, Y.-T. Kim, K.-H. Hur, Doping behaviors of dysprosium, yttrium and holmium in BaTiO₃ ceramics, Journal of the European Ceramic Society, 29 (2009) 1735-1741.

- [90] J.D. Bak, J.C. Wright, Site-selective Spectroscopy of the solid-state defect chemistry in erbium-doped barium titanate, *The Journal of Physical Chemistry B*, 109 (2005) 18391-18399.
- [91] V. Mitić, V.B. Pavlović, L. Kocić, V. Paunović, D. Mančić, Application of the intergranular impedance model in correlating microstructure and electrical properties of doped BaTiO₃, *Science of sintering*, 41 (2009) 247-256.
- [92] V.V. Mitic, Z.S. Nikolic, V. Paunovic, D. Mancic, L. Zivkovic, V.B. Pavlovic, B. Jordovic, Influence of Rare-Earth Dopants on Barium Titanate Ceramics Microstructure and Corresponding Electrical Properties, *J. Am. Ceram. Soc.*, 39.1 (2010) 132–137.
- [93] A. Honda, S.i. Higai, Y. Motoyoshi, N. Wada, H. Takagi, Theoretical study on interactions between oxygen vacancy and doped rare-earth elements in barium titanate, *Japanese Journal of Applied Physics*, 50 (2011) 09NE01.
- [94] S. Sato, Y. Nakano, A. Sato, T. Nomura, Mechanism of improvement of resistance degradation in Y-doped BaTiO₃ based MLCCs with Ni electrodes under highly accelerated life testing, *Journal of the European Ceramic Society*, 19 (1999) 1061-1065.
- [95] Y. Nakano, A. Satoh, A. Hitomi, T. Nomura, *Ceramic Transactions, Vol. 32, Dielectric Ceramics, Processing, Properties, and Application*, Am. Ceram. Soc, (1993) 119-128.
- [96] A. Hitomi, Liu, X., Shrout, T.R. and Randall, C.A., in *The 8th US-Japan Seminar on Dielectric and Piezoelectric Ceramics*, edited by R.Gururaja, (1997) 44.
- [97] J.K. Lee, K.S. Hong, J.W. Jang, Roles of Ba/Ti ratios in the dielectric properties of BaTiO₃ ceramics, *Journal of the American Ceramic Society*, 84 (2001).
- [98] V. Paunović, L. Živković, V. Mitić, Influence of rare-earth additives (La, Sm and Dy) on the microstructure and dielectric properties of doped BaTiO₃ ceramics, *Science of sintering*, 42 (2010) 69-79.
- [99] R.D. Shannon, Revised effective ionic radii and systematic studies of interatomic distances in halides and chalcogenides, *Acta Crystallographica Section A, Crystal Physics, Diffraction, Theoretical and General Crystallography*, 32.5 (1976) 751-767.
- [100] D.W. Hahn, Y.H. Han, Electrical properties of Yb-doped BaTiO₃, *Japanese journal of applied physics*, 48 (2009) 111406.

- [101] J.H. Jeong, M.G. Park, Y.H. Han, Defect chemistry of Y doped BaTiO₃, *Journal of Electroceramics*, 13 (2004) 805-809.
- [102] Y.H. Han, J.B. Appleby, D.M. Smyth, Calcium as an acceptor impurity in BaTiO₃, *Journal of the American Ceramic Society*, 70 (1987) 96-100.
- [103] N.H. Chan, R.K. Sharma, D.M. Smyth, Nonstoichiometry in Acceptor-Doped BaTiO₃, *Journal of the American Ceramic Society*, 65 (1982) 167-170.
- [104] J. Clayton, H. Takamura, R. Metz, H.L. Tuller, B.J. Wuensch, The electrical and defect properties of Bi₃Zn₂Sb₃O₁₄ pyrochlore: a grain-boundary phase in ZnO-based varistors, *Journal of Electroceramics*, 7 (2001) 113-120.
- [105] M.A.A. Issa, N.M. Molokhia, S.A. Nasser, Factors affecting the permittivity of Gd-doped BaTiO₃, *Journal of Physics D: Applied Physics*, 17 (1984) 571.
- [106] K. Takada, H. Ichimura, D.M. Smyth, Equilibrium Conductivity for Er Doped BaTiO₃, *Japanese Journal of Applied Physics*, 26 (1987) 42.
- [107] J.H. Kim, Y.H. Han, Effects of Y₂O₃ Addition on the Microstructure and Electrical Property of TiO₂-excess BaTiO₃, in, *Trans Tech Publ*, pp. 1025-1028.
- [108] J.H. Kim, S.H. Yoon, Y.H. Han, Effects of Y₂O₃ addition on electrical conductivity and dielectric properties of Ba-excess BaTiO₃, *Journal of the European Ceramic Society*, 27 (2007) 1113-1116.
- [109] V.N. Tsygankov, V.V. Safonov, Doping effects on the properties of BaTiO₃-based solid solutions, *Inorganic materials*, 38 (2002) 397-399.
- [110] P. Blanchart, J.F. Baumard, P. Abelard, Effects of Yttrium Doping on the Grain and Grain-Boundary Resistivities of BaTiO₃ for Positive Temperature Coefficient Thermistors, *Journal of the American Ceramic Society*, 75 (1992) 1068-1072.
- [111] M.H. Lin, H.Y. Lu, Site-occupancy of yttrium as a dopant in BaO-excess BaTiO₃, *Materials Science and Engineering: A*, 335 (2002) 101-108.
- [112] Y. Liu, E.E. McCabe, D.C. Sinclair, A.R. West, Synthesis, structure and properties of the hexagonal perovskite, h-BaTi_{1-x}Ho_xO_{3-x/2}, *Journal of Materials Chemistry*, 19 (2009) 5201-5206.
- [113] M. Marjanović, D. Dimitrijević, V. Paunović, Z. Prijić, Microstructural and dielectrical characterization of Ho doped BaTiO₃ ceramics, *Serbian Journal of Electrical Engineering*, 11 (2014) 35-46.

- [114] Y. Liu, A.R. West, Semiconductivity in Acceptor-Doped $\text{BaTi}_{1-x}\text{Ho}_x\text{O}_{3-x/2-\delta/2}$, *Journal of the American Ceramic Society*, 96 (2013) 1512-1520.
- [115] L. Li, M. Wang, D. Guo, R. Fu, Q. Meng, Effect of Gd amphoteric substitution on structure and dielectric properties of BaTiO_3 -based ceramics, *Journal of Electroceramics*, 30 (2013) 129-132.
- [116] A. Feteira, G.M. Keith, M.J. Rampling, C.A. Kirk, I.M. Reaney, K. Sarma, N.M. Alford, D.C. Sinclair, Synthesis and characterisation of Ga-doped hexagonal BaTiO_3 , *Crystal engineering*, 5 (2002) 439-448.
- [117] L. Ben, D.C. Sinclair, Anomalous Curie temperature behavior of A-site Gd-doped BaTiO_3 ceramics: The influence of strain, *Applied Physics Letters*, 98 (2011) 092907.
- [118] C.L. Freeman, J.A. Dawson, J.H. Harding, L.B. Ben, D.C. Sinclair, The Influence of A-Site Rare Earth Ion Size in Controlling the Curie Temperature of $\text{Ba}_{1-x}\text{RE}_x\text{Ti}_{1-x/4}\text{O}_3$, *Advanced Functional Materials*, 23 (2013) 491-495.
- [119] J.P. Hernández Lara, M. Pérez Labra, F.R. Barrientos Hernández, J.A. Romero Serrano, E.O. Ávila Dávila, P. Thangarasu, A. Hernández Ramirez, Structural Evolution and Electrical Properties of BaTiO_3 Doped with Gd^{3+} , *Materials Research*, (2017) 0-0.
- [120] J. Nowotny, M. Rekas, Defect chemistry of BaTiO_3 , *Solid State Ionics*, 49 (1991) 135-154.
- [121] T. Murakami, T. Miyashita, M. Nakahara, E. Sekine, Effect of Rare-Earth Ions on Electrical Conductivity of BaTiO_3 Ceramics, *Journal of the American Ceramic Society*, 56 (1973) 294-297.
- [122] I. Ueda, S. Ikegami, Oxidation phenomena in semiconducting BaTiO_3 , *Journal of the Physical Society of Japan*, 20 (1965) 546-552.
- [123] V.J. Tennery, R.L. Cook, Investigation of Rare-Earth Doped Barium Titanate, *Journal of the American Ceramic Society*, 44 (1961) 187-193.
- [124] S.M. Park, Y.H. Han, Dielectric relaxation of oxygen vacancies in Dy-doped BaTiO_3 , *Journal of the Korean Physical Society*, 57 (2010) 458-463.
- [125] Y. Pu, W. Chen, S. Chen, H.T. Langhammer, Microstructure and dielectric properties of dysprosium-doped barium titanate ceramics, *Ceramica*, 51 (2005) 214-218.

- [126] J. Daniels, K.H. Härdtl, R. Wernicke, The PTC effect of barium titanate, *Philips Technical Review*, 38 (1979) 73-82.
- [127] G.H. Jonker, Some aspects of semiconducting barium titanate, *Solid-State Electronics*, 7 (1964) 895-903.
- [128] M.D. Glinchuk, I.P. Bykov, S.M. Kornienko, V.V. Laguta, A.M. Slipenyuk, A.G. Bilous, O.I. V'Yunov, O.Z. Yanchevskii, Influence of impurities on the properties of rare-earth-doped barium-titanate ceramics, *Journal of Materials Chemistry*, 10 (2000) 941-947.
- [129] P. Yongping, Y. Wenhui, C. Shoutian, Influence of rare earths on electric properties and microstructure of barium titanate ceramics, *Journal of Rare Earths*, 25 (2007) 154-157.
- [130] M. Prades, H. Beltrán, E. Cordoncillo, P.J. Alonso, N. Masó, A.R. West, Non-ohmic phenomena in Mn-doped BaTiO₃, *physica status solidi (a)*, 209 (2012) 2267-2272.
- [131] P. Ren, N. Masó, A.R. West, Hole conductivity in oxygen-excess BaTi_{1-x}Ca_xO_{3-x+δ}, *Physical Chemistry Chemical Physics*, 15 (2013) 20943-20950.
- [132] Y. Liu, A.R. West, Semiconductor-Insulator Transition in Undoped Rutile, TiO₂, *Ceramics*, *Journal of the American Ceramic Society*, 96 (2013) 218-222.
- [133] H. Beltrán, M. Prades, N. Masó, E. Cordoncillo, A.R. West, Enhanced Conductivity and Nonlinear Voltage-Current Characteristics of Nonstoichiometric BaTiO₃ Ceramics, *Journal of the American Ceramic Society*, 94 (2011) 2951-2962.
- [134] N. Kumar, E.A. Patterson, T. Frömling, D.P. Cann, DC-bias dependent impedance spectroscopy of BaTiO₃-Bi(Zn_{1/2}Ti_{1/2})O₃ ceramics, *Journal of Materials Chemistry C*, 4 (2016) 1782-1786.
- [135] N. Kumar, E.A. Patterson, T. Frömling, D.P. Cann, Conduction Mechanisms in BaTiO₃-Bi(Zn_{1/2}Ti_{1/2})O₃ Ceramics, *Journal of the American Ceramic Society*, (2016).
- [136] L. Gil Escrig, M. Prades, H. Beltrán, E. Cordoncillo, N. Masó, A.R. West, Voltage-Dependent Bulk Resistivity of SrTiO₃: Mg Ceramics, *Journal of the American Ceramic Society*, 97 (2014) 2815-2824.
- [137] N. Masó, H. Beltrán, E. Cordoncillo, P. Escribano, A.R. West, Electrical properties of Fe-doped BaTiO₃, *Journal of Materials Chemistry*, 16 (2006) 1626-1633.

- [138] N. Masó, A.R. West, Electronic conductivity in yttria-stabilized zirconia under a small dc bias, *Chemistry of Materials*, 27 (2015) 1552-1558.
- [139] N. Masó, M. Prades Tena, H. Beltrán Mir, E. Cordoncillo Cordoncillo, D.C. Sinclair, A.R. West, Field enhanced bulk conductivity of acceptor-doped $\text{BaTi}_{1-x}\text{Ca}_x\text{O}_{3-x}$ ceramics, (2010).
- [140] J.J. Biendicho, A.R. West, Impedance characterisation of LiFePO_4 ceramics, *Solid State Ionics*, 226 (2012) 41-52.
- [141] Q.-L. Zhang, N. Masó, Y. Liu, H. Yang, A.R. West, Voltage-dependent low-field resistivity of CaTiO_3 : Zn ceramics, *Journal of Materials Chemistry*, 21 (2011) 12894-12900.
- [142] H. Beltrán, M. Prades, N. Masó, E. Cordoncillo, A.R. West, Voltage-Dependent Low-Field Bulk Resistivity in BaTiO_3 : Zn Ceramics, *Journal of the American Ceramic Society*, 93 (2010) 500-505.
- [143] M. Prades, N. Masó, H. Beltrán, E. Cordoncillo, A.R. West, Field enhanced bulk conductivity of BaTiO_3 : Mg ceramics, *Journal of Materials Chemistry*, 20 (2010) 5335-5344.
- [144] P. Ren, N. Masó, Y. Liu, L. Ma, H. Fan, A.R. West, Mixed oxide ion and proton conduction and p-type semiconduction in $\text{BaTi}_{0.98}\text{Ca}_{0.02}\text{O}_{2.98}$ ceramics, *Journal of Materials Chemistry C*, 1 (2013) 2426-2432.
- [145] Y. Liu, A.R. West, Voltage-dependent resistance of undoped rutile, TiO_2 , ceramics, *Applied Physics Letters*, 103 (2013) 263508.
- [146] N. Masó, H. Beltrán, M. Prades, E. Cordoncillo, A.R. West, Field-enhanced bulk conductivity and resistive-switching in Ca-doped BiFeO_3 ceramics, *Physical Chemistry Chemical Physics*, 16 (2014) 19408-19416.
- [147] T.B. Adams, D.C. Sinclair, A.R. West, Characterization of grain boundary impedances in fine- and coarse-grained $\text{CaCu}_3\text{Ti}_4\text{O}_{12}$ ceramics, *Physical review B*, 73 (2006) 094124.
- [148] Y. Jiao, A. Hellman, Y. Fang, S. Gao, M. Käll, Schottky barrier formation and band bending revealed by first-principles calculations, *Scientific reports*, 5 (2015).
- [149] M. Li, Z. Shen, M. Nygren, A. Feteira, D.C. Sinclair, A.R. West, Origin (s) of the apparent high permittivity in $\text{CaCu}_3\text{Ti}_4\text{O}_{12}$ ceramics: clarification on the contributions from internal barrier layer capacitor and sample-electrode contact effects, *Journal of Applied Physics*, 106 (2009) 104106.

- [150] F. Greuter, G. Blatter, Electrical properties of grain boundaries in polycrystalline compound semiconductors, *Semiconductor Science and Technology*, 5 (1990) 111.
- [151] C.-F. Yang, An equivalent circuit for CuO modified surface barrier layer capacitors, *Japanese journal of applied physics*, 36 (1997) 188.
- [152] A.J. Moulson, J.M. Herbert, *Electroceramics: materials, properties, applications*, John Wiley & Sons, 2003.
- [153] T.B. Adams, *Barrier Layer Capacitors Based on $\text{CaCu}_3\text{Ti}_4\text{O}_{12}$* , University of Sheffield, 2005.
- [154] P. Salamon, D. Fernández-García, J.J. Gómez-Hernández, A review and numerical assessment of the random walk particle tracking method, *Journal of contaminant hydrology*, 87 (2006) 277-305.
- [155] D.B. Strukov, G.S. Snider, D.R. Stewart, R.S. Williams, The missing memristor found, *nature*, 453 (2008) 80-83.
- [156] M. Vujisić, N. Marjanović, I. Fetahović, K. Stanković, P. Osmokrović, Influence of radiation on titanium dioxide memristors, *Scientific Publications of the State University of Novi Pazar Series A: Applied Mathematics, Informatics and mechanics*, 4 (2012) 75-82.
- [157] J.F. Scott, F.D. Morrison, P. Zubko, D.J. Jung, P. Baxter, M.M. Saad, J.M. Gregg, R.M. Bowman, High-field conduction in barium titanate, *arXiv preprint cond-mat/0409585*, (2004).
- [158] D.P. Cann, C.A. Randall, Electrode effects in positive temperature coefficient and negative temperature coefficient devices measured by complex-plane impedance analysis, *Journal of applied physics*, 80 (1996) 1628-1632.
- [159] P. Leret, J.F. Fernandez, J. De Frutos, D. Fernandez-Hevia, Nonlinear I–V electrical behaviour of doped $\text{CaCu}_3\text{Ti}_4\text{O}_{12}$ ceramics, *Journal of the European Ceramic Society*, 27 (2007) 3901-3905.
- [160] D. Joung, A. Chunder, L. Zhai, S.I. Khondaker, Space charge limited conduction with exponential trap distribution in reduced graphene oxide sheets, *Applied Physics Letters*, 97 (2010) 093105.
- [161] T. Hölbling, R. Waser, Simulation of the charge transport across grain boundaries in p-type SrTiO_3 ceramics under dc load: Debye relaxation and dc bias

dependence of long-term conductivity, *Journal of applied physics*, 91 (2002) 3037-3043.

[162] J. Svensson, E.E.B. Campbell, Schottky barriers in carbon nanotube-metal contacts, *Journal of applied physics*, 110 (2011) 16.

[163] A. Branwood, O.H. Hughes, J.D. Hurd, R.H. Tredgold, Evidence for space charge conduction in barium titanate single crystals, *Proceedings of the Physical Society*, 79 (1962) 1161.

[164] G.A. Cox, R.H. Tredgold, Hole drift mobility in BaTiO_3 single crystals, *Physics Letters*, 11 (1964) 22-23.

[165] A. Branwood, R.H. Tredgold, The electrical conductivity of barium titanate single crystals, *Proceedings of the Physical Society*, 76 (1960) 93.

[166] G.A. Cox, R.H. Tredgold, Double space charge injection in solids, *Physics Letters*, 4 (1963) 199-200.

[167] G.A. Cox, R.H. Tredgold, Time dependence of the electrical conductivity in strontium titanate single crystals, *British Journal of Applied Physics*, 16 (1965) 427.

[168] A. Branwood, J.D. Hurd, R.H. Tredgold, Dielectric breakdown in barium titanate, *British Journal of Applied Physics*, 13 (1962) 528.

2. Experimental Procedure

2.1 Sample Preparation

Three mixing methods were used for preparing the required compositions.

2.1.1 Hand Mixing (*HM*) of Reagents

Undoped BaTiO₃ and rare-earth (RE) element-doped BaTiO₃ powder were synthesized using solid state reaction. High purity oxides and/or carbonates [BaCO₃, TiO₂ and RE₂O₃ (Y₂O₃, Ho₂O₃, Gd₂O₃, Dy₂O₃, Er₂O₃ and Yb₂O₃)] were used as the reactants. After drying (Table 2-1), the required amounts of reactants were weighed (typical batch size, 10 g) using a top pan balance according to the stoichiometric formulae. The reactants were mixed in acetone and milled using a mortar and pestle for approximately 30 minutes to ensure uniform mixing. After drying, the powder was pressed into pellets uniaxially under 0.4 tonne in a 20 mm dia die made of stainless steel. The samples were reacted either on platinum foil on a bed of sacrificial powder (taken from the same material as the pellet) or directly on Pt foil and heated at 10 °C/min and maintained for ~ 12 hours at 1000 °C in order to remove CO₂ and start the reaction.

The samples were crushed and repelleted by uniaxially pressing under 0.4 tonne. The pressing was applied using an 8mm diameter stainless steel die. Some pellets were then placed in a Cold Isostatic Press (CIP) to increase their density. Pelleted samples were placed on platinum foil on refractory brick and heated, at 1350-1550 °C followed by either slow cool or rapid quench. The reaction required several days for some samples and grinding was carried out on a daily basis[1-3]. An amount of the same powder was spread out to act as a sacrificial powder between the pellets and the platinum foil. Figure 2-1 shows schematically the processing stages.

2.1.2 Ball Milling (*BM*) Route

Mixtures of reactant powders, (once they were dried and weighed) were ball-milled in a plastic jar with Y₂O₃-stabilised zirconia milling balls, as with the hand mixing method. The mixtures were wet-mixed in isopropanol using a horizontal ball milling machine for 24 hours. Then, the mixed slurries were oven-dried (at 100 °C for around 12 h to remove the isopropanol), deagglomerated using a brush, and passed through a sieve.

The powders were pelleted uniaxially under 0.4 tonne in a 20 mm dia die, placed on sacrificial powder on foil Pt and heated at 1000 °C for 12 hours (heating rate 10 °C/min). The calcined powders were then remilled for 24 hours and the oven-drying, deagglomeration and sieving procedures repeated. Finally, pellets were prepared as in section 2.1.1.

Table 2-1 Details of raw materials.

Reagent	Supplier	Purity / %	Drying temperature / °C
BaCO ₃	Aldrich	99.8	180
TiO ₂	Aldrich	99.9	800
Y ₂ O ₃	Aldrich	99.99	800
Ho ₂ O ₃	Aldrich	99.9	800
Gd ₂ O ₃	Aldrich	99.99	800
Dy ₂ O ₃	Alfa Aesar	99.99	800
Er ₂ O ₃	Alfa Aesar	99.99	800
Yb ₂ O ₃	Aldrich	99.99	800

2.1.3 Planetary Ball Milling (PBM) Route

Mechanical milling (FRITSCH Planetary Mill PULVERISETTE 7 premium line) was used on powder samples (once they were dried and weighed). The mill had a grinding bowl with tungsten carbide balls; samples were wet mixed in isopropanol for 20 h with a rotation speed of 250 rpm. The mixed slurries were oven-dried (at 150 °C for ~ 6 h to remove the isopropanol), deagglomerated with a brush, sieved and heated at 1000 °C for 12 hours. The calcined powders were milled for 20 hours at 450 rpm, oven-dried, deagglomerated and sieved. Finally, pellets were prepared and fired as in section 2.1.1.

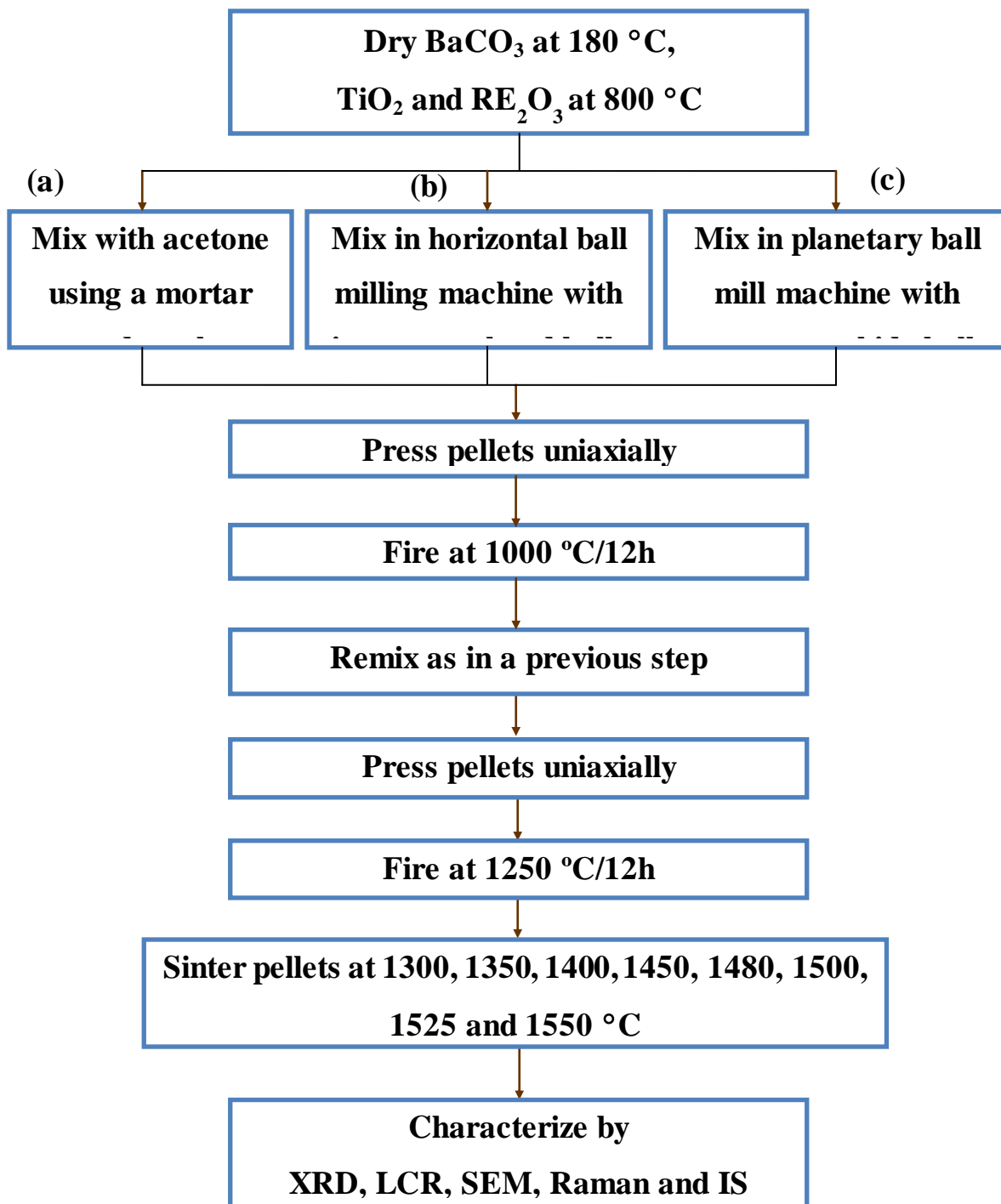


Figure 2-1 Schematic representation of the processing stages using (a) hand-mixed reagents (b) horizontal ball milling route (c) planetary ball milling route.

2.2 Structural Characterisation

2.2.1 X-Ray Powder Diffraction

In order to investigate the crystallography, phase diagram, solution limit and completion of reaction, an X-ray Powder Diffraction (XRD) study was performed.

Two Stoe diffractometers were used. A Stadi-P Image Plate, IP (Stoe and Cie GmbH, Darmstadt) was used for phase identification. An agate mortar and pestle was used to grind the sintered samples. A few milligrams were placed on acetate foil, covered with Elmer's white glue, and placed in a circular holder in the rotating stage of the diffractometer system. Data were acquired over the range $20 \leq 2\theta \leq 100$ °C using monochromated Cu K α radiation ($\lambda = 1.5406$ Å) and processed using WinXPOW software.

A small linear position sensitive detector (PSD) was used to collect XRD data for lattice parameter determination. A Si external standard was used to calibrate the instrument.

2.2.2 Density Measurement

There are many factors which have an influence on the density, such as particle size distribution of the powder and the sintering temperature. The volume of the unit cell was calculated from the lattice parameters obtained from XRD data and then used to calculate the theoretical X-ray density. The sintered pellet density was calculated experimentally using a micrometre to measure the dimensions of the pellet (radius and thickness). The bulk density of sintered pellets was calculated by dividing its mass by volume.

$$\text{Experimental density} = \frac{\text{Mass of pellet}}{\text{Pellet volume (thickness} \times \text{area)}} = \frac{\text{Grammes}}{\pi r^2 \times t} \quad (\text{g/cm}^3) \quad (2-1)$$

The theoretical x-ray density of each component can be determined using the formula:

$$\begin{aligned} \text{Theoretical x-ray density} &= \frac{\text{Mass of unit cell}}{\text{Volume of unit cell}} = \frac{\text{Formula mass} \times Z}{V \times N_A \times 10^{-24}} \\ &= \frac{FW \times Z \times 1.66}{V_{cell}} \quad (\text{g/cm}^3) \quad (2-2) \end{aligned}$$

where:

t: thickness of pellet (cm)

r: radius (cm)

FW: formula weight (g)

Z: formula units per unit cell, Z = 6 for h-BT.

V_{cell} : volume of the unit cell from XRD data (\AA^3)

NA: Avogadro constant = 6.022141×10^{23} (mol^{-1})

Pellet density as % of theoretical x-ray density: $\frac{D_{\text{exp}}}{D_{\text{xrd}}} \times 100$

2.2.3 Differential Scanning Calorimetry (DSC)

Samples were analysed by DSC [4] using a Netzsch DSC404C (Selb, Germany) controlled by Netzsh Proteus software in order to observe the ferroelectric transition temperatures. DSC measurements were performed from room temperature to 200 °C with heating at a rate 10 °C/min in argon and then cooling from 200 °C to room temperature at the same rate. The reversibility was checked by comparison between heating and cooling. The detection of phase transition temperatures with small enthalpy change requires a large sample mass. Enthalpy values were calculated from the area under the DSC transition peak using the instrument software [5, 6].

2.2.4 Scanning Electron Microscopy (SEM)

It is useful technique to determine the homogeneity and observe the texture, topography and surface features of materials and can show the distribution of elements throughout the material. SEM was carried out on final sintered products to determine microstructural properties such as the morphology and grain size distribution. SEM samples were initially prepared by grinding sintered pellets by 800, 1200 and 2500 grit silicon carbide waterproof sand paper to remove the surface defects. Pellets were then polished with 6, 3 and 1 μm diamond polish pastes on synthetic polishing cloths. Acetone and Isopropanol were used to clean all pellets. Pellets then were heated to perform thermal etching for 1 hour at a temperature 90% of their sintering temperature which corresponded to temperatures ~ 200 °C below the sintering

temperature, resulting in preferred removal of material at grain boundaries. The etched samples were mounted on aluminium stubs using conductive silver paste (Agar Scientific Ltd., Stansted, UK). A ~50 nm conductive carbon layer was then sputtered onto the surface to facilitate Energy Dispersive Spectroscopy (EDS) and to avoid accumulation of charges on surface of sample under the electron beam. Determination of microstructure information was performed using a FEI Inspect F microscope operating at 5 kV at working distance of 10 mm with a Link analytical energy dispersive spectroscopy (EDS) X-ray detector (Link Analytical Ltd., UK) which was used for different samples to determine the chemical composition. LINK ISIS software was used to record and analyse the data.

2.2.5 Raman Spectroscopy

The Raman technique has become more versatile for studying different behaviours and is used to investigate oxide materials, specifically, to detect the subtle structural distortions in perovskites materials even when they are too subtle to be detected by diffraction techniques [7, 8]. Since the vibrational spectrum has a shorter characterization length scale than that required for diffraction experiments, therefore this technique is an excellent microprobe for the local structure details that may be important for the interpretation of the properties of ferroelectric materials [8-10]. Local structural deformations arise as result of the difference in ionic radii of host and dopant [11].

Raman spectroscopy was performed using a THMS600 stage (Linkam Scientific Instrument limited England) Spectrometer. Spectra were excited using a green LASER with wavelength of 514.5 nm and a power of 20 mW focused onto a ~2 μm spot size. A Renishaw InVia micro-Raman spectrometer was used to excite and record in back scattering geometry unpolarised Raman spectra. The range over 100-1000 cm^{-1} were recorded to collect the data. A TMS94 temperature controller was used to control the temperature. The accuracy in the measurement of temperature was ± 1 $^{\circ}\text{C}$.

2.3 Electrical Property Characterisation

2.3.1 Sample Preparation

Both the density and geometric factor of pellets were measured. Some pellets, sintered at different temperatures, were ground flat and parallel to remove surface

layers that might have been produced during sintering. Electrode paste (Pt) was brushed onto opposite surfaces of the pellets and heated to 900 °C for ~ 120 minutes. Either In/Ga (60:40 mole ratio) alloy electrode or Ag were rubbed on the quenched samples at room temperature.

2.3.2 Polarisation-Electric Field Measurements

P-E hysteresis loop is an important characteristic of ferroelectrics. Ferroelectric materials are characterised by the existence of a spontaneous polarisation P_S which occurs below the critical temperature T_C and the reorientation between two or more equivalent directions can be induced when a sufficiently large electric field is applied across opposite faces of the crystal [12]. For BT, Ti is displaced very slightly off its regular octahedral site; it displaces by ~ 6% of the Ti–O bond length from the centre of the octahedron towards an oxygen at one of the corners; Ba^{2+} as well is displaced slightly in the same direction. Because of the resulting charge displacement of Ti atoms, the creation of a large dipole moment of the resulting structure and the spontaneous polarization is observed in this material which is a feature of ferroelectricity in BT [1]. Reorientation of the dipole can be observed by application of an external electric field. The ready reversibility of spontaneous electric polarization is responsible for the property of ferroelectricity and is accompanied by a hysteresis loop on thermal cycling [13]. A remanent polarisation (P_r) persists even after the applied field is removed and is the key factor for featuring ferroelectric property [1, 14].

The room temperature polarisation – electric field measurements were performed using an aix-ACCT TF2000FE- HV ferroelectric test unit (aix-ACCT Inc., Germany) linked to a computer. A Radiant RT66A high voltage interface (Albuquerque, New Mexico, USA) was used to connect the ferroelectric test system with a high voltage amplifier (4 kV maximum voltage, model 609E-6, Trek, Inc., Medina, New York, USA). For polarisation (P) vs. electric field (E), all samples were thinned to between ~ 0.7 and 0.9 mm with Ag electrodes. Specimens were subjected to a cyclic electric field by applying a triangular waveform with frequency 1 Hz.

An electric current was induced by application of an electric field. Integration of current with respect to time generated the electric charge, and enabled calculation of the polarisation in terms of surface charge density. For P - E data as a function of

temperature, sufficient time was given to samples to achieve thermal equilibrium within ± 0.2 °C. The sample holder was submersed fully in silicone oil during testing to increase the range of applied voltage without electric arcing and to prevent breakdown.

2.3.3 Impedance Spectroscopy (IS)

Samples for IS were placed in a conductivity jig inside a tube furnace as shown in Figure 2-2. Four impedance instruments were used variously during this project: HP-4192A impedance analyser, frequency range 5 Hz -13 MHz; Agilent impedance analyzer (model Agilent E4980A, Agilent Technologies, Inc., USA) frequency range 20 Hz - 2 MHz, applied AC voltage of amplitude 100 mV and DC voltage between 0 and 10V; Solartron, SI 1260 impedance analyser, frequency range 0.01 Hz to 1 MHz, AC measuring voltage of 100 mV; A broadband dielectric spectrometer (Turnkey Concept 50, Novocontrol Technologies GmbH & Co. KG, Hundsangen, Germany), frequency range 1 Hz –10 MHz. Electrical properties were measured between -263 °C and 700 °C in different atmospheres (O₂, air and N₂); sometimes a DC bias was applied. The data analysis used ZView software.

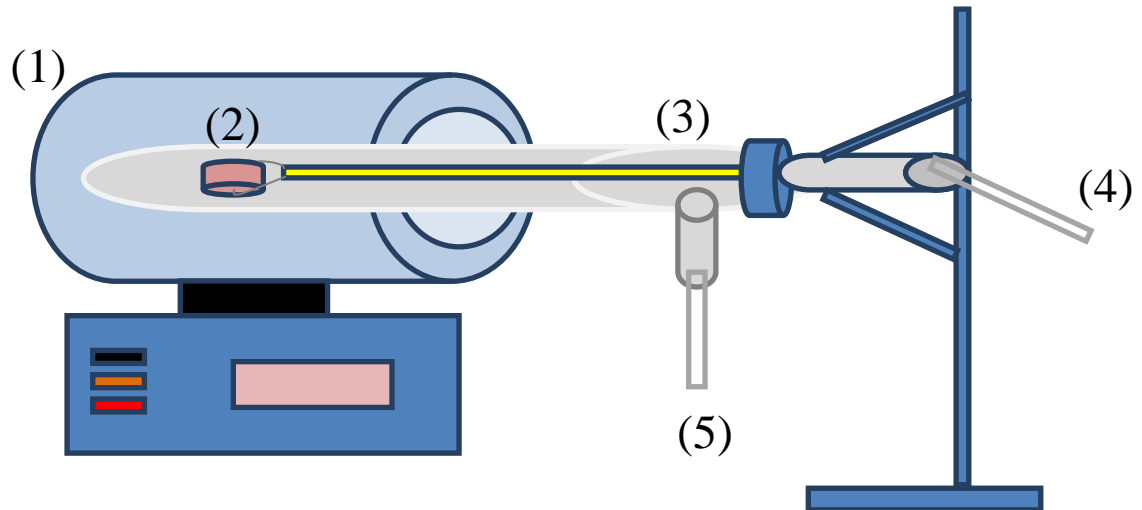


Figure 2-2: Impedance setup, (1) furnace, (2) pellet, (3) conductivity jig. For different atmospheres, the jig has: (4) gas inlet and (5) gas outlet.

2.3.3.1 Basic electrical and impedance spectroscopy theory:

Impedance Spectroscopy is an important tool and useful technique for many electroceramic materials [15-18] including dielectrics and ferroelectrics to

characterise the electrical properties, distinguish different regions of a ceramic, investigate intrinsic behaviour and determine the electrical microstructure [19]. The technique depends on measuring the in-phase and out-of-phase components of the current with applied voltage over a wide range of frequencies, typically $\sim (10^{-2}$ to 10^7 Hz) [16]. Variables such as cooling rate, temperature, DC bias and atmosphere can be controlled during its measurements. Impedance analysis is commonly-used to investigate electro-active regions, such as intra-granular (bulk) and inter-granular (grain boundary, electrode-sample interface) contributions.

IS data can be analysed using four basic formalisms: complex impedance (Z^*), complex permittivity (ϵ^*), complex electric modulus (M^*) and complex admittance (Y^*), which are related to each other and can be calculated from these transformations [20-22]:

$$\epsilon^* = (M^*)^{-1} \quad (2-3)$$

$$M^* = j\omega C_0 Z^* \quad (2-4)$$

$$Y^* = (Z^*)^{-1} \quad (2-5)$$

$$Y^* = j\omega C_0 \epsilon^* \quad (2-6)$$

where (ϵ' , M' , Z' , Y') and (ϵ'' , M'' , Z'' , Y'') are real and imaginary components, $j = \sqrt{-1}$, $C_0 = \epsilon_0 A/l$ is the vacuum capacitance of the cell and electrodes with an air gap in place of the sample, ϵ_0 is the permittivity of free space (8.854×10^{-14} F/cm), l is the thickness and A is the area.

Determination of the most appropriate equivalent circuit to provide a good representation of the electrical properties of a sample is very important for analysis and interpretation of impedance data. Resistance, R and capacitance, C is used to represent electro-active regions which are connected in parallel for the most common equivalent circuit models [23]. The RC element is used to determine the impedance and electrical modulus. In most impedance results, the grain-core (bulk) component is characterised, ideally, by an equivalent RC circuit with a resistor in parallel, Fig 2-3.

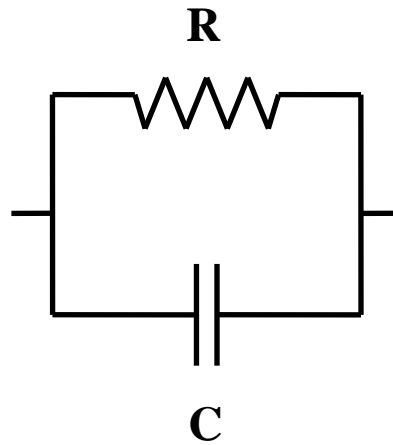


Figure 2-3: Equivalent circuit for an ideal parallel RC element.

For this element, the equations for the different formalisms are:

$$Y^* = \frac{1}{R} + j\omega C = Y' + jY'' \quad (2-7)$$

$$Z^* = (Y^*)^{-1} = \left(\frac{1}{R} + j\omega C\right)^{-1} = Z' - jZ'' \quad (2-8)$$

Data can be presented in several ways, as complex planes, eg Z'' vs Z' , or as spectroscopic plots, eg Z'' vs $\log(f)$, or as $\tan \delta$, eg ϵ''/ϵ' vs $\log(f)$.

For this circuit, Figure 2-3, the Z'' vs $\log(f)$ spectroscopic plot gives a Debye peak

with the general form:
$$\text{Debye peak} = \frac{\omega\tau}{1+(\omega RC)^2} \quad (2-9)$$

where τ is the relaxation time or time constant of the RC element given by:

$$\tau = RC \quad (2-10)$$

The Debye peak is scaled according to the resistance, R since

$$Z'' = R \frac{\omega\tau}{1+(\omega\tau)^2} \quad (2-11)$$

The height of the peak $Z''_{\max} = R/2 \quad (2-12)$

The frequency of the peak max is given by

$$\omega_{\max} RC = 1 \quad (2-13)$$

where (ω_{\max}) is defined as the angular frequency at the maximum of a Debye peak:

$$\omega_{\max} = 2\pi f_{\max} \quad (2-14)$$

The M'' vs $\log(f)$ plot has a similar Debye peak, but is scaled according to the inverse of the capacitance, C

$$M'' = \frac{C_0}{C} \left[\frac{\omega\tau}{1+(\omega\tau)^2} \right] \quad (2-15)$$

In this thesis, data are presented in several ways, as Z'' vs Z' , as Z''/M'' vs $\log(f)$, as $\log C'$ vs $\log(f)$.

For each of these, an ideal parallel RC element gives the diagrams shown in Fig 2-4 and 2-5.

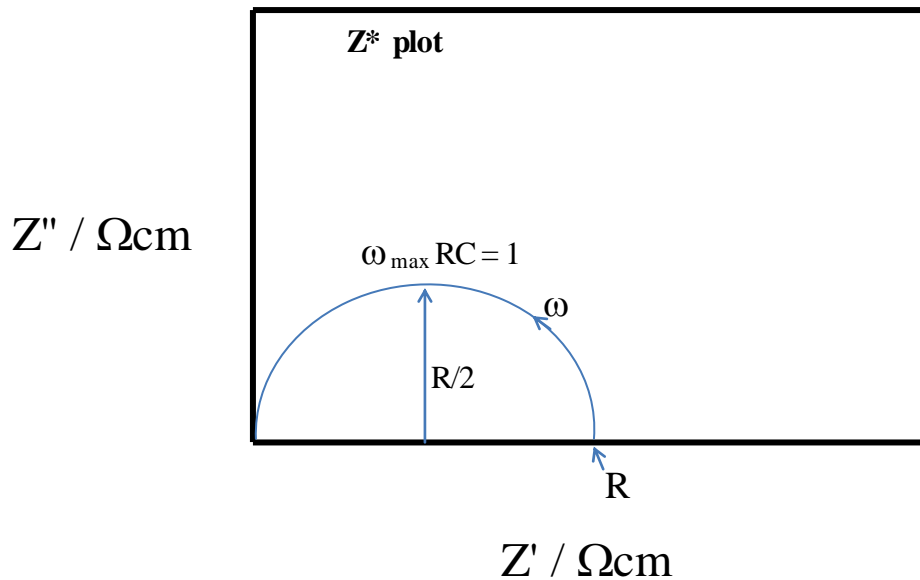


Figure 2-4: Schematic Z^* plot for electrically homogeneous materials and an ideal parallel RC element.

One semicircle is observed in the Z^* complex plane plot and a Debye peak in the spectroscopic plots of the imaginary components Z'' and M'' vs $\log(f)$.

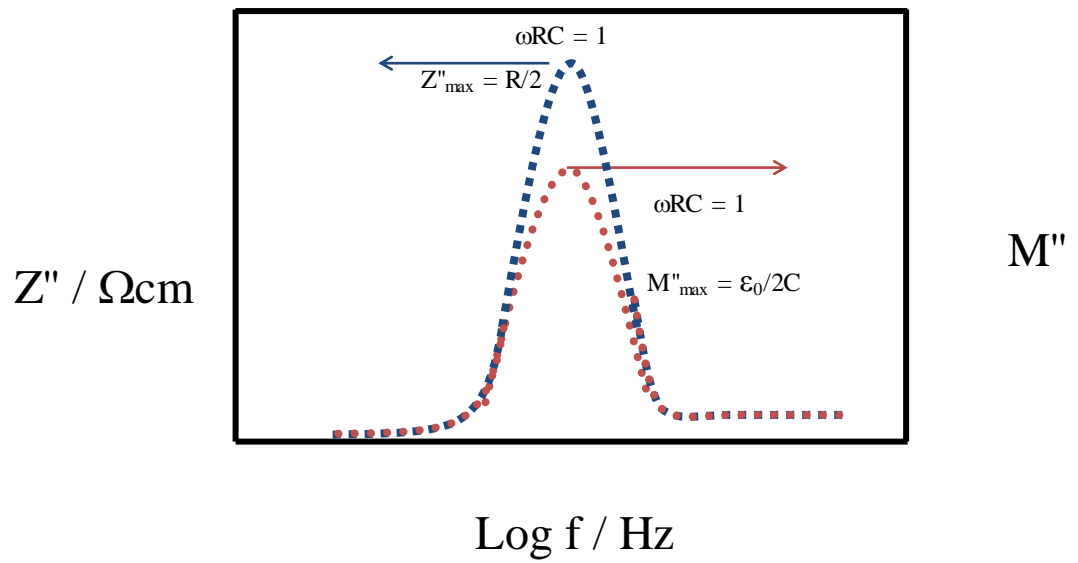


Figure 2-5: Z'' and M'' spectroscopic plots versus $\log(f)$ for a parallel RC element.

For an inhomogeneous material that typically contains grain (bulk) and grain boundary impedances, a more complex circuit consisting of two parallel RC elements in series is usually used, Figure 2-6. Two complex plane semicircles are obtained as shown in Figure 2-7 which indicate the presence of two electro-active-regions. Realisation of the most appropriate equivalent circuit is essential [17, 24] and is directly related to the origin of impedance effects [25].

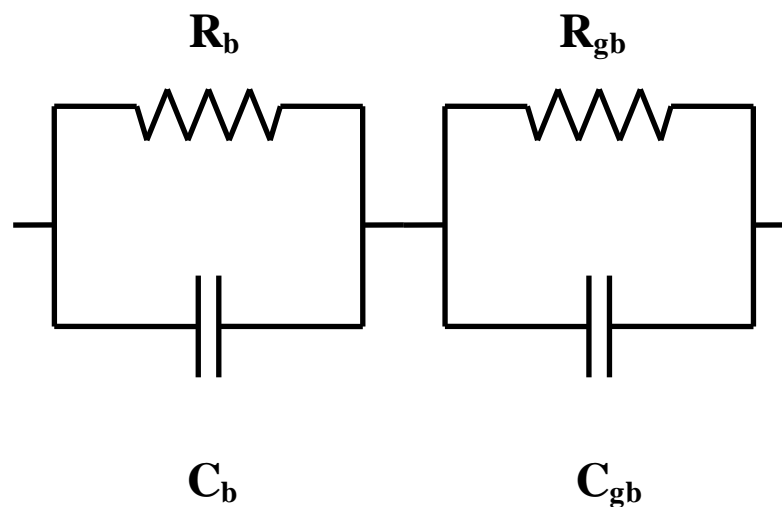


Figure 2-6: Two parallel RC elements in series which represent the possible equivalent circuit for a typical electroceramic.

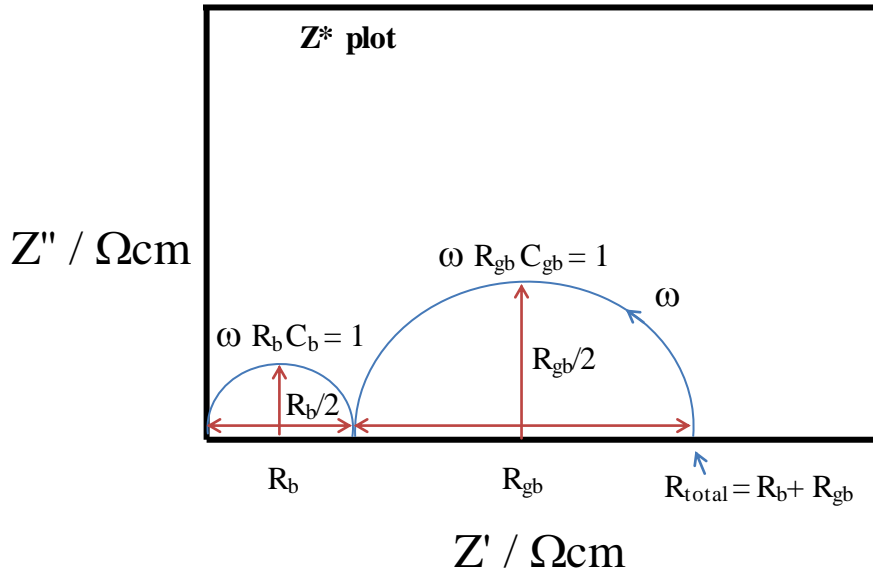


Figure 2-7: Schematic Z^* plot for electrically inhomogeneous materials.

Each component has a different relaxation time, τ , given by $\tau = RC$, for an electrically heterogeneous material. The relaxation times are a characteristic intrinsic property and independent of sample geometry. For an inhomogeneous ceramic, the following is often true: $R_{gb} \gg R_b$ and $C_{gb} \gg C_b$ in which case $\tau_{gb} > \tau_b$ and $\omega_{(max)gb} < \omega_{(max)b}$.

Two arcs are seen in the impedance complex plane. The high frequency arc passes through the origin of the plot. The large arc at low frequency is usually related to the resistive grain boundary response, whereas the smaller arc at high frequency is usually related to the bulk response. Z^* plots are useful to emphasise the most resistive components in the samples. In many cases, bulk data are difficult to obtain from Z^* plots if $R_{gb} \gg R_g$, because a single arc may be observed which is dominated by the grain boundary resistance.

Values of resistance and capacitance can be extracted directly from impedance data. The resistance values can be calculated from intercepts of the real axis. The equation $\omega_{max} RC=1$ can be used to calculate capacitance values at the maximum value of imaginary impedance Z'' at the top of each semicircle in Z^* plot. Z^* plots are usually dominated by the grain boundary component with high resistance values while grain capacitance are much smaller than the grain boundary capacitance. Values of resistance and capacitance of the grain and grain boundary components can be

independently calculated from Debye peak in spectroscopic plots of Z'' and M'' against \log (frequency) which occur at $\omega_{\max} RC = 1$ for the different electroactive regions, Figure 2-8 and 2-9. The arc of the complex impedance Z^* plane plot corresponds to the Debye peak for Z' and M'' .

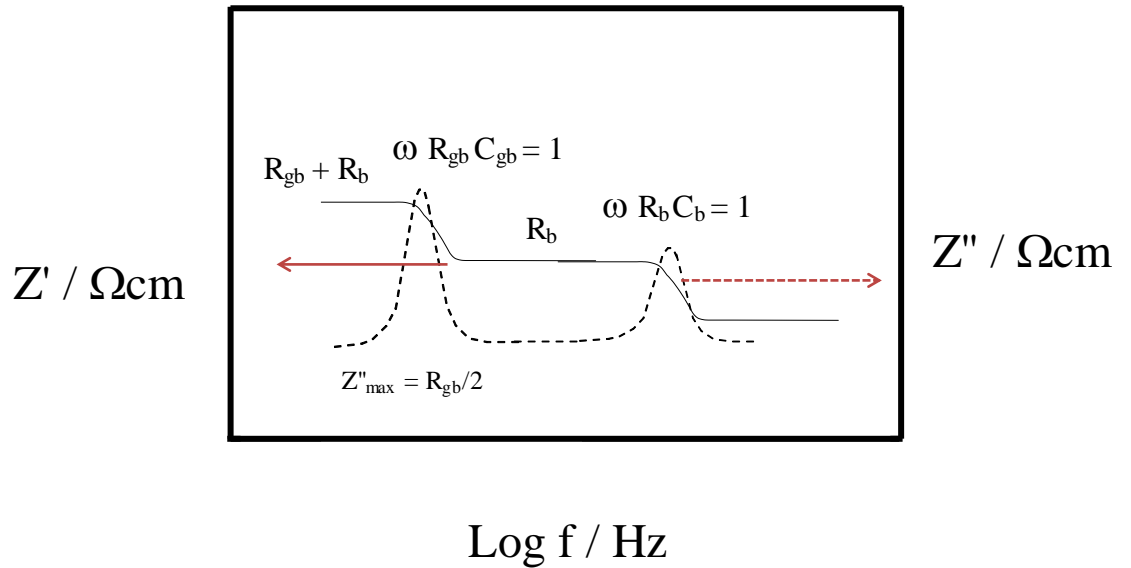


Figure 2-8: Z' and Z'' spectroscopic plots versus \log (f) for two parallel RC elements.

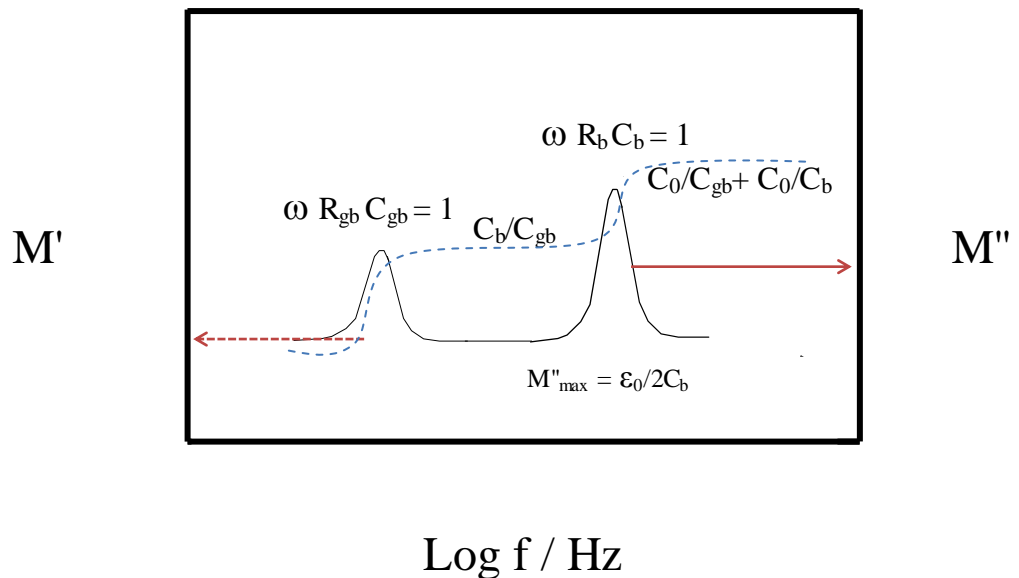


Figure 2-9: M' and M'' spectroscopic plots versus \log (f) for two parallel RC elements.

M''_{\max} is used to determine the value of the bulk capacitance according to:

$$C_b = \frac{\epsilon_0}{2M''_{\max}} F \text{cm}^{-1} \quad (2-16)$$

Grain boundary resistance values R_{gb} can be calculated using R''_{\max} values with the following equation:

$$R = 2 * R''_{\max} \quad (2.17)$$

Electric modulus and fixed frequency data can be used to calculate values of the relative permittivity (ϵ_r) using:

$$\epsilon_r = \frac{C_b}{\epsilon_0} = \frac{1}{\epsilon_0 M'} = \frac{1}{2 * M''_{\max}} \quad (2-18)$$

Figures 2-8 and 2-9 show frequency-independent regions which occur as plateaux. There is change in frequency with no change in Z' and M' . Figures 2-8 and 2-9 illustrate that low frequencies and high frequencies relax out the grain boundary and the bulk responses respectively. Figure 2-10 provides similar behaviour for the frequency-dependant response of permittivity against $\log(f)$.

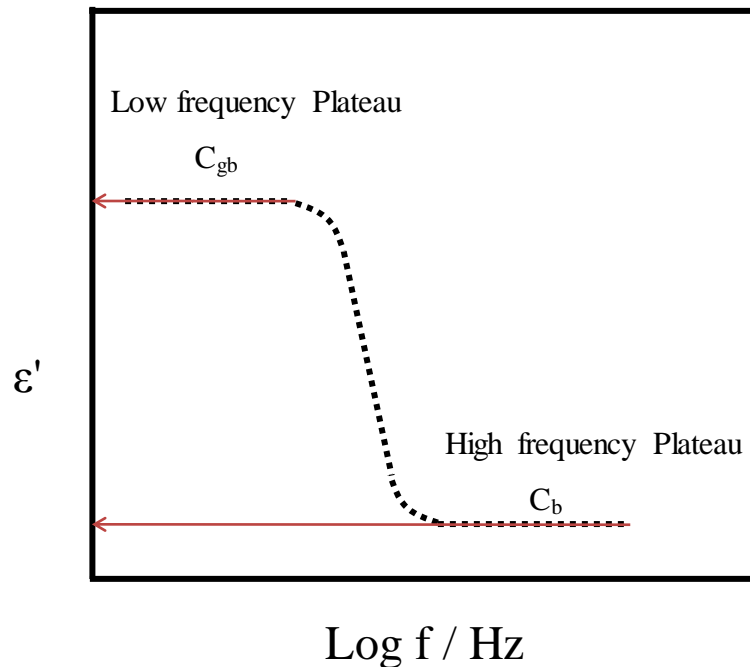


Figure 2-10: ϵ' versus $\log(f)$ for two parallel RC elements.

Brickwork model of g and gb regions in a ceramic placed between metal electrodes:

It is well-known that ceramics consist of grains, grain boundaries and pores, all of which can contribute to an electrical response [17]. The ‘‘Brick layer model’’ (BLM) is a useful model to interpret intra-granular and inter-granular regions of a ceramic [16, 26, 27], with ideally, large cube-shaped grains and narrow grain boundaries as flat layers between grains, Figure 2-11. l_1 , l_2 and l_3 are the thickness of grain, grain boundary and surface layer respectively. The equivalent circuit is comprised of three parallel RC elements linked in series. The magnitude of the capacitance is classified in Table 2-2. Their values can be used to identify the regions responsible for IS data. The value of capacitance depends on thickness as given by:

$$\frac{C_b}{C_{gb}} = \frac{l_{gb}}{l_b} \quad (2-19)$$

A thicker layer will have lower capacitance value. Table 2-2 shows that a grain boundary capacitance is higher than a bulk capacitance according to the brick layer model since $l_1 > l_2$. Therefore, it determines the relationship between capacitance and volume fraction, $C_b < C_{gb}$.

The capacitance value of a grain boundary is expected to be much higher than that for the bulk since their thicknesses are typically 5-100 μm for the bulk and $\ll 1\mu\text{m}$ for the grain boundary regions.

Table 2-2: Capacitance values and their possible interpretation [16].

Capacitance (F)	Phenomenon Responsible
10^{-12}	Bulk
10^{-11}	Minor, second phase
$10^{-11} - 10^{-8}$	Grain boundary
$10^{-10} - 10^{-9}$	Bulk ferroelectric
$10^{-9} - 10^{-7}$	Surface layer
$10^{-7} - 10^{-5}$	Sample electrode interface
10^{-4}	Electrochemical reactions

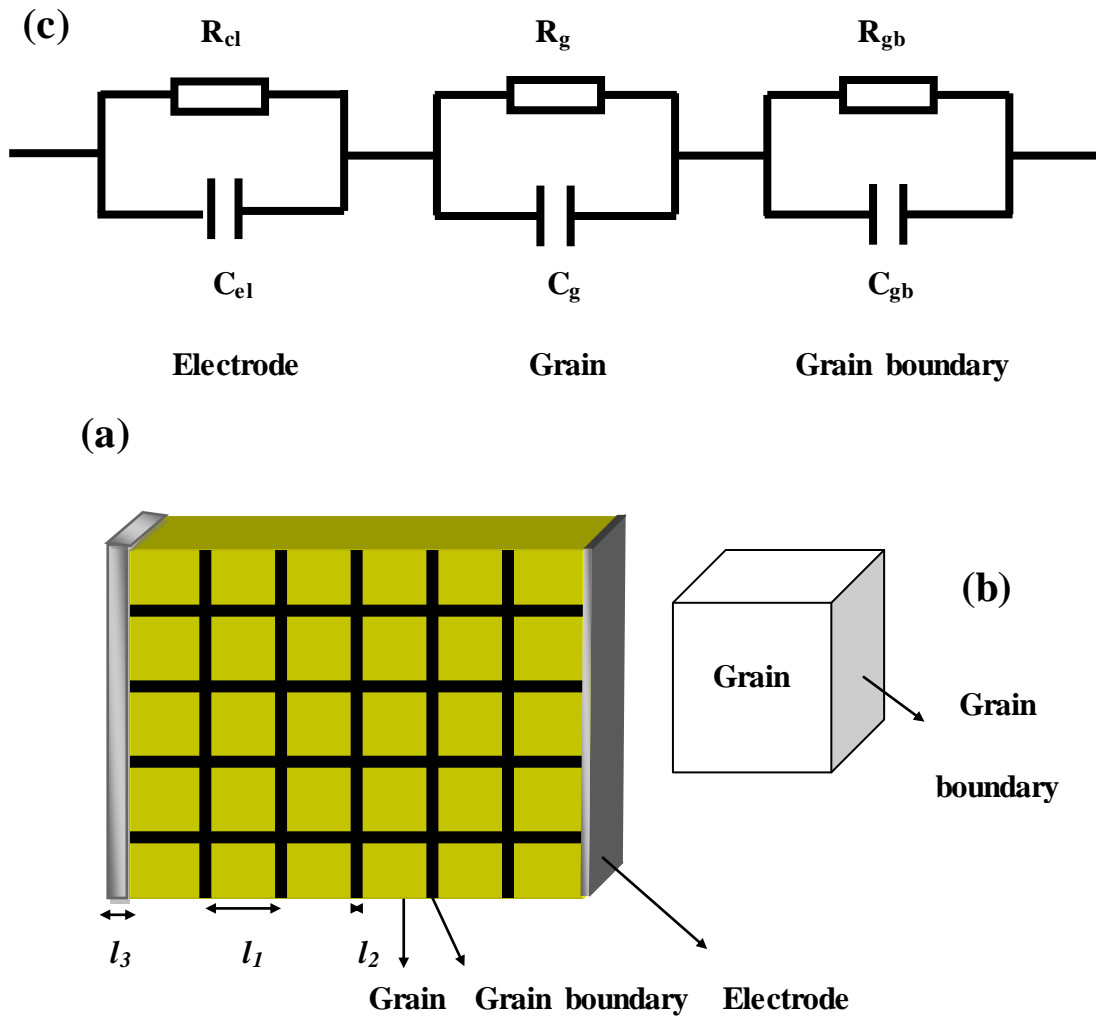


Figure 2-11: (a) The brick layer model of a polycrystalline material in a ceramic placed between metal electrodes, (b) magnification of grain and grain boundary without electrode, (c) The equivalent circuit for the brick layer model.

Plots of Z^* and/or Z'' , M'' are used to determine the degree of non-ideality and / or the degree of inhomogeneity. Figure 2-12 shows depression angle which is used to calculate the non-ideality degree [28]. The angle of depression (α) should be zero for an ideal parallel RC element with frequency-independent R, C values. Increasing heterogeneity leads to an increase in α . An ideal Debye peak for Z'' and M'' has Full Width Half Maximum (FWHM) of 1.14 decades [25, 29], whereas $FWHM > 1.14$ decades may occur for inhomogeneous ceramics. Increasing separation of M'' , Z'' peak maxima indicates an increase in inhomogeneity. Inhomogeneity such as, cation segregation or the presence of a second phase gives rise to broadened peaks.

Deviation from ideal behaviour is observed in the impedance response of most ceramics even though they are homogenous. Constant phase elements (CPE) are used to represent any non-ideality of the impedance response.

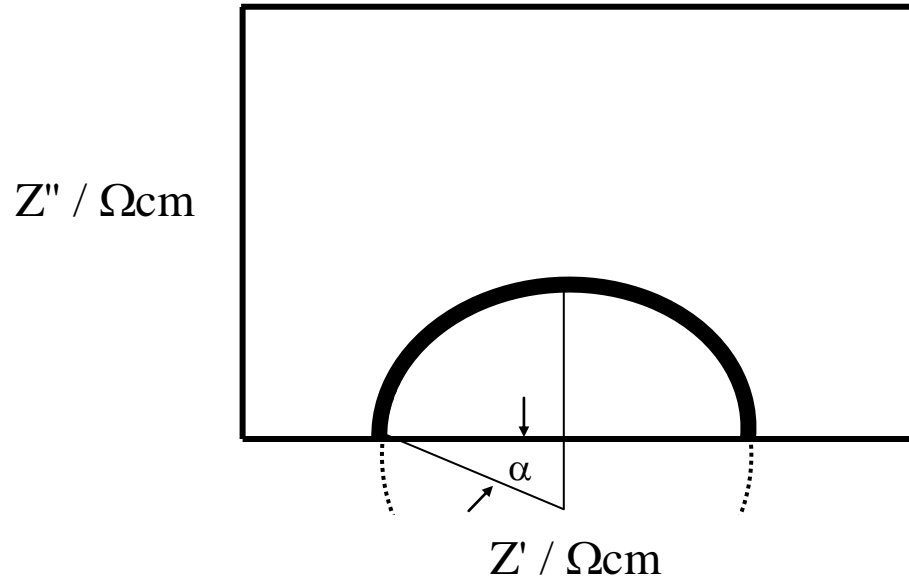


Figure 2-12: The depression angle (α) is presented in Z^* plot.

2.3.3.2 Arrhenius plot:

Arrhenius plots are used to represent the effect of temperature on conductivity:

$$\sigma = \sigma_0 e^{(-E_A/k_b T)} \quad (2-20)$$

where:

σ = conductivity

σ_0 = the pre-exponential factor

E_A = the activation energy

k_b = Boltzmann's constant

T = temperature (K)

An Arrhenius plot is presented as log conductivity against $1000/T(K)$. Conductivity values are obtained from intercepts on Z^* plots or peak maxima in Z'' , M'' plots.

The gradient of slopes of Arrhenius plots can be used to find the activation energy.

2.3.4 Fixed frequency capacitance measurement: LCR (L= Inductance, C= Capacitance and R= Resistance) measurements

Fixed frequency electrical property measurements were carried out in air as a function of temperature using a Hewlett Packard LCR meter Model 4284A. The two opposite flat surfaces of pellets with electrodes made from Pt paste, Ag paste and In-Ga alloy paste were attached to a conductivity jig and placed in a non-inductively wound tube furnace near the thermocouples. Data were read through a computer connected via a GP-IB interface card and analysed using software (HP 4284A LCR Meter). Capacitance and dielectric loss ($\tan\delta$) values were measured every 60 seconds for a total of 300 scans for temperatures of 25-250 °C using a furnace ramp rate of 1 °C/min, frequencies of 1 kHz, 10 kHz, 100 kHz, 250 kHz and 1 MHz and analysed using MS-Excel. The relative permittivity was calculated from:

$$\epsilon_r = \frac{C}{\epsilon_0} \times \frac{t}{A} \quad (2-21)$$

where, C = Capacitance (Farads – F), t = thickness of pellet without electrode (meters –m) ϵ_0 = permittivity in vacuum ($8.85419 \times 10^{-12} \text{ Fm}^{-1}$), and A = Area of flat surface of pellet (m^2).

2.4 References

- [1] A.R. West, Basic solid state chemistry, Wiley New York, 1988.
- [2] A. Moulson, J. Herbert, Electroceramics Chapman and Hall, New York, (1990) 41.
- [3] A.R. West, Solid state chemistry and its applications, John Wiley & Sons, 2007.
- [4] G. Höhne, W. Hemminger, H.J. Flammersheim, Differential scanning calorimetry, Springer Science & Business Media, 2003.
- [5] L.M. Nollet, Handbook of Food Analysis: Physical characterization and nutrient analysis, CRC Press, 2004.
- [6] S. Lee, Z.-K. Liu, M.-H. Kim, C.A. Randall, Influence of nonstoichiometry on ferroelectric phase transition in BaTiO₃, Journal of Applied Physics, 101 (2007) 054119.
- [7] M. Zaghrioui, A. Bulou, P. Lacorre, P. Laffez, Electron diffraction and Raman scattering evidence of a symmetry breaking at the metal-insulator transition of NdNiO₃, Physical Review B, 64 (2001) 081102.
- [8] A. Feteira, D.C. Sinclair, J. Kreisel, Average and local structure of (1-x)BaTiO₃-xLaYO₃ (0 ≤ x ≤ 0.50) ceramics, Journal of the American Ceramic Society, 93 (2010) 4174-4181.
- [9] F. Jiang, S. Kojima, Raman scattering of 0.91 Pb (Zn_{1/3}Nb_{2/3}) O₃-0.09 PbTiO₃ relaxor ferroelectric single crystals, Japanese journal of applied physics, 38 (1999) 5128.
- [10] A. Feteira, D.C. Sinclair, M.T. Lanagan, Effects of average and local structure on the dielectric behavior of (1-x) BaTiO₃-xLaYO₃ (0 ≤ x ≤ 0.40) ceramics, Journal of Applied Physics, 108 (2010) 014112.
- [11] L.B. McCusker, R.B. Von Dreele, D.E. Cox, D. Louer, P. Scardi, Rietveld refinement guidelines, Journal of Applied Crystallography, 32 (1999) 36-50.
- [12] H.D. Megaw, Ferroelectricity in crystals, (1957).
- [13] D. Sinclair, J. Paul Attfield, The influence of A-cation disorder on the Curie temperature of ferroelectric ATiO₃ perovskites, Chemical Communications, (1999) 1497-1498.
- [14] M.H. Harunsani, Characterisation of mixed-metal oxides prepared by hydrothermal synthesis, (2013).

- [15] N. Hirose, A.R. West, Impedance spectroscopy of undoped BaTiO₃ ceramics, *Journal of the American Ceramic Society*, 79 (1996) 1633-1641.
- [16] J.T.S. Irvine, D.C. Sinclair, A.R. West, Electroceramics: characterization by impedance spectroscopy, *Advanced Materials*, 2 (1990) 132-138.
- [17] A.R. West, D.C. Sinclair, N. Hirose, Characterization of electrical materials, especially ferroelectrics, by impedance spectroscopy, *Journal of electroceramics*, 1 (1997) 65-71.
- [18] J.R. Macdonald, *Impedance spectroscopy*, Wiley New York etc, 1987.
- [19] D.C. Sinclair, F.D. Morrison, A.R. West, Applications of combined impedance and electric modulus spectroscopy to characterise electroceramics, *Int. Ceram.*, (2000) 33-34.
- [20] I.M. Hodge, M.D. Ingram, A.R. West, Impedance and modulus spectroscopy of polycrystalline solid electrolytes, *Journal of Electroanalytical Chemistry and Interfacial Electrochemistry*, 74 (1976) 125-143.
- [21] D.C. Sinclair, A.R. West, Impedance and modulus spectroscopy of semiconducting BaTiO₃ showing positive temperature coefficient of resistance, *Journal of Applied Physics*, 66 (1989) 3850-3856.
- [22] A.K. Behera, N.K. Mohanty, S.K. Satpathy, B. Behera, P. Nayak, Investigation of complex impedance and modulus properties of Nd doped 0.5 BiFeO₃-0.5 PbTiO₃ multiferroic Composites, *Central European Journal of Physics*, 12 (2014) 851-861.
- [23] C.J. Cheng, D. Kan, S.H. Lim, W.R. McKenzie, P.R. Munroe, L.G. Salamanca-Riba, R.L. Withers, I. Takeuchi, V. Nagarajan, Structural transitions and complex domain structures across a ferroelectric-to-antiferroelectric phase boundary in epitaxial Sm-doped BiFeO₃ thin films, *Physical Review B*, 80 (2009) 014109.
- [24] E.J. Abram, D.C. Sinclair, A.R. West, A strategy for analysis and modelling of impedance spectroscopy data of electroceramics: doped lanthanum gallate, *Journal of Electroceramics*, 10 (2003) 165-177.
- [25] J.S. Dean, J.H. Harding, D.C. Sinclair, Simulation of Impedance Spectra for a Full Three-Dimensional Ceramic Microstructure Using a Finite Element Model, *Journal of the American Ceramic Society*, 97 (2014) 885-891.
- [26] J. Fleig, J. Maier, The impedance of ceramics with highly resistive grain boundaries: validity and limits of the brick layer model, *Journal of the European Ceramic Society*, 19 (1999) 693-696.

- [27] S.M. Haile, D.L. West, J. Campbell, The role of microstructure and processing on the proton conducting properties of gadolinium-doped barium cerate, *Journal of materials research*, 13 (1998) 1576-1595.
- [28] G. Friesen, M.E. Özsar, E.D. Dunlop, Impedance model for CdTe solar cells exhibiting constant phase element behaviour, *Thin Solid Films*, 361 (2000) 303-308.
- [29] D.C. Sinclair, A.R. West, Effect of atmosphere on the PTCR properties of BaTiO₃ ceramics, *Journal of materials science*, 29 (1994) 6061-6068.

Chapter 3: Effect of dc bias and pO₂ on the conductivity of undoped-BaTiO₃

3.1 Introduction

Ferroelectric BaTiO₃ is a dielectric material that is used widely in many varied ceramics applications in the electronics and electroceramic industries such as multilayer ceramic capacitors (MLCC), actuators, piezoelectric sensors, ferroelectric memories (FRAM), electro-optic devices, transducers, positive temperature coefficient of resistance (PTCR) thermistors and dielectric memories (DRAM) [1-7]. The properties of barium titanate depend on a number of compositional and processing parameters such as: dopant ions, application of a dc bias voltage during measurements, sample preparation techniques and the ceramic processing conditions, especially the temperature, rate of subsequent cooling, time, pressure and sintering atmosphere.

A substantial number of powder synthesis methods have been used for the preparation of barium titanate. The most common is synthesis by conventional solid-state reaction of mixed powders of BaCO₃ and TiO₂ at temperatures higher than 1200 °C [8].

BaCO₃ and TiO₂ reagents have been mixed by various ways prior to heating. These include hand mixing *HM*, horizontal ball milling *BM* and planetary ball milling *PBM*. BaTiO₃ powder produced by *PBM* possessed a much higher sinterability than those powders synthesized by *HM* and *BM* of reagents [9]. The sintering temperature of a ceramic using *BM* was 150 °C higher than that using *PBM* [10]. BaTiO₃ was obtained at 800 °C by *PBM* [11] whereas, *HM* required higher temperatures. The average particle size of PTCR powders prepared using *PBM* was much smaller than *BM* [12].

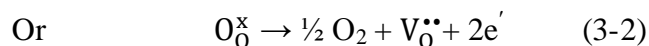
Planetary ball milling causes changes in the free energy, leading to the creation of new surfaces, changes in crystal lattice [13], reduction of the modest particle size and production of a stress field. These effects could alter the permittivity and the dielectric temperature dependence [9].

BaTiO₃ undergoes a transition from a ferroelectric tetragonal polymorph to a paraelectric cubic polymorph upon heating above 130 °C (Curie temperature) at which ϵ' passes through a maximum [14, 15] depending on the microstructure,

crystallinity, domain structure and defect structure [16-18]. The ferroelectricity in BaTiO₃ arises from a displacement of the titanium ions away from the centrosymmetric position within the TiO₆ octahedra [19] along the *c*-axis [20] because Ti ions are too small to occupy the centrosymmetric position. This result leads to spontaneous polarisation. Ti ions are displaced ~ 0.1 Å from this central position. Ti ions undergo a displacement relative to the surrounding oxygens related to the hybridisation between Ti 3d and oxygen 2p states [21]. Therefore, a dipole moment of the unit cells is formed. Ferroelectric domains form as a result of cooperative dipole-dipole interaction [22]. Tetragonal BaTiO₃-based ceramics possess a low tan δ and a high dielectric constant value due to asymmetry within the crystal structure. Therefore, BaTiO₃ is a good dielectric material used for ceramic capacitors [23].

BaTiO₃ with typical first order phase transition has a sharp peak in ε' [24]. At the Curie temperature, dielectric polarization increases which in turn causes an increase in permittivity [15]. At the Curie point, the free energy is equal for the ferroelectric phase [25] and that of the paraelectric phase [26]. Below T_C, the free energy of the tetragonal (ferroelectric) state is lower than that of the cubic (paraelectric) BaTiO₃ state. In the paraelectric state above T_C, the Curie-Weiss temperature can be accessed experimentally from the Curie-Weiss law of permittivity to show that BaTiO₃ obeys Curie-Weiss behaviour.

BaTiO₃ is an insulator at room temperature but the semiconducting behaviour that is commonly observed without direct donor doping or impurities is attributed to loss of oxygen from the crystal lattice [27] during firing at high temperatures, ≥ 1350 °C in air or at low partial pressure of oxygen above ~ 1200 °C [28-38]. Oxygen loss occurs by the idealized reaction:



The liberated electrons reduce Ti⁴⁺ to Ti³⁺ and give rise to leakage conductivity and device degradation [39]. This behaviour leads to n-type semiconducting materials with dark-coloured samples and general formula BaTi_{1-x}⁴⁺Ti_x³⁺O_{3-x/2}.

Oxygen loss from stoichiometric BaTiO₃ is too small to be detected clearly by thermogravimetry. Nevertheless, it can change the electrical properties from insulating to n-type semiconducting [40].

Oxygen loss is associated with different factors such as temperature, atmosphere, pellet density, ceramic microstructure and rate of heating-cooling. Samples can be insulating or semiconducting depending on the amount and distribution of oxygen loss. Electrical inhomogeneity can be observed with different processing conditions. Heating samples in O₂ helps to reduce the amount of oxygen loss [14].

Semiconductivity in BaTiO₃ has been investigated by many authors. The origin of semiconductivity is varied and may involve impurities, direct donor doping and oxygen loss, all of which lead to electron injection into the crystal structure [2, 28].

A PTCR effect in BaTiO₃ can be found under certain conditions. A modest PTCR phenomenon is observed in samples quenched from high temperatures [28]. The materials exhibit a core-shell structure [41].

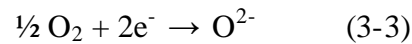
The high dielectric constant of BaTiO₃ depends on synthesis route (purity, density, grain size) [42], temperature, frequency, dopants [43], polarization of electrode and Schottky barrier development at the electrode-ceramic interface which is attributed to a non-ohmic electrode contact. Using different types of electrode can give different results. Non-ohmic electrode contacts leading to PTCR effect in BaTiO₃ can be obtained by using Au electrodes. In contrast, non-ohmic electrode contacts can be eliminated by applying In-Ga alloy electrodes which has a lower electron work function [44-46].

It has recently been shown that the electrical properties of BT, doped BT and other titanate perovskites are modified by application of a small dc bias [35, 40, 47-59]. If the materials are in n-type, then the conductivity decreases with a dc bias but, by contrast, with p-type materials, the conductivity increases with a dc bias [55]. This effect has been seen with n-type Mn-doped BT and donor-doped rutile [58] and also in p-type BT doped with acceptors Zn [54], Mg [56] and Ca [50]. In general, the ceramic conductivity changes by one to two orders of magnitude on application of a small dc bias for temperatures above about 300 °C. The changes are fully reversible on removing the bias and the time taken for the changes to occur varies from a few

hours at 300 °C to a few minutes at 600 °C. For stoichiometric BT and BT doped with isovalent dopants such as Ca for Ba, there is little effect of dc bias on the conductivity [50].

Similar changes are seen in both the bulk and grain boundary impedances of ceramic samples and are not associated with sample-electrode interfacial effects such as voltage-dependent Schottky barriers. The effect is usually independent of the type of electrode that is used. It is a low field effect and can be observed with voltages as low as 1 volt corresponding to a field gradient of 10 volts per cm and is an intrinsic property all of samples [48, 49].

The effect can be understood most easily by first considering the behaviour of n-type materials whose conductivity decreases on application of a dc bias. Similar changes are seen on varying the atmosphere surrounding the sample and in particular, the effect of increasing oxygen partial pressure is to decrease the conductivity as a consequence of the following changes at the sample surface:



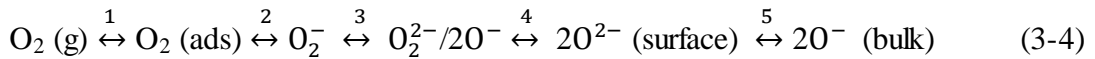
Thus, with increasing oxygen partial pressure, oxygen molecules absorb on the sample surface and ionise by picking up electrons from the sample surface and interior; as a consequence, conductivity decreases.

For p-type materials, two processes are involved with the changes that occur on application of a bias voltage. First, electrons are trapped at the sample surface in a similar way to what happens with n-type materials. Second, electrons are created inside the sample and near the surface by ionisation of underbonded oxide ions. This creates singly-charged O^- ions which can be regarded as holes and are the source of the p-type conductivity and subsequent increase in p-type conductivity with a dc bias [49, 53, 54, 56].

Underbonded oxide ions are those which are surrounded by an insufficient amount of the positive charge that is necessary to stabilise the divalent oxide ion. In the gas phase, divalent oxide ions are unstable and spontaneously dissociate into monovalent oxide ions and electrons. In the solid state in most crystal structures, however, divalent oxide ions are stable because they are surrounded by an effective charge of 2+. In acceptor doped materials such as Mg-doped BT, the oxide ions near to the

Mg dopant are underbonded and it is suggested that these are able to ionise readily on application of a small bias voltage [56].

It has been suggested that changes at sample surfaces are responsible for variation in conductivity both with changing oxygen partial pressure and with a small bias voltage. The surface equilibria involving oxygen consist of several stages, as shown below [58]:



Several of these stages involve electron transfer and therefore, will influence the electrical properties of the material. Before it was discovered that the properties of bulk materials could be changed by application of a small bias voltage, it was thought that bulk properties would be independent of a small voltage and therefore, any observed voltage-dependent changes would be attributable to interfacial phenomena such as Schottky barrier formation since a Schottky barrier is not a material barrier but is simply a voltage barrier. It now seems likely that the electrical properties of ceramic materials can be modified by reactions at sample surfaces which involve electron transfer processes. Although many studies into the electrical properties of doped BT ceramics have been reported, to date there has been very little consideration of the effect of applied voltage on the properties. One objective of the studies reported in this thesis is to consider the effect of voltage on the electrical properties of rare earth doped BT.

3.2 Experimental Procedure

BaTiO₃ powders were mixed using three different methods: hand mixing of reagents, ball milling and planetary ball milling using BaCO₃ (Aldrich 99.8 %) and TiO₂ (Aldrich 99.9 %). Samples were fired at different temperatures 1350-1450 °C in air for 12-24h. After heating, the samples were either left inside the furnace to cool to room temperature or withdrawn from the furnace and quenched in air.

Phase analysis was carried out using XRD which was used also to calculate lattice parameters. Two Stoe diffractometers were used, a Stoe Stadi-P image plate detector for phase identification and a position sensitive detector for lattice parameter determination.

DSC was used to study the transition from the tetragonal to cubic phase from room temperature to 200 °C, with heating at rate 10 °C/min in argon.

The electrical properties of BaTiO₃ ceramic pellets were investigated by IS. Powders were pressed uniaxially in a stainless steel die. Pressed pellets were placed on sacrificial powder of the same composition on platinum foil and sintered between 1350-1450 °C for 12h in air.

Dielectric characteristics were measured with a Hewlett Packard LCR meter Model 4284A with data recorded over several frequencies in the range 1 kHz to 1 MHz from room temperature to 200 °C.

IS measurements were carried out in air between room temperature and 700 °C, over the frequency range 20 Hz - 2 MHz using electrodes fabricated from Pt paste, Ag paste and liquid In-Ga alloy using an Agilent (E4980A) impedance analyser with an ac measurement voltage of 0.1 V and dc voltage between 0 and 10V. Measurements were obtained in N₂, air, and O₂ atmospheres at 400 °C across the frequency range 0.01 Hz to 1 MHz using a Solartron, SI 1260 with an applied voltage of 100 mV.

3.3 Results

3.3.1 XRD study of undoped BaTiO₃

The XRD patterns of undoped barium titanate prepared by hand mixing *HM*, ball milling *BM* and planetary ball milling *PBM* are shown in Figure 3-1. The patterns show well-defined peaks. The samples were phase-pure and fully indexed on a tetragonal unit cell with space group P4mm, Table 3-1 without secondary impurity phases. Lattice parameters are in good agreement with ICDD card # 5-626 [60] and are consistent with lattice parameters for BT reported elsewhere [61].

The theoretical density (DT) was determined from unit-cell contents and volume. The relative densities of all samples, calculated from pellet mass and dimensions were 83.1 – 91.3 % of the value expected for fully dense pellets, Table 3-1. The values of lattice parameters for *HM*, *BM* and *PBM* are similar. The value of density for *HM* decreased slightly compared to *BM* and *PBM*. The *PBM* has the highest density as a result of high energy ball milling and formation of fine particles [62] whereas, *HM* has the lowest density.

3.3.2 Electrical and structural characteristics of undoped BaTiO₃

3.3.2.1 LCR results

Permittivity data and $\tan \delta$ are plotted against temperature for pellets of three samples which were heated as shown in Table 3-1. Data measured at 250 kHz are shown in Figure 3-2 (a) and (b). ϵ' increases to a maximum in the range ~ 1627- 8433, Figure 3-2 (a) at the Curie temperature T_C . The value of ϵ'_{\max} for *PBM* was highest. The value of *BM* permittivity is lower than reported in the literature which is attributed both to the smaller grain size [63] and low densification and high porosity [9]. A normal ferroelectric behaviour was observed and ϵ' showed a sharp peak attributable to the tetragonal to cubic phase transition [64] with no apparent broadening of the ferroelectric transition [15]. Above T_C , in the paraelectric state, the temperature dependence of the dielectric constant obeys the Curie-Weiss law, Figure 3-4. The Curie-Weiss behaviour did not show any considerable deviations. No samples showed any significant frequency dependence of permittivity as shown for *HM* in Figure 3-3 and therefore, the peak in ϵ' could be used to extract T_C . Permittivity data are plotted in Curie-Weiss form in Figure 3-4 and C_w values listed in Table 3-2. The difference between T_C and T_0 values is attributed to the first-order transition of

barium titanate which is described by Devonshire's theory [65]. All samples showed non-leaky dielectric behaviour except *HM* which showed some conductivity with dielectric loss values ~ 0.035 , Figure 3-2 (b) which is in good agreement with literature data [66, 67]. The general behaviour is similar for all samples exhibiting a peak in $\tan \delta$ in which local maximum (peaks) were observed ~ 120 °C, in accordance with literature data. This result corresponds to the maximum permittivity value which occurred at the phase transition from the ferroelectric (tetragonal) to paraelectric (cubic) phase. Below the maximum value, $\tan \delta$ for *HM* and *PBM* initially decrease and then increase with increasing temperature. The reduction in the value of dielectric loss is quite pronounced for *PBM* from 0.019 at room temperature to 0.01 at ~ 100 °C, while, a slight drop was observed for *HM* at low temperatures.

3.3.2.2 Differential Scanning Calorimetry (DSC)

DSC on *HM* and *BM* showed a sharp ferroelectric-paraelectric (FE-PE) phase transition, Figure 3-5. The value of T_{\max} at the phase transition temperature of *BM* is very similar to that obtained by LCR measurement. A slight difference for *HM* between DSC and LCR values was observed as a result of changes in sintering temperature and cooling rate.

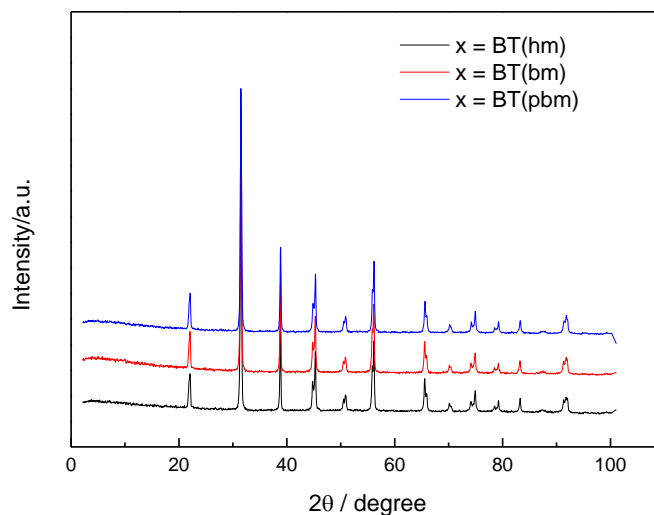


Figure 3-1: Room temperature XRD patterns of BaTiO₃ for *HM*, *BM* and *PBM* samples sintered at 1350-1450 °C for 12h in air and either quenched or slow-cooled.

Table 3-1: Crystal structure, lattice parameters, c/a ratio, unit cell volume, measured density (D_m), theoretical density (D_T) and relative density (D_{rel}).

Sample	Unit cell	a (Å)	c (Å)	c/a ratio (tetragonality)	V (Å ³)	D_m	D_T	(D_{rel}) (%)
HM 1350-12h, SC Pt electrodes	Tetragonal (P4mm)	3.994(1)	4.033(1)	1.0098	64.34(2)	5.00	6.02	83.1
BM 1350-12h, Q In-Ga electrodes	Tetragonal (P4mm)	3.992(1)	4.032(1)	1.0100	64.24(3)	5.32	6.03	88.3
PBM 1350-12h, Q Ag electrodes	Tetragonal (P4mm)	3.992(5)	4.031(5)	1.0098	64.25(1)	5.44	6.03	90.3

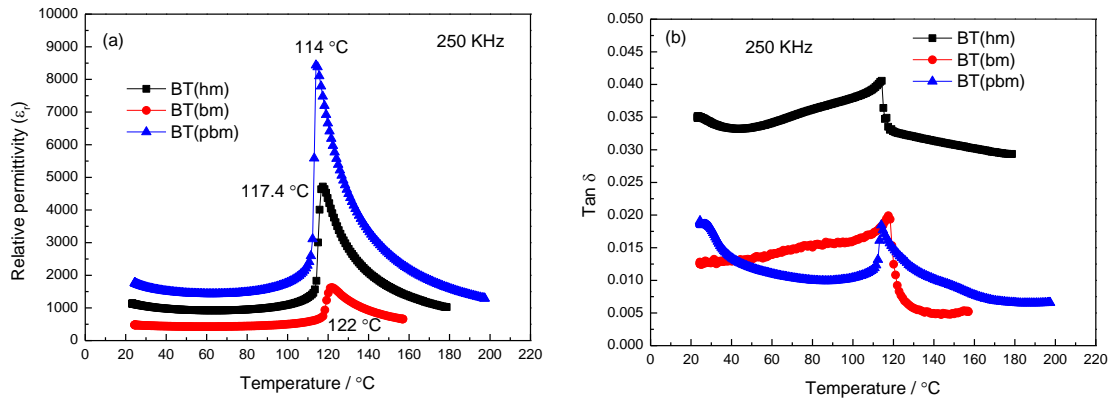


Figure 3-2: Fixed frequency measurements at 250 kHz of (a) relative permittivity (b) dielectric loss ($\tan \delta$) versus temperature.

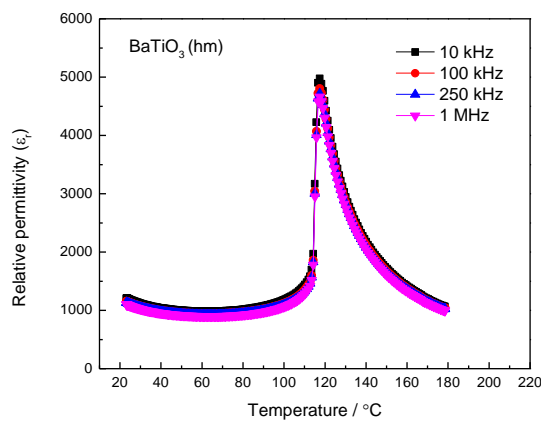


Figure 3-3: Temperature dependence of the relative permittivity for *HM* at fixed frequencies from 10 kHz – 1MHz.

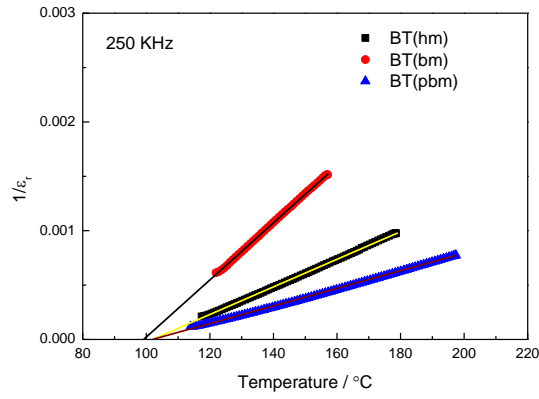


Figure 3-4: Curie-Weiss plots of permittivity at 250 kHz.

Table 3-2: Values of T_C , T_o , $T_C - T_o$ and C_w .

Sample	T_C (°C) from ϵ'	T_C (°C) from DSC	T_o (°C)	$T_C - T_o$ (°C)	C_w (10^5 K)
HM	117(1) at (1350-12h SC)	133(1) at (1400-12h Q)	103(2)	14(3)	0.782
BM	122(1)	129(1)	99(2)	23(3)	0.377
PBM	114(1)		102(3)	12(4)	1.240

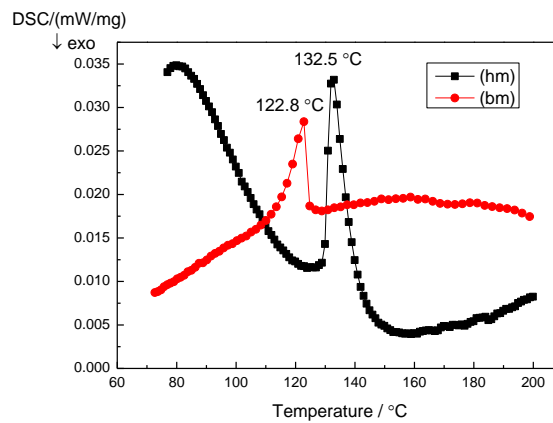


Figure 3-5: DSC trace of $BaTiO_3$ for *HM* and *BM* sintered at 1400-12h Q in air.

3.3.2.3 Raman Spectroscopy Results

Raman spectra were obtained at room temperature as shown in Figure 3-6. All data are consistent with previously reported results [68-71]. The sharp peak at $\sim 305 \text{ cm}^{-1}$ is a feature of tetragonal barium titanate as a fingerprint of ferroelectric behaviour (long-range ordering of dipoles) [72], which is connected with the transverse E1 (C_{4v}) symmetry [17, 70, 73, 74]. The spectra of BaTiO_3 ceramics show six peaks, specifically, narrow peaks at 170 and 305 cm^{-1} , asymmetric broader bands (with full-width at half-maximum (FWHM) of about $40\text{--}70 \text{ cm}^{-1}$) with peaks at 263, 512, and 718 cm^{-1} , and a small peak at 470 cm^{-1} [75, 76]. The identities of these peaks demonstrate the existence of BaTiO_3 indicating the absence of impurities [76, 77]. In the cubic phase, the peaks at 262, 514, and 717 cm^{-1} are much broader and more symmetrical. These peaks are associated with the effect of second-order or displacement disorder of the Ti atoms from the octahedral site centre [78, 79]. The band at 718 cm^{-1} is a highly broad, weak peak in the cubic phase and is usually a special characteristic of the tetragonal phase [71]. No modes were observed around 800 cm^{-1} . At reciprocal wavelength range around 800 cm^{-1} , the occurrence of an A_{1g} octahedral breathing mode was observed which corresponds to a Raman inactive mode for simple perovskites, especially since the mode is symmetrical and does not give rise to a change in polarization [71, 80].

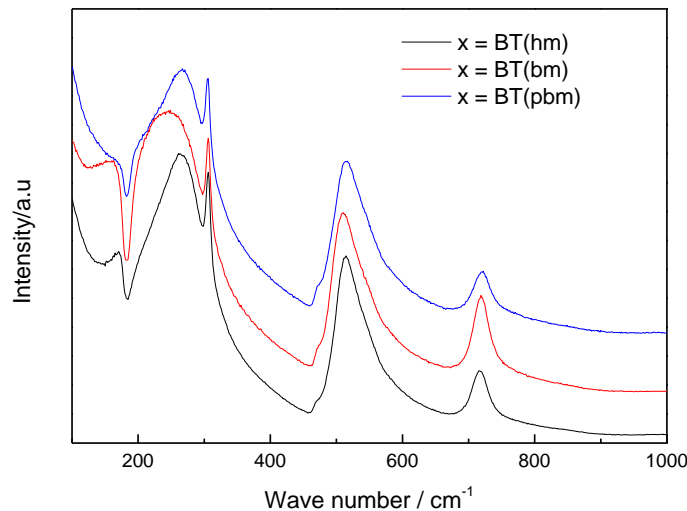


Figure 3-6: Room-temperature Raman spectra for BaTiO_3 .

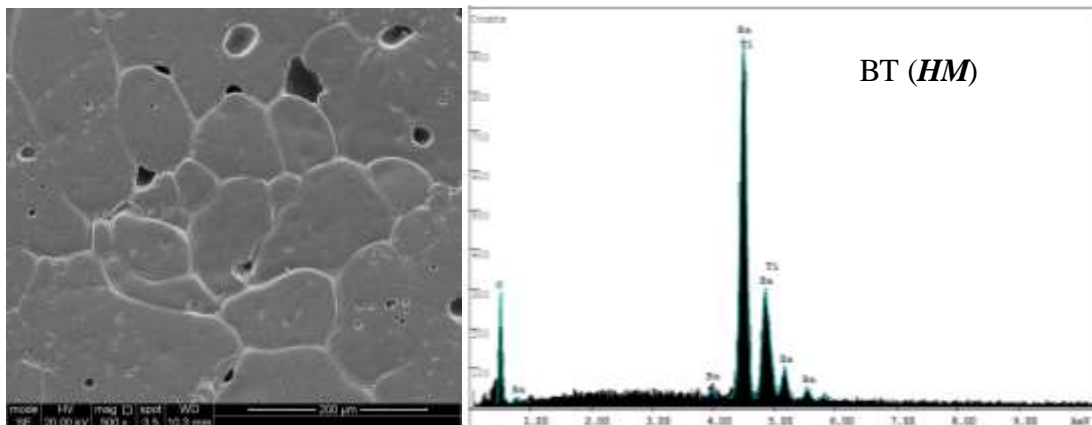
3.3.2.4 SEM Results

The ceramic microstructure of thermally etched surfaces determined by SEM is shown in Figure 3-7. No secondary phases on sample surfaces were observed, in either SEM backscattered images or EDS traces. The grain size is ~100-200 , 5 and 200 μm for *HM*, *BM* and *PBM* respectively which showed an exaggerated grain growth size for *HM* and *PBM*; similar result was observed in the literature [22] whereas, grain growth is inhibited for *BM*.

Exaggerated grain growth is a recognized feature in barium titanate based ceramics [81] which is maybe attributed to high temperature sintering especially with long periods of sintering which give rise to materials with large grain sizes, e.g. $> 50 \mu\text{m}$ [19, 82-84] particularly in the presence of a small amount of Ti-rich phase [85].

Exaggerated grain growth is associated with twinning induced by small but significant amounts of oxygen loss [86]. Several authors suggested that the existence of parallel (111) twin boundaries in grains of cubic BaTiO_3 seems to be the prerequisite intrinsic condition for anisotropic grain growth [87-89].

The SEM micrographs indicated that the grain size and distribution are uniform. *PBM* has a lower porosity than other samples.



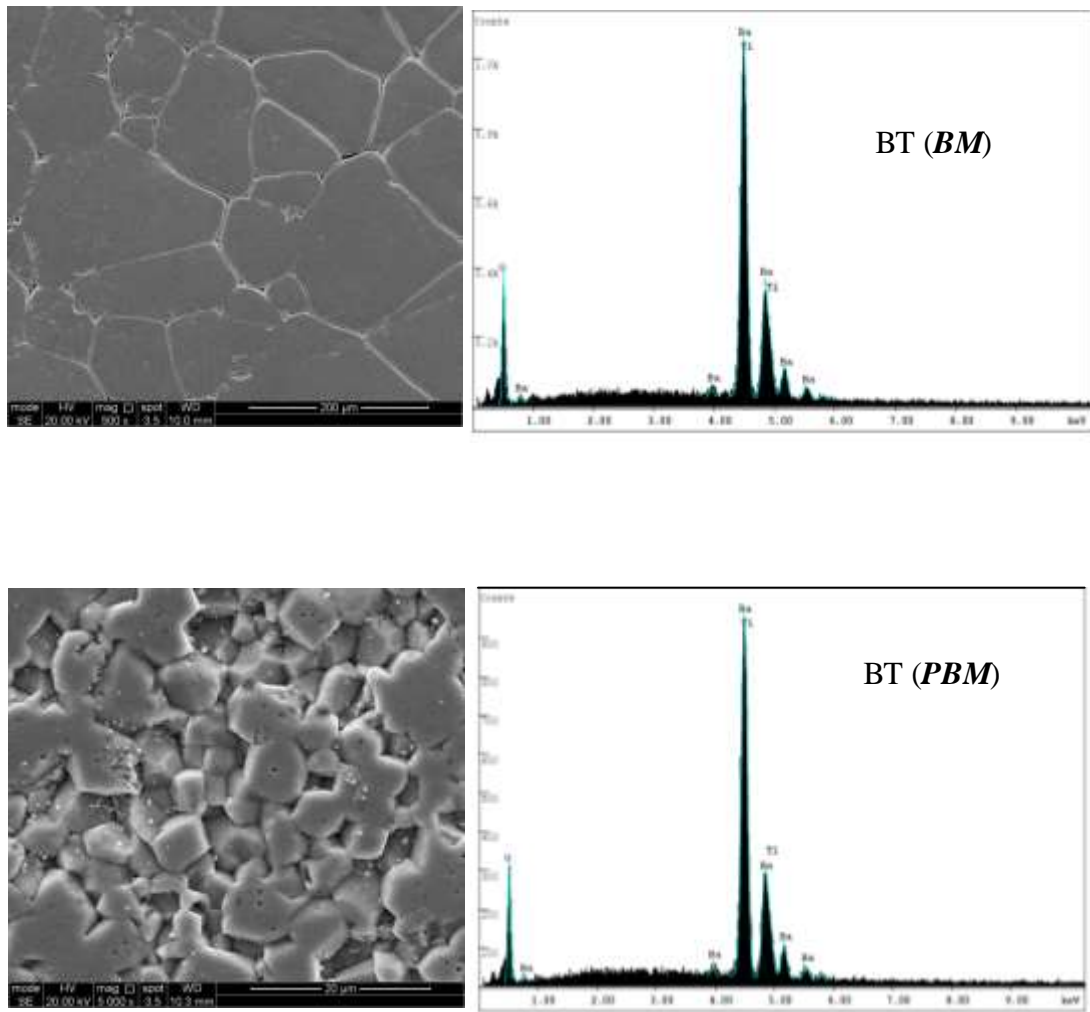


Figure 3-7: SEM images and EDS traces of BaTiO₃.

3.3.2.5 Impedance Spectroscopy Results

A selection of results in this section are presented on BaTiO₃ prepared by mixing in three ways, *HM*, *BM* and *PBM*, heated at different temperatures, either slow-cooled or quenched and with different electrodes. The three milling routes gave similar results and mainly those for *HM* are presented with a brief summary of *BM* and *PBM* results. The samples studied are listed in Table 3-3. Some samples were reheated under different conditions. Therefore, a new sample label was used for each step.

Table 3-3: Detailed conditions of samples prepared by hand mixing.

Sample	Heating temperature	Electrode type	Cooling
1	1350 °C for 12 h in air	Pt	Slow-cooled, 10 °C/min
2	1400 °C for 12 h in air	Ag	Slow-cooled, 10 °C/min
3	Sample (2) reheated sequentially at 1350 for 4 h, 1300 °C for 4 h, 1200 °C for 4 h, in air	Ag	Slow-cooled, 10 °C/min
4	Sample (1) reheated in air at 1350 °C for 12 h	Pt	Air-quenched
5	Sample (1) reheated in air at 1400 °C for 24 h	In-Ga	Air-quenched
6	Sample (4) was polished and reheated in air at 1400 °C for 10 minutes	In-Ga	Air-quenched
7	Sample (4) was polished and reheated in air at 1400 °C for 10 minutes	Ag	Air-quenched
8	1380 °C for 30 minutes in air	Pt	Air-quenched
9	1400 °C for 12h in air, reheated at 1400 °C for 1h in air	Pt	Air-quenched
10	1400 °C for 12h in air, reheated at 1300 °C	Ag	Air-quenched
11	1350 °C for 12h in air, reheated at 1335 °C	Ag	Air-quenched
12	Sample (3) was reheated at 1200 °C for 1 h, in air	Ag	Air-quenched
13	1450 °C for 12 h, in air	In-Ga	Air-quenched

3.3.2.5.1 Slow-cooled samples

(1) Typical impedance data

Sample (1) slow cooled from 1350 °C was measured at different temperatures by IS with Pt electrodes on stepwise heating and cooling over the temperature range 25-750 °C in air. A typical set of impedance data, Figure 3-8 showed it to be electrically

heterogeneous. The *HM* samples were insulating at room temperature. The impedance complex plane plot at 453 °C, Figure 3-8 (a), shows two arcs which can be modeled by the ideal equivalent circuit with two parallel RC elements in series. The grain boundary arc at low frequencies is much larger than the grain arc at high frequencies. The total resistance ($R_{(t)} = R_g + R_{gb}$) was obtained from the real, Z' axis intercept at lower frequencies. $R_g = R_1$ and $R_{gb} = R_2$. Resistance and capacitance values were extracted from Z^* . $R_{(t)}$ is $\sim 2 \times 10^5 \Omega\text{cm}$, where $R_g = 2.80 \times 10^4 \Omega\text{cm}$, $R_{gb} = 1.72 \times 10^5 \Omega\text{cm}$, $C_g = 2.85 \times 10^{-11} \text{Fcm}^{-1}$ and $C_{gb} = 7.40 \times 10^{-9} \text{Fcm}^{-1}$.

Z'' and M'' spectroscopic plots, (b), show that the Z'' plot contains two peaks, which correspond to the two semicircle arcs in the complex plane, but they are not well-resolved and were dominated by the low frequency peak, whereas the M'' plot shows a single peak at higher frequency, which corresponds to the higher frequency Z^* semicircle arc. M'' peaks represent the bulk component of the sample at the higher frequency with the lowest capacitance value. The f_{max} for Z'' and M'' peaks are separated by three orders of magnitude. This indicates an inhomogeneous microstructure. The Debye-like peaks in Z'' and M'' spectra and arc in Z^* were seen at temperatures ≥ 375 °C.

The Y' data show two plateaus, (c). The low frequency plateau is equal to $(R_T)^{-1}$, whereas, the high frequency plateau is associated with both resistance and capacitance and does not simply correspond to R_1^{-1} but corresponds to $\frac{R_1 C_1 + R_2 C_2}{R_1 R_2 (C_1 + C_2)}$.

Spectroscopic plots of capacitance, C' against frequency, (d), suggest the presence of two components that correspond to the bulk capacitance C_b at high frequency and an interfacial or grain boundary capacitance, C_{gb} at low frequency. The values of the bulk capacitance were around $\sim (2 - 3) \times 10^{-11} \text{Fcm}^{-1}$, whereas, the values of the low frequency interfacial or grain boundary capacitance were difficult to estimate since the plateau region was not well defined in the low frequency C' plots. In addition, the equation for the low frequency plateau is more complex than a simple capacitance.

Figure 3-9 shows the change in the capacitance values of the bulk component at high frequency, (b), obtained using M'' spectroscopic plots against $\log f$ at different temperatures. With increasing temperature, M''_{max} becomes larger, (a), and therefore, C_b becomes smaller. This behaviour is well-known for ferroelectric materials in the

paraelectric region above T_C [48] and is presented as a Curie-Weiss decay at higher temperatures, (b).

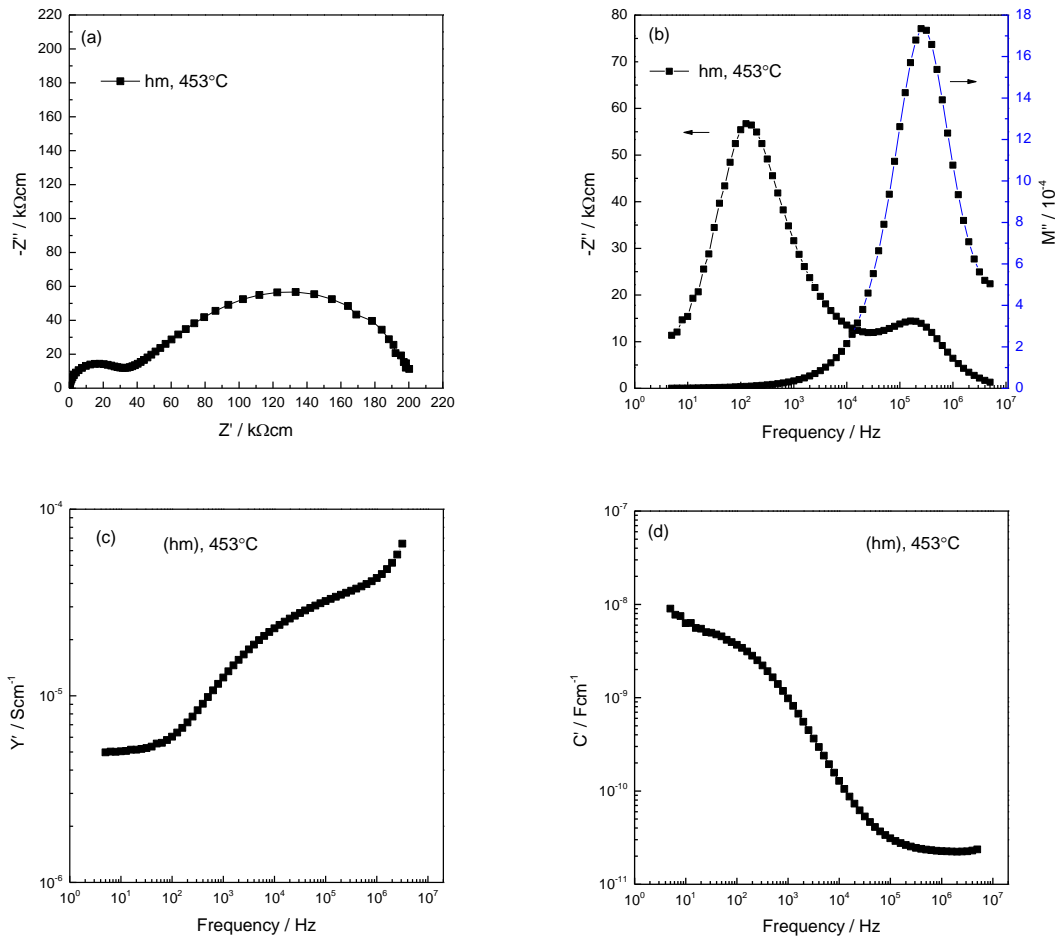


Figure 3-8: 453 °C IS data for sample (1) slow cooled from 1350 °C, (a) Z^* plot, (b) $-Z''$, M'' plots, (c) Y' plot and (d) C' plot.

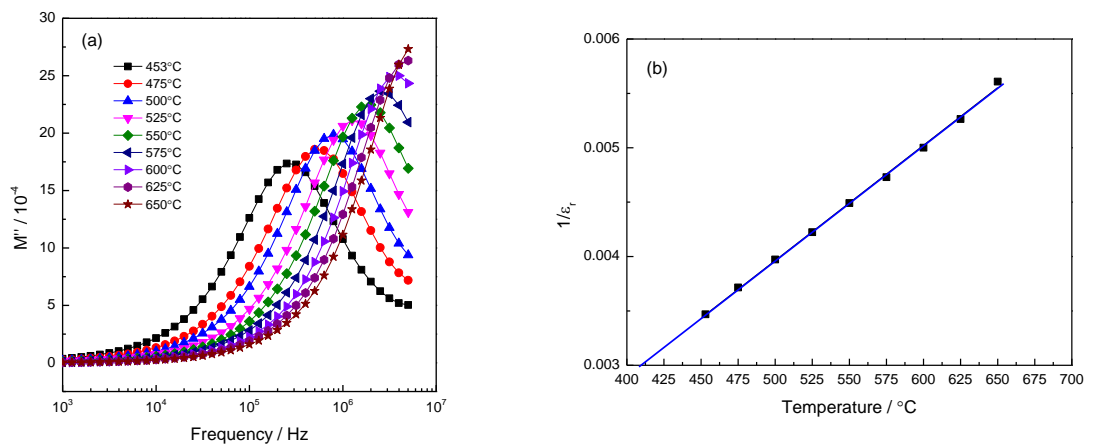


Figure 3-9: (a) Spectroscopic plot of M'' against $\log f$ at different temperatures, (b) Curie-Weiss plot of bulk permittivity.

From the impedance data, the conductivity of the high and low frequency components was extracted from Z^* plots. The activation energy (E_A) values were evaluated from the slope of the linear portion of the conductivity Arrhenius plots, Figure 3-10. Bulk conductivity has activation energy ~ 0.85 eV. The sample is reasonably insulating with bulk conductivity $\sim 4.03 \times 10^{-5} \Omega^{-1} \text{cm}^{-1}$ at 453°C , whereas, the grain boundary conductivity has lower value $\sim 8.82 \times 10^{-6} \Omega^{-1} \text{cm}^{-1}$ but with higher activation energy, 1.33 eV.

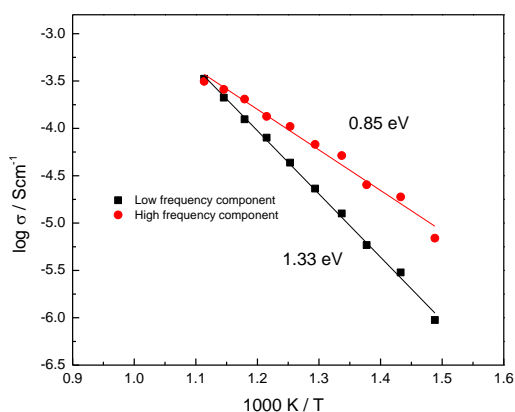


Figure 3-10: Arrhenius plots of conductivity against reciprocal temperature for the high and low frequency components.

Both *BM* and *PBM* samples were sintered at 1400°C for 12 h in air and characterised at different temperatures using an impedance analyser with Ag electrodes. IS measurements were then made on stepwise heating and cooling over the temperature range 25 - 650°C in air.

The conductivity data for the high and low frequency components at different temperatures are shown in Figure 3-11. IS data showed similar results to *HM*, Figure 3-12 and therefore the conductivity results were not influenced by the milling procedure.

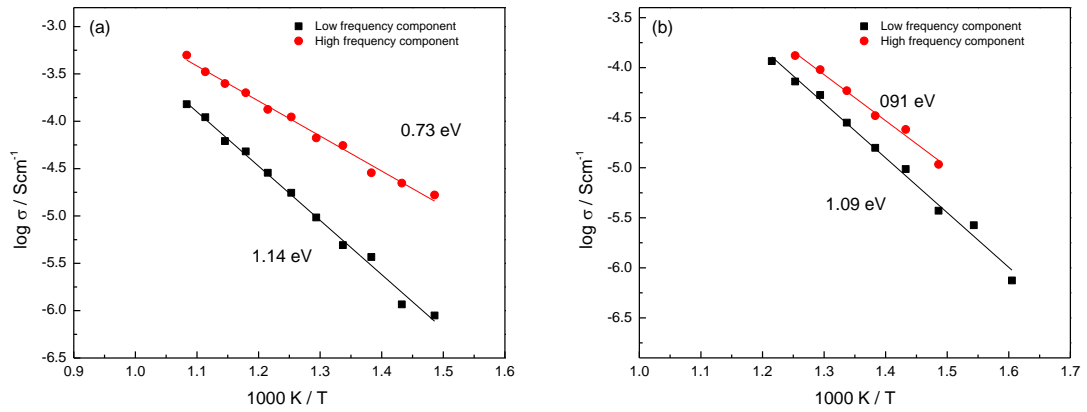


Figure 3-11: Arrhenius plots of total conductivity data against reciprocal temperature for (a) *BM* and (b) *PBM*.

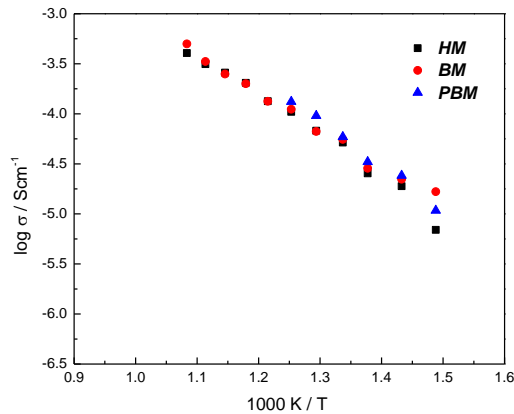


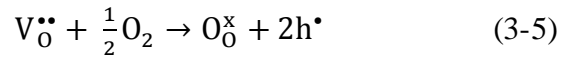
Figure 3-12: Arrhenius plots of bulk conductivity against reciprocal temperature for *HM*, *BM* and *PBM*.

(2) Effect of oxygen partial pressure

To study the response of BaTiO_3 to $p\text{O}_2$ at $400\text{ }^\circ\text{C}$, IS data were collected for sample (3) slow cooled from $1200\text{ }^\circ\text{C}$. The purpose of the step-wise and slow cooling for sample (3) compared with sample (2) slow cooled from $1400\text{ }^\circ\text{C}$ was to eliminate as much as possible any oxygen deficiency caused by sintering at high temperature. Impedance data were collected at $400\text{ }^\circ\text{C}$ in variable oxygen partial pressure by changing the atmosphere in the sequence $\text{Air} \rightarrow \text{N}_2 \rightarrow \text{O}_2 \rightarrow \text{Air}$ to check the reversibility of any changes to the initial values, as shown in Figure 3-13.

The general shapes of the impedance plots are similar in the different atmospheres but the resistance values are highest in N_2 and lowest in O_2 with intermediate values in air. Results are summarised in Table 3-4. With increasing $p\text{O}_2$, O_2 molecules are absorbed on the sample surface. Electrons are withdrawn from the sample to create

O^{2-} ions. The reduction in resistance is a result of a p-type conduction mechanism and hole creation according to [49] [54]:



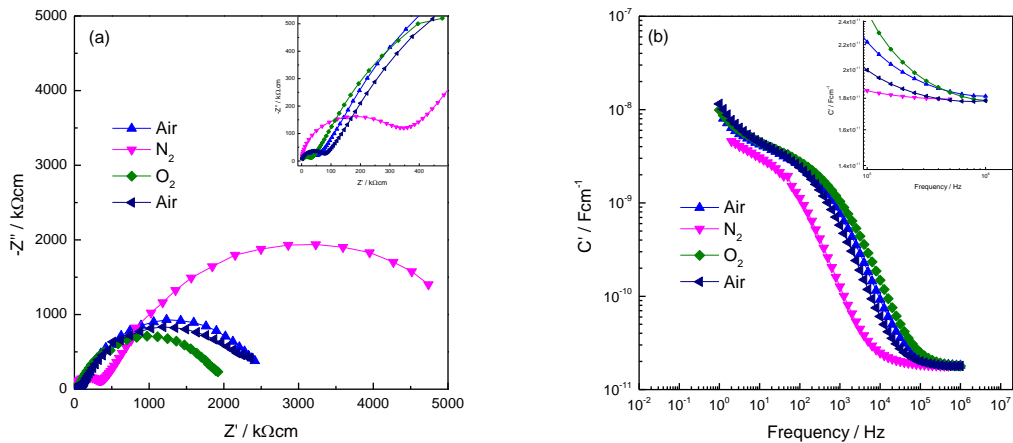
where $V_O^{\bullet\bullet}, O_O^x$ and h^{\bullet} represent oxygen vacancies, oxygen ions in the lattice with neutral charge and positive electron holes, respectively.

Only a small difference of resistance was observed between air and O_2 because of the small difference in oxygen partial pressure between them.

On reversing the different atmospheres after a constant resistance had been obtained, the change in R_g and R_{gb} was fully reversible but the times taken were temperature dependent.

Table 3-4: Resistance and capacitance data at 400 °C in different atmospheres.

	O_2	Air	N_2
$R_g / \Omega\text{cm}$	4.50×10^4	6.01×10^4	3.80×10^5
$R_{gb} / \Omega\text{cm}$	2.29×10^6	2.68×10^6	5.13×10^6
C_g / Fcm^{-1}	1.90×10^{-11}	1.82×10^{-11}	1.80×10^{-11}



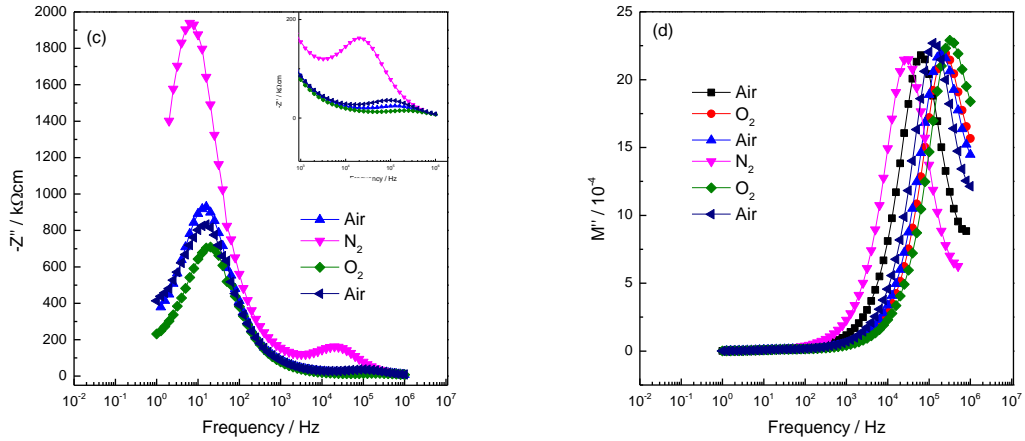


Figure 3-13: 400 °C IS data for sample (3) slow cooled from 1200 °C, (a) Z^* plot, (b) C' plot, (c) $-Z''$ plot and (d) M'' plot in different atmospheres.

(3) Effect of sintering temperature

Grain and grain boundary resistances decreased on sintering at 1400 °C, sample (2), compared to the sample sintered at 1350 °C sample (1), Figure 3-14 which may be attributed qualitatively to increased loss of oxygen at higher temperature. A quantitative assessment of the effect of sintering temperature is difficult, however, because (i) the rate of reoxidation during cooling has a major influence on the resulting conductivity and (ii) the sample microstructure may be different after sintering at 1350 and 1400 °C and this may affect reoxidation rates. This result indicates that the processing conditions influence the electrical properties. Oxygen loss usually occurs increasingly at high temperatures while partial or complete reoxidation occurs at lower temperatures. This is studied in more detail later for samples quenched from different temperatures.

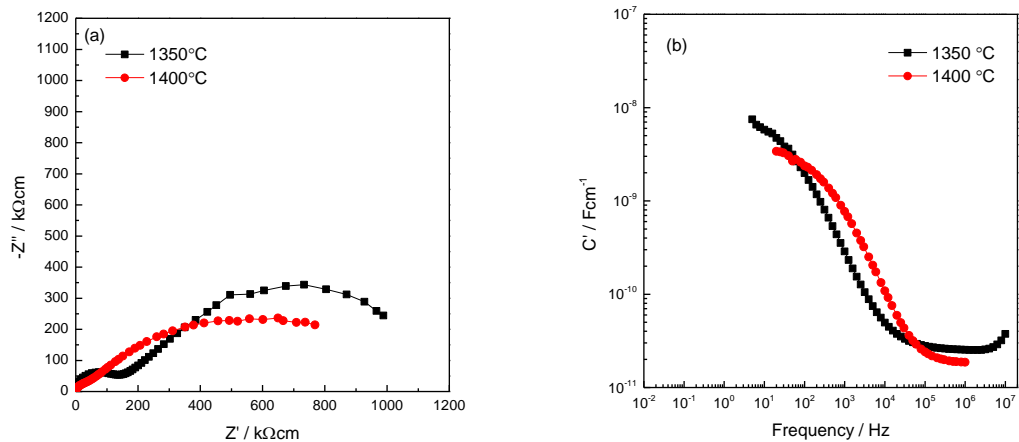


Figure 3-14: 400 °C, (a) Z^* plot data and (b) C' plot for samples (1) slow cooled from 1350 °C and (2) slow cooled from 1400 °C.

(4) Effect of application of a small dc bias voltage

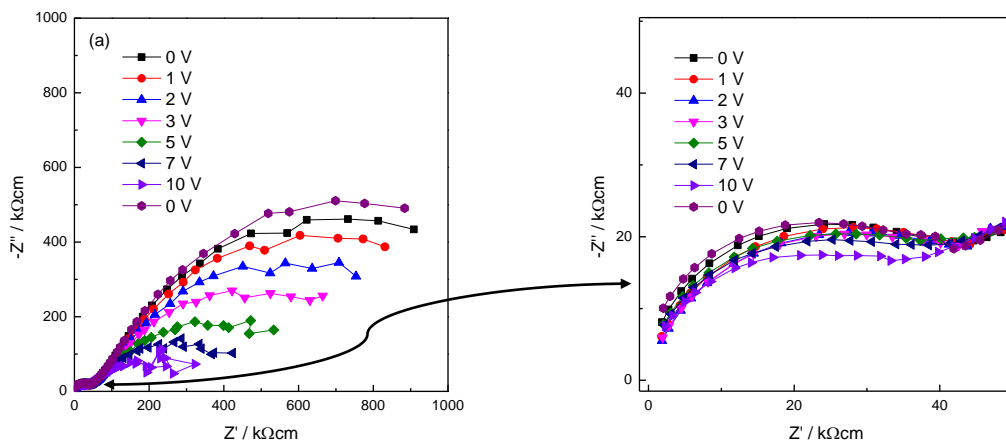
Sample (2) slow cooled from 1400 °C was characterised at 400 °C by IS with Ag electrodes.

Typical Z^* plots with a small dc bias voltage, in the range 0 to 10 V, which was applied across the pellet are shown in Figure 3-15(a). R_g and R_{gb} decrease with increasing dc bias which is fully reversible (returned to the original value on removing the bias) after a steady state had been reached, Figure 3-16 (a) and (b). R_{gb} decreases by \sim one order of magnitude between 0 and 10 V bias. The change in bulk is smaller than the change in grain boundary resistance. Results are summarised in Table 3-5.

Table 3-5: Resistance data at 400 °C with different dc bias voltage.

Resistance	0 V	10 V
$R_g / \Omega\text{cm}$	5.01×10^4	4.82×10^4
$R_{gb} / \Omega\text{cm}$	1.15×10^6	2.51×10^5

The C' spectrum in Figure 3-15(b) shows C_2 is mostly unchanged, whereas C_1 increases by $\sim 10\%$ with increasing dc bias and returns to its original state after removing the dc bias, Figure 3-17.



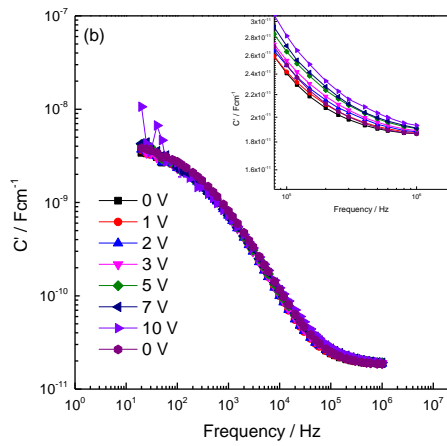


Figure 3-15: 400 °C IS data for sample (2) slow cooled from 1400 °C, (a) Z^* plot and (b) C' plot over the voltage range from 0 to 10 V, and then on removal of the dc bias.

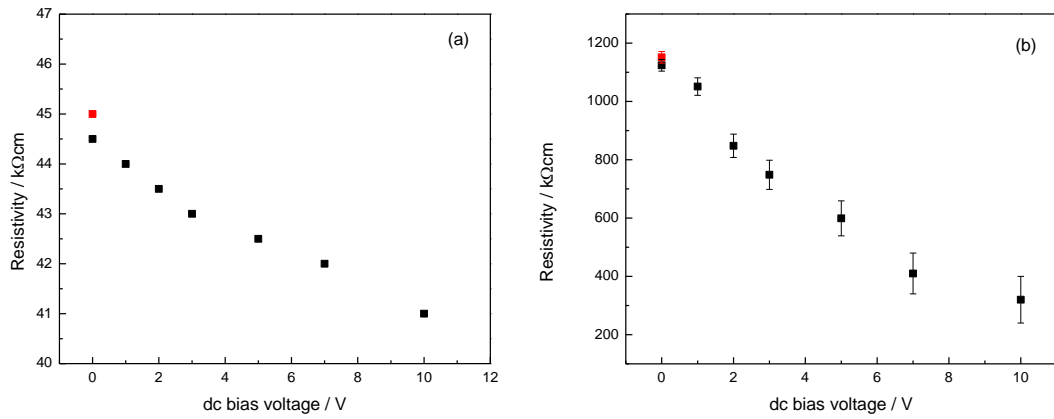


Figure 3-16: (a) R_1 , (b) R_t versus voltage (V) at 400 °C. The red symbol shows the resistivity after removal of the dc bias.

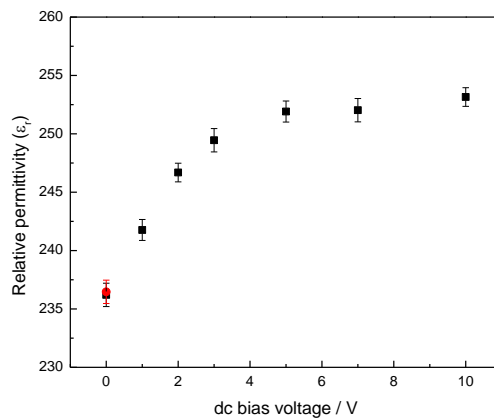


Figure 3-17: bulk permittivity (calculated from M''_{\max}) versus voltage (V) at 400 °C.

The effect of bias was also studied for sample (3) slow cooled from 1200 °C. Similar behaviour and conclusions to that of sample (2) slow cooled from 1400 °C was observed but with larger resistance values (not shown).

All slow-cooled samples (1, 2 and 3) show that the conduction mechanism is p-type which was observed by IS measurements in different atmospheres, and confirmed by application of the dc bias.

Resistance data as a function of time for sample (3) at 300 °C are shown in Figure 3-18 on application of a 10V bias (a) and on subsequent removal of the bias (b). On application of the bias, the resistance gradually decreased and had reached a steady state after approx. 2h. On removing the bias, the resistance increased reversibly and had reached its initial value after approx. 35 mins.

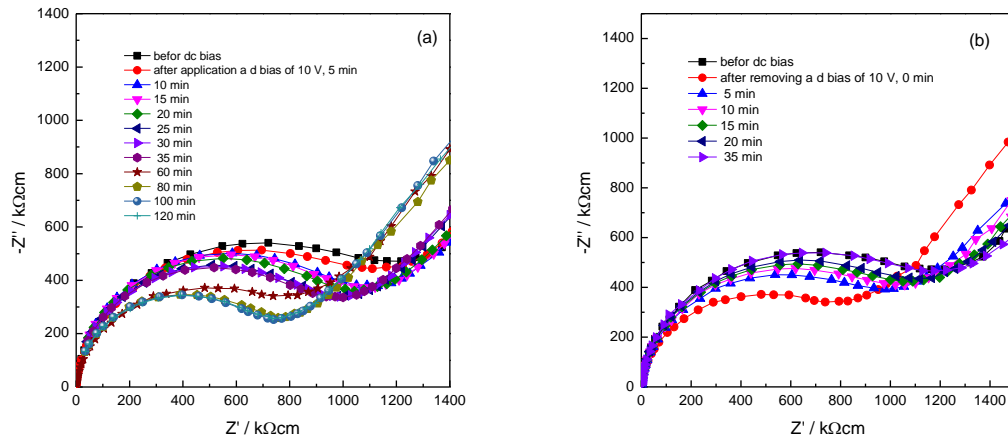


Figure 3-18: Bulk resistance as a function of time in air at 300 °C for sample (3) slow cooled from 1200 °C (a) on application of a 10V bias and (b) subsequent removal the bias.

3.3.2.5.2 Quenched samples

Results are presented using samples (4-12).

(1) P-type conductivity samples

(A) Typical impedance data

Many samples made by *HM*, *BM* and *PBM* were completely insulating at RT. A typical complex impedance plane plot of sample (10) quenched from 1300 °C shows two arcs at 400 °C, Figure 3-19. The high frequency arc was attributed to the bulk response, the low frequency arc to grain boundary impedance. Resistance and

capacitance values are extracted from Z^* . $R_{(t)}$ is $\sim 3.07 \times 10^5 \Omega\text{cm}$, where $R_g = 5.09 \times 10^3 \Omega\text{cm}$, $R_{gb} = 3.02 \times 10^5 \Omega\text{cm}$, $C_g = 1.60 \times 10^{-11} \text{Fcm}^{-1}$ and C_{gb} is around $7.90 \times 10^{-9} \text{Fcm}^{-1}$.

Figure 3-19 (b), (c) and (d) show similar behaviour to the slow cooled sample which was shown in Figure 3-8.

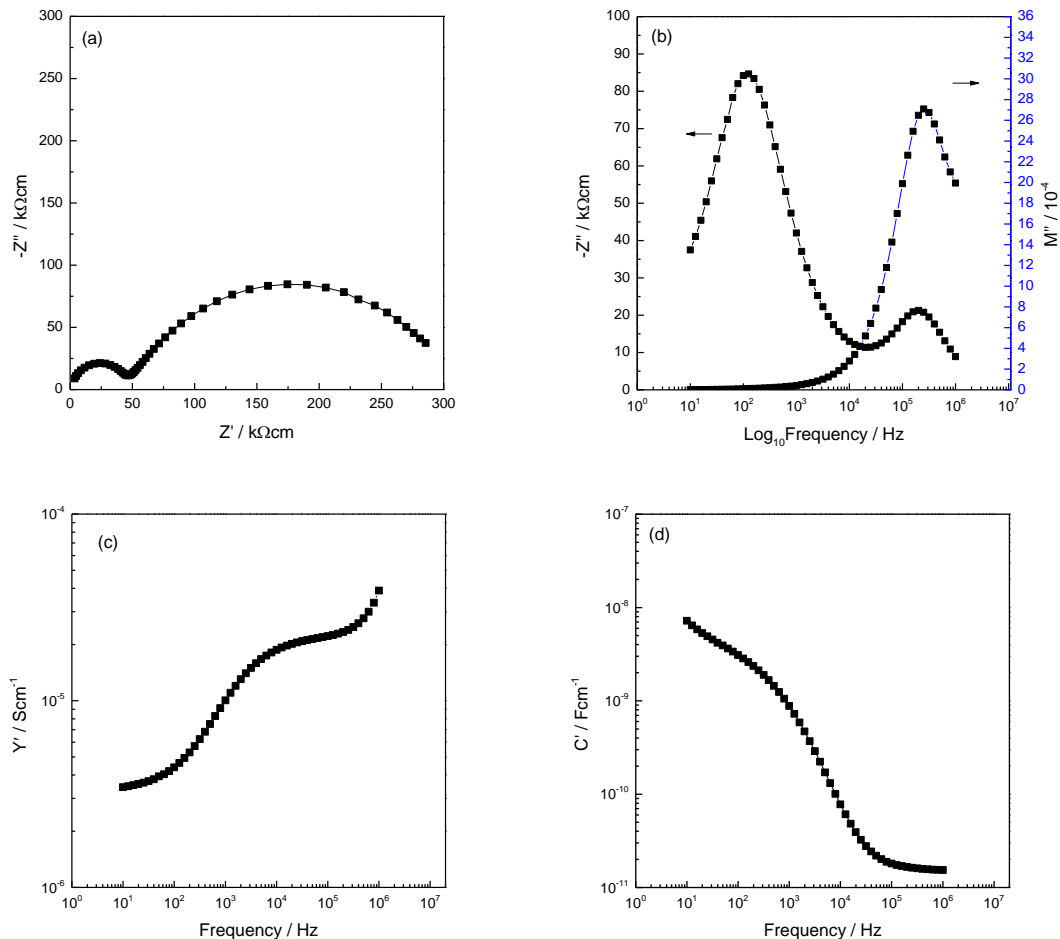


Figure 3-19: 400 °C IS data for sample (10) quenched from 1300 °C, (a) Z^* plot, (b) $-Z''$, M'' plots, (c) Y' plot and (d) C' plot.

(B) Effect of oxygen partial pressure

Sample (10) quenched from 1300 °C was characterised at 400 °C with Ag electrodes by changing the atmosphere in the sequence $\text{Air} \rightarrow \text{O}_2 \rightarrow \text{N}_2 \rightarrow \text{O}_2$. The impedance results are rather different from those for samples (7,8). Figure 3-20, (a) shows three components, a high frequency arc of resistance R_1 , a large intermediate frequency arc R_2 , and a small low frequency arc or tail of associated resistance R_3 .

C' data, in Figure 3-20 (b) increase at low frequencies toward a third capacitance, C_3 with a value of $> 10^{-7} \text{ Fcm}^{-1}$ which is attributed to the sample–electrode interface. C_3 corresponds to the small, low frequency, third arc seen in Z^* plots. The values of the resistances are lowest in O_2 (a). M'' spectra exhibit a single, high frequency peak, (c) which displaces to higher frequency with increasing $p\text{O}_2$, consistent with a reduction in resistance R_3 and p-type behaviour.

The key conclusion is that both resistances R_1 and R_2 show p-type behaviour.

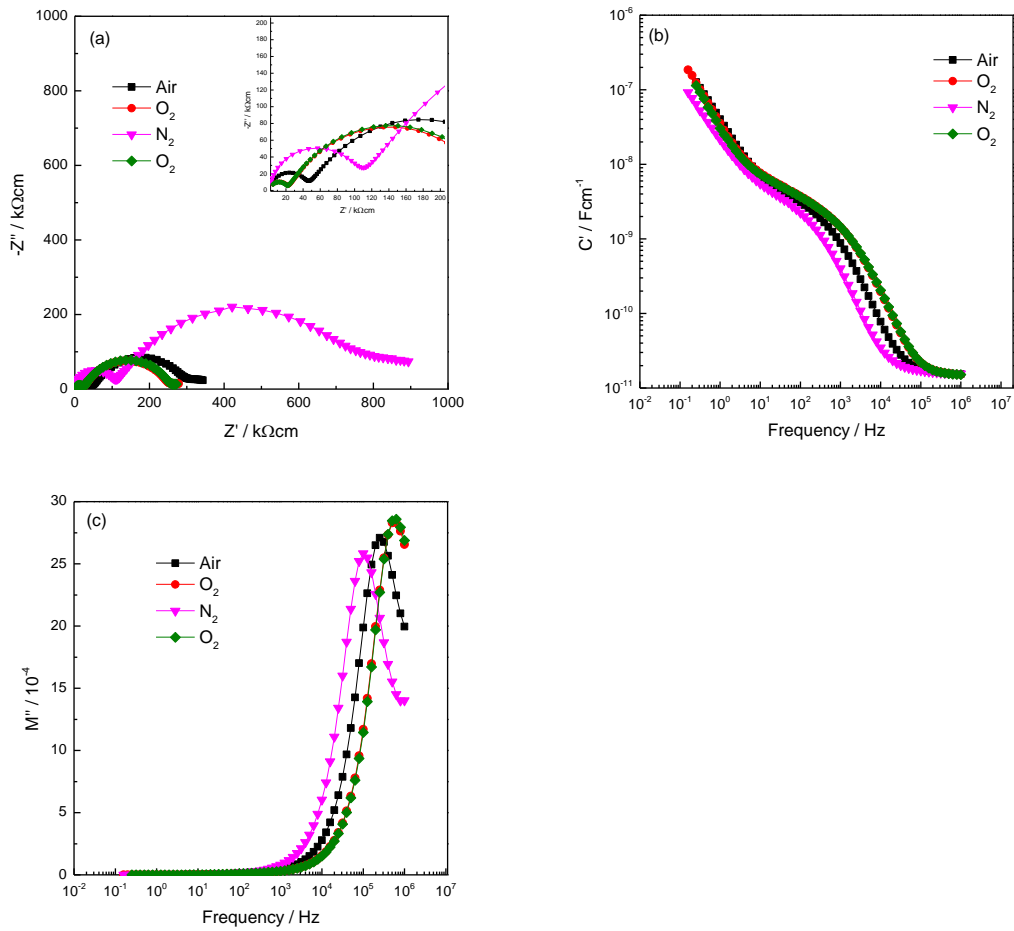


Figure 3-20: 400 °C IS data for sample (10) quenched from 1300 °C, (a) Z^* plot, (b) C' plot, and (c) M'' plot in different atmospheres.

The influence of application of two kinds of atmosphere (Air and N_2) on the bulk and grain boundary conductivity with the p-type behaviour at different temperatures was also studied.

R_b , R_{gb} and R_t for sample (11) quenched from 1335 °C at 500 °C, measured in air and N_2 are shown in Figure 3-21. The R_T is dominated by R_{gb} for both air and N_2 atmospheres. The ratio of R_b (N_2 /air) is $\sim 2.87:1$ whereas R_{gb} (N_2 /air) is $\sim 2.05:1$. This temperature shows that R_g is more sensitive than R_{gb} under different atmospheres.

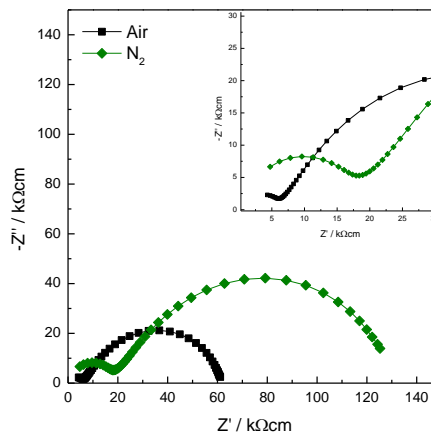


Figure 3-21: 500 °C Z^* plot for sample (11) quenched from 1335 °C, measured in air and N_2 .

Conductivity (σ_b , σ_{gb} and σ_t) data for sample (11) quenched from 1335 °C which were extracted from Z^* data in air and N_2 are plotted against reciprocal temperature between 400 and 900 °C in Arrhenius format, Figure 3-22 (a) and (b). Changing the atmosphere from N_2 ($pO_2 \sim 10$ Pa) to air ($pO_2 \sim 10^4$ Pa) displays an increase in conductivity indicative of p-type behaviour with activation energies for σ_b and σ_{gb} of ~ 0.65 and 1.23 eV. Bulk and grain boundary conductivity data (c) and (d) illustrate the change in σ_b and σ_{gb} with temperature in air and N_2 . The difference in σ_b was half an order of magnitude (c), whereas σ_{gb} did not show a big change in different atmospheres, (d). At 400 °C, the bulk conductivity is greater than the grain boundary conductivity in with air or N_2 . Thus, the total conductivity was dominated by the grain boundary conductivity.

With increasing temperature, because the activation energy of σ_{gb} is higher than that of σ_b , $\sigma_{gb} \sim \sigma_b$ at ~ 750 °C in air and ~ 700 °C in N_2 . At 900 °C, the grain boundary conductivity is greater than the bulk conductivity and therefore, the total conductivity was dominated by the bulk conductivity.

The bulk and grain boundary conductivities are very processing-dependent and a crossover with different activation energies associated with microstructure was observed. At low temperatures, the equivalent circuit of bulk and grain boundary impedances is in series but when they crossover, they do not necessarily have this circuit. It may change to a parallel circuit. For different atmospheres, both bulk and grain boundary show the same effect with same activation energy and parallel plots. The difference is due to change in number of carriers.

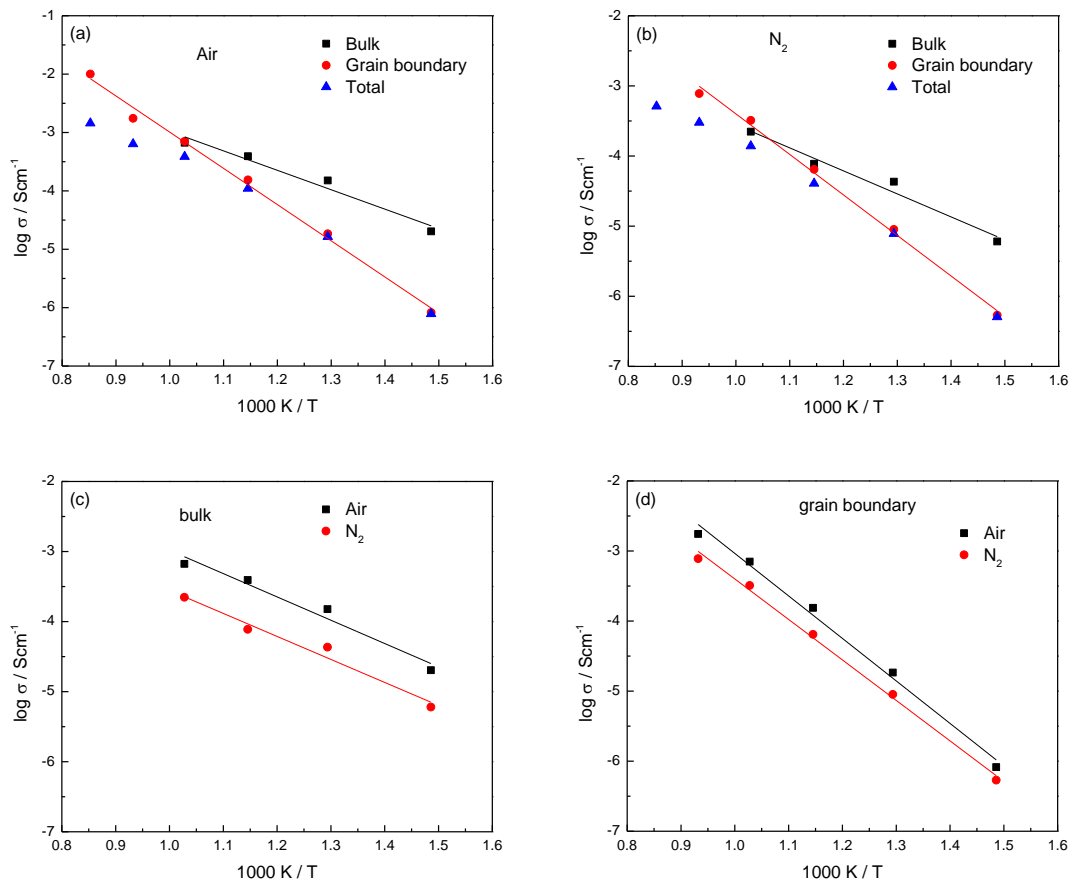


Figure 3-22: Arrhenius plots of σ_b , σ_{gb} and σ_t in air for sample (11) quenched from 1335 °C (a), and N_2 (b), and of σ_b in air and N_2 (c) and σ_{gb} in air and N_2 (d).

The bulk, grain boundary and total contributions were plotted to show the deconvolution of conductivity at 600 °C under air and N_2 atmospheres as shown in Figure 3-23 (a). The slopes are not be accurate in this figure due to the use of only two data points. As $m=1/\text{slope}$, σ_b illustrates the p-type behaviour with $m \sim +5.8$

whereas, σ_{gb} did not illustrate a big change under air and N_2 atmospheres with a small slope value as $m = +10.8$. A little pO_2 dependence was observed as well for σ_t as σ_{gb} behaviour which is expected since that σ_t was dominated by σ_{gb} $m = +6.4$.

Figure 3-23 (b) shows the bulk conductivity between $\log(pO_2/Pa)$ from 0.23 (N_2) to 4.32 (air) at temperatures from 400-700 °C. These two values (0.23 and 4.32) are actually assumed from literature [90] and not certain since there is no purity was observed in furnace but only assumption.

It was reported that at 700 °C, there is switching from p-type to n-type behaviour at $\log P_{O_2}^0 \sim -1$ and the decrease of temperature gives rise to move the switching to the lower pO_2 [90-92]. Therefore, no significant effect was observed for the bulk conductivity either with air or N_2 at < 700 °C by the broad conductivity minimum at pO_2 . The total conductivity shows a little dependence of pO_2 as result of σ_{gb} behaviour which has a large value and dominates the total conductivity with showing no sensitivity to pO_2 .

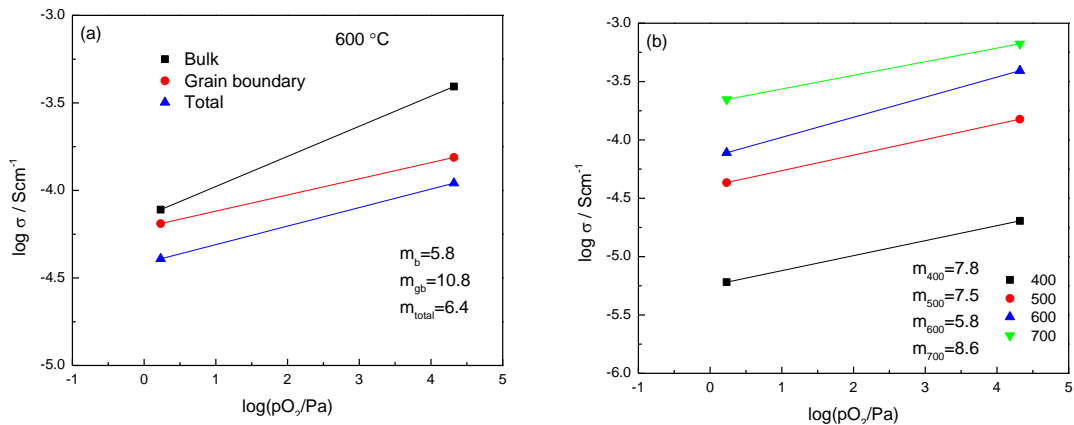


Figure 3-23: Log σ against $\log pO_2$ plots for σ_b , σ_{gb} and σ_t in air and N_2 at 600 °C for sample (11) quenched from 1335 °C (a) and $\log \sigma_b$ against $\log pO_2$ for temperatures 400–700 °C, (b) $m=1/slope$.

(C) Effect of application of a small dc bias voltage

Sample (10) quenched from 1300 °C shows that R_1 and R_2 decrease gradually and reversibly with increasing dc bias voltage from 0 to 10 V confirming enhanced p-type conductivity, Figures 3-24 and 3-25.

The C' spectroscopic plot shows very little dependence on dc bias at low frequency, Figure 3-24, (c). The curves shift to higher frequency because the resistance decreased. A similar shift is seen in M'' plots, Figure 3-24, (b).

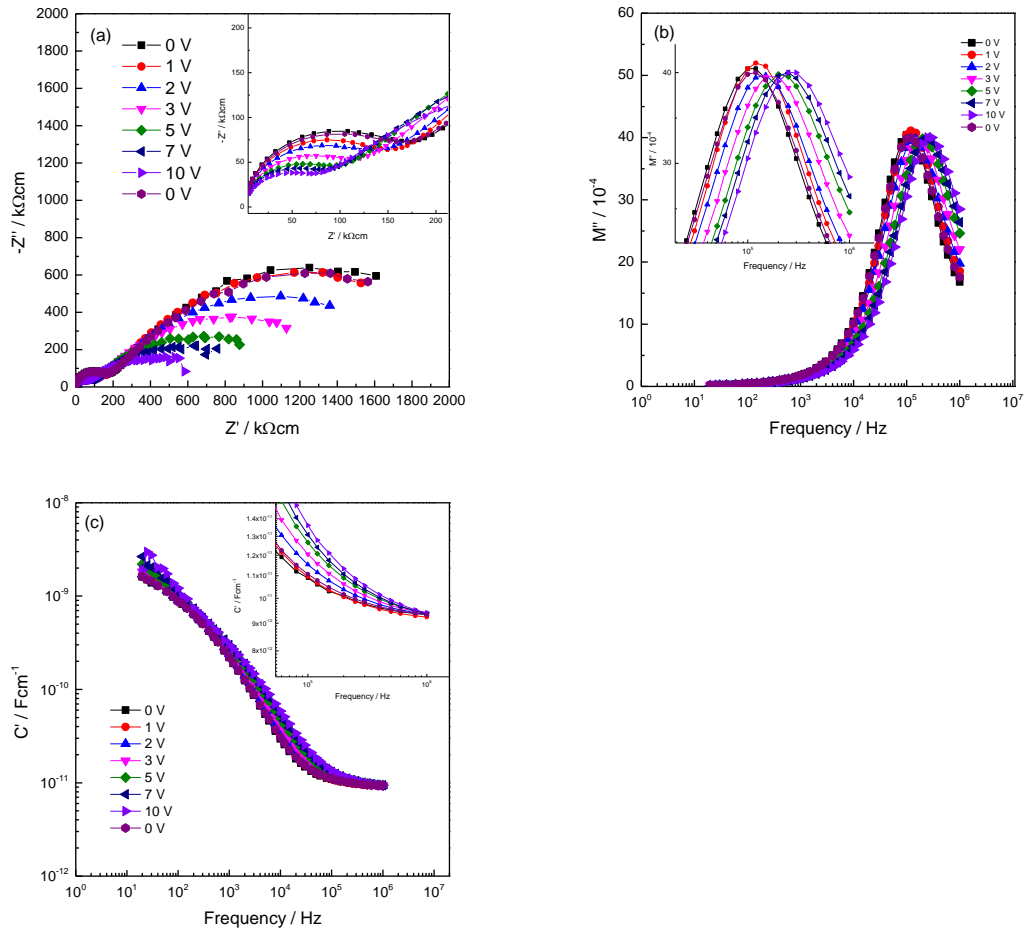


Figure 3-24: 400 °C IS data for sample (10) quenched from 1300 °C, (a) Z^* plot, (b) M'' plot and (c) C' plot over the voltage range from 0 to 10 V, and then on removal of the dc bias.

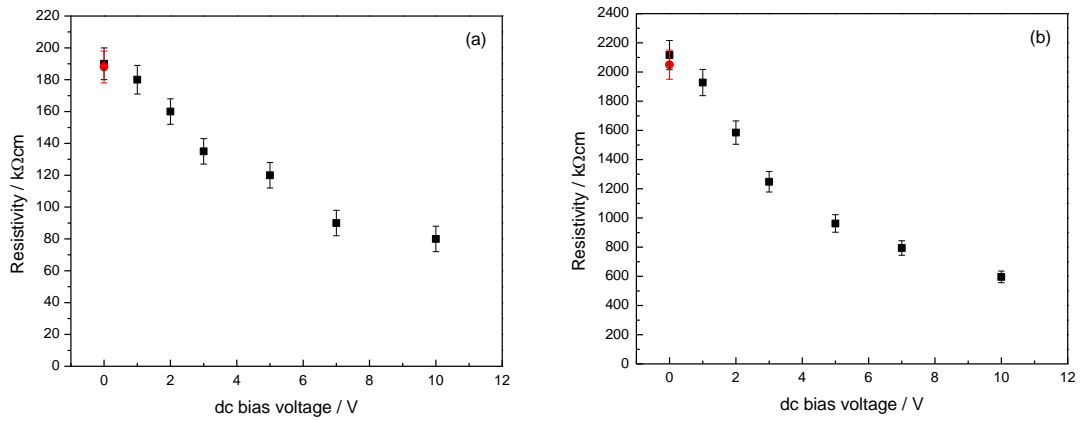


Figure 3-25: (a) R_1 , (b) R_2 versus voltage (V) at 400 °C.

Figure 3-26 shows R_1 data at 400 °C as a function of time for sample (11) quenched from 1335 °C after application of a 10 V dc bias, and after subsequent removal of the dc bias.

Application of dc bias led to a rapid decrease in resistance initially which then levelled off to an approximately constant value. On removing the dc bias, sample resistance increased until it reached its original value. The recovery was time-dependent and appeared to occur in two stages with only a slight increase between 54-100 minutes but a further rapid increase at longer times. The original value was finally regained after 205 minutes.

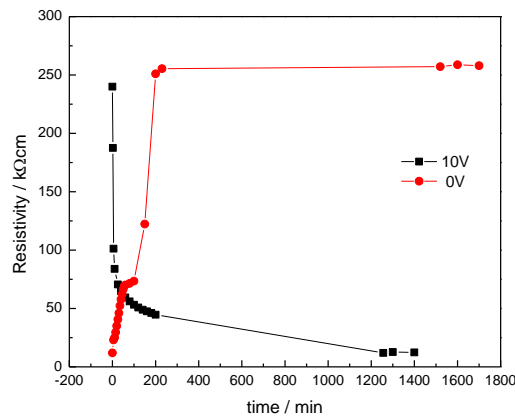


Figure 3-26: Bulk resistance at 400 °C for sample (11) quenched from 1335 °C with 10V bias and after removing the dc bias at different times in air.

(2) N-type conductivity or Schottky barrier samples

(A) Typical impedance data

For sample (5) quenched from 1400 °C, a broad asymmetric arc was observed, even at room temperature, in the Z^* plot, Figure 3-27 (a), with total resistance ~ 4.35 k Ω cm. The C' plots, Figure 3-27 (b), showed high capacitance, incomplete plateaus at low frequency followed by a dispersion toward low capacitance at high frequency. The capacitance value of the low frequency component is $\sim (1-5) \times 10^{-8}$ Fcm $^{-1}$. The capacitance value of the high frequency component could not be obtained due to insufficient data in the C' plot at high frequencies. Combined Z'' , M'' plots showed two components; the Z'' spectrum is dominated by a low frequency broad peak, with full width half maximum greater than expected for an ideal Debye peak, with an associated room temperature resistance ~ 2.64 k Ω cm, Figure 3-27 (c). The M'' spectrum shows only the low frequency onset of a peak as the peak maximum is off-scale, Figure 3-27 (c).

From these data, it is clear that the Z^* data are dominated by the low frequency component with capacitance $\sim (1-5) \times 10^{-8}$ Fcm $^{-1}$. The bulk resistance of the sample, R_1 , can not be measured since the bulk M'' peak is off-scale (c) and a separate bulk arc in Z^* at high frequency can not be resolved. However, R_1 is small and the quenched samples are much more conductive than slow-cooled samples. The conductivity is attributed to oxygen loss at high temperature, giving BaTiO $_{3-\delta}$ or Ba Ti $_{1-2\delta}^{4+}$ Ti $_{2\delta}^{3+}$ O $_{3-\delta}$. The electrons liberated can jump between Ti $^{3+}$ and Ti $^{4+}$ ions [33].

Total conductivity (σ_t) data are plotted against temperature in Figure 3-28. It shows the characteristic PTCR effect with a large resistance rise at the Curie temperature, Figure 3-29.

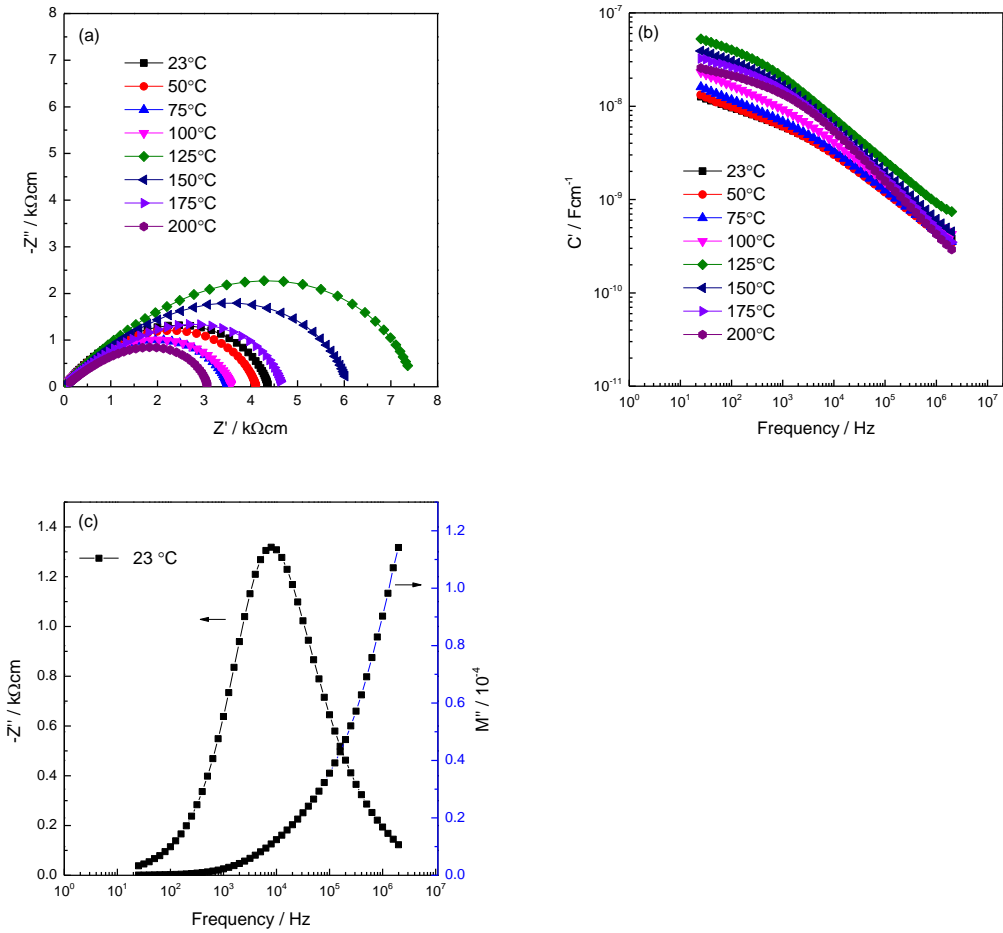


Figure 3-27: IS data for sample (5) quenched from 1400 °C, (a) Impedance complex plane plot, (b) C' plot, (c) Z'' , M'' plots at different temperatures with In-Ga electrodes.

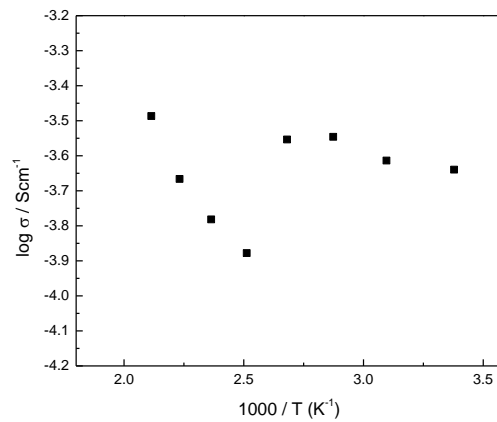


Figure 3-28: Arrhenius plots of total conductivity against reciprocal temperature showing a PTCR effect at ~ 120 °C.

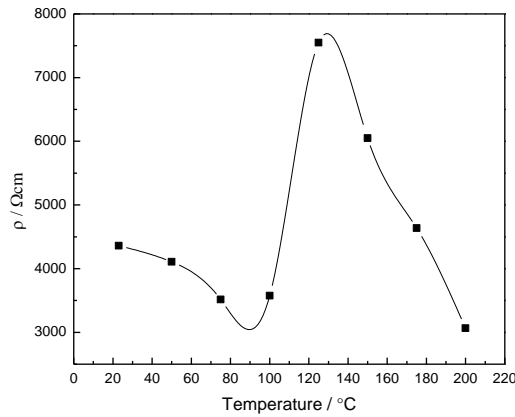
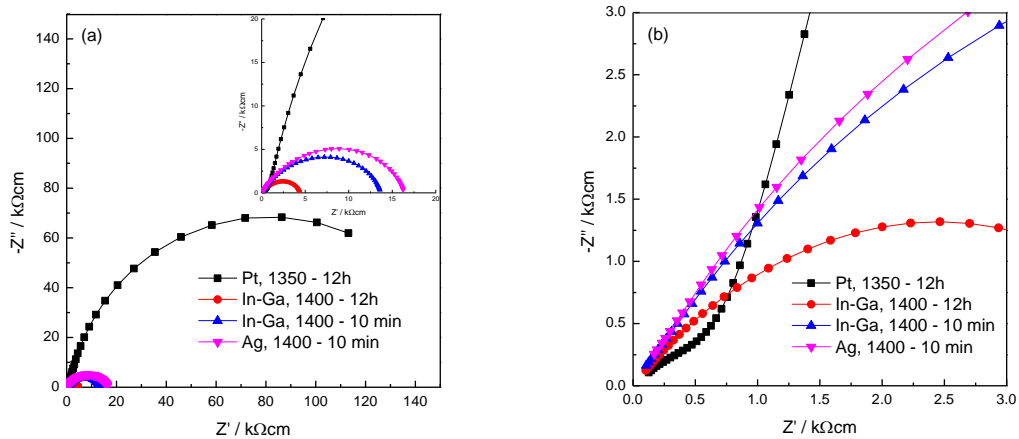


Figure 3-29: Total resistivity as function of temperature.

(B) Effect of electrode material

IS measurements were made using different electrodes, Figure 3-30 (a). For quenched samples (4-7), sample (4) (quenched from 1350 °C with pre-attached Pt electrodes) showed two overlapping arcs with a high frequency intercept $\sim 500 \Omega\text{cm}$ at room temperature, (b). With In-Ga and Ag electrodes, a single broad arc is seen in Z^* which may contain a high frequency arc, similar to that seen with Pt, but which is not resolved. Pt is much more resistive than In-Ga and Ag.

C' data (e) show a clear, low frequency plateau with Pt, but with In-Ga and Ag lower frequency data would be required to see a (probable) low frequency plateau. The low frequency C' data exceed 10 nF. At higher frequencies, all those samples show a dispersion to lower C' values but insufficient data are available to see any high frequency plateau.



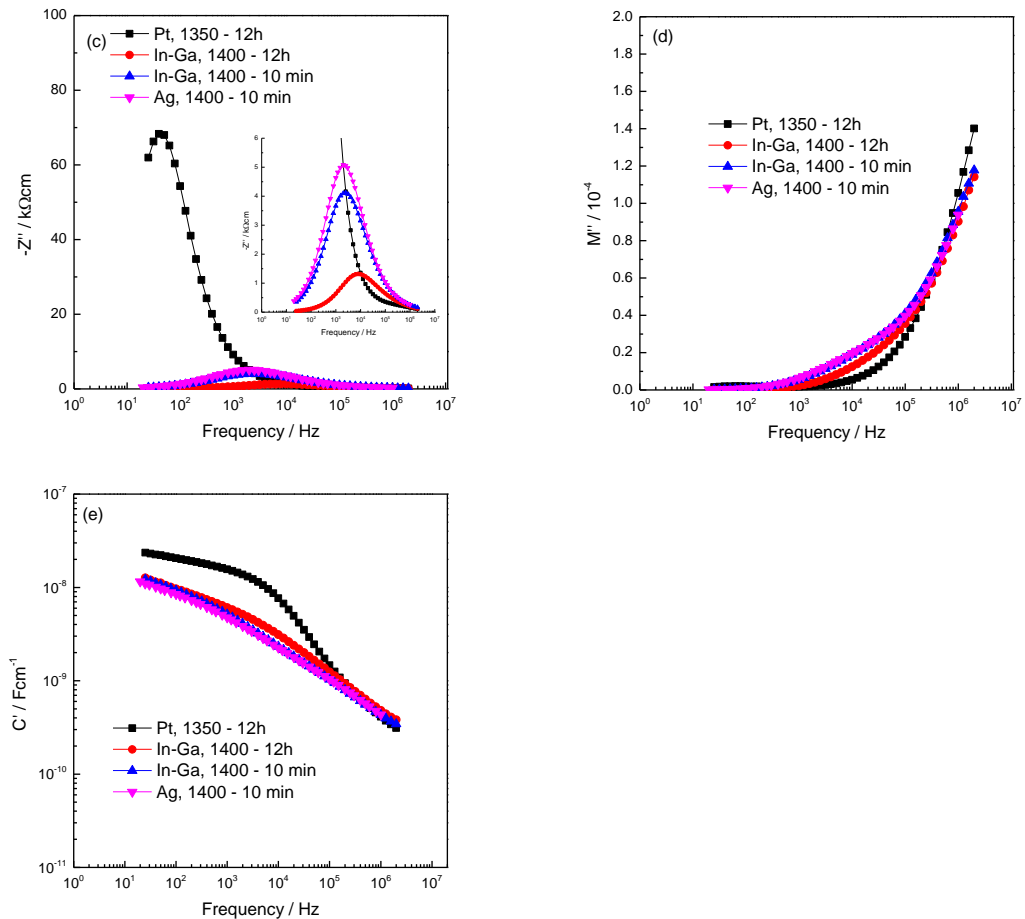


Figure 3-30: IS data for samples (4-7), (a), (b) Z^* plot, (c) Z'' plot, (d) M'' plot and (e) C' plot at room temperature.

In addition to the above which appear to be electrode material-dependent, Schottky barriers may also form at the sample-electrode interface associated with partial oxidation of the sample surface, similar to the Schottky barrier created at grain-grain contacts.

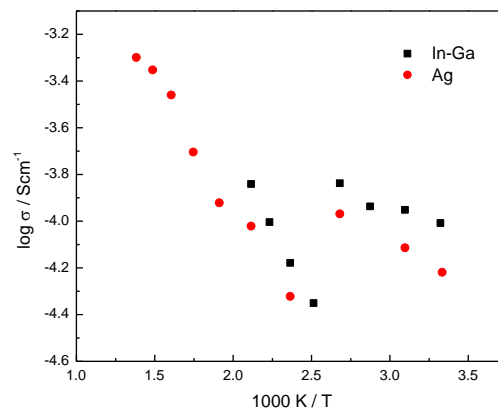


Figure 3-31: Arrhenius plots of total conductivity data against reciprocal temperature.

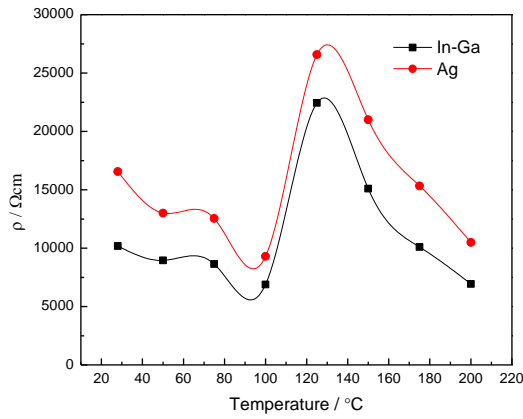


Figure 3-32: Total resistivity as function of temperature.

(C) Effect of oxygen partial pressure

Impedance data for sample (7) quenched from 1400 °C were collected at 400 °C by changing the atmosphere in the sequence Air → N₂ → O₂ → Air. In Figure 3-33, (a) impedance, Z*, shows a single distorted semicircle, which indicates the existence of two electrical components as clearly shown by the corresponding Z''/M'' spectroscopic plots, Figure 3-33, (b).

The values of the total resistance are lowest in N₂. The total resistance decreases from ~ 11.15×10³ Ωcm in O₂ to 9.70×10³ Ωcm in N₂.

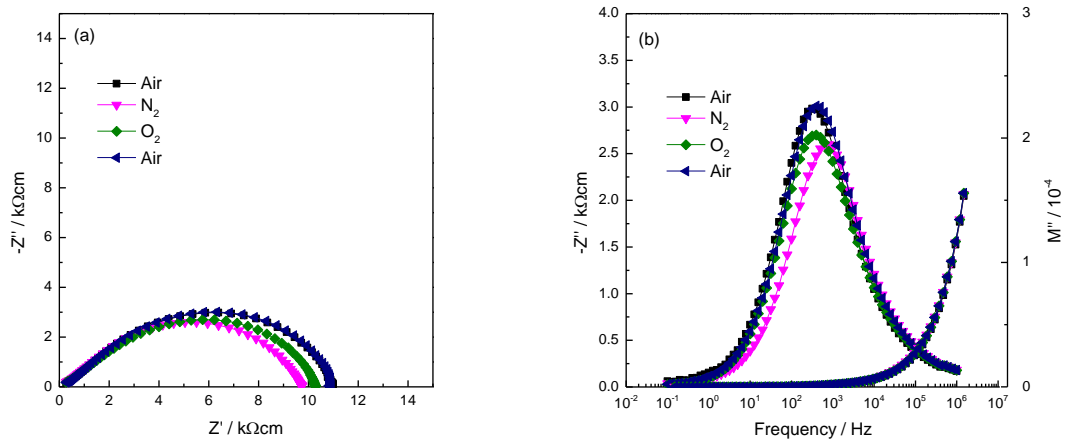


Figure 3-33: 400 °C IS data for sample (7) quenched from 1400 °C, (a) Z* plot, (b) Z'', M'' plots in different atmospheres.

Impedance data for sample (8) quenched from 1380 °C were collected at 400 °C by changing the atmosphere in the sequence O₂ → Air → N₂ → O₂ → Air. The total resistance decreased from ~ 1.21×10⁶ Ωcm in O₂ to 9.01×10⁵ Ωcm in N₂, Figure 3-34 (a) but sample (8) has lower conductivity than sample (7). Figure 3-34 (b) shows that the low frequency capacitance is higher than the low frequency capacitance of SC sample, Figure 3-14 (b).

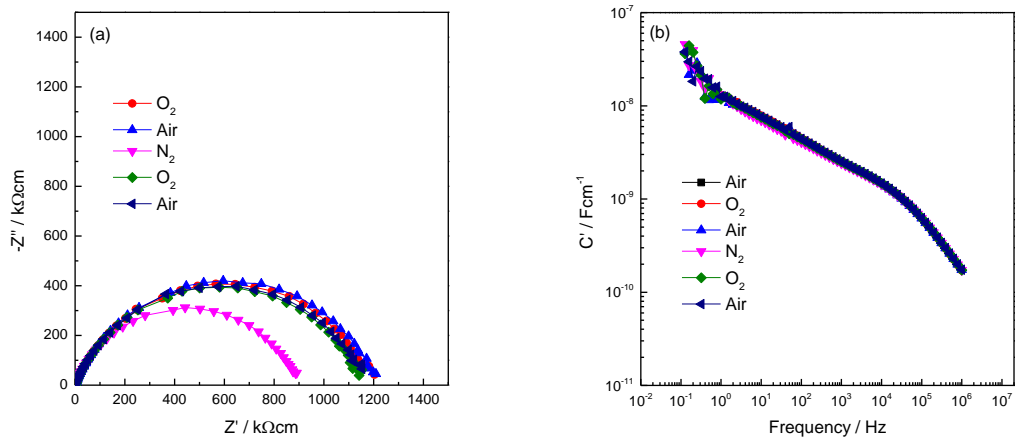


Figure 3-34: 400 °C IS data for sample (8) quenched from 1380 °C, (a) Z* plot and (b) C' plot in different atmospheres.

(D) Effect of application of a small dc bias voltage

Impedance measurements for sample (7) quenched from 1400 °C illustrated a change in resistance values with application of a dc bias voltage, Figure 3-35 (a). Conductivity increased gradually ~ 5 times with increasing dc bias voltage from 0 to 10 V. The conductivity increase was reversible on removing the bias, Figure 3-35 and 36.

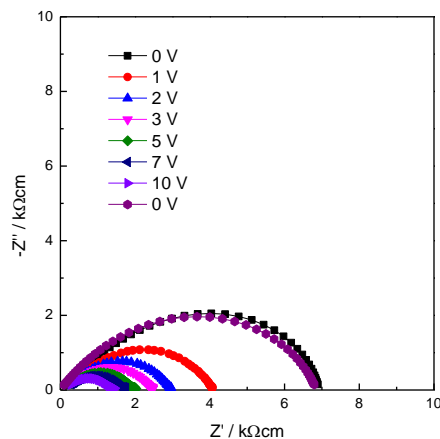


Figure 3-35: 400 °C IS data for sample (7) quenched from 1400 °C, (a) Z^* plot, (b) Z' , M'' plots over the voltage range from 0 to 10 V, and then on removal of the dc bias.

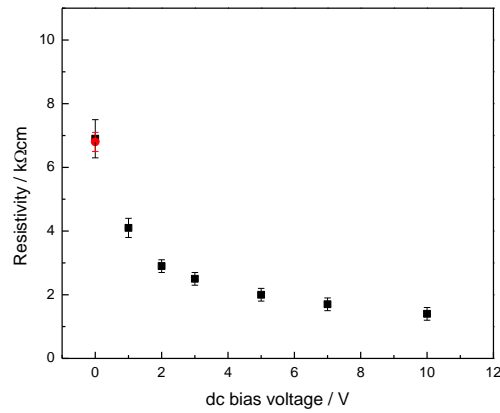


Figure 3-36: R_t versus voltage (V) at 400 °C.

The effects of dc bias on samples (7) and (8) were also similar, Figure 3-37 (a).

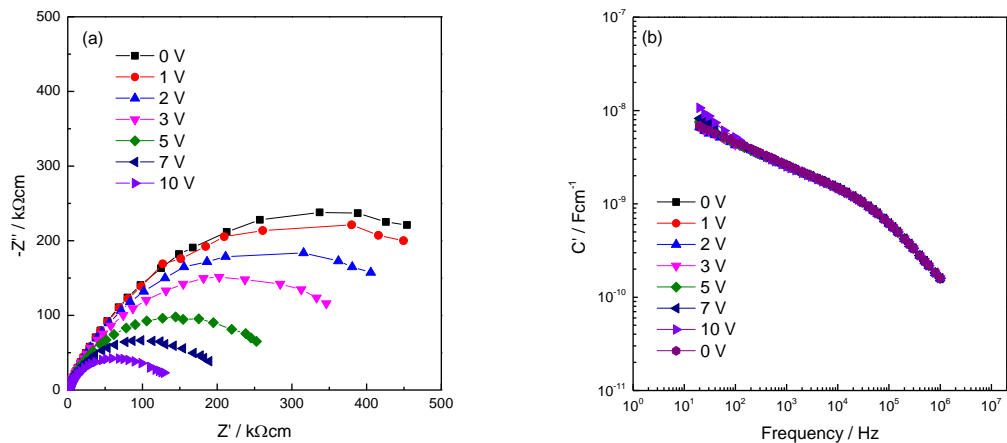


Figure 3-37: 400 °C IS data for sample (8) quenched from 1380 °C, (a) Z^* plot and (b) C' plot over the voltage range from 0 to 10 V, and then on removal of the dc bias.

Sample (13) quenched from 1450 °C shows that bulk resistance increased gradually and reversibly with increasing dc bias voltage from 0 to 10 V confirming enhanced n-type conductivity, Figures 3-38.

In order to determine whether impedance data were time-dependent on application / removal of a dc bias, results are shown in Figure 3-39 for sample (9) quenched from 1400 °C. On application of a 10 V bias, the resistance decreased and gradually recovered its original value 240 minutes after removing the bias.

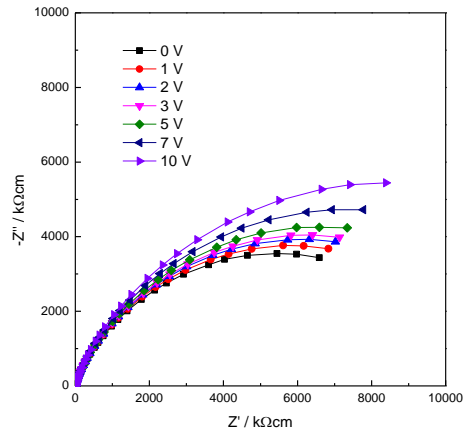


Figure 3-38: Z^* plot at 50K for sample (13) quenched from 1450 °C before applying and after removing a dc bias of 10V with In-Ga electrodes.

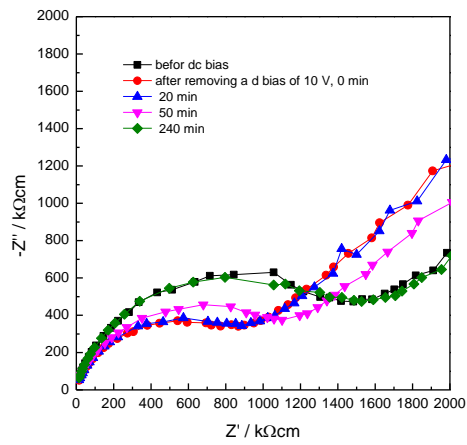


Figure 3-39: Bulk resistance at 300 °C for sample (9) quenched from 1400 °C before applying and after removing a dc bias of 10V at different times in air.

3.4 Discussion

The three different milling processes used to investigate the effect of various preparation routes on undoped BT ceramics are pestle and mortar, roller ball milling and planetary ball milling. XRD indicated that all the samples were tetragonal single phase. All the observed peaks could be indexed on P4mm space group for all three sets of samples. The relative densities of all samples, calculated from pellet mass and dimensions were in the range 83.1 – 91.3 % of the value expected for fully dense pellets. The lattice parameters were in good agreement with the values found in the literature. SEM images of the etched surface for *HM* and *PBM* routes show an exaggerated grain growth which is very common behaviour in barium titanate ceramics during conventional sintering in a muffle furnace at high temperatures, i.e. $\geq 1350^{\circ}\text{C}$ and/or for long sintering periods [19, 93, 94]. This behaviour may be associated with twinning which is caused by losing a small amount of oxygen [81, 86]; sample *BM* did not show an exaggerated grain growth. A notable porosity was observed for *HM* especially at some triple junctions between the grains.

Raman spectroscopy was performed at room temperature for *HM*, *BM* and *PBM* ceramics. It shows clearly all the features reported for single crystals of BaTiO_3 in the literature [76, 77].

Electrical properties of the *HM*, *BM* and *PBM* samples were measured by LCR and impedance spectroscopy. LCR data show that the maximum values of the permittivity for different synthesis routes were in the range ~ 1627- 8433 at the Curie temperature. The permittivity exhibits a sharp increase of the dielectric constant at the ferroelectric-paraelectric transition.

There was a clear difference in ϵ'_{max} values which may perhaps be attributed to the different ceramic density obtained. The value of ϵ'_{max} for *PBM* was highest which may be associated with its higher density. The value of *BM* permittivity is lower than reported in the literature which is attributed either to the smaller grain size [63] or low densification and high porosity [9]. The ϵ'_{max} values for this project are in good agreement with other literature data [10, 15, 63, 66, 75, 95-99].

IS was performed to establish the electrical properties of the grain and grain boundary regions of ceramics measured under varying conditions, i.e. sintering temperature, dc bias, atmosphere, and time. IS data were studied for two kinds of sample: (i) slow-cooled and (ii) quenched. For both, the effect of application of a small dc bias and varying pO_2 were studied. The results can be interpreted using the following schemes, Figure 3-40:

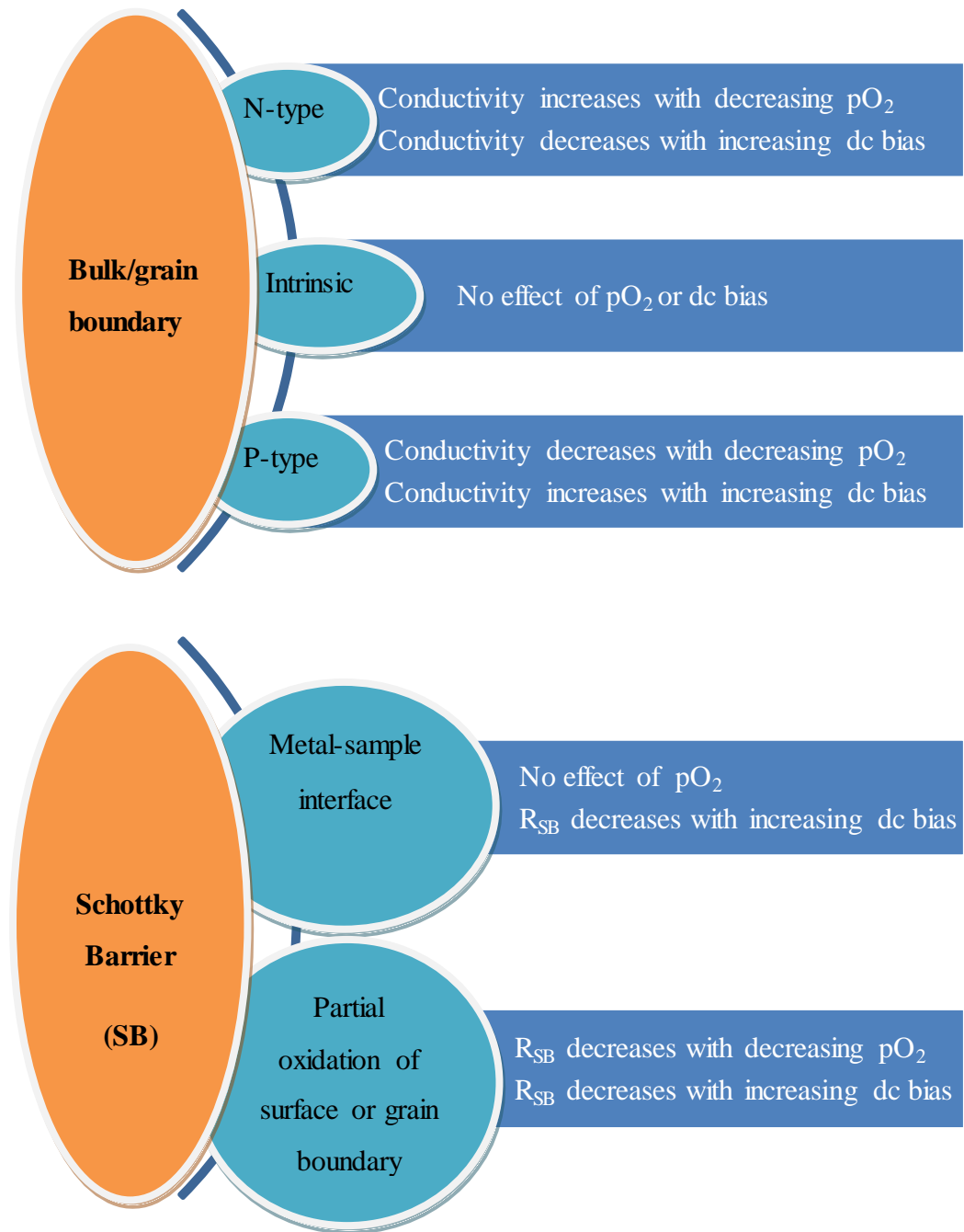


Figure 3-40: Schematic mechanisms for bulk/grain boundary and Schottky Barrier (SB) impedances.

In addition, the following features of R and C values help in the interpretation of impedance data:

- The magnitude of capacitance values is a good indicator to distinguish between SB and bulk/grain boundary impedances.
- If the resistance shows a PTCR effect, it is probably associated with a Schottky barrier impedance.
- If R_b/R_{gb} is small then any additional large resistance may be associated with a Schottky barrier.
- If the resistance depends on electrode material, then it is probably associated with a Schottky barrier impedance at the sample-electrode interface.

Using these guidelines, the interpretation of the results reported here is as follows:

Slow-cooled samples:

The behaviour of slow cooled (SC) BaTiO₃ was as expected, insulating at room temperature with resistivity > 10 MΩcm; samples were electrically inhomogeneous and all showed a similar response. Two arcs were apparent in the impedance complex plane plots at temperatures ≥ 400 °C; at lower temperatures, the resistance was too large to measure. In most cases, the data were analysed using a simplified equivalent circuit consisting of two parallel resistor-capacitor (RC) elements placed in series, R_bC_b , (or R_1C_1) representing the grains and $R_{gb}C_{gb}$, (or R_2C_2) representing the grain boundary regions. For SC samples, the grain boundary arc was usually much larger than that of the bulk arc.

The conductivity data of the three different milling routes for slow cooled samples showed no significant differences. This confirms that the conductivity results were not influenced by the milling procedure. The bulk E_A was in the range ~ 0.75-0.93 eV, which is significantly less than half the band gap of BT, ~ 3.0 eV, which would give rise to an expected intrinsic activation energy of ~ 1.5 eV. Intergap states must exist, therefore, and could be associated with oxygen loss or the incorporation of accidental aliovalent impurities such as Al and Fe from the reagent-grade TiO₂ raw material [91, 92].

The p-type conduction can be obtained as result of unintended frozen-in metal vacancies which can arise by heating samples at high temperature with impurities as small levels of contamination, such as Fe^{3+} or different impurities which usually exist with TiO_2 or different reagents of valence $< +4$ on the Ti-sites [100-103]. These impurities can act as acceptor dopants and create oxygen vacancies for charge compensation which may be partially responsible as a source of p-type conduction [104].

Oxygen vacancies are the origin of p-type conduction as they reduce oxygen loss during high temperature processing [105].

Grain boundary conductivity data have activation energies, $E_A \sim 1.09 - 1.33$ eV. Conductivity data show linear Arrhenius plots with $\sigma_1 > \sigma_2$ at lower temperature but at high temperatures $\sim \geq 650$ °C, $\sigma_1 \cong \sigma_2$. This observation is in good agreement with literature data [49, 90, 106].

IS data showed that both R_1 and R_2 decrease with dc bias and therefore both showed p-type conductivity behaviour. Similar decrease in R with dc bias has been reported for numerous examples of acceptor-doped (Ba, Sr, Ca) TiO_3 [35, 47, 55]. There are several possible sources of holes. First is acceptor impurities such as Fe^{3+} . Second is oxygen uptake from the atmosphere which receive electrons from lattice O^{2-} ions to form O^- ions [40].

The changes in R_1 and R_2 with dc bias were time-dependent and were reversible on removing the bias. Thermally-activated diffusion processes may be involved in controlling the rates as well as the ionisation / reformation of underbonded O^- ions.

The dc bias results are in good agreement with those of the literature which was very recently also observed by Cann [47]. They found that both R_1 and R_2 decreased on application of a small bias and could not be associated with interfacial phenomena such as variation in Schottky barrier height.

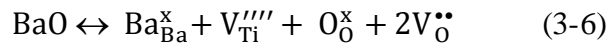
There is a partial disagreement over the results obtained here and those for the bulk material response reported by West et al. [49, 56]. They observed only a small bias dependence for stoichiometric BaTiO_3 but a more significant bias dependence for nonstoichiometric BaTiO_3 , both BaO-deficient and TiO_2 -deficient. The resistance of both bulk and grain boundary components was independent of applied voltage for stoichiometric BaTiO_3 [49] and dependent on bias for nonstoichiometric BaTiO_3 ,

showing time dependent, non-ohmic, low-field characteristics at temperatures $> \sim 200$ °C.

Only a small dc bias effect was observed as well with isovalent dopants with partial replacement of Ba on the A sites by Ca. This may be because isovalent dopants do not give rise to departures from local electroneutrality [50].

Although the results reported in this chapter were on nominally stoichiometric BaTiO₃, there are various ways in which nonstoichiometric BT can be formed such as contamination by the milling media and stoichiometry variations during calcination, associated with Ba loss. Barium loss could occur due to reaction with the platinum containers. Quenched samples from elevated temperatures are often affected by a slight oxygen nonstoichiometry, while slow-cooled samples show that gradients of oxygen concentration might lead to core-shell structures [49]. Oxygen-deficient samples could be obtained at high-temperatures depending on pellet density and atmosphere.

P-type behaviour may appear due to the presence of impurities or dopants that may have been introduced, deliberately or inadvertently, into the sample. Nonstoichiometric BT could be regarded as acceptor-doped in which the dopants are zero-valent cation vacancies (titanium or barium vacancies) which require some adjacent oxygen vacancies to achieve charge balance as shown by the following defect reactions:



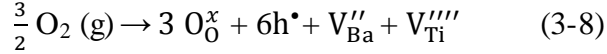
or



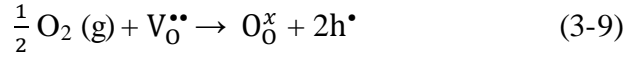
The change in conductivity with dc bias of the grain boundary component was much higher than that of the bulk: R_{gb} with dc bias was $\sim 21.8\%$ of the original value without dc bias whereas for R_{b} it was $\sim 96.2\%$. This behaviour is qualitatively similar to that observed by West et al. [49] for their solid state sample. A small decrease for R_1 was observed whereas, R_2 reduced much more than R_1 with dc bias. In contrast, their sol-gel sample showed very little bias-dependence: R_1 was mostly unchanged and R_2 showed a much smaller decrease compared to the solid state sample.

A qualitatively similar reduction in resistance of both bulk and grain boundary regions occurs on increasing the oxygen partial pressure in the surrounding atmosphere, which shows that conduction is p-type, consistent with literature data obtained by Sinclair et al. and Cann et al. [49, 90, 104, 106, 107].

The resistance decrease is reversible on reducing the oxygen partial pressure. BaTiO₃ picks up oxygen at the surface by the nominal mechanism:



Or if acceptor-type impurities are present as:



Increasing pO₂ is associated with more O₂ molecules absorbed at the surface. The molecules ionise by trapping electrons. Electrons are withdrawn from the sample to form the O²⁻ ions and holes are therefore created. In the literature, the source of the holes is usually taken to be impurities such as Fe³⁺ which ionise to Fe⁴⁺ but more recently, it has been suggested that underbonded O²⁻ ions may ionise [108]. The number of mobile positive hole carriers was increased as a result on removal of electrons.

This behaviour is the reverse of the expected behaviour for barium titanate where oxygen removal gives rise to electron injection into the Ti 3d orbitals, n-type conduction and a reduction in resistance.

Capacitance data show a bulk capacitance value of 20 pFcm⁻¹ which is a typical value of BaTiO₃ at temperature > T_c with relatively high permittivity, ε_r of ~ 226. A poorly-resolved second capacitance of 9 nFcm⁻¹ was observed at low frequency which was 20–30 times the value of the high frequency capacitance and is attributed to a grain boundary capacitance. The difference in magnitudes of C_g and C_{gb} are typical of poorly-sintered ceramics. Neither C₁ nor C₂ showed much change with either dc bias and pO₂. Data for C₂ were obtained only at high temperatures and therefore, it is not known whether C₂ is ferroelectric or nonferroelectric.

The effect of sintering temperature was also studied. The increase of sintering temperature increased the conductivity of grain and grain boundary, probably as a

result of extra loss of oxygen at higher temperature. Reoxidation rates are sensitive to cooling conditions however and can change the conductivity dramatically.

In summary, SC BT is insulating with p-type behaviour that could be associated with a slight departure from a Ba:Ti ratio of 1:1, caused by possible Ba loss during sintering. The holes may be associated with underbonded oxide ions or unavoidable impurities such as Fe^{3+} .

Quenched samples:

Many samples made by *HM*, *BM* and *PBM* were completely insulating at RT for both SC and Q. Some Q samples however showed a much higher σ with lower density, as a consequence of loss of oxygen at high temperatures which was preserved during quenching. The loss increases with quench temperature. Electrons are liberated and enter the crystal lattice by occupying the 3d orbitals on Ti. The high conductivity is associated with partial occupancy of Ti 3d orbitals. Secondly, the low frequency C' data indicate a plateau that is approximately 10 times greater in Q samples, > 10 nF, compared with ≤ 5 nF for SC samples. The main impedance of Q samples may therefore contain a Schottky barrier impedance. In particular, the low frequency impedance arc and the low frequency C' plateau may be attributable to a Schottky barrier with values denoted as R_3 and C_3 .

For some Q samples, a Schottky barrier impedance was observed and the Schottky barrier height was rather different for In-Ga, Ag and Pt electrodes and the associated resistance R_3 was largest with Pt. The C_3 value represents the thickness of the depletion layer associated with the Schottky barrier, which is greatest for In-Ga and Ag whereas the barrier height R_3 is greatest for Pt.

Total conductivity (σ_t) data for samples quenched from 1400 °C with In-Ga and Ag electrodes show a PTCR effect on heating through the Curie temperature. This also is an indication that the resistance responsible is associated with an interfacial voltage barrier such as a Schottky barrier.

The Schottky barrier is a voltage barrier accompanied by charge transfer across an interface [51]. Schottky barriers may form either at grain boundaries or at the sample-electrode contacts. Firstly, they may form at grain boundaries as a result of partial oxidation (during cooling/annealing) of reduced samples [109]. An Internal Barrier

Layer Capacitor (IBLC) effect is a result of this oxidation. The barrier layers act as an extrinsic source of impedance [45, 110-112]. The potential barrier is produced at the grain boundary by electron trapping at surface acceptor states which are associated with either second phases or interfacial states. When the reduced sample undergoes partial oxidation, oxygen molecules pick up electrons and dissociate. The surface becomes negatively charged creating a capacitor with a positively-charged depletion layer at the grain surface. Thus, partial oxidation is required to form Schottky barriers of this nature at grain boundaries.

Secondly, Schottky barriers may form at the semiconducting sample surface and metal electrode interface, which is associated with the energy mismatch between the Fermi levels of the sample and electrode metal, ie the difference between the metal electrode work function and semiconductor electron affinity [109, 113-116], leading to spill-over of charge carriers between sample and electrode; one side becomes negative and the other side becomes positive. Generation of a depletion layer then occurs at the sample surface leading to a voltage barrier, or Schottky barrier [51]. Many factors can change the sample-electrode effect such as: the work function, nature of the metal electrode and the existence of interface states at the sample surface [109, 117, 118].

The bulk conductivity was too high to measure or to be separated from the total conductivity for the sample sintered at 1400 °C and instead, Z^* plots gave only the total resistance. This appeared to be dominated by the Schottky barrier whereas, the sample sintered at 1350 °C and lower showed two components. For quenched samples, the M'' spectrum was dominated by a high frequency incline with $f_{\max} > 10^7$ Hz as the peak maximum representing the sample bulk/grain boundary is off-scale and the maxima occurs outside the measured frequency range.

In-Ga electrodes are a well-known electrode material to provide an ohmic contact [46, 119]. It has been suggested that using In-Ga as contact is a useful way to avoid Schottky barrier formation at the electrode-sample interface [46]. The similar results with all three electrodes may show that a grain boundary-related Schottky barrier is dominant at low frequency, especially since In-Ga electrodes are considered to yield ohmic contacts (negligible electrode resistance) when used in samples with

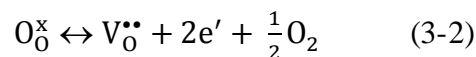
semiconducting BaTiO₃ that does not form a Schottky barrier at the ceramic-electrode interface [46].

A sample-electrode Schottky barrier effect was apparently not observed as no difference was observed using different types of electrodes such as In-Ga and Ag. Since this result is not associated with an interface, as is commonly observed with a Schottky barrier at a sample-electrode contact, it is sample-related and probably related to oxidation of sample surfaces, either at the pellet outer surface or internal grain boundaries.

There may be two kinds of gb: with/without a SB.

The low frequency capacitance C' is different for SC and Q samples. For SC, 1350 °C at room temperature, C₁=1.02×10⁻¹⁰ Fcm⁻¹ and C₂=1.33×10⁻¹⁰ Fcm⁻¹; for Q, 1350, C₁=3.11 ×10⁻¹⁰ Fcm⁻¹ and C₂=2.5 ×10⁻⁸ Fcm⁻¹. The C value of the low frequency component for the Q sample is much higher than for SC which shows that the region responsible is a much thinner effect and is therefore attributed to a Schottky barrier, C₃.

The application of dc bias is standard practice during impedance measurements which usually provides a good way to separate Schottky barrier-type effects from material-related sample impedances. The application of different atmospheres (air, oxygen and nitrogen) was also studied to clarify dc bias results especially since the change in resistance with atmosphere for some samples can be interpreted in two ways. For the Q sample, R_T appears to demonstrate predominantly n-type behaviour but, the Schottky barrier height may also be sensitive to pO₂, depending on the mechanism of Schottky barrier formation. The conductivity increase with decreasing oxygen partial pressure is probably due to low level of oxygen loss, accompanied by partial reduction of Ti⁴⁺ to Ti³⁺ ions [6] according to the defect model by the following idealized reduction reaction, which is displaced to the right hand side in low pO₂ [91, 100]:



There was a clear difference in behaviour between dc bias and pO₂ results for the sample quenched from 1380 and a slow-cooled sample. For the Q sample, R_t decreased with increasing dc bias whereas it decreased in a reducing atmosphere. By

contrast, the resistance of SC samples decreased with increasing dc bias but increased in a reducing atmosphere. Therefore, further investigation was carried out on different samples to try and clarify these differences in behaviour.

The main reason for the differences appears to depend on whether the main impedance component is a Schottky barrier or is a true sample resistance. From previous work on doped BT [54, 56], n-type materials show a decrease in conductivity with either increasing pO_2 or dc bias; p-type materials show the opposite effect with an increase in conductivity with either increasing pO_2 or dc bias; intrinsic materials appear to show little or no effect. For Schottky barriers, the barrier height and therefore the resistance decreases with dc bias; the effect of pO_2 on Schottky barriers is less clear and depends on whether O_2 adsorption/desorption affects the barrier height. This in turn, depends on whether the Schottky barrier is caused by a Fermi level mismatch at the electrode-sample interface, or partial oxidation at grain-grain interfaces.

It was important to quench samples from different temperatures to compare their results with that of the sample quenched from 1380 °C. This investigation confirmed that there were different conduction behaviours between samples quenched from $\sim \geq 1380$ °C and $\sim \leq 1380$ °C. Early results had shown that Q temperature has a big effect. The sample quenched from 1400 °C showed a high conductivity and apparent n-type behaviour. After that, quenching from lower temperature (1380 °C), still gave n-type behaviour but with lower conductivity. P-type conductivity was observed for samples quenched from $\sim < 1380$ °C.

The distinction between n-type, p-type and the Schottky barrier effects can be observed with different quench temperature. There are two possibilities:

- 1- SC samples and Q samples from $\sim < 1380$ °C clearly show p-type behaviour whereas, n-type behaviour was observed for some Q samples from $\sim \geq 1380$ °C whereas, was p-type for others. For example, Figure 3-41 shows the conductivity and activation energy of samples quenched from 1200 and 1400 °C. The conduction mechanism is different. Quenching from 1400 °C shows much higher conductivity, lower activation energy and therefore n-type

behaviour. P-type behaviour was observed for sample quenched from 1200 °C.

- 2- Some Q samples from $\sim \geq 1380$ °C are dominated by Schottky barrier because the obtained behaviour is expected for Schottky barrier at grain boundary. Schottky barrier will decrease with bias. If the Schottky barrier is at grain boundary, this is a slow process because a Schottky barrier at grain boundary forms only when oxidation occurs, whereas with no oxidation, the Fermi level is the same and there is no Schottky barrier. With oxidation, oxide ions are trapped and the depletion layer gives rise to the Schottky barrier. Schottky barrier at sample surface could be observed with partial oxidation which is different from the Schottky barrier of metal contacts.

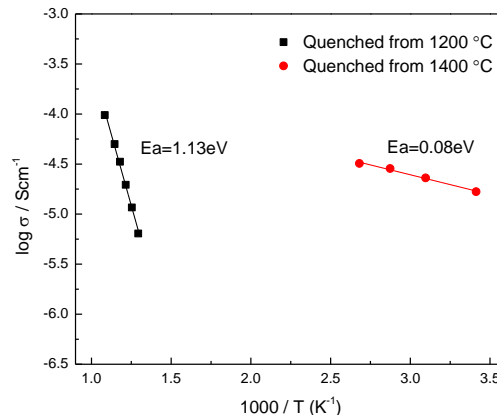
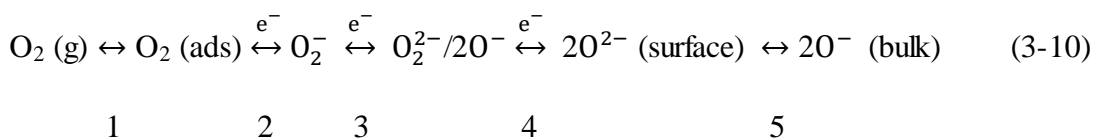


Figure 3-41: Arrhenius plots of R_t for samples (5) quenched from 1400 °C and (12) quenched from 1200 °C.

For p-type conduction, the enhanced conductivity is controlled by the O^- ions especially with immobilisation of the ionised electrons at sample surfaces which is associated with changing the equilibria between various oxygen species. Therefore, the driving force for ionisation of underbonded oxide ions was provided by the dc bias. Dynamic equilibrium in the following sequence of successive steps may potentially occur especially at oxide surfaces, involving absorbed oxygen [35, 52, 53, 55, 58, 59]:



Several stages are involved in the equilibria shown in (3-10). Each of stages 2, 3, and 4 involves electron transfer. These steps may lead to change in the conductivity. The existence of partially reduced oxygen species was observed at sample surface, such as the superoxide ion O_2^- [120].

Step 1 shows the adsorption of oxygen molecules at the sample surface. This could cause electron traps; the superoxide ion O_2^- can form as result of picking up electron from the sample, step 2. The peroxide ions, O_2^{2-} can be formed as result of picking up a second electron by the superoxide ions, step 3. The peroxide ions, O_2^{2-} might cause dissociation to form O^- , step 4. The O^{2-} ions can be formed, step 5 as result of step 4 which may be associated with some stability at sample surface in an under-bonded environment or picking up additional electrons.

It is well-known that at high temperatures, the change in equilibrium conditions such as reducing pO_2 leads to change from p-type to n-type for pure and doped $BaTiO_3$ [121, 122].

The change of the conduction type from p-type to n-type or the appearance of Schottky barrier effect was observed for some samples above 1380 °C which is influenced by oxygen loss. Dc bias data show that the resistance decreased with increasing the voltage which is probably as result of Schottky barrier effect. No clear oxygen deficiency was observed at temperatures below 1380 °C. O_2 molecules are adsorbed onto the sample surface with creation of O^- species that are considered to be the principal source of holes. The adsorbed oxygen is observed either with slow cooled samples or on annealing samples at lower temperatures. An increased conductivity was observed with a decrease in annealing temperature and is attributed to an increase in hole concentration; this increase is less than for samples of BT that were acceptor-doped BT that were on the Ti site [49, 50, 53-56] as result of increasing the high concentration of underbonded oxide ions.

The conductivity data were studied either below or above T_C . Conductivity data show two linear Arrhenius plots either side of T_C as result of PTCR effect and their temperature dependences are clearly different.

Conductivity (σ_b , σ_{gb} and σ_t) data for a sample quenched from 1300 °C were also studied for in air and N_2 , showing p-type conduction since air conductivity was larger than N_2 conductivity which is consistent with the literature data [90, 103].

σ_b data were influenced by the atmosphere, showing that conductivity in air is larger than in N_2 by \sim half order of magnitude where σ_{gb} data are significantly insensitive to changing the atmosphere.

The bulk and grain boundary conductivity changed with temperature. At 400 °C, $\sigma_g > \sigma_{gb}$ either with air or N_2 . $\sigma_{gb} \cong \sigma_b$ at \sim 750 °C in air and \sim 700 °C in N_2 . At 900 °C, $\sigma_{gb} > \sigma_g$ either with air or N_2 .

3.5 Conclusions

The electrical properties of undoped-BT for all routes are strongly dependent on the sintering temperature, cooling rate, dc bias and atmosphere (pO_2).

All slow cooled samples are electrically inhomogeneous by presenting two components corresponding to the bulk and grain boundary regions.

Different milling routes showed similar conductivity data. No effect of milling on conductivity was observed.

Many Q samples made by *HM*, *BM* and *PBM* were completely insulating at RT but conductive material was observed with some quenched sample which is associated with loss a small amount of oxygen with lower density.

Oxygen-deficient sample quenched from 1380 °C shows n-type behaviour or Schottky barrier effect with increasing the conductivity and a decrease in activation energy whereas, p-type was observed for sample quenched from below 1380 °C and sometimes from above 1380 °C or slow cooled as samples show a decrease in resistance with increasing dc bias voltage and an increase in resistance with decreasing pO_2 . The decrease in conductivity with decreasing pO_2 is consistent with p-type conduction mechanism.

3.6 References

- [1] D.K. Rana, Synthesis and Characterization of Bi doped BaTiO₃ ceramic, (2010).
- [2] Y. Liu, A.R. West, Ho-doped BaTiO₃: Polymorphism, phase equilibria and dielectric properties of BaTi_{1-x}Ho_xO_{3-x/2}: 0≤x≤0.17, Journal of the European Ceramic Society, 29 (2009) 3249-3257.
- [3] B. Huybrechts, K. Ishizaki, M. Takata, The positive temperature coefficient of resistivity in barium titanate, Journal of materials science, 30 (1995) 2463-2474.
- [4] P. Fiorenza, R. Lo Nigro, P. Delugas, V. Raineri, A.G. Mould, D.C. Sinclair, Direct imaging of the core-shell effect in positive temperature coefficient of resistance-BaTiO₃ ceramics, Applied Physics Letters, 95 (2009) 2904.
- [5] J.A. Dawson, C.L. Freeman, L.B. Ben, J.H. Harding, D.C. Sinclair, An atomistic study into the defect chemistry of hexagonal barium titanate, Journal of Applied Physics, 109 (2011) 084102.
- [6] G.M. Keith, M.J. Rampling, K. Sarma, N.M. Alford, D.C. Sinclair, Synthesis and characterisation of doped 6H-BaTiO₃ ceramics, Journal of the European Ceramic Society, 24 (2004) 1721-1724.
- [7] H.-I. Yoo, C.-R. Song, D.-K. Lee, BaTiO_{3-δ}: defect structure, electrical conductivity, chemical diffusivity, thermoelectric power, and oxygen nonstoichiometry, Journal of electroceramics, 8 (2002) 5-36.
- [8] G.H. Haertling, Ferroelectric ceramics: history and technology, Journal of the American Ceramic Society, 82 (1999) 797-818.
- [9] V.P. Pavlović, M.V. Nikolić, Z. Nikolić, G. Branković, L. Živković, V.B. Pavlović, M.M. Ristić, Microstructural evolution and electric properties of mechanically activated BaTiO₃ ceramics, Journal of the European Ceramic Society, 27 (2007) 575-579.
- [10] L. Wu, M.-C. Chure, K.-K. Wu, W.-C. Chang, M.-J. Yang, W.-K. Liu, M.-J. Wu, Dielectric properties of barium titanate ceramics with different materials powder size, Ceramics International, 35 (2009) 957-960.
- [11] L.B. Kong, J. Ma, H. Huang, R.F. Zhang, W.X. Que, Barium titanate derived from mechanochemically activated powders, Journal of alloys and compounds, 337 (2002) 226-230.

- [12] M. Ma, Y. Wang, Y. Lu, W. Wu, Y. Li, Effect of ball mill method on microstructure and electrical properties of BaTiO₃ based PTCR ceramics, *Ceramics International*, 41 (2015) S804-S808.
- [13] B.D. Stojanović, V.B. Pavlović, V.P. Pavlović, S. Djurić, B.A. Marinković, M.M. Ristić, Dielectric properties of barium-titanate sintered from tribophysically activated powders, *Journal of the European Ceramic Society*, 19 (1999) 1081-1083.
- [14] F.D. Morrison, D.C. Sinclair, A.R. West, Electrical and structural characteristics of lanthanum-doped barium titanate ceramics, *Journal of Applied Physics*, 86 (1999) 6355-6366.
- [15] S.A. Lokare, Structural and Electrical Properties of BaTiO₃ prepared by Solid State Route.
- [16] M.C. Ferrarelli, C.C. Tan, D.C. Sinclair, Ferroelectric, electrical, and structural properties of Dy and Sc co-doped BaTiO₃, *Journal of Materials Chemistry*, 21 (2011) 6292-6299.
- [17] A. Feteira, D.C. Sinclair, The influence of nanometric phase separation on the dielectric and magnetic properties of (1-x)BaTiO₃-xLaYbO₃ (0 ≤ x ≤ 0.60) ceramics, *Journal of Materials Chemistry*, 19 (2009) 356-359.
- [18] R.A.C. Amoresi, A.A. Felix, E.R. Botero, N.L.C. Domingues, E.A. Falcão, M.A. Zaghete, A.W. Rinaldi, Crystallinity, morphology and high dielectric permittivity of NiO nanosheets filling Poly (vinylidene fluoride), *Ceramics International*, 41 (2015) 14733-14739.
- [19] I.J. Clark, T. Takeuchi, N. Ohtori, D.C. Sinclair, Hydrothermal synthesis and characterisation of BaTiO₃ fine powders: precursors, polymorphism and properties, *Journal of materials chemistry*, 9 (1999) 83-91.
- [20] D. Sinclair, J. Paul Attfield, The influence of A-cation disorder on the Curie temperature of ferroelectric ATiO₃ perovskites, *Chemical Communications*, (1999) 1497-1498.
- [21] R.E. Cohen, Origin of ferroelectricity in perovskite oxides, *Nature*, 358 (1992) 136-138.
- [22] L. Ben, D.C. Sinclair, Anomalous Curie temperature behavior of A-site Gd-doped BaTiO₃ ceramics: The influence of strain, *Applied Physics Letters*, 98 (2011) 092907.

- [23] D. Hennings, Barium titanate based ceramic materials for dielectric use, *International journal of high technology ceramics*, 3 (1987) 91-111.
- [24] M.E. Lines, A.M. Glass, *Principles and applications of ferroelectrics and related materials*, Oxford university press, 1977.
- [25] F. Seitz, D. Turnbull, *SOLID STATE PHYSICS. ADVANCES IN RESEARCH AND APPLICATIONS. VOLUME 18*, Solid State Physics (US), 18 (1966).
- [26] C. Wang, *Theories and Methods of First Order Ferroelectric Phase Transitions*, INTECH Open Access Publisher, 2010.
- [27] S. Leng, G. Li, L. Zheng, W. Shi, Y. Zhu, Effect of donor concentration on the PTCR behavior of Y-doped $\text{BaTiO}_3\text{-(Bi}_{1/2}\text{Na}_{1/2})\text{TiO}_3$ ceramics, *Journal of Materials Science: Materials in Electronics*, 24 (2013) 431-435.
- [28] H. Beltrán, E. Cordoncillo, P. Escribano, D.C. Sinclair, A.R. West, Oxygen loss, semiconductivity, and positive temperature coefficient of resistance behavior in undoped cation-stoichiometric BaTiO_3 ceramics, *Journal of applied physics*, 98 (2005) 4102.
- [29] F.D. Morrison, D.C. Sinclair, A.R. West, An Alternative Explanation for the Origin of the Resistivity Anomaly in La-Doped BaTiO_3 , *Journal of the American Ceramic Society*, 84 (2001) 474-476.
- [30] F.D. Morrison, D.C. Sinclair, A.R. West, Characterization of Lanthanum-Doped Barium Titanate Ceramics Using Impedance Spectroscopy, *Journal of the American Ceramic Society*, 84 (2001) 531-538.
- [31] F.D. Morrison, A.M. Coats, D.C. Sinclair, A.R. West, Charge compensation mechanisms in La-doped BaTiO_3 , *Journal of Electroceramics*, 6 (2001) 219-232.
- [32] F.D. Morrison, D.C. Sinclair, A.R. West, Doping mechanisms and electrical properties of La-doped BaTiO_3 ceramics, *International Journal of Inorganic Materials*, 3 (2001) 1205-1210.
- [33] M.M. Gallego, A.R. West, Effect of annealing treatments on positive temperature coefficient of resistance properties of barium titanate ceramics and a new model for the positive temperature coefficient of resistance effect, *Journal of Applied Physics*, 90 (2001) 394-403.
- [34] C.L. Freeman, J.A. Dawson, H.R. Chen, L. Ben, J.H. Harding, F.D. Morrison, D.C. Sinclair, A.R. West, Energetics of Donor-Doping, Metal Vacancies, and

Oxygen-Loss in A-Site Rare-Earth-Doped BaTiO₃, *Advanced Functional Materials*, 23 (2013) 3925-3928.

[35] N. Masó, A.R. West, Electronic conductivity in yttria-stabilized zirconia under a small dc bias, *Chemistry of Materials*, 27 (2015) 1552-1558.

[36] O. Saburi, Semiconducting bodies in the family of barium titanates, *Journal of the American Ceramic Society*, 44 (1961) 54-63.

[37] A.B. Alles, V.R.W. Amarakoon, V.L. Burdick, Positive temperature coefficient of resistivity effect in undoped, atmospherically reduced barium titanate, *Journal of the American Ceramic Society*, 72 (1989) 148-151.

[38] J. Daniels, K.H. Hardtl, D. Hennings, R. Wernicke, Defect Chemistry And Electrical-Conductivity of Doped Barium-Titanate Ceramics, in, PHILIPS RESEARCH LABORATORIES BUILDING WBP ROOM NO. 42, EINDHOVEN, NETHERLANDS, 1976.

[39] M. Prades, N. Maso, H. Beltran, E. Cordoncillo, A.R. West, Polymorphism of BaTiO₃ acceptor doped with Mn³⁺, Fe³⁺, and Ti³⁺, *Journal of the American Ceramic Society*, 91 (2008) 2364-2366.

[40] P. Ren, N. Masó, A.R. West, Hole conductivity in oxygen-excess BaTi_{1-x}Ca_xO_{3-x+δ}, *Physical Chemistry Chemical Physics*, 15 (2013) 20943-20950.

[41] M. Kuwabara, E. Matsuyama, S. Takahashi, H. Shimooka, Y. Urakawa, PTCR characteristics in undoped barium titanate ceramics with core-shell type duplex microstructures, in, *IEEE*, pp. 758-759.

[42] L. Guo, H. Luo, J. Gao, L. Guo, J. Yang, Microwave hydrothermal synthesis of barium titanate powders, *Materials Letters*, 60 (2006) 3011-3014.

[43] M.M. Vijatović, J.D. Bobić, B.D. Stojanović, History and challenges of barium titanate: Part II, *Science of Sintering*, 40 (2008) 235-244.

[44] P. Lunkenheimer, R. Fichtl, S.G. Ebbinghaus, A. Loidl, Nonintrinsic origin of the colossal dielectric constants in CaCu₃Ti₄O₁₂, *Physical review B*, 70 (2004) 172102.

[45] T.B. Adams, D.C. Sinclair, A.R. West, Characterization of grain boundary impedances in fine- and coarse-grained CaCu₃Ti₄O₁₂ ceramics, *Physical review B*, 73 (2006) 094124.

- [46] D.P. Cann, C.A. Randall, Electrode effects in positive temperature coefficient and negative temperature coefficient devices measured by complex-plane impedance analysis, *Journal of applied physics*, 80 (1996) 1628-1632.
- [47] N. Kumar, E.A. Patterson, T. Frömling, D.P. Cann, DC-bias dependent impedance spectroscopy of $\text{BaTiO}_3\text{-Bi}(\text{Zn}_{1/2}\text{Ti}_{1/2})\text{O}_3$ ceramics, *Journal of Materials Chemistry C*, 4 (2016) 1782-1786.
- [48] N. Masó, H. Beltrán, E. Cordoncillo, P. Escribano, A.R. West, Electrical properties of Fe-doped BaTiO_3 , *Journal of Materials Chemistry*, 16 (2006) 1626-1633.
- [49] H. Beltrán, M. Prades, N. Masó, E. Cordoncillo, A.R. West, Enhanced Conductivity and Nonlinear Voltage–Current Characteristics of Nonstoichiometric BaTiO_3 Ceramics, *Journal of the American Ceramic Society*, 94 (2011) 2951-2962.
- [50] N. Masó, M. Prades Tena, H. Beltrán Mir, E. Cordoncillo Cordoncillo, D.C. Sinclair, A.R. West, Field enhanced bulk conductivity of acceptor-doped $\text{BaTi}_{1-x}\text{Ca}_x\text{O}_{3-x}$ ceramics, (2010).
- [51] J.J. Biendicho, A.R. West, Impedance characterisation of LiFePO_4 ceramics, *Solid State Ionics*, 226 (2012) 41-52.
- [52] M. Prades, H. Beltrán, E. Cordoncillo, P.J. Alonso, N. Masó, A.R. West, Non-ohmic phenomena in Mn-doped BaTiO_3 , *physica status solidi (a)*, 209 (2012) 2267-2272.
- [53] Q.-L. Zhang, N. Masó, Y. Liu, H. Yang, A.R. West, Voltage-dependent low-field resistivity of $\text{CaTiO}_3\text{: Zn}$ ceramics, *Journal of Materials Chemistry*, 21 (2011) 12894-12900.
- [54] H. Beltrán, M. Prades, N. Masó, E. Cordoncillo, A.R. West, Voltage-Dependent Low-Field Bulk Resistivity in $\text{BaTiO}_3\text{: Zn}$ Ceramics, *Journal of the American Ceramic Society*, 93 (2010) 500-505.
- [55] L. Gil Escrig, M. Prades, H. Beltrán, E. Cordoncillo, N. Masó, A.R. West, Voltage-Dependent Bulk Resistivity of $\text{SrTiO}_3\text{: Mg}$ Ceramics, *Journal of the American Ceramic Society*, 97 (2014) 2815-2824.
- [56] M. Prades, N. Masó, H. Beltrán, E. Cordoncillo, A.R. West, Field enhanced bulk conductivity of $\text{BaTiO}_3\text{: Mg}$ ceramics, *Journal of Materials Chemistry*, 20 (2010) 5335-5344.

- [57] P. Ren, N. Masó, Y. Liu, L. Ma, H. Fan, A.R. West, Mixed oxide ion and proton conduction and p-type semiconduction in $\text{BaTi}_{0.98}\text{Ca}_{0.02}\text{O}_{2.98}$ ceramics, *Journal of Materials Chemistry C*, 1 (2013) 2426-2432.
- [58] Y. Liu, A.R. West, Voltage-dependent resistance of undoped rutile, TiO_2 , ceramics, *Applied Physics Letters*, 103 (2013) 263508.
- [59] N. Masó, H. Beltrán, M. Prades, E. Cordoncillo, A.R. West, Field-enhanced bulk conductivity and resistive-switching in Ca-doped BiFeO_3 ceramics, *Physical Chemistry Chemical Physics*, 16 (2014) 19408-19416.
- [60] International Centre for Diffraction Data, Powder Diffraction Database. International Centre for Diffraction Data, Newton Square, PA, 1994.
- [61] T. Mitsui, W.B. Westphal, Dielectric and X-Ray Studies of $\text{Ca}_x\text{Ba}_{1-x}\text{TiO}_3$ and $\text{Ca}_x\text{Sr}_{1-x}\text{TiO}_3$, *Physical Review*, 124 (1961) 1354.
- [62] S.H. Ra, S.H. Kim, C.Y. Jeong, H.S. Kim, Y.W. Lee, The effect of ball-mill treatment on powder characteristics, compaction and sintering of UO_2 , (2001).
- [63] H. Beltran, E. Cordoncillo, P. Escribano, D.C. Sinclair, A.R. West, Insulating Properties of Lanthanum-Doped BaTiO_3 Ceramics Prepared by Low-Temperature Synthesis, *Journal of the American Ceramic Society*, 87 (2004) 2132-2134.
- [64] A. Feteira, D.C. Sinclair, I.M. Reaney, Synthesis and Characterization of $\text{BaTi}_{1-x}\text{Ga}_x\text{O}_{3-\delta}$ ($0 \leq x \leq 0.15$) Ceramics, *Journal of the American Ceramic Society*, 89 (2006) 2105-2113.
- [65] A.F. Devonshire, XCVI. Theory of barium titanate: Part I, *The London, Edinburgh, and Dublin Philosophical Magazine and Journal of Science*, 40 (1949) 1040-1063.
- [66] N. Masó, H. Beltrán, E. Cordoncillo, D.C. Sinclair, A.R. West, Polymorphism and Dielectric Properties of Nb-Doped BaTiO_3 , *Journal of the American Ceramic Society*, 91 (2008) 144-150.
- [67] A. Feteira, K. Sarma, N.M. Alford, I.M. Reaney, D.C. Sinclair, Microwave Dielectric Properties of Gallium-Doped Hexagonal Barium Titanate Ceramics, *Journal of the American Ceramic Society*, 86 (2003) 511-513.
- [68] Z. Lazarevica, N. Romcevica, M. Vijatovicb, N. Paunovica, M. Romcevica, B. Stojanovicb, Z. Dohcevic-Mitrovica, Characterization of barium titanate ceramic powders by Raman spectroscopy, in, *Proceedings of the Tenth Annual Conference of the Materials Research Society of Serbia*, 2008.

- [69] H. Hayashi, T. Nakamura, T. Ebina, In-situ Raman spectroscopy of BaTiO₃ particles for tetragonal–cubic transformation, *Journal of Physics and Chemistry of Solids*, 74 (2013) 957-962.
- [70] U.M. Pasha, H. Zheng, O.P. Thakur, A. Feteira, K.R. Whittle, D.C. Sinclair, I.M. Reaney, In situ Raman spectroscopy of A-site doped barium titanate, *Applied Physics Letters*, 91 (2007) 2908.
- [71] J. Pokorný, U.M. Pasha, L. Ben, O.P. Thakur, D.C. Sinclair, I.M. Reaney, Use of Raman spectroscopy to determine the site occupancy of dopants in BaTiO₃, *Journal of Applied Physics*, 109 (2011) 114110.
- [72] Y. Shiratori, C. Pithan, J. Dornseiffer, R. Waser, Raman scattering studies on nanocrystalline BaTiO₃ Part II—consolidated polycrystalline ceramics, *Journal of Raman Spectroscopy*, 38 (2007) 1300-1306.
- [73] D. Maurya, A. Kumar, V. Petkov, J.E. Mahaney, R.S. Katiyar, S. Priya, Local structure and piezoelectric instability in lead-free (1– x)BaTiO₃-xA(Cu_{1/3}Nb_{2/3})O₃ (A= Sr, Ca, Ba) solid solutions, *RSC Advances*, 4 (2014) 1283-1292.
- [74] B.D. Begg, K.S. Finnie, E.R. Vance, Raman Study of the Relationship between Room-Temperature Tetragonality and the Curie Point of Barium Titanate, *Journal of the American Ceramic Society*, 79 (1996) 2666-2672.
- [75] T. Nagai, K. Iijima, H.J. Hwang, M. Sando, T. Sekino, K. Niihara, Effect of MgO doping on the phase transformations of BaTiO₃, *Journal of the American Ceramic Society*, 83 (2000) 107-112.
- [76] C.H. Perry, D.B. Hall, Temperature Dependence of the Raman Spectrum of BaTiO₃, *Physical Review Letters*, 15 (1965) 700.
- [77] A. Feteira, D.C. Sinclair, J. Kreisel, Average and local structure of (1–x)BaTiO₃– xLaYO₃ (0≤ x≤ 0.50) ceramics, *Journal of the American Ceramic Society*, 93 (2010) 4174-4181.
- [78] M. DiDomenico Jr, S.H. Wemple, S.P.S. Porto, R.P. Bauman, Raman Spectrum of Single-Domain BaTiO₃, *Physical Review*, 174 (1968) 522.
- [79] Y.J. Jiang, L.Z. Zeng, R.P. Wang, Y. Zhu, Y.L. Liu, Fundamental and Second-Order Raman Spectra of BaTiO₃, *Journal of Raman spectroscopy*, 27 (1996) 31-34.

- [80] I.G. Siny, R. Tao, R.S. Katiyar, R. Guo, A.S. Bhalla, Raman spectroscopy of Mg-Ta order-disorder in $\text{BaMg}_{13}\text{Ta}_2\text{O}_3$, *Journal of Physics and Chemistry of Solids*, 59 (1998) 181-195.
- [81] A. Feteira, G.M. Keith, M.J. Rampling, C.A. Kirk, I.M. Reaney, K. Sarma, N.M. Alford, D.C. Sinclair, Synthesis and characterisation of Ga-doped hexagonal BaTiO_3 , *Crystal engineering*, 5 (2002) 439-448.
- [82] S.-F. Liu, I.R. Abothu, S. Komarneni, Barium titanate ceramics prepared from conventional and microwave hydrothermal powders, *materials Letters*, 38 (1999) 344-350.
- [83] B. Li, X. Wang, L. Li, Synthesis and sintering behavior of BaTiO_3 prepared by different chemical methods, *Materials chemistry and physics*, 78 (2003) 292-298.
- [84] Y.C. Huang, W.H. Tuan, Exaggerated grain growth in Ni-doped BaTiO_3 ceramics, *Materials Chemistry and Physics*, 105 (2007) 320-324.
- [85] Y.K. Cho, S.J.L. Kang, D.Y. Yoon, Dependence of Grain Growth and Grain-Boundary Structure on the Ba/Ti Ratio in BaTiO_3 , *Journal of the American Ceramic Society*, 87 (2004) 119-124.
- [86] M. Drogenik, A. Popović, L. Irmančnik, D. Kolar, V. Kraševc, Release of oxygen during the sintering of doped BaTiO_3 ceramics, *Journal of the American Ceramic Society*, 65 (1982).
- [87] D. Kolar, U. Kunaver, A. Rečnik, Exaggerated anisotropic grain growth in hexagonal barium titanate ceramics, *physica status solidi (a)*, 166 (1998) 219-230.
- [88] O. Eibl, P. Pongratz, P. Skalicky, H. Schmelz, Formation of (111) twins in BaTiO_3 ceramics, *Journal of the American Ceramic Society*, 70 (1987).
- [89] H. Schmelz, A. Meyer, The evidence for anomalous grain growth below the eutectic temperature in BaTiO_3 ceramics, in, pp. 436.
- [90] I.J. Clark, F.B. Marques, D.C. Sinclair, The influence of grain boundary impedances on the p-type conductivity of undoped BaTiO_3 ceramics, *Journal of the European Ceramic Society*, 22 (2002) 579-583.
- [91] N.H. Chan, R.K. Sharma, D.M. Smyth, Nonstoichiometry in undoped BaTiO_3 , *Journal of the American Ceramic Society*, 64 (1981) 556-562.
- [92] N.H. Chan, R.K. Sharma, D.M. Smyth, Nonstoichiometry in Acceptor-Doped BaTiO_3 , *Journal of the American Ceramic Society*, 65 (1982) 167-170.

- [93] T. Takeuchi, Y. Suyama, D.C. Sinclair, H. Kageyama, Spark-plasma-sintering of fine BaTiO₃ powder prepared by a sol-crystal method, *Journal of materials science*, 36 (2001) 2329-2334.
- [94] L. Zhang, O.P. Thakur, A. Feteira, G.M. Keith, A.G. Mould, D.C. Sinclair, A.R. West, Comment on the use of calcium as a dopant in X8R BaTiO₃-based ceramics, *Applied physics letters*, 90 (2007) 2914.
- [95] M.H. Frey, Z. Xu, P. Han, D.A. Payne, The role of interfaces on an apparent grain size effect on the dielectric properties for ferroelectric barium titanate ceramics, *Ferroelectrics*, 206 (1998) 337-353.
- [96] F.D. Morrison, D.C. Sinclair, J. Skakle, A.R. West, Novel Doping Mechanism for Very-High-Permittivity Barium Titanate Ceramics, *Journal of the American Ceramic Society*, 81 (1998) 1957-1960.
- [97] C. Miclea, C. Tanasoiu, I. Spanulescu, C.F. Miclea, A. Gheorghiu, L. Amarande, M. Cioangher, C.T. Miclea, Microstructure and properties of barium titanate ceramics prepared by mechanochemical synthesis, *Rom. J. Inform. Sci. Technol*, 10 (2007) 335-345.
- [98] W. Li, Z. Xu, R. Chu, P. Fu, J. Hao, Structure and electrical properties of BaTiO₃ prepared by sol-gel process, *Journal of Alloys and Compounds*, 482 (2009) 137-140.
- [99] A.B. Alles, R. Vanalstine, W. Schulze, Dielectric properties and aging of fast-fired barium titanate, *Lat. Am. Appl. Res*, 35 (2005) 29-35.
- [100] N.H. Chan, D.M. Smyth, Defect chemistry of BaTiO₃, *Journal of The Electrochemical Society*, 123 (1976) 1584-1585.
- [101] Y. Tsur, C.A. Randall, Point defect concentrations in barium titanate revisited, *Journal of the American Ceramic Society*, 84 (2001) 2147-2149.
- [102] R. Moos, K.H. Härdtl, Dependence of the intrinsic conductivity minimum of SrTiO₃ ceramics on the sintering atmosphere, *Journal of the American Ceramic Society*, 78 (1995) 2569-2571.
- [103] D.M. Smyth, *The defect chemistry of metal oxides*, Oxford University Press. ISBN-10: 0195110145. ISBN-13: 9780195110142, 1 (2000) 304.
- [104] N. Kumar, E.A. Patterson, T. Frömling, D.P. Cann, Conduction Mechanisms in BaTiO₃-Bi(Zn_{1/2}Ti_{1/2})O₃ Ceramics, *Journal of the American Ceramic Society*, (2016).

- [105] Y.H. Han, J.B. Appleby, D.M. Smyth, Calcium as an acceptor impurity in BaTiO₃, *Journal of the American Ceramic Society*, 70 (1987) 96-100.
- [106] O.P. Thakur, A. Feteira, B. Kundys, D.C. Sinclair, Influence of attrition milling on the electrical properties of undoped-BaTiO₃, *Journal of the European ceramic society*, 27 (2007) 2577-2589.
- [107] M.J. Rampling, SYNTHESIS AND CHARACTERISATION OF UNDOPED AND DOPED HEXAGONAL BARIUM TITANATE, PhD thesis, The University of Sheffield, (2003).
- [108] C. Hamann, H. Burghardt, T. Frauenheim, *Electrical conduction mechanisms in solids*, Vch Pub, 1988.
- [109] M. Li, A. Feteira, D.C. Sinclair, Relaxor ferroelectric-like high effective permittivity in leaky dielectrics/oxide semiconductors induced by electrode effects: A case study of CuO ceramics, *Journal of Applied Physics*, 105 (2009) 114109.
- [110] A.J. Moulson, J.M. Herbert, *Electroceramics Materials, Property, Applications*, 52–68, in, London: Chapman & Hall, 1990.
- [111] R. Bodeux, D. Michau, M. Josse, M. Maglione, Dielectric properties of tetragonal tungsten bronze films deposited by RF magnetron sputtering, *Solid State Sciences*, 38 (2014) 112-118.
- [112] V. Shut, S. Kostomarov, A. Gavrilov, PTCR barium titanate ceramics obtained from oxalate-derived powders with varying crystallinity, *Journal of Materials Science*, 43 (2008) 5251-5257.
- [113] E.H. Rhoderick, R.H. Williams, *Metal-semiconductor contacts*, Clarendon Press Oxford, 1988.
- [114] S.M. Sze, K.K. Ng, *Physics of semiconductor devices*, John wiley & sons, 2006.
- [115] L.J. Brillson, Interface bonding, chemical reactions, and defect formation at metal-semiconductor interfaces, *Journal of Vacuum Science & Technology A*, 25 (2007) 943-949.
- [116] P.T. Landsberg, *Basic Properties of Semiconductors*, Elsevier, 2013.
- [117] K. Ip, B.P. Gila, A.H. Onstine, E.S. Lambers, Y.W. Heo, K.H. Baik, D.P. Norton, S.J. Pearton, S. Kim, J.R. LaRoche, Improved Pt/Au and W/Pt/Au Schottky contacts on n-type ZnO using ozone cleaning, *Applied physics letters*, 84 (2004) 5133.

- [118] Q.L. Gu, C.C. Ling, X.D. Chen, C.K. Cheng, A.M.C. Ng, C.D. Beling, S. Fung, A.B. Djurišić, L.W. Lu, G. Brauer, Hydrogen peroxide treatment induced rectifying behavior of Au-ZnO contact, *Applied physics letters*, (2007).
- [119] H.S. Maiti, R.N. Basu, Complex-plane impedance analysis for semiconducting barium titanate, *Materials research bulletin*, 21 (1986) 1107-1114.
- [120] C.-Y. Yoo, B.A. Boukamp, H.J.M. Bouwmeester, Oxygen surface exchange kinetics of erbia-stabilized bismuth oxide, *Journal of Solid State Electrochemistry*, 15 (2011) 231-236.
- [121] C.-R. Song, H.-I. Yoo, J.-Y. Kim, Mn-doped BaTiO₃: electrical transport properties in equilibrium state, *Journal of Electroceramics*, 1 (1997) 27-39.
- [122] H.-I. Yoo, T.-S. Oh, H.-S. Kwon, D.-K. Shin, J.-S. Lee, Electrical conductivity–defect structure correlation of variable-valence and fixed-valence acceptor-doped BaTiO₃ in quenched state, *Physical Chemistry Chemical Physics*, 11 (2009) 3115-3126.

Chapter 4: Phase assemblages, polymorphism and solid solutions of Y-doped BaTiO₃

4.1 Introduction

In most applications, BaTiO₃ is rarely used in its pure form [1]. The electrical properties can be modified by adding a small amount of dopants. The perovskite structure of BaTiO₃ has received a wide range of substitution. Rare-earth elements have received much attention, since the conductivity and electrical degradation in operating devices can be controlled, in particular, by those cations [2-7].

Doping is useful to tailor different properties of the material to particular applications [8, 9].

The properties of barium titanate doped with rare-earth ions depend on the site of substitution, Ba/Ti ratio, dopant solid solubility limit and charge compensation mechanism. When BT is doped with a rare earth metal (such as La³⁺, Y³⁺ or Nd³⁺), n-type semiconductivity is often obtained. With such doped materials large increases in the specific resistivity are found as the temperature increases above T_C. This behaviour is known as the Positive Temperature Coefficient of Resistivity (PTCR) [10]. The PTCR phenomenon, which has been explained by the Heywang and Jonker model [11, 12], can be attributed to the existence of a potential barrier (ϕ_0) at the grain boundary as a result of electron trapping at interface acceptor states [13, 14].

The solid solution limit of a dopant ion in the BaTiO₃ lattice is basically dependent on its possible incorporation at either Ba or/and Ti sites, the (Ba/Ti) ratio and the possible charge compensation mechanism(s) [15].

Rare-earth metals possess the ability to reduce the temperature dependence of the relative dielectric constant as well as the propensity to decrease the dissipation factor of dielectric ceramics [16-18]. Trivalent rare earth cations have moderate atomic radii between those of Ba²⁺ (1.61 Å, 12 coordination) and Ti⁴⁺ (0.61 Å, 6 coordination) ions. Whether rare earth cations occupy Ba- and/or Ti-sites depends on the ionic radii of the dopants.

This chapter aims to investigate the crystal chemistry and electrical properties of Y-doped BaTiO₃ to determine the possibility of formation of an extensive range(s) of

solid solution and the polymorphism of Y-doped BaTiO₃. Two solid solution joins: (Y-B) ie titanium site substitution accompanied by oxygen vacancies and (Y-AB) self-compensation are studied in detail and the resulting electrical properties measured with particular emphasis on establishing the conditions under which semiconductivity occurs and whether a resistivity minimum occurs with increasing Y content.

4.1.1 Effect of yttrium (Y) as a dopant in barium titanate

Yttrium is a rare earth element that has a cation of intermediate-size [18-20]. Yttrium oxide is an effective additive for improving the insulation resistance of BaTiO₃-based dielectric materials used in manufacturing multilayer ceramic capacitors (MLCC) with Ni electrodes [21-24]. The Y³⁺ dopant leads to enhanced temperature stability of BT dielectric [25] and inhibits grain growth and prevents exaggerated grain growth in PTCR ceramics, when the Y³⁺ species concentration is above a certain threshold level [26]. Y plays a critical role in shifting the Curie temperature of BT. The Y³⁺ concentration changes the lattice parameters [4, 27]. The reduction of sinterability of BT was observed by adding Y because Y₂O₃ has a high melting point (2,425 °C) [28, 29]. The general sintering temperatures were in the range ~ 1250-1300 °C even when some other oxide additives are added [24, 30].

When using a rare-earth element as a dopant, small rare-earth ions tend to occupy the B-site while large rare-earth ions occupy the A-site [18, 31-33]. Rare-earth elements of intermediate size, such as Y³⁺ can occupy both sites with variable partitioning for each site [18, 34]. For a long time it has been believed that Y can only occupy Ba or Ti sites at low concentrations ~ < 3 at.% even with excess BaO or TiO₂ [35, 36]. Randall et al mention that Y is amphoteric and is able to occupy both A and B sites but the higher solid solubility is on the Ba site [37].

Y is reported to dope BaTiO₃ on either A or B sites and therefore act as donor or acceptor [27, 38]. It is reported to act as a donor in the presence of excess TiO₂ because an excess of the host cations (Ti⁴⁺) causes substitution of Y³⁺ for Ba²⁺. Y can act as an acceptor by substituting into the B site when excess BaO is present. In this case, the ionised oxygen vacancy that is created compensates for the reduced charge from Y³⁺ [20, 39]. The substitution process depends on the Ba:Ti ratio and the solubility of dopants [19, 34, 38, 40, 41]. Processing conditions such as sintering

atmosphere and oxygen pressure are believed to influence the substitution mechanisms [20].

For Y^{3+} the coordination number in Y_2O_3 is 7 whereas the coordination number of Y cations in the fluorite structure (such as the case of Y_2O_3 with oxygen vacancies) is equal to 8. Since the coordination preference of Y is more similar to that of Ti than to Ba, Y prefers to occupy the Ti-site when $BaTiO_3$ is sintered at low temperature [28].

In Table 4-1, the ionic radii of Ba, Ti and Y are indicated [35]. The radii of rare-earth elements in 12-coordination were estimated by extrapolation using the relationship between ionic radius and coordination number [18].

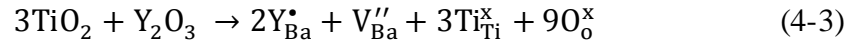
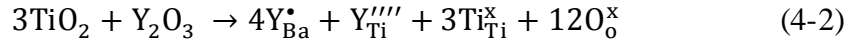
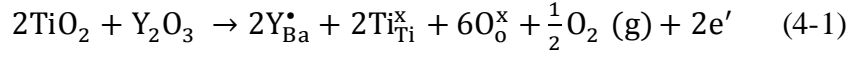
Table 4-1: Effective ionic radii of Ba^{2+} , Ti^{4+} and Y^{3+} [32, 35].

Ion	Ionic radius (Å)	
	6 coordination	12 coordination
Ba^{2+}		1.610
Ti^{4+}	0.605	
Y^{3+}	0.900	1.234

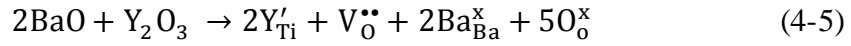
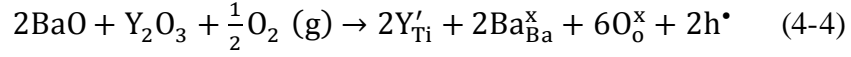
There is an adjustment of cation or oxygen numbers to preserve the charge balance, which is known as an ionic mechanism while with an electronic mechanism, preserving electroneutrality is associated with adding electrons to the crystal lattice or removing electrons from the crystal lattice.

The method of incorporating Y into $BaTiO_3$ is believed to significantly determine its electrical properties [42]. In the case of Y_2O_3 incorporation with different compensation methods [41], Lewis and Catlow [43] have shown that electron compensation for Ba site occupancy is more favourable since the diffusion of Ba occurs slowly. In the case of Ti site occupancy, the compensation of oxygen vacancy is dominant. In some instances, self-compensation might occur since both sites are occupied [39].

The existence of charge imbalance, due to the differences in valence, is compensated via several mechanisms [38]. In the Kröger-Vink notation, and when Ba^{2+} is substituted, three mechanisms might arise, demonstrated by (eq'ns 4-1 – 4-3) [22, 41].

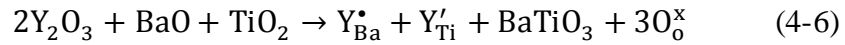


On the other hand, when Ti^{4+} is substituted, the two mechanisms that might occur are as shown in Eq4 and Eq5.



It is also possible that all of these mechanisms (demonstrated by eq'ns 4-1 – 4-5) occur simultaneously. However, depending on conditions such as overall composition, temperature and partial pressure of oxygen, one of the mentioned mechanisms will dominate [38, 44]. The dominance of a certain mechanism will usually determine the electrical properties of the doped material.

Self-compensation does not need any charge compensation mechanism as follows:



The process of substituting Y at the Ba sites (where Y behaves as a donor dopant, equation 4-1, when Y concentration is less than 0.5 at .%) can be used to modify and tailor the PTC effect in the BaTiO_3 semiconductor [41, 45]. The reduction from Ti^{4+} to Ti^{3+} occurs because the positive charge obtained from Ba substitution compensates for the charge difference between Ba^{2+} and Y^{3+} , resulting in the production of n-type semiconducting behaviour. Alternatively, compensation can result from the cation vacancies [34, 39, 43].

The site of incorporation of Y^{3+} dopants into BaTiO_3 and the mechanism of charge compensation has been the subject of many studies, but there remains a lack of agreement regarding the final phase assemblage, dielectric properties and polymorphic phase transition region, especially with contradictory results in the literature. Therefore, further investigations are required to study the effect of various processing conditions to achieve better understanding of the correlation of the phase diagram results, charge compensation mechanisms and electrical properties.

4.2 Experimental Procedure

Yttrium-doped BaTO₃ powder was synthesized using the solid state method with three sample mixing methods: *HM*, *BM* and *PBM* and with compositions located on the acceptor (A), donor (D) and self-compensation (SC) joins. BaCO₃, TiO₂ and Y₂O₃ were used as reactants. Compositions were heated at 1350-1550 °C in air for several days with daily regrinding. Samples were finally heated at various temperatures and for different times and either slow-cooled (SC) or quenched (Q) to room temperature.

The ternary phase diagram of the yttrium-doped BaTO₃ solid solutions limit has been investigated by XRD, and lattice parameters determined.

Electrical properties were studied using LCR meter and IS. This chapter represents results for doping levels ≥ 1 %.

4.3 Results

4.3.1 Crystal structure and phase diagram study of Y-doped BaTiO₃

All feasible doping mechanisms involving electronic and ionic compensation in Y-doped BaTiO₃ are listed in Table 4-2 and their location is marked on the ternary phase diagram, Figure 4-1, which is a ternary section of the quaternary system Ba-Ti-Y-O. The measurements presented here are based on three ideal mechanisms. The results are divided into three types of doping; acceptor, self-compensation and donor doping as doping mechanism (3), (1) and (2), respectively.

Table 4-2: Five plausible categories of mechanisms for Y-doped BaTiO₃.

	Doping mechanism	Structural consequences	Formula	End-member (real or hypothetical)
1	Stoichiometric double doping, $Y_{Ba}^{\bullet} + Y_{Ti}'$	Retain ABO ₃ stoichiometry	$Ba_{1-y}Ti_{1-y}Y_{2y}O_3$	Y ₂ O ₃
2	Donor doping, electronic compensation with Ti^{3+}	Retain ABO ₃ stoichiometry	$Ba_{1-v}Y_vTiO_3$	YTiO ₃
3	Acceptor, Y_{Ti}'	Oxygen vacancies, $V_O^{\bullet\bullet}$	$BaTi_{1-x}Y_xO_{3-x/2}$	BaYO _{2.5}
4,5	Donor doping, Y_{Ba}^{\bullet}	Cation vacancies (V_{Ti}'''' or V_{Ba}'')	$Ba_{1-z}Y_zTi_{1-z/4}O_3$ or $Ba_{1-3\omega}Y_{2\omega}TiO_3$	YTi _{3/4} O ₃ or Y _{2/3} TiO ₃

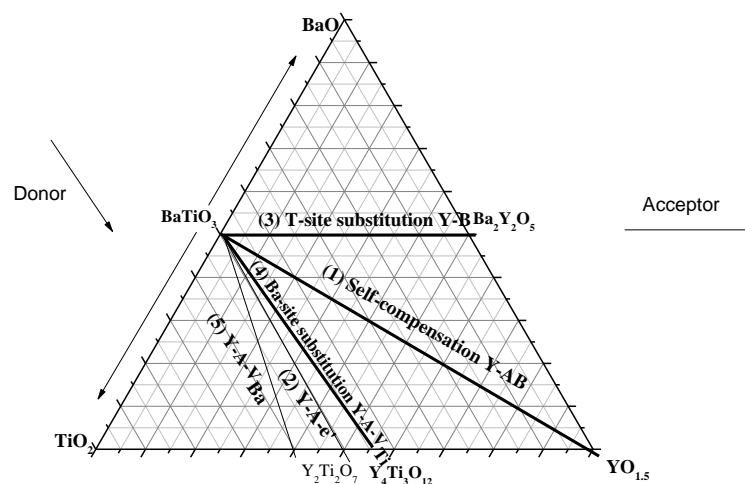


Figure 4-1: Schematic ternary phase diagram showing possible compensation mechanisms for Y-doped BaTiO₃.

1. Self-compensation mechanism, $Ba_{1-y}Ti_{1-y}Y_{2y}O_3$

Self-compensation occurs when trivalent dopants substitute on both Ba^{2+} and Ti^{4+} sites in the same amounts (Y-AB). It prevails when $Ba/Ti=1$. No other charge compensation mechanism is required even with existence of a difference in the valence between Y^{3+} and both Ba^{2+} and Ti^{4+} . Their effective charge will not affect the electroneutrality condition and the material remains stoichiometric as ABO_3 .

XRD results are shown for $y = 0.01, 0.025, 0.05, 0.075, 0.10, 0.125, 0.15, 0.20$ and 0.25 in Figure 4-2, no phases other than tetragonal and cubic BT were detected for $y \leq 0.075$. The diffraction patterns for $y < 0.05$ were fully indexed on the $P4mm$ space group and were consistent with the tetragonal polymorph of BT. Peaks for $y = 0.01$, and 0.025 showed splitting. At $y = 0.05$ a transformation from tetragonal to (pseudo) cubic symmetry was observed and the peak splitting disappeared. $0.05 \leq y \leq 0.075$ were single phase and cubic with space group $Pm\bar{3}m$. For $y > 0.075$, a second phase was observed. $Y_2Ti_2O_7$ was identified at $y = 0.10$. Another phase $Ba_3Ti_2YO_{8.5}$ was observed at higher y .

From the measured XRD patterns, the calculated lattice parameters and c/a ratios as a function of y are shown in Figure 4-3 (a). The (c/a) ratio decreases and the unit cell volume increases with y , Figure 4-3 (b, c).

By comparing the various results, it is concluded that the solid solution limit on the (SC) join is at $y = 0.075$.

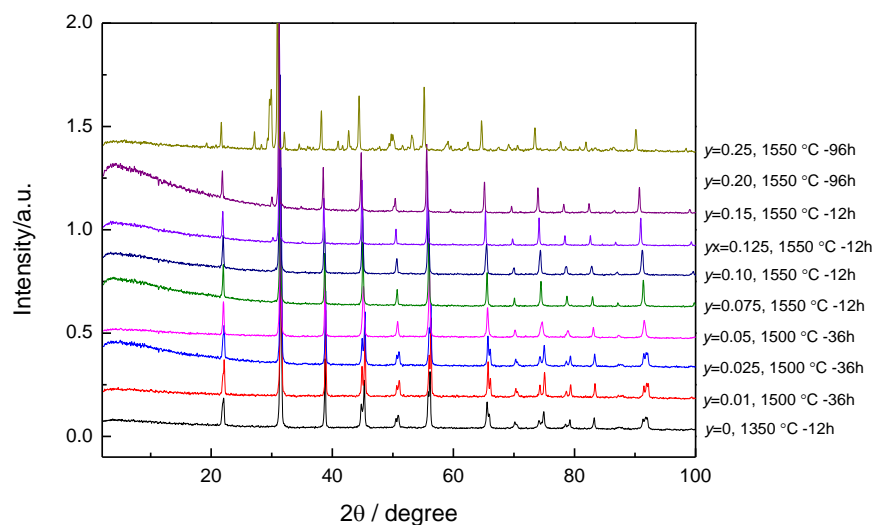


Figure 4-2: X-ray diffraction patterns for compositions $Ba_{1-y}Ti_{1-y}Y_{2y}O_3$ sintered at different temperatures in air.

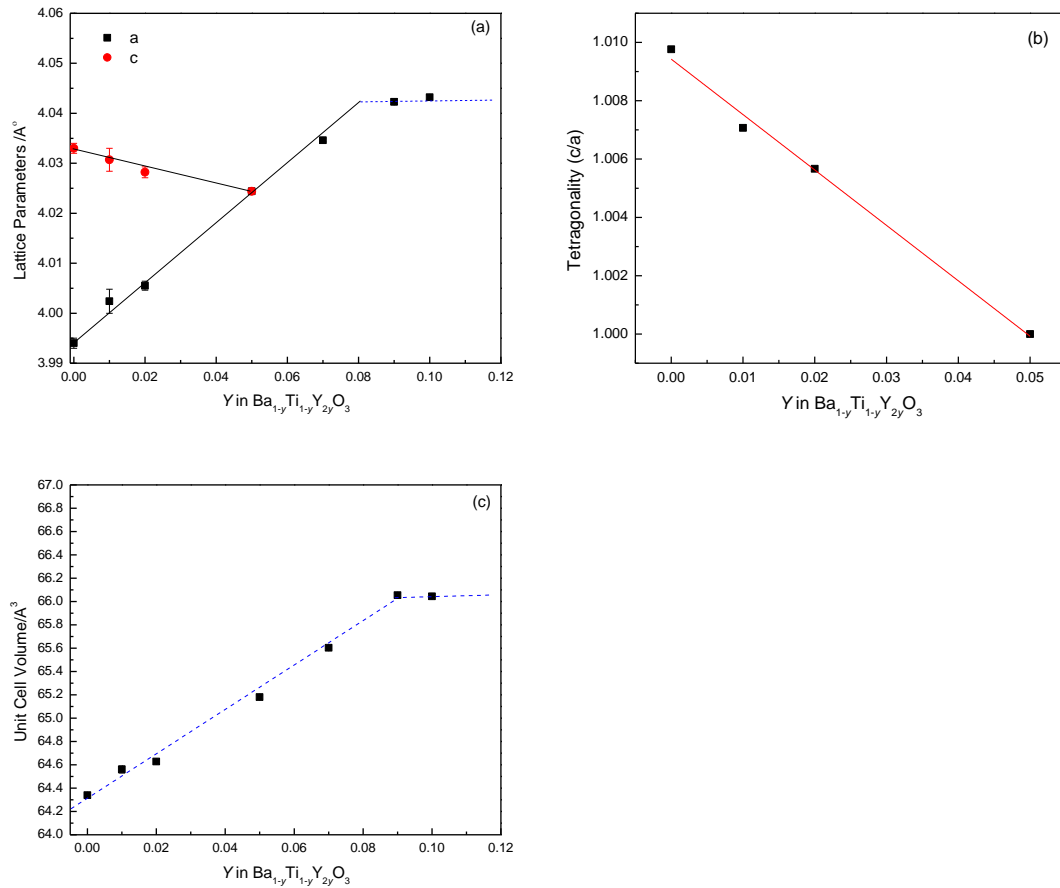


Figure 4-3: Variation of (a) lattice parameters, (b) tetragonality and (c) unit cell volume as a function of y.

2. Donor doping mechanism, Ba_{1-ν}TiY_νO₃

In this mechanism, Y ions occupy the Ba site (Y-A) together with electronic compensation. Y³⁺ behaves as a donor when Ba/Ti < 1.

XRD data for $\nu = 0.01, 0.015, 0.02$ and 0.10 are shown in Figure 4-4. No secondary phase was found over the range $0 < \nu < 0.015$. Formation of secondary phases of (Ba₆Ti₁₇O₄₀) and (Y₂Ti₂O₇) was observed at higher ν . It therefore appears that the solid solution limit on the (D) join is at $\nu = 0.015$.

The lattice parameters, the tetragonality and unit cell volume are plotted as a function of Y content in Figure 4-5. Both *a*-axis and *c*-axis increase with increasing Y, and the tetragonality slightly increases from 1.00976 to 1.01103. Figure 4-5 (c) illustrates that the unit cell volume increased with increasing Y content (ν).

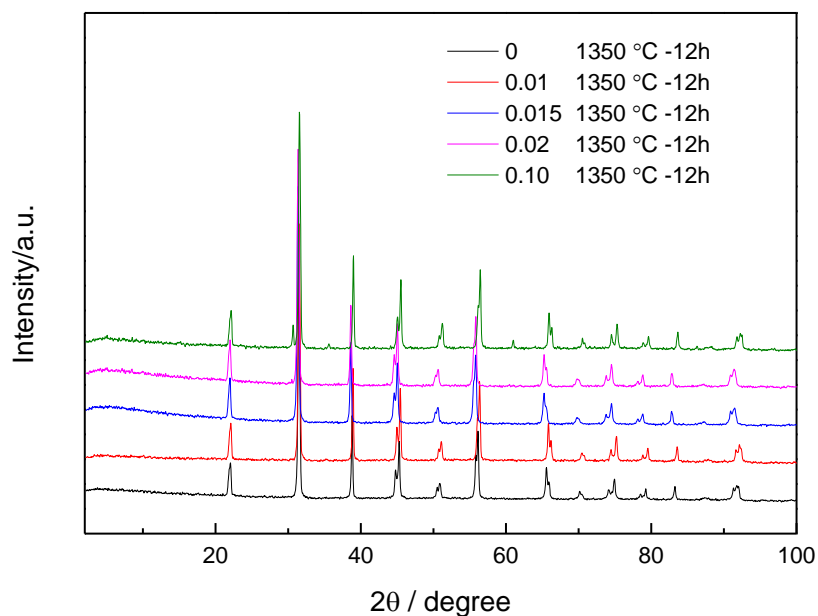


Figure 4-4: X-ray diffraction patterns for compositions $\text{Ba}_{1-y}\text{TiY}_y\text{O}_3$ sintered in air.

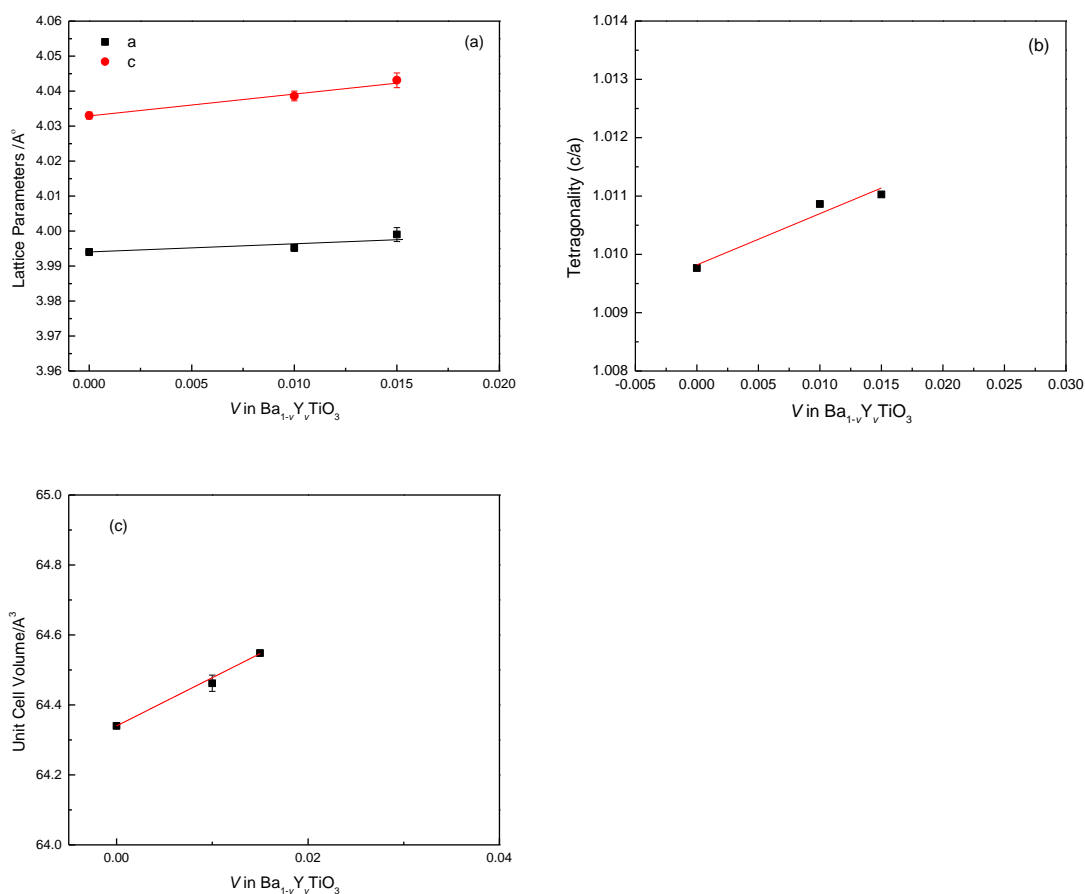


Figure 4-5: Variation of (a) lattice parameters, (b) tetragonality and (c) unit cell volume as a function of nominal yttrium content (ν) in $\text{Ba}_{1-\nu}\text{Y}_\nu\text{TiO}_3$ samples.

3. Acceptor doping mechanism, $\text{BaTi}_{1-x}\text{Y}_x\text{O}_{3-x/2}$

In this mechanism, the acceptor doping is compensated by oxygen vacancies as a result of Y ions occupying the Ti site (Y-B). Y^{3+} behaves as an acceptor when $\text{Ba/Ti} > 1$.

The aims of the present section have been to resolve the discrepancies between different reported results since different solid solution limits and phases are reported. The transition between cubic and hexagonal polymorphs was investigated by studying samples in isothermal steps on both heating and cooling cycles followed by slow cooling to room temperature. Initial experiments were performed to establish essential conditions to produce complete chemical reaction and an equilibrium state. The behaviour was studied by two ways in which samples were in contact with platinum or placed on sacrificial powder.

The main XRD results for pellets in contact with platinum are listed and summarized in Table 4-3.

Table 4-3: Summary of the main X-ray results for compositions $\text{BaTi}_{1-x}\text{Y}_x\text{O}_{3-x/2}$, where $x = 0.02$ (BTY02), 0.05 (BTY05) and 0.10 (BTY10) prepared for the pellet in contact with platinum.

Composition	Temperature	Time	XRD results
BTY02	1250	12 hours	Tetragonal/cubic
	1300	1 day	Tetragonal/cubic
	1400	1 day	Tetragonal/cubic
	1500	1 day	Mixture T/C+H
	1525	2 hours	Mixture T/C+H
	1550	2 hours	Mixture T/C+H
	1525→1400 (reversible)	1 day	Tetragonal/cubic
BTY05	1400	5 days	Tetragonal/cubic
	1500	1 day	Tetragonal/cubic
	1525	2 hours	Mixture T/C+H
	1550	2 hours	Mixture T/C+H
BTY10	1300	2.5 days	Tetragonal/cubic
	1500	1 day	Hexagonal
	1300→1550	2 hours	Tetragonal/cubic
	1550→1300 (reversible)	2.5 day	Tetragonal/cubic

Results for samples heated at 1450–1550 °C in contact with platinum, showed that equilibrium usually was reached only very slowly and with difficulties. Initial XRD results are shown for $x = 0.02$, 0.05 and 0.10 in Figure 4-6. It can be seen that the

temperature of the cubic-hexagonal transition appears to increase with Y content. For $x = 0.10$, transformation from hexagonal to the cubic polymorph was obtained from 1500 to 1400 °C with heating times of 2.5 days. Full reversibility was obtained for $x = 0.02$, which transformed from tetragonal to a mixture of phases at 1500 °C and then converted back to tetragonal at 1400 °C.

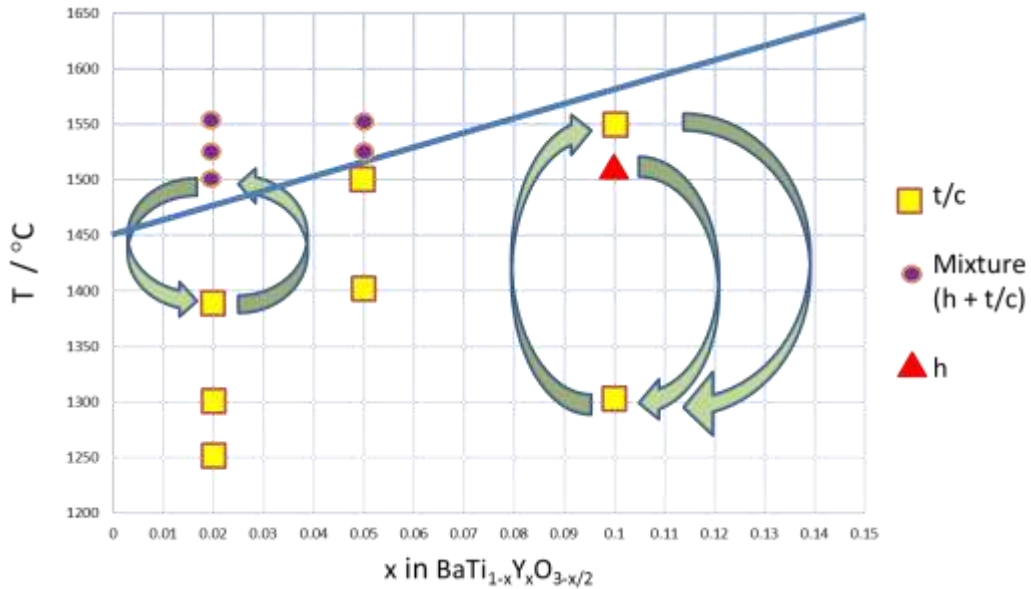


Figure 4-6: XRD diagram of $BaTi_{1-x}Y_xO_{3-x/2}$, measured at room temperature for samples sintered at different temperatures for pellets in contact with platinum for *HM* samples. t/c= tetragonal/cubic and h= hexagonal.

The representative XRD results for pellets placed on sacrificial powder in platinum containers $x = 0.02, 0.03, 0.05, 0.07, 0.09, 0.10, 0.12$ and 0.15 are summarized in Table 4-4.

The polymorphic changes obtained at different compositions were found to be not fully reversible on heat/cool cycles and therefore appear not to represent thermodynamic equilibrium.

Table 4-4: Summary of significant X-ray results for pellets placed on sacrificial powder on Pt foil.

Composition	Temperature	Time	XRD results
BTY(0.0001)	1350	12 hours	Tetragonal
BTY(0.0003)	1350(q)	12 hours	Tetragonal
BTY(0.0005)	1350(q)	12 hours	Tetragonal

BTY(0.001)	1350	12 hours	Tetragonal
BTY(0.01)	1450	24 hours	Tetragonal
BTY02	1200(q)	24 hours	Tetragonal/cubic
	1250(q)	24 hours	Tetragonal/cubic
	1300	24 hours	Tetragonal/cubic
	1350(q)	24 hours	Tetragonal/cubic
	1400	2 days	Tetragonal/cubic
	1400(q)	12 hours	Tetragonal/cubic
	1400(q)	24 hours	Tetragonal/cubic
	1450	12 hours	Tetragonal/cubic
	1450(q)	24 hours	Tetragonal/cubic
	1500	12 hours	Mixture T/C+H
	1525	12 hours	Mixture T/C+H
	1550	12 hours	Mixture T/C+H
	1550	88 hours	Mixture T/C+H
	1550	100 hours	Mixture T/C+H
BTY03 (<i>PBM</i>)	1400(q)	15 hours	Tetragonal/cubic
BTY05	1200(q)	24 hours	Mixture T/C+H
	1250(q)	24 hours	Mixture T/C+H
	1250(q)	100 hours	Tetragonal/cubic
	1300	24 hours	Mixture T/C+H
	1350	12 hours	Mixture T/C+H
	1350(q)	24 hours	Mixture T/C+H
	1350(q)	24 hours	Tetragonal/cubic
	1400	4 days	Mixture T/C+H
	1400	12 hours	Mixture T/C+H
	1400(q)	24 hours	Mixture T/C+H
	1400(q)	24 hours	Tetragonal/cubic
	1450	12 hours	Mixture T/C+H
	1450	24 hours	Mixture T/C+H
	1450	1 hour	Mixture T/C+H
	1450(q)	24 hours	Mixture T/C+H
	1450(q)	24 hours	Tetragonal/cubic
	1500	12 hours	Hexagonal
	1500	12 hours	Mixture T/C+H
	1500(q)	24 hours	Mixture T/C+H
	1525	12 hours	Mixture T/C+H
1550	12 hours	Tetragonal/cubic	
1550	100 hours	Mixture T/C+H	
BTY05+2%TiO ₂	1500	12 hours	Pseudo cubic
BTY05+2%SiO ₂	1500	24 hours	Tetragonal
BTY05+2%SiO ₂	1500	2.5 days	Tetragonal
BTY07 (<i>PBM</i>)	1400(q)	15 hours	Tetragonal/cubic
BTY09 (<i>BM</i>)	1350(q)	12 hours	Mixture T/C+H
	1515	12 hours	Mixture T/C+H
	1550	12 hours	Mixture T/C+H
	1550	43 hours	Mixture T/C+H
	1550	100h	Cubic
	1200(q)	24 hours	Mixture T/C+H
	1250(q)	24 hours	Mixture T/C+H
	1250(q)	100 hours	Mixture T/C+H
	1300	24 hours	Mixture T/C+H

BTY10	1350	12 hours	Mixture T/C+H
	1350(q)	24 hours	Mixture T/C+H
	1400	12 hours	Mixture T/C+H
	1400(q)	24 hours	Mixture T/C+H
	1450	1 hour	Mixture T/C+H
	1450	12 hours	Mixture T/C+H
	1450	24 hours	Mixture T/C+H
	1450(q)	24 hours	Mixture T/C+H
	1500	12 hours	Mixture T/C+H
	1500	1 day	Hexagonal
	1500(q)	24 hours	Mixture T/C+H
	1525	12 hours	Mixture T/C+H
	1550	12 hours	Mixture T/C+H
	1550	88 hours	Mixture T/C+H
	1550	100 hours	Mixture T/C+H
BTY10 + 2%TiO ₂ (BM)	1500	12 hours	Cubic
BTY10 + 2%BaCO ₃ (BM)	1500	12 hours	Hexagonal
BTY12	1350	12 hours	Mixture T/C+H
	1400	12 hours	Mixture T/C+H
	1400	48 hours	Mixture T/C+H
	1450	12 hours	Mixture T/C+H
	1450	24 hours	Mixture T/C+H
	1500	12 hours	Hexagonal
	1525	12 hours	Mixture T/C+H
	1550	12 hours	Mixture T/C+H
	1550	88 hours	Mixture T/C+H
BTY15	1350	12 hours	Mixture H+BT _{2/3} Y _{1/3}
	1400	12 hours	Mixture H+BT _{2/3} Y _{1/3}
	1400	48 hours	Mixture T/C+H
	1450	12 hours	Mixture H+BT _{2/3} Y _{1/3}
	1450	24 hours	Hexagonal
	1500	12 hours	Mixture H+BT _{2/3} Y _{1/3}
	1525	12 hours	Mixture T/C+H
	1550	12 hours	Mixture T/C+H
	1550	88 hours	Mixture T/C+H

$\text{BT}_{2/3}\text{Y}_{1/3} = \text{BaTi}_{2/3}\text{Y}_{1/3}\text{O}_{2.833}$ (Hexagonal phase)

The cubic to hexagonal phase transition region was considered by exposing the samples to heat treatments in the range 1400–1550 °C followed by different cooling rates: SC at 10 °C/min or Q. The transition was sluggish either with SC or Q. This indicates that the cooling rate after heat treatment and its effect on the phase purity is not essential. Figure 4-7 shows the XRD diagram for the pellet placed on sacrificial powder on Pt foil. The temperature of the cubic-hexagonal transition is not observed clearly with changing Y content. A two-phase, cubic+ hexagonal region opens up with increasing Y content. The hexagonal phase is observed initially at $x=0.05$ but it is destabilized and the transition from cubic to hexagonal region occurs with increasing temperatures at increasing Y content.

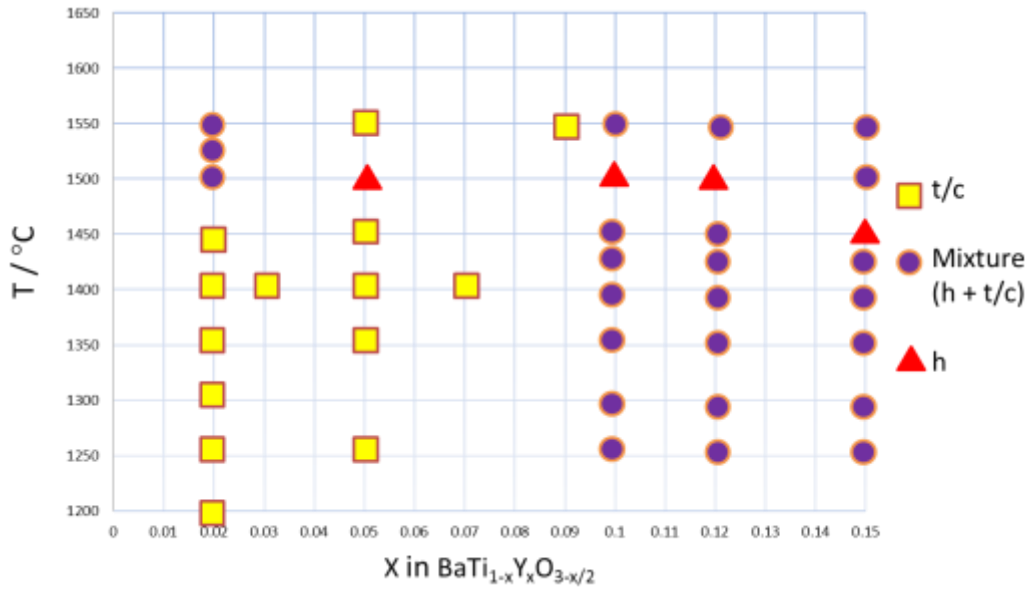


Figure 4-7: XRD diagram of $\text{BaTi}_{1-x}\text{Y}_x\text{O}_{3-x/2}$, measured at room temperature for samples sintered at different temperatures for the pellet placed on sacrificial powder on platinum foil.

Figure 4-8 shows the XRD patterns for samples sintered at different temperatures in air. The cubic region covered the composition range $0.05 \leq x \leq 0.10$. The region for $x < 0.05$ gave the tetragonal phase. The hexagonal polymorph was observed at $0.05 \leq x \leq 0.15$. At $x > 0.15$, a small amount of secondary phase $\text{Ba}_3\text{Tl}_2\text{YO}_{8.5}$ was observed. This confirms that solubility of Y on the Ti-site is ~ 15 mol %.

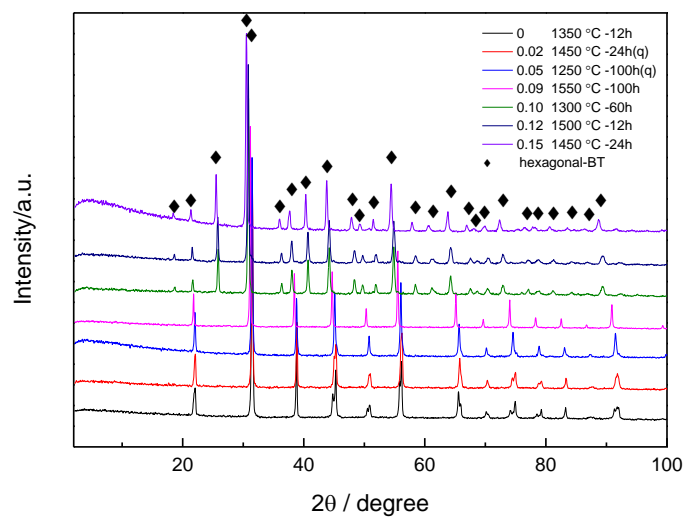


Figure 4-8: X-ray diffraction patterns at different temperatures in air.

Polymorphism and phase transition temperature of Y-Doped BaTiO₃ on Ti site

It is notable that at high Y concentrations, the hexagonal phase of BT was the first product of reaction. There were difficulties to obtain a pure phase, which needed long periods of time to convert the sample to cubic phase. The formation of metastable phases occurred probably at the initial stage of reaction. Prolonged heating was needed to obtain the complete transformation. Most compositions gave a mixture of phases: mainly tetragonal-cubic mixed with hexagonal phase. Determination of the thermodynamic status of the hexagonal/cubic polymorphs was difficult.

Figure 4-9 shows the XRD pattern of $x = 0.10$; the hexagonal polymorph of BaTiO₃ was obtained at 1300 °C after 60 hours and transformed to cubic polymorph after 120 hours.

Figure 4-10 shows a new hexagonal phase with space group P6₃/mmc which was observed at BaTi_{0.666}Y_{0.334}O_{2.833}. The unit cell parameters at room temperature are $a = 5.9292(7)$ Å and $c = 29.531(3)$ Å in good agreement with the literature [46, 47]. It is supposed that the following chemical reaction occurred [48]:

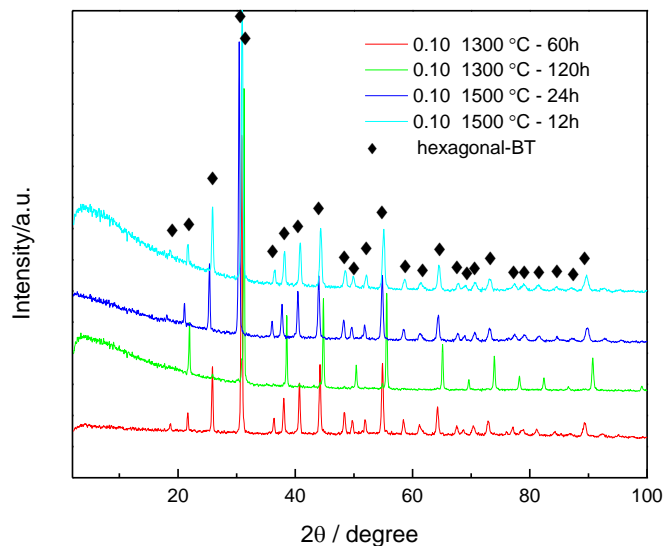


Figure 4-9: X-ray diffraction patterns for the composition BaTi_{0.90}Y_{0.10}O_{2.95} sintered at 1300 and 1500 °C for 12-120h in air.

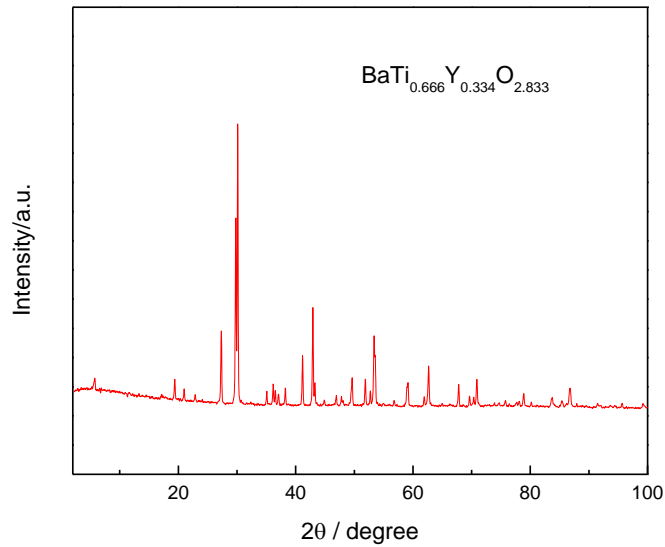
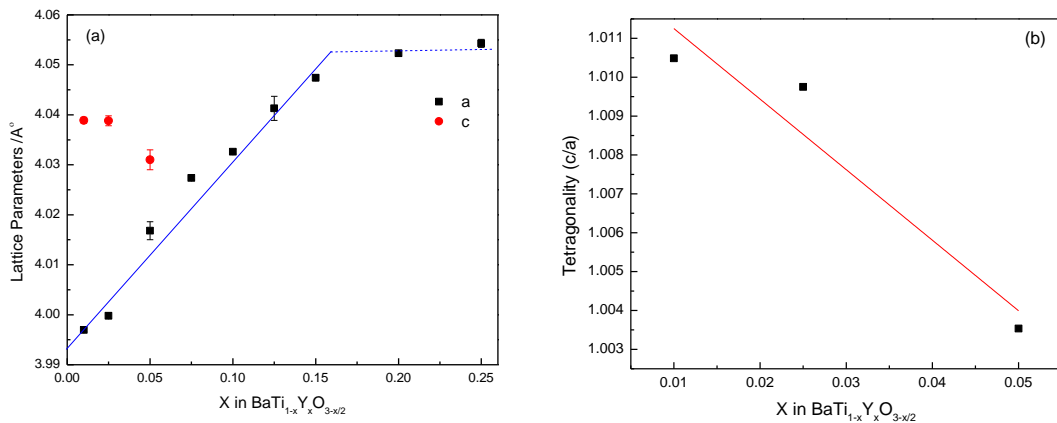


Figure 4-10: X-ray diffraction patterns for the composition $\text{BaTi}_{0.666}\text{Y}_{0.334}\text{O}_{2.833}$ sintered at $1500\text{ }^\circ\text{C}$ for 12h in air.

The values of the a and c parameters and unit cell volume as a function of x are presented in Figure 4-11, (a). (a) increases almost linearly with increasing (x). The changes in (a) as a function of the Y concentration were greater than the changes in (c). The tetragonal polymorph progressively transforms to cubic at $\sim x = 0.05$. Figure 4-11, (b) shows the tetragonality (the ratio of c/a) of a tetragonal phase in decreased with increasing Y^{3+} dopant. The unit cell volume increased almost linearly with x , Figure 4-11, (c) suggesting that the Y^{3+} ions substituted for Ti^{4+} ions in the barium titanate lattice because Ti^{4+} is smaller than the ionic size of Y^{3+} [38, 49, 50]. In conclusion, the solid solution limit in the A join is at $x = 0.15(2)$.



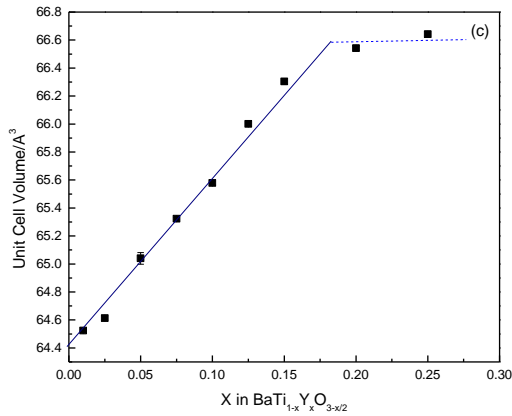


Figure 4-11: Variation of (a) lattice parameters, (b) tetragonality and (c) unit cell volume as a function of x .

Influence of excess titania, silica or barium carbonate

SiO₂ and TiO₂ excess (1–2 mol%) are well-known additives to enhance densification during sintering, as a result of liquid phase formation and lowering of the sintering temperature [9, 51, 52]. It is also expected that a liquid phase may form for samples in contact with Pt. 2% TiO₂ was added to the composition, BaTi_{0.95}Y_{0.05}O_{2.975} + 2% TiO₂, to obtain a liquid phase at high temperature. A pseudo-cubic phase was obtained at 1500 °C for 12 hours, Figure 4-12. However, an excess of TiO₂ changes the compensation mechanism from an oxygen vacancy mechanism (BaTi_{1-x}Y_xO_{3-x/2}) to a self-compensation mechanism (Ba_{1-x}Ti_{1-x}Y_{2x}O₃).

An alternative method to create a liquid phase is by addition of SiO₂. In papers [36, 41, 53] an agate jar was used which may have caused contamination from balls and media. Therefore, 2% SiO₂ was added to give the formula BaTi_{0.95}Y_{0.05}O_{2.975} + 2% SiO₂, and fired at 1500 °C for 60 hours. A pure tetragonal phase was obtained with no secondary phases, Figure 4-12.

2% TiO₂ was added to give BaTi_{0.90}Y_{0.10}O_{2.95} + 2% TiO₂ and 2% BaCO₃ to give BaTi_{0.90}Y_{0.10}O_{2.95} + 2% BaCO₃. Both samples were fired at 1500 °C for 12 hours. A pure cubic phase and hexagonal phase, respectively were obtained with no secondary phases, Figure 4-13.

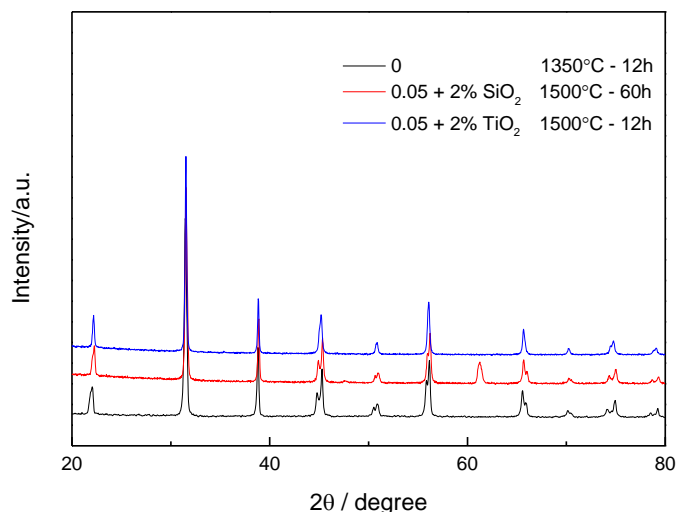


Figure 4-12: X-ray diffraction patterns for the mechanism $\text{BaTi}_{0.95}\text{Y}_{0.05}\text{O}_{2.975} + 2\%$ TiO_2 and $\text{BaTi}_{0.95}\text{Y}_{0.05}\text{O}_{2.975} + 2\%$ SiO_2 sintered at $1500\text{ }^\circ\text{C}$ in air.

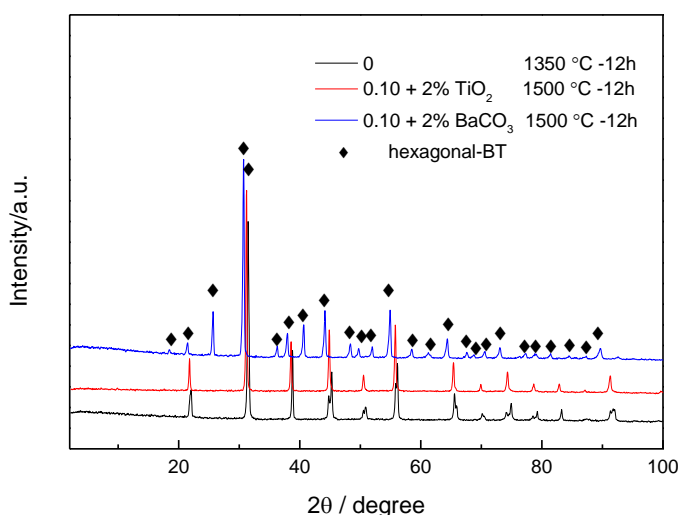


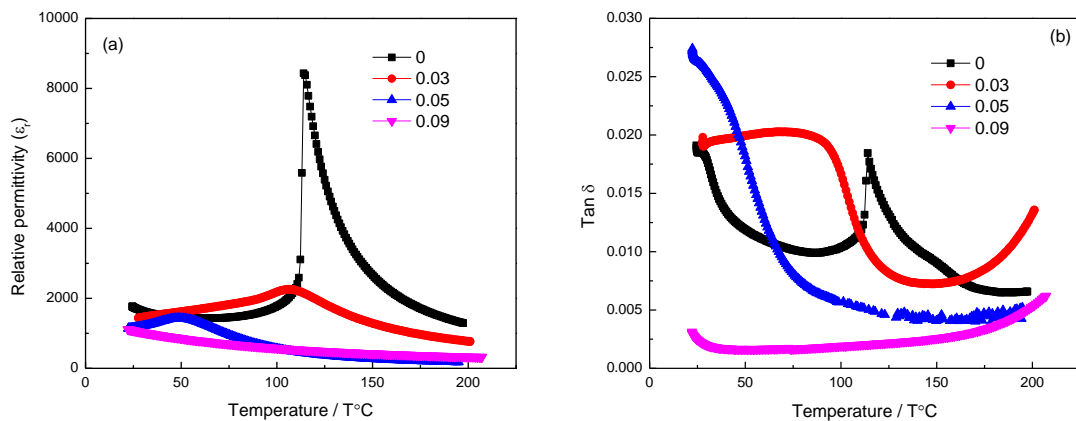
Figure 4-13: X-ray diffraction patterns for the mechanism $\text{BaTi}_{0.90}\text{Y}_{0.10}\text{O}_{2.95} + 2\%$ TiO_2 and $\text{BaTi}_{0.90}\text{Y}_{0.10}\text{O}_{2.95} + 2\%$ BaCO_3 sintered at $1500\text{ }^\circ\text{C}$ for 12h in air.

4.3.2 Electrical and structural characteristics

4.3.2.1 LCR results

The temperature dependence of ϵ' for pellets of Y-B, Y-AB and Y-A measured at 250 kHz are shown in Figures 4-14 (a), 4-15 (a) and 4-16 (a). All samples showed non-leaky dielectric behaviour. The permittivity showed a sharp peak at T_C for all (Y-A) samples and for low dopant concentrations at $x, y < 0.03$ for (Y-B) and (Y-AB) samples. The permittivity maximum for $x = 0.03$ was ~ 2400 for (Y-B) and 8600 for $y = 0.025$ for (Y-AB), and decreased substantially with increasing x, y either with (Y-B) or (Y-AB) whereas, a slight increase was observed for (Y-A). Figures 4-14

(b), 4-15 (b) show generally a decrease in the dielectric loss with increasing x , y whereas, Figure 4-16 (b) shows a slight increase with increasing v . Permittivity data are plotted in Curie-Weiss form in Figures 4-14 (c), 4-15 (c) and 4-16 (c). C_w values are listed in Tables 4-5, 4-6 and 4-7. All samples in the range $0 \leq x \leq 0.03$, illustrated Curie-Weiss behaviour with small deviations at high concentrations. The result of fitting a set of data shows that the gradient exhibits the dependence on the Y-dopant concentration. High dopant concentrations show that the maximum permittivity has a broad peak that shifts towards lower temperature with increasing x . Perhaps it is the result of the coalescence of the individual phase transitions. At temperatures close to T_C , the data showed significant deviation from Curie-Weiss behaviour which show a deviation from the Curie-Weiss law below ~ 113 and 105 °C for $x = 0.03$ and 0.05 for (Y-B), Figure 4-14 (c) and ~ 129.7 and 100.3 °C for $y = 0.05$ and 0.075 for (Y-AB), Figure 4-15 (c). For $x = (0.03, 0.05)$ for (Y-B) and $y = (0.05)$ for (Y-AB), typical characteristics of relaxor ferroelectric behaviour were observed with a permittivity maximum that is strongly dependent on frequency, Figures 4-17 (a), (c) and (e). $\tan \delta$ data were also shown in (b), (d) and (f). Figures 4-18 (a), (b) and (c) show the frequency dependence of the relative permittivity over a wide frequency range. The temperature maximum values of the permittivity for (Y-B), (Y-AB) and (Y-A) were equal for all frequencies. The permittivity maximum values were frequency-independent for (Y-B) and (Y-A), whereas, (Y-AB) composition was dependent on the frequency. Increasing frequency lead to decreasing permittivity maximum values but the temperature of the maximum permittivity was frequency-independent, which is different from the result obtained with ferroelectric relaxors where both the permittivity and its maximum temperature are frequency-dependent.



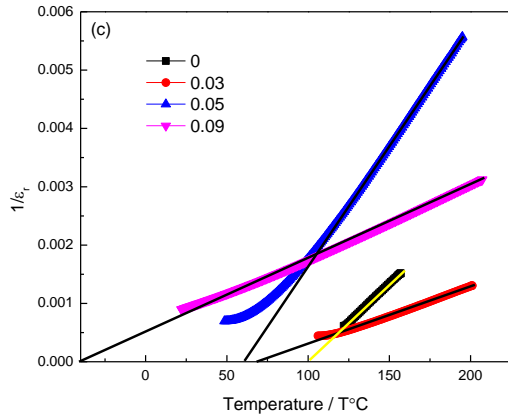


Figure 4-14: Fixed frequency measurements at 250 kHz of (a) relative permittivity, (b) dielectric loss ($\tan \delta$) versus temperature and (c) Curie-Weiss plots for $\text{BaTi}_{1-x}\text{Y}_x\text{O}_{3-x/2}$ samples.

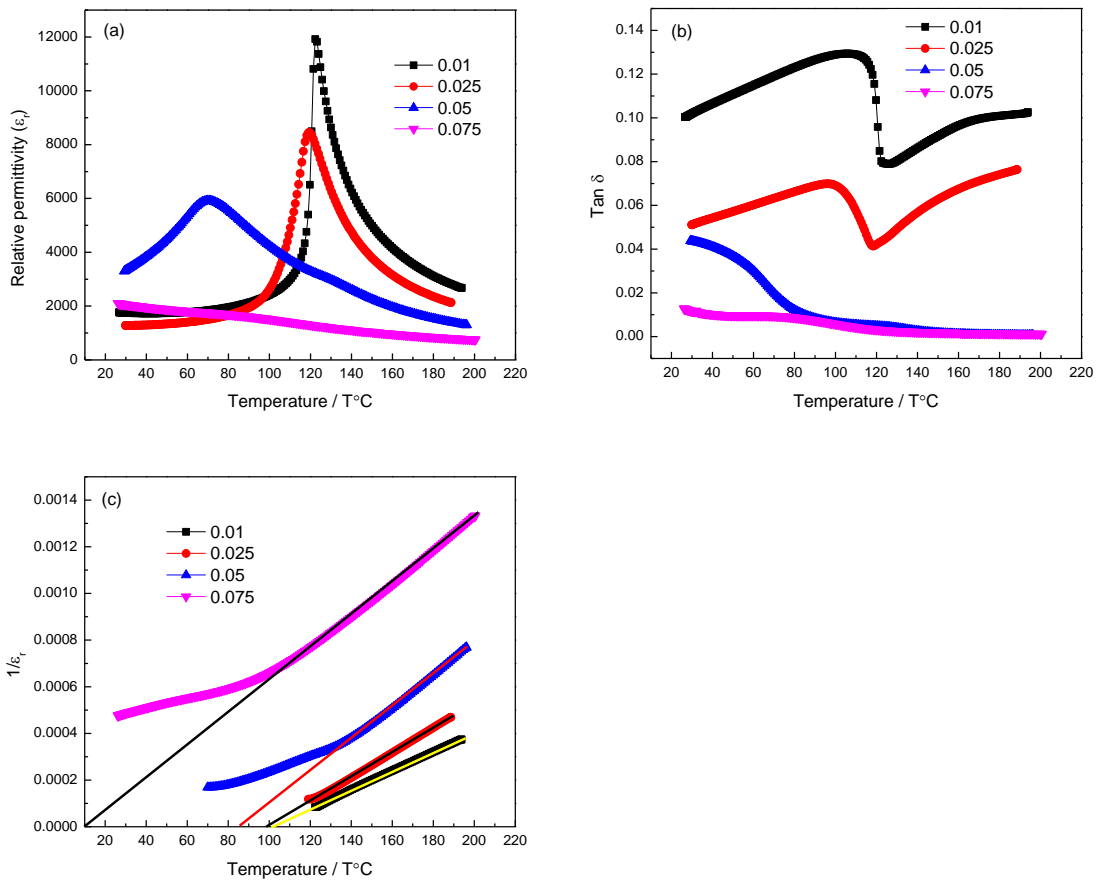


Figure 4-15: Fixed frequency measurements at 250 kHz of (a) relative permittivity, (b) dielectric loss ($\tan \delta$) versus temperature and (c) Curie-Weiss plots for $\text{Ba}_{1-y}\text{Ti}_y\text{O}_3$ samples.

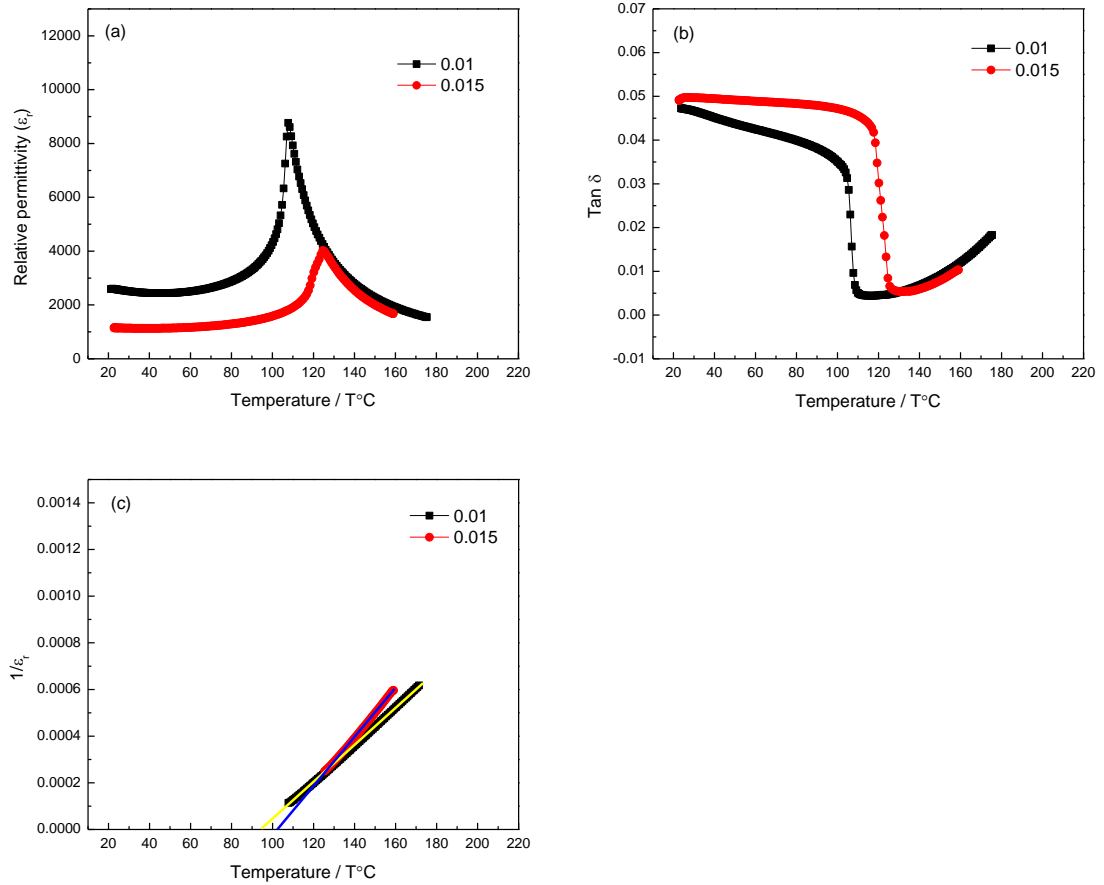


Figure 4-16: Fixed frequency measurements at 250 kHz of (a) relative permittivity, (b) dielectric loss ($\tan \delta$) versus temperature and (c) Curie-Weiss plots for $\text{Ba}_{1-x}\text{Y}_x\text{TiO}_3$ samples.

Table 4-5: Values of T_C , T_o , $T_C - T_o$ and C_w for (Y-B) compositions.

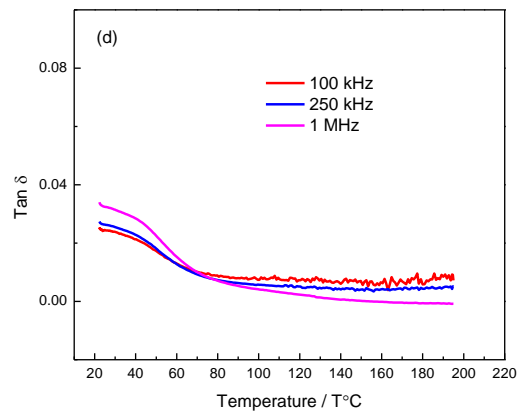
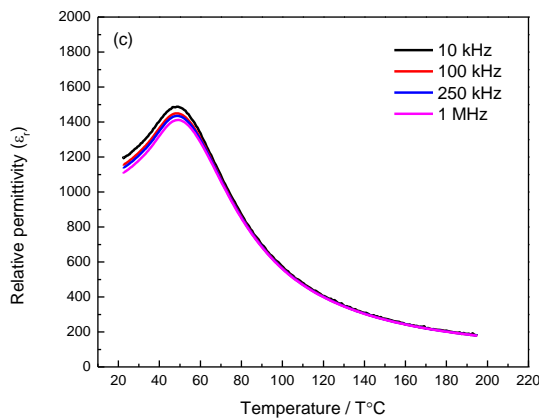
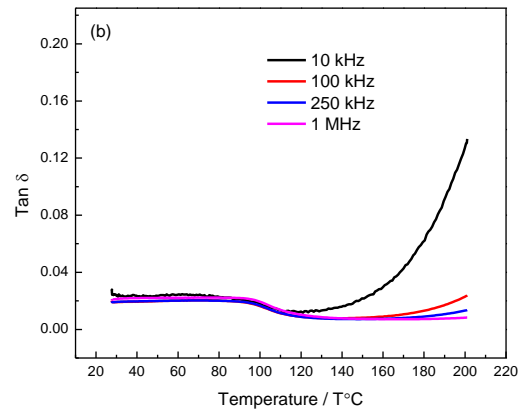
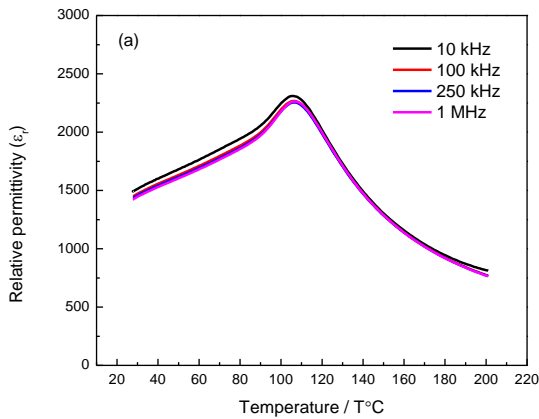
Sample	T_C ($^{\circ}\text{C}$)	T_o ($^{\circ}\text{C}$)	$T_C - T_o$ ($^{\circ}\text{C}$)	C_w (10^5 K)
0	114(1)	102(3)	12(4)	1.240
0.03	106.1	68.8	37.3	1.039
0.05	48.5	61.0	-12.5	0.253
0.09	-	-39.9	-	0.828

Table 4-6: Values of T_C , T_o , $T_C - T_o$ and C_w for (Y-AB) compositions.

Sample	T_C ($^{\circ}\text{C}$)	T_o ($^{\circ}\text{C}$)	$T_C - T_o$ ($^{\circ}\text{C}$)	C_w (10^5 K)
0.01	122.3	101.9	20.4	2.452
0.25	119.1	99.5	19.6	1.902
0.05	69.9	85.6	-15.7	1.454
0.075	-	9.6	-	1.457

Table 4-7: Values of T_C , T_o , $T_C - T_o$ and C_w for (Y-A) compositions.

Sample	T_C ($^{\circ}\text{C}$)	T_o ($^{\circ}\text{C}$)	$T_C - T_o$ ($^{\circ}\text{C}$)	C_w (10^5 K)
0	114(1)	102(3)	12(4)	1.240
0.01	106.3	94.6	11.7	1.248
0.015	124.8	102.75	22.05	0.949



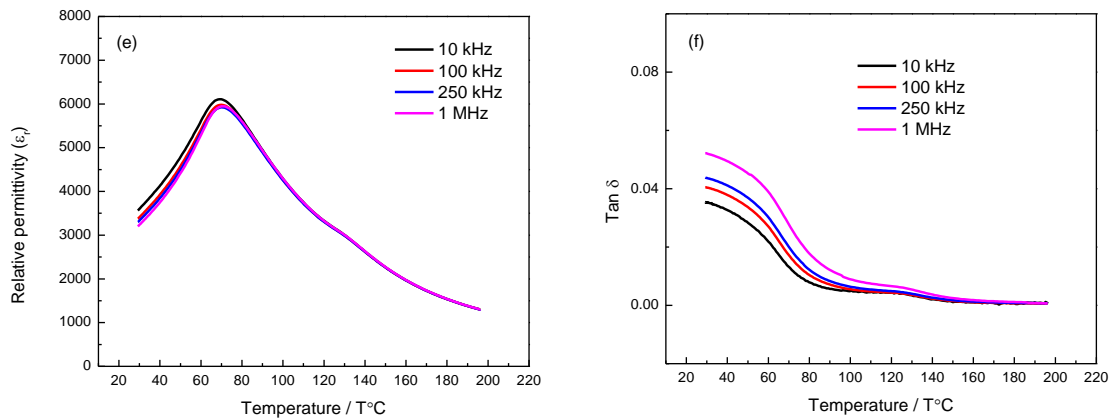


Figure 4-17: Temperature and frequency dependence of permittivity and $\tan \delta$ in composition (a,b) $x = 0.03$ for (Y-B), (c,d) $x = 0.05$ for (Y-B) and (e,f) $y = 0.05$ for (Y-AB).

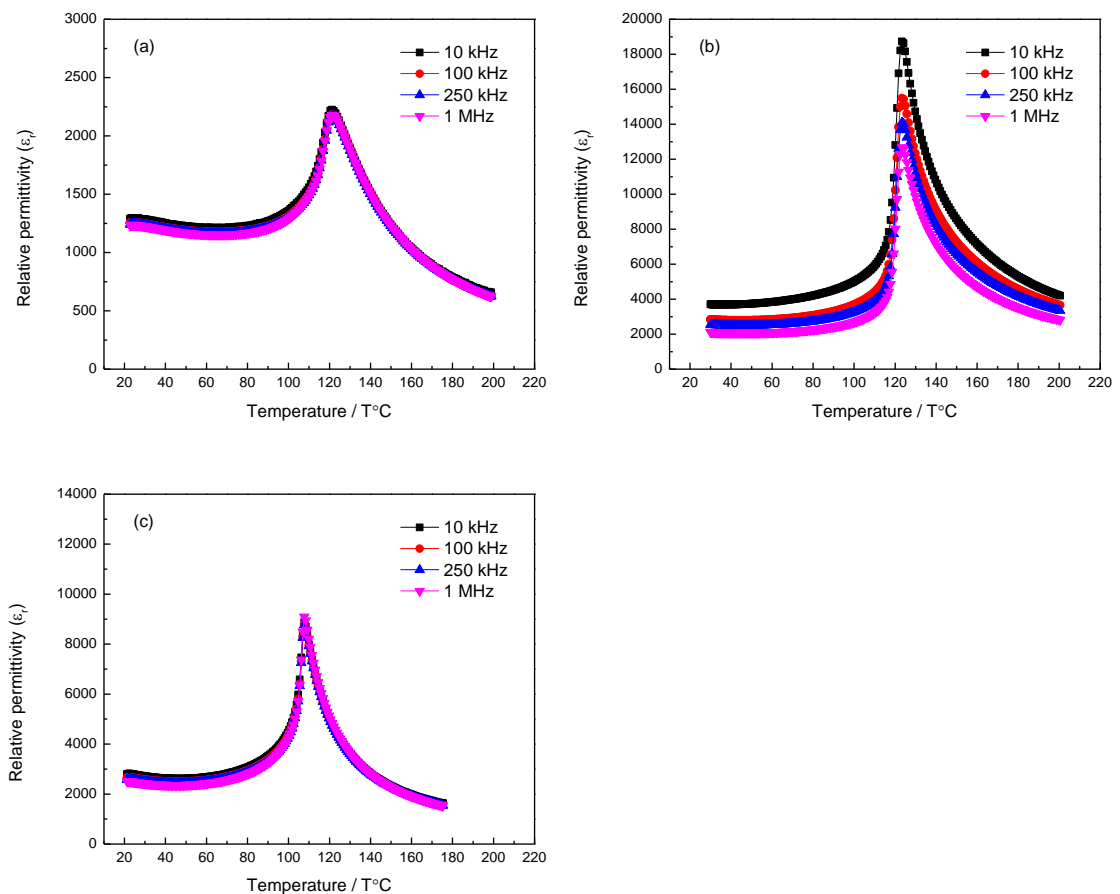
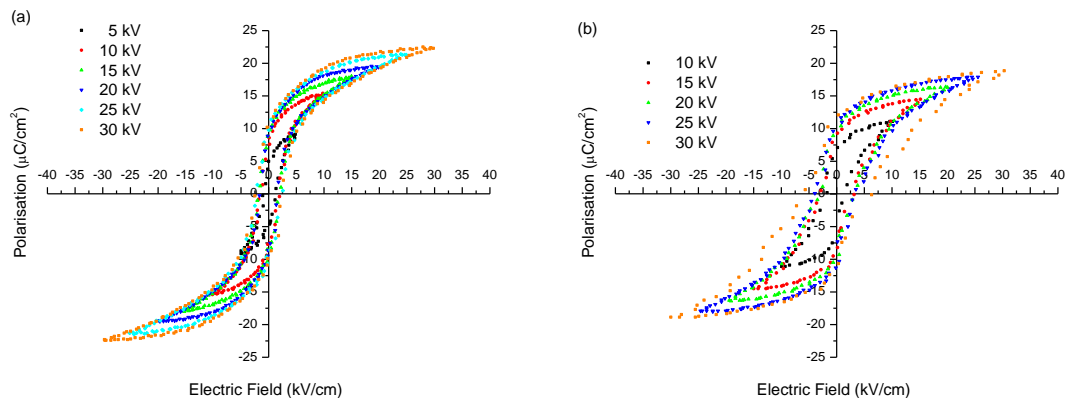


Figure 4-18: Temperature and frequency dependence of permittivity for x, y and $\nu = 0.01$ in composition of (a) (Y-B), (b) (Y-AB) and (c) (Y-A).

4.3.2.2 Hysteresis Loop Results

Generally, hysteresis loop shapes depict the quality and nature of specimens studied. To examine the development of the ferroelectric domains in the pellets, a comparison of electrical polarisation (P) vs. electric field (E) hysteresis loops for $x = 0$ to 0.07 were carried out at room temperature using a maximum E of 40 kV cm^{-1} . The results for pellets of Y-B, Y-AB and Y-A are shown in Figure 4-19 (a-h). The remanent polarisation, P_r , coercive field, E_C , saturation polarisation, P_S values derived from the hysteresis loops under an electrical field of 20 kV/cm are listed in Tables 4-8, 4-9 and 4-10 which are close to the data reported in the literature of undoped BT [54-60]. Clear hysteresis loops were observed for $0 \leq x \leq 0.05$ and the shape of the hysteresis loop depends on Y^{3+} content. In general, if an increase of x value is followed by a decrease of both P_S and P_r , it may be associated with increasing substitution of the large Y in the Ti site. This behaviour gives rise to reduction in tetragonality of the TiO_6 octahedra. Thus, they lose their polarity and subsequent formation of a polar domain structure. Table 4-8 shows that E_C increased with increasing x up to $\sim 5.00 \text{ kV cm}^{-1}$ for $x = 0.05$, three times that of $x = 0$, but then decreased slightly to $\sim 3.98 \text{ kV cm}^{-1}$ for $x = 0.07$. A similar behaviour was observed, Table 4-9 where E_C increased to 3.70 for $y = 0.025$ then decreased to 0.47 for $y = 0.075$. For $x = 0.07$, a very narrow hysteresis loop was observed. The hysteresis loop was lost upon the addition of Y from $x = 0.10$ onwards (not shown).

This trend is similar to the results reported in [61] for BaTiO_3 with Ho concentration between $0 \leq x \leq 0.07$, showing ferroelectric behaviour.



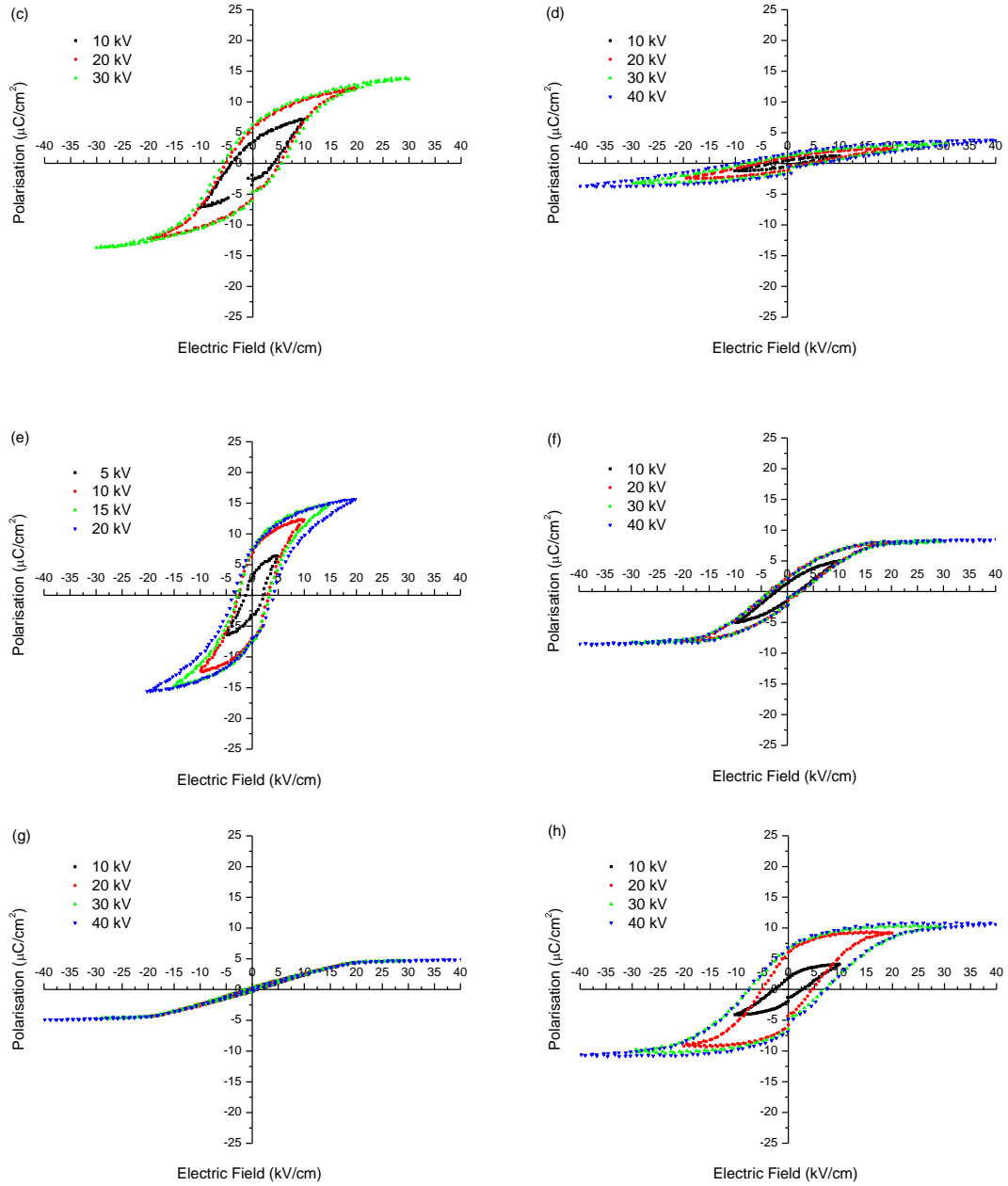


Figure 4-19: P-E loops at room temperature for (a) undoped BaTiO_3 , for $\text{BaTi}_{1-x}\text{Y}_x\text{O}_{3-x/2}$: (b) $x=0.01$, (c) $x=0.05$, (d) $x=0.07$, for $\text{Ba}_{1-y}\text{Ti}_{1-y}\text{Y}_{2y}\text{O}_3$: (e) $y=0.025$, (f) $y=0.05$, (g) $y=0.075$ and for $\text{Ba}_{1-v}\text{Ti}_v\text{O}_3$: (h) $v=0.015$ ceramics.

Table 4-8: P_S , P_r and E_C for $BaTi_{1-x}Y_xO_{3-x/2}$.

Compositions	P_S ($\mu C/cm^2$)	P_r ($\mu C/cm^2$)	E_C (kV/cm)
0	19.56	9.42	1.68
0.01	16.35	9.81	2.79
0.05	12.14	5.74	5.00
0.07	2.29	0.83	3.98

Table 4-9: P_S , P_r and E_C for $Ba_{1-y}Ti_{1-y}Y_{2y}O_3$.

Compositions	P_S ($\mu C/cm^2$)	P_r ($\mu C/cm^2$)	E_C (kV/cm)
0	19.56	9.42	1.68
0.025	15.49	7.38	3.70
0.05	8.00	2.07	2.79
0.075	4.32	0.36	0.47

Table 4-10: P_S , P_r and E_C for $Ba_{1-v}TiY_vO_3$.

Compositions	P_S ($\mu C/cm^2$)	P_r ($\mu C/cm^2$)	E_C (kV/cm)
0	19.56	9.42	1.68
0.015	9.40	5.98	4.90

4.3.2.3 Raman Spectroscopy Results

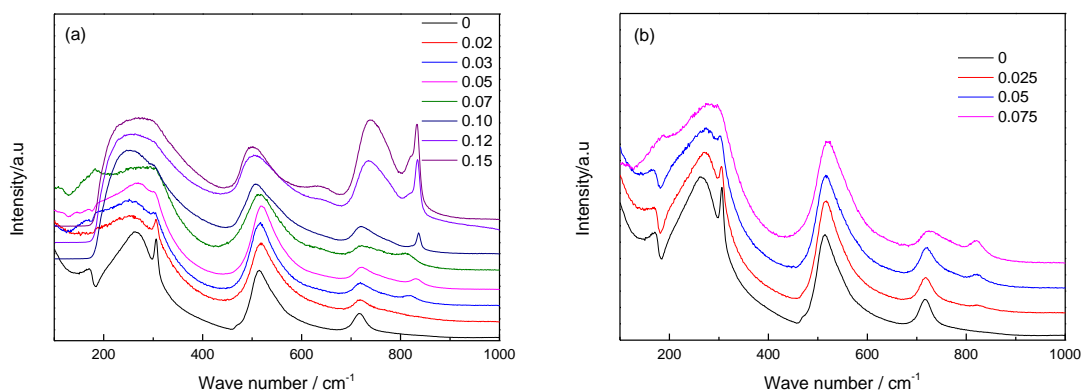
Raman spectra obtained for pellets of Y-B, Y-AB and Y-A at room temperature are shown in Figure 4-20.

Firstly, The spectra of undoped BT display six obviously noticeable characteristics with intense Raman lines at 170 and 305 cm^{-1} , broad bands peaking at 262, 514, and 717 cm^{-1} (which are often attributed to second-order effects), and a small but distinct peak at 470 cm^{-1} , in agreement with literature values [62-68]. These peaks confirm that no detectable impurity phase was observed as all the peaks correspond to the Raman spectra of undoped $BaTiO_3$. The addition of Y^{3+} has a dramatic impact on the observed modes. The synchronous effect of Y^{3+} for Ti substitution on the crystal structure of a perovskite, BT gives rise to an additional peak centred at high wave

number $\sim 819 \text{ cm}^{-1}$ which is the most important feature [69], accompanied by their frequency shifts. The vibrations resulting from the oxygen shift and also correlated with the existence of oxygen vacancies cause the high frequency mode at $\sim 800 \text{ cm}^{-1}$ [70]. The presence of one or more B-site species becomes Raman active which is indicated by the A_{1g} octahedral breathing mode at $\sim 800 \text{ cm}^{-1}$. The relative intensity of this mode is associated with substitution of ions on the B-site [62].

The continuous and significant increase of intensity was observed with increasing Y^{3+} concentration, suggesting it is a mode associated with Y^{3+} . Other clear changes were found in the region of $100\text{-}340 \text{ cm}^{-1}$ with increasing Y^{3+} concentration. Some new modes appear, others disappear, some start to broaden and frequency shifting was observed for others. For instance, at $x = 0.10$, the vanishing of the peak at 305 cm^{-1} eventually was shown. The resonance dip at 170 cm^{-1} was also affected by small amounts of Y^{3+} . A broad band peaking at 717 cm^{-1} , associated with mixed longitudinal mode with $A_1 (C_{4v})$ and $E_1 (C_{4v})$ symmetry [71, 72], was obtained with increasing Y^{3+} concentration. These are attributed to the decreasing tetragonality of BT with increasing Y^{3+} concentration. The three bands at $170, 262$ and 305 cm^{-1} , reduce in intensity with increasing Y^{3+} concentration, resulting in a broad and practically structureless band extending from 174 to 342 cm^{-1} for $x \geq 0.12$. For $x \geq 0.07$, Raman spectra of the cubic polymorph are typified by two asymmetric broad bands at 262 cm^{-1} and 514 cm^{-1} in good agreement with those reported in the literature [72].

Secondly, Figure 4-20 (b) and (c) show similar behaviour for the same concentrations.



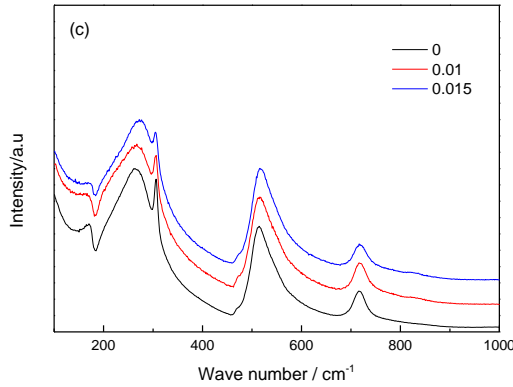


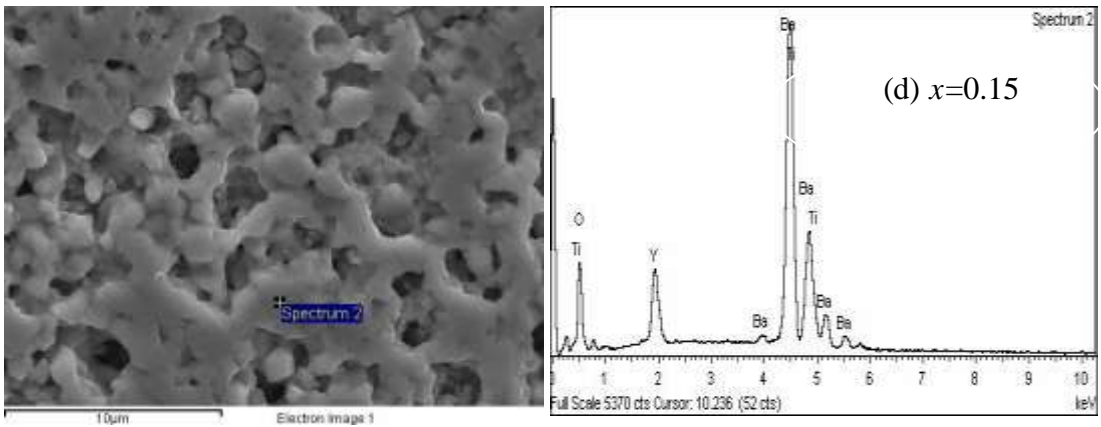
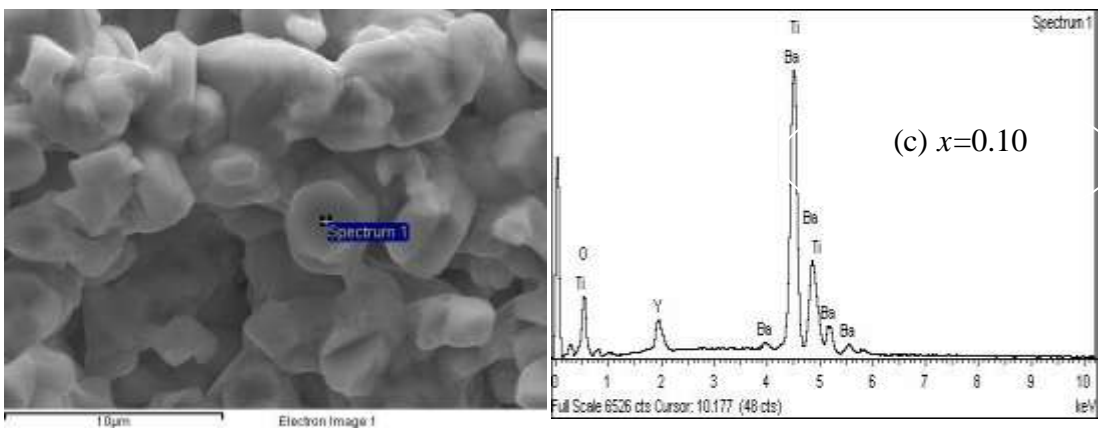
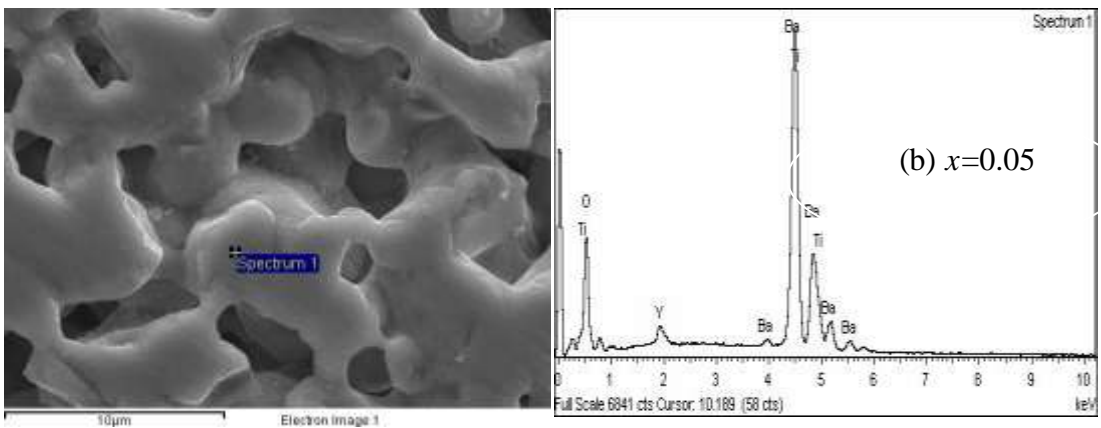
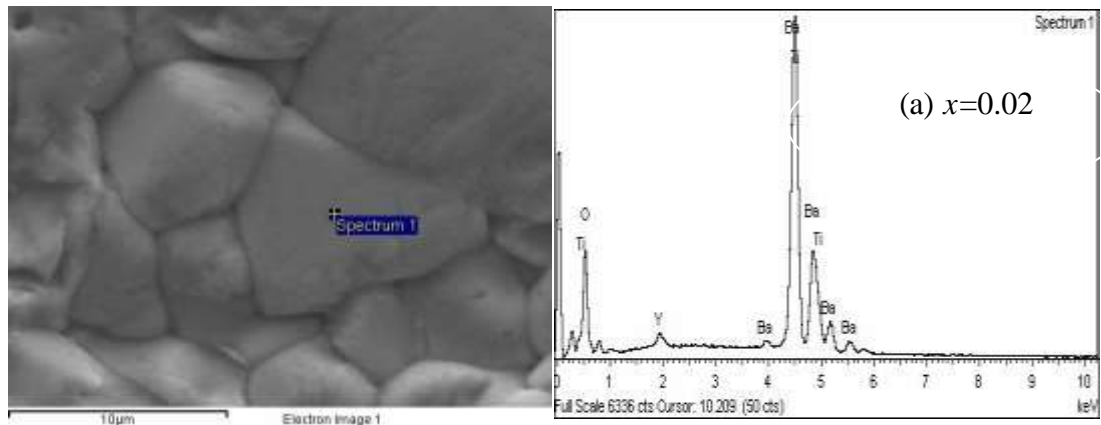
Figure 4-20: Room-temperature Raman spectra for (a) Y-B ($0 \leq x \leq 0.15$) (b) Y-AB ($0 \leq y \leq 0.075$) and (c) Y-A ($0 \leq \nu \leq 0.015$).

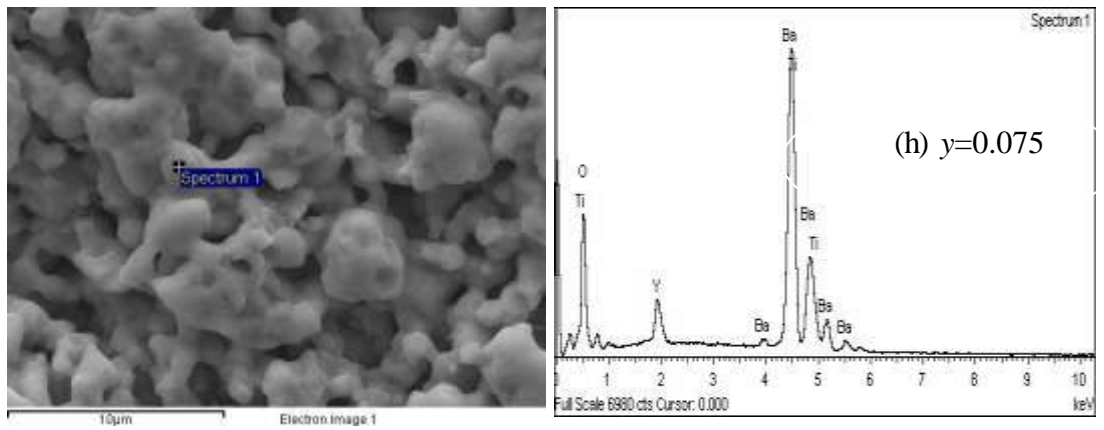
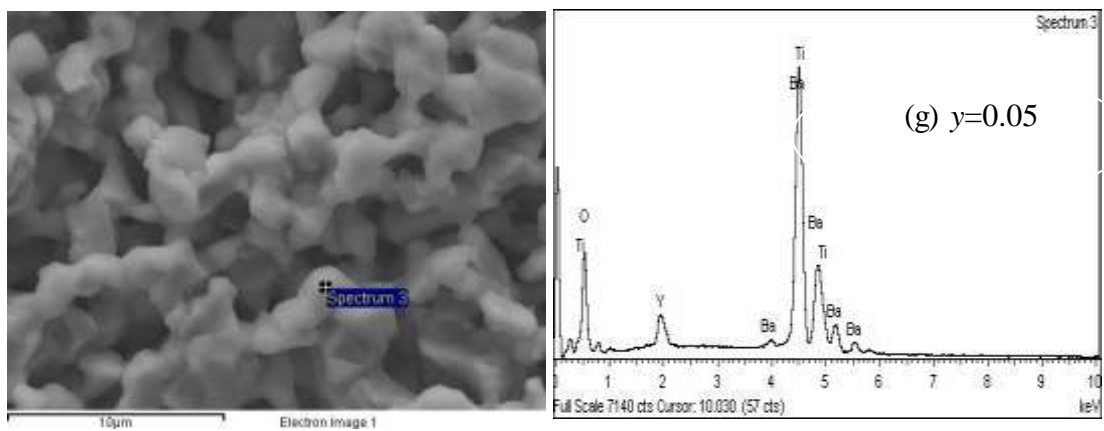
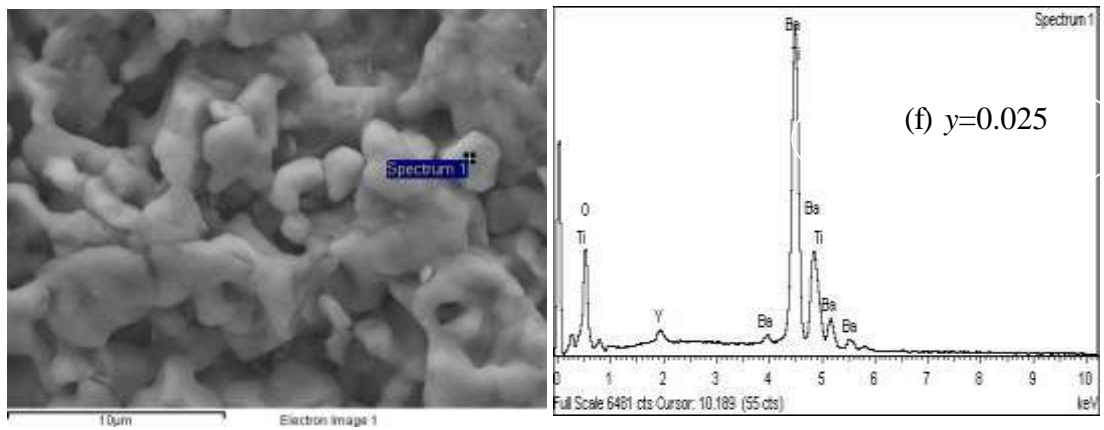
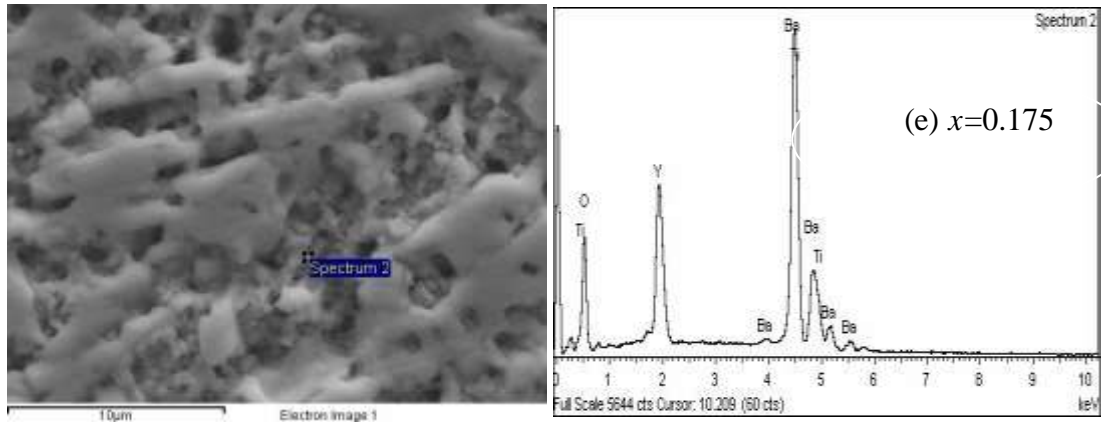
4.3.2.4 SEM Results

SEM micrographs of the ceramic microstructures and EDS analysis of the micro-composition of polished and thermally etched sections for (a-e) Y-B ($0.02 \leq x \leq 0.175$), (f-h) Y-AB ($0.025 \leq y \leq 0.125$) and (i) Y-A ($\nu = 0.015$) are shown in Figure 4-21. There is a clear reduction in average grain size of the ceramics doped with Y^{3+} . This indicates that Y^{3+} substitution leads to suppression of grain growth. The microstructures consisted of small grains, as compared with that in undoped BT with average grain size $\sim 1\text{--}10 \mu\text{m}$. A non-uniform grain size distribution was observed clearly for high Y content such as $x = 0.175$, showing needle-shaped grains.

Pellet densities were obtained by dividing the geometrical density calculated from pellet mass and dimensions by the values for fully dense pellets, calculated from the unit-cell dimensions and contents. The densities of samples were 82 – 96 %. Some samples seem to be quite porous due to low relative densities.

EDS analysis of samples doped with low concentrations such as $x = 0.02$, 0.025 and 0.015 did not show any Y-rich regions, indicating a uniform incorporation of dopants within the samples. The appearance of Y-rich regions between grains was observed with increasing dopant content.





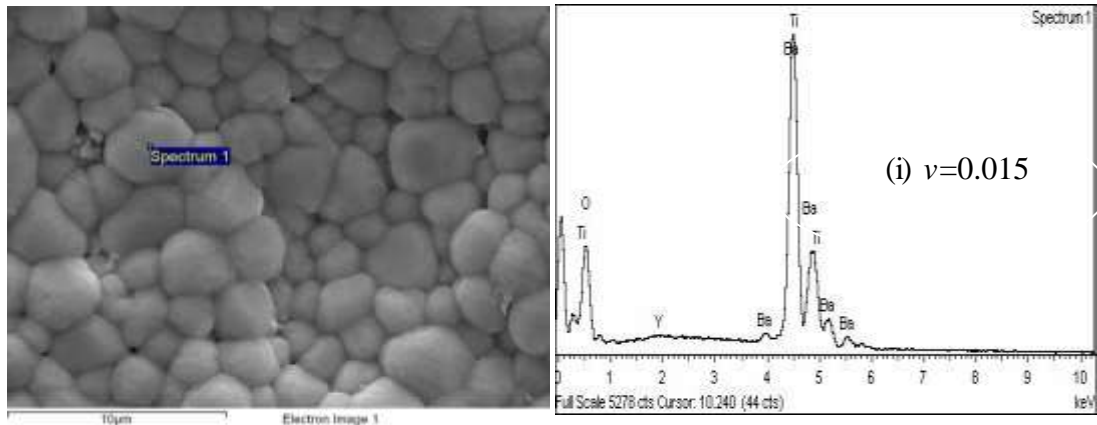


Figure 4-21: SEM images and EDS traces for (a-e) Y-B ($0.02 \leq x \leq 0.175$), (f-h) Y-AB ($0.025 \leq y \leq 0.125$) and (i) Y-A ($\nu = 0.015$).

4.3.2.5 IS Results

(A) Y-B samples:

(1) Typical impedance data

Impedance measurements were made, as a function of temperature, for samples in the range $0.02 < x < 0.15$. Samples with $0 < x < 0.07$ were all electrically heterogeneous and both bulk and grain boundary regions were insulating whereas samples with $0.09 \leq x \leq 0.15$ were mostly homogenous and dominated by the insulating bulk component. Typical IS data of samples $x = 0.02$ and 0.10 are given in Figures 4-22 to 4-25. All samples were highly insulating at room temperature. IS data for all samples could only be collected at temperatures > 300 °C, as the samples were too resistive at lower temperatures with resistance > 10 MΩcm but showed modest levels of semiconductivity at high temperatures.

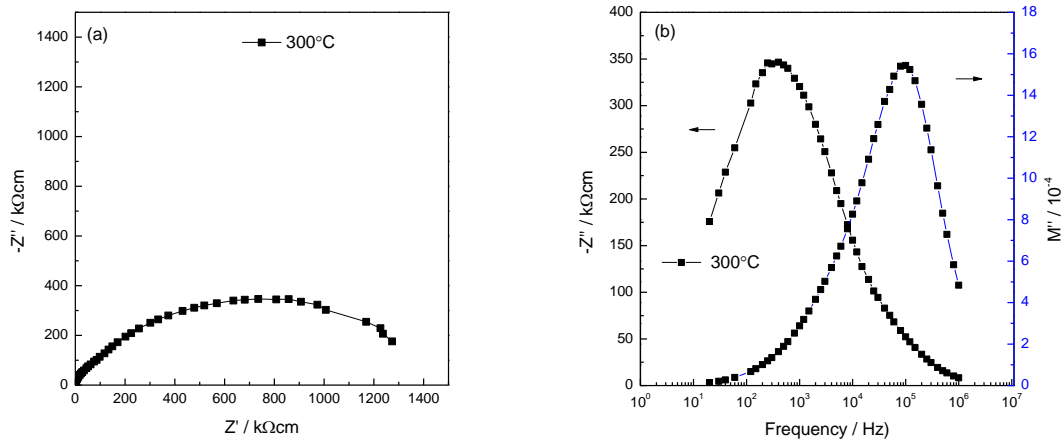
Complex impedance plane (Z^*) plots are given for $x = 0.02$ at 300 °C, Figure 4-22 (a). They show that the sample contained one distorted semicircle, corresponding to the contribution of bulk and grain boundary resistances which together, dominate the total resistance. IS data are represented, ideally, by a series combination of two parallel RC elements. The total resistance, R_T , was determined to be ~ 1400 kΩcm. R_b and R_{gb} were not determined because the high frequency arc was not resolved but can be seen clearly and may be estimated from the f_{max} value of the high frequency M'' peak. The Z''/M'' against $\log f$ plots showed a single peak in Z'' spectra at low

frequency and another single peak in M'' spectra at high frequency, Figure 4-22 (b). The M'' peak represents the smallest capacitance in the sample and highlights the bulk response with $C_b = \sim 1.90 \times 10^{-11} \text{ Fcm}^{-1}$ and $R_b = \sim 55.53 \text{ k}\Omega\text{cm}$ at 300°C .

A Y' spectroscopic plot, Figure 4-22 (c), shows two plateaus; a frequency independent plateau attributed to the dc conductivity, R^{-1} , at lower frequency and another plateau at high frequency.

The same data presented as spectroscopic plots of capacitance, C' , Figure 4-22 (d), show a high frequency plateau which is attributed to the sample bulk, C_1 . Its value is $\sim 1.90 \times 10^{-11} \text{ Fcm}^{-1}$. A low frequency shallow dispersion region in capacitance is observed with much higher associated capacitance.

Figure 4-23 shows conductivity Arrhenius plots of the total, bulk and grain boundary conductivities. All obey the Arrhenius law. σ_T was obtained from the low-frequency intersects of Z^* . The overall impedance response was dominated by the lower-frequency component because it has much higher resistance than the high-frequency one. σ_T and σ_{gb} fall onto two sets of parallel lines with similar activation energy, ~ 0.84 and 0.87eV , respectively, whereas the bulk, σ_b , data show curved Arrhenius behaviour with lower activation energy $\sim 0.59 \text{ eV}$.



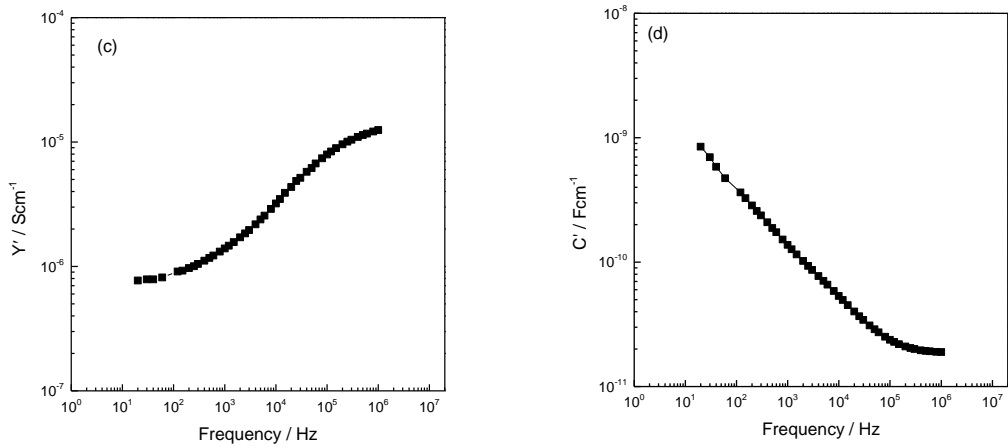


Figure 4-22: 300 °C IS data for $x = 0.02$, slow cooled from 1400 °C, (a) Z^* plot, (b) - Z'' , M'' plots, (c) Y' plot and (d) C' plot.

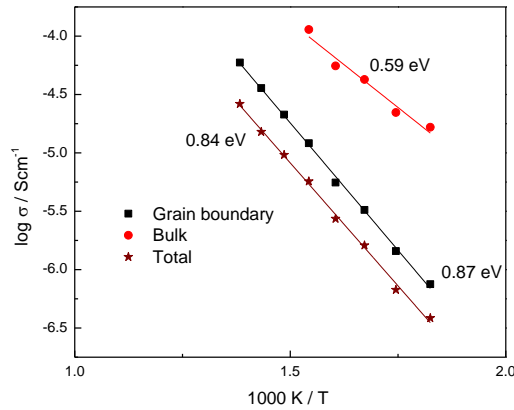


Figure 4-23: Arrhenius plots of the total, bulk and grain boundary conductivity data against reciprocal temperature for $x = 0.02$, slow cooled from 1400 °C.

The impedance response is shown for $x = 0.10$ in Figure 4-24. Above 200 °C the sample revealed a simple response with a single, essentially undistorted semi-circular arc in the complex impedance plot, Z^* . R_T at 401 °C is $1.09 \times 10^5 \Omega\text{cm}$; $C_T \sim 3.66 \text{ pFcm}^{-1}$ which indicate bulk response with $\epsilon' \sim 42$. Single Debye peaks in the Z'' and M'' plots were at the same frequency, Figure 4-24 (b) which emphasizes the electrical homogeneity of the sample. The Y' spectroscopic plot shows a low frequency independent plateau with a slight dispersion at higher frequencies, Figure 4-24 (c). This probably indicates the inclusion of a bulk CPE. That would also be responsible for the low frequency dispersion in C' . Capacitance (C') spectroscopic plots, Figure 4-24 (d), exhibited a frequency/temperature-independent plateau at high frequencies $\sim 5.00 \times 10^{-12} \text{ Fcm}^{-1}$, attributed to the sample bulk component. A

dispersion of capacitance was observed at a lower frequency which increased slightly with increasing temperature. An Arrhenius plot of σ_T , Figure 4-25, is linear with activation energy ~ 0.72 eV.

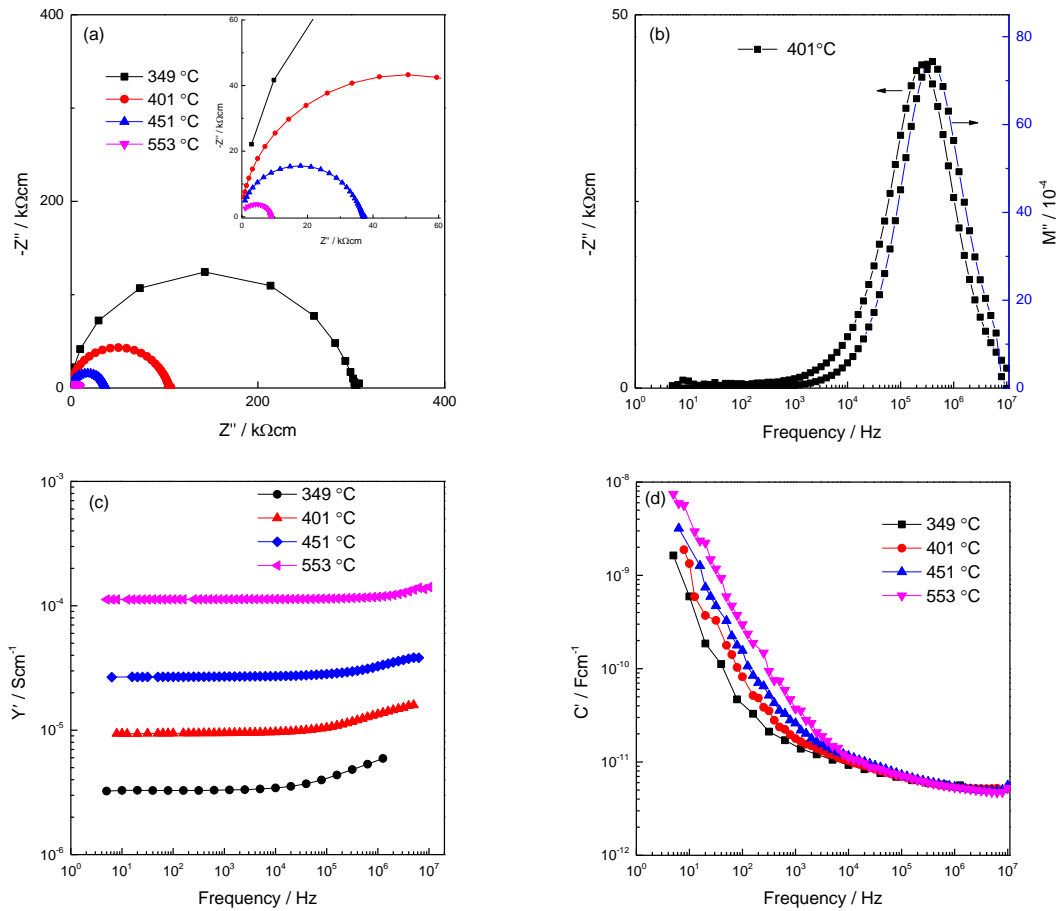


Figure 4-24: IS data for $x = 0.10$, slow cooled from 1500 °C, (a) Z^* plot, (b) $-Z''$, M'' plots, (c) Y' plot and (d) C' plot.

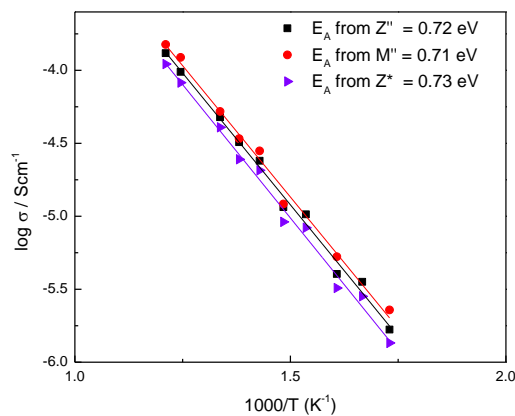


Figure 4-25: Arrhenius plots of the conductivity; data were extracted from Z^* , Z'' and M'' against reciprocal temperature for $x = 0.10$, slow cooled from 1500 °C.

Conductivity Arrhenius plots and activation energies over the range of $x = 0.02-0.15$ are shown in Figure 4-26 and Table 4-11. E_A values are between 0.73 and 1.1 eV. E_A and σ did not exhibit any apparent systematic trend with x .

Table 4-11: Heating temperature, electrode type, cooling rate and E_A for bulk, grain boundary and the total conductivity.

x	Heating temperature	Electrode type	Cooling rate	E_A (M'') (eV)	E_A (Z'') (eV)	E_A (Z^*) (eV)
0.02 Tetragonal	1450 °C for 24 h in air	Pt	Slow-cooled, 10 °C/min	0.59	0.87	0.84
0.03 <i>PBM</i> Tetragonal	1450 °C for 24 h in air	Ag	Air-quenched	0.69	0.96	0.93
0.05 Cubic	1450 °C for 24 h	Pt	Slow-cooled, 10 °C/min	1.06	1.06	0.92
0.09 <i>BM</i> Cubic	1550 °C for 100 h in air	Pt	Slow-cooled, 10 °C/min	0.89	0.91	0.9
0.10 Hexagonal	1500 °C for 24 h in air	Pt	Slow-cooled, 10 °C/min	0.71	0.72	0.73
0.12 Hexagonal	1500 °C for 24 h in air	Pt	Slow-cooled, 10 °C/min	1.08	1.12	1.1
0.15 Hexagonal	1450 °C for 24 h in air	Pt	Slow-cooled, 10 °C/min	0.96	1.02	1.01

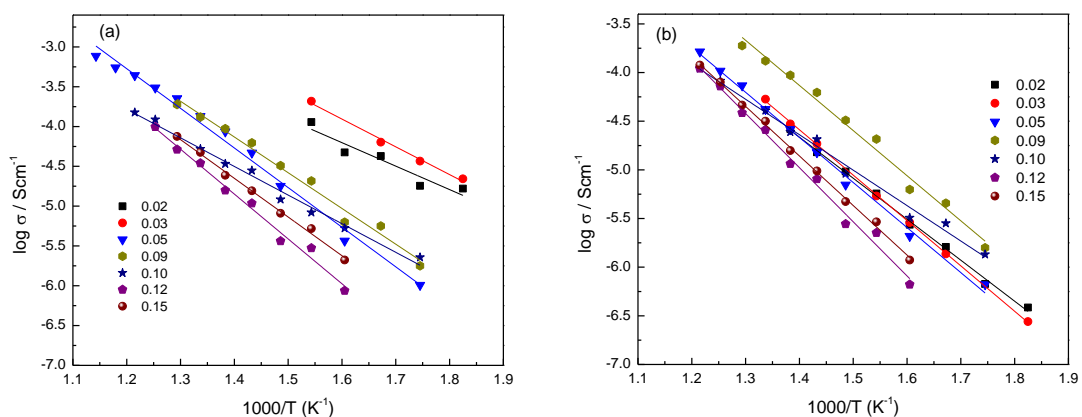


Figure 4-26: Arrhenius plot of bulk (a) and grain boundary (b) for Y-B samples.

Samples were insulating at room temperature even after quenching in air. For example for $x = 0.05$, no significant difference was observed between SC and Q sample, Figure 4-27 and Q sample is still p-type and did not change to n-type. Different samples Q from 1400 °C with different electrodes show an insulating behaviour and no evidence of semiconductivity, Figure 4-28.

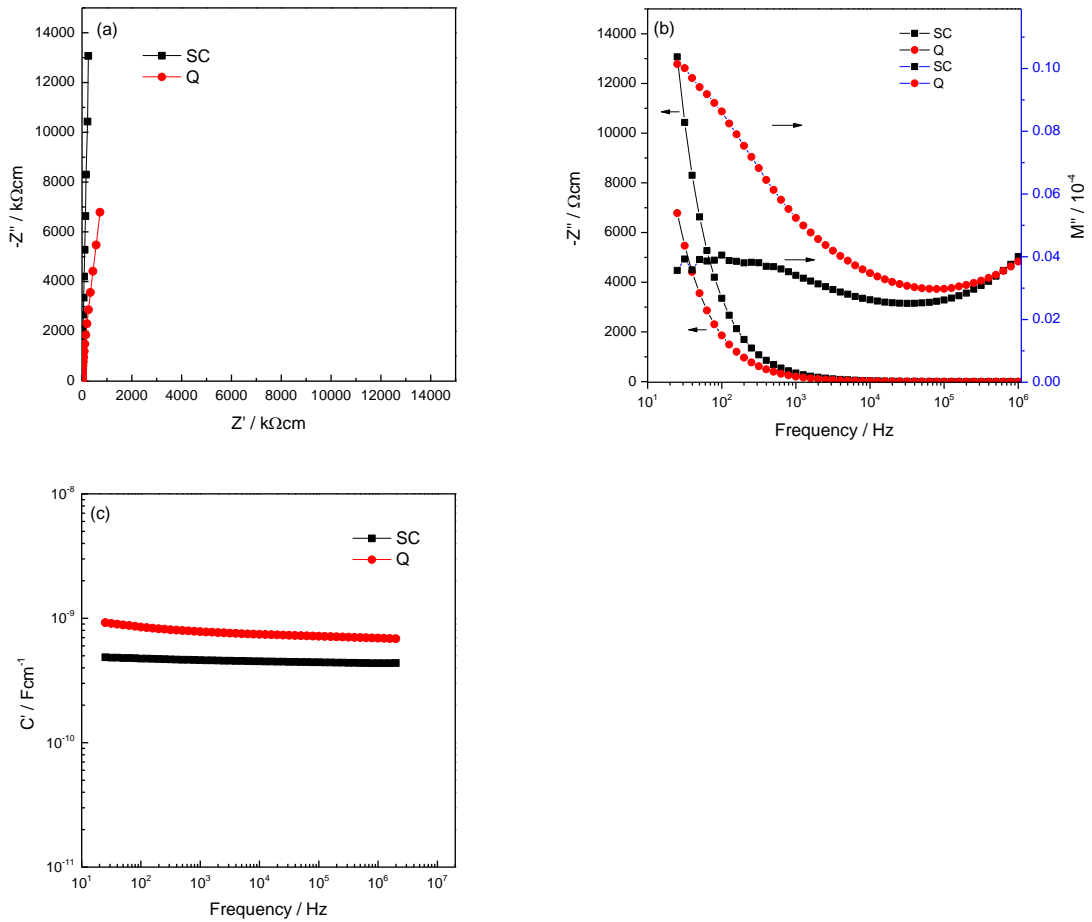
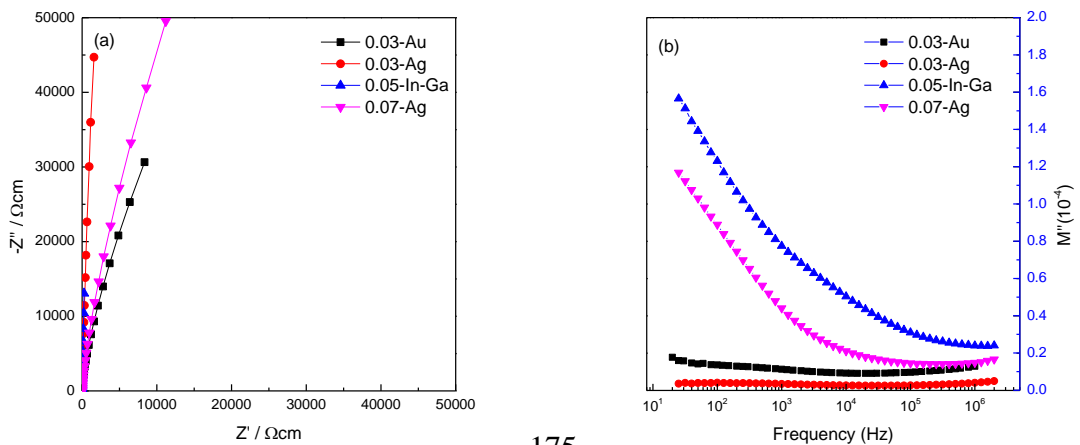


Figure 4-27: RT, IS data for $x = 0.05$, slow cooled and quenched from 1400 °C, (a) Z^* plot, (b) $-Z''$, M'' plots, (c) C' plot.



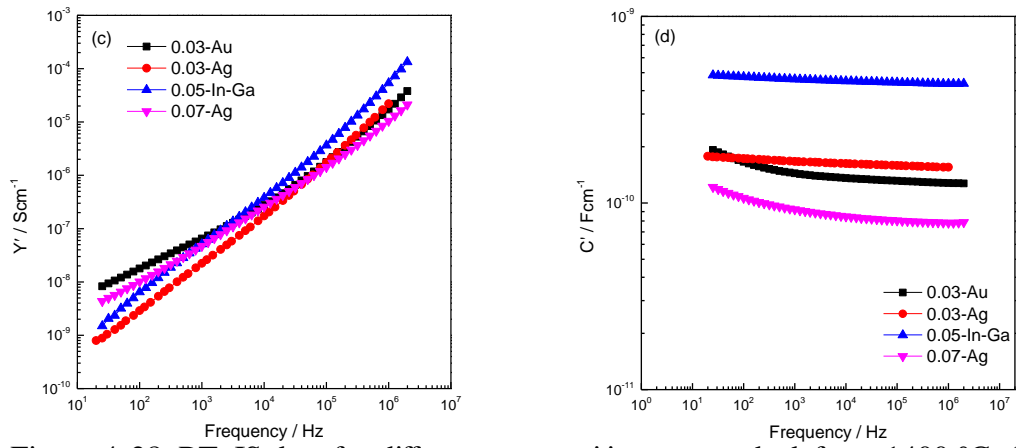


Figure 4-28: RT, IS data for different compositions, quenched from 1400 °C, (a) Z^* plot, (b) $-Z''$, M'' plots, (c) C' plot.

(2) Effect of oxygen partial pressure

Z^* data for $x = 0.05$ measured in O_2 , air and N_2 are shown in Figure 4-29. The resistance increased from $\sim 3.76 \times 10^4 \Omega\text{cm}$ in O_2 to $8.49 \times 10^5 \Omega\text{cm}$ in N_2 indicative of p-type conductivity, Figure 4-29 (a).

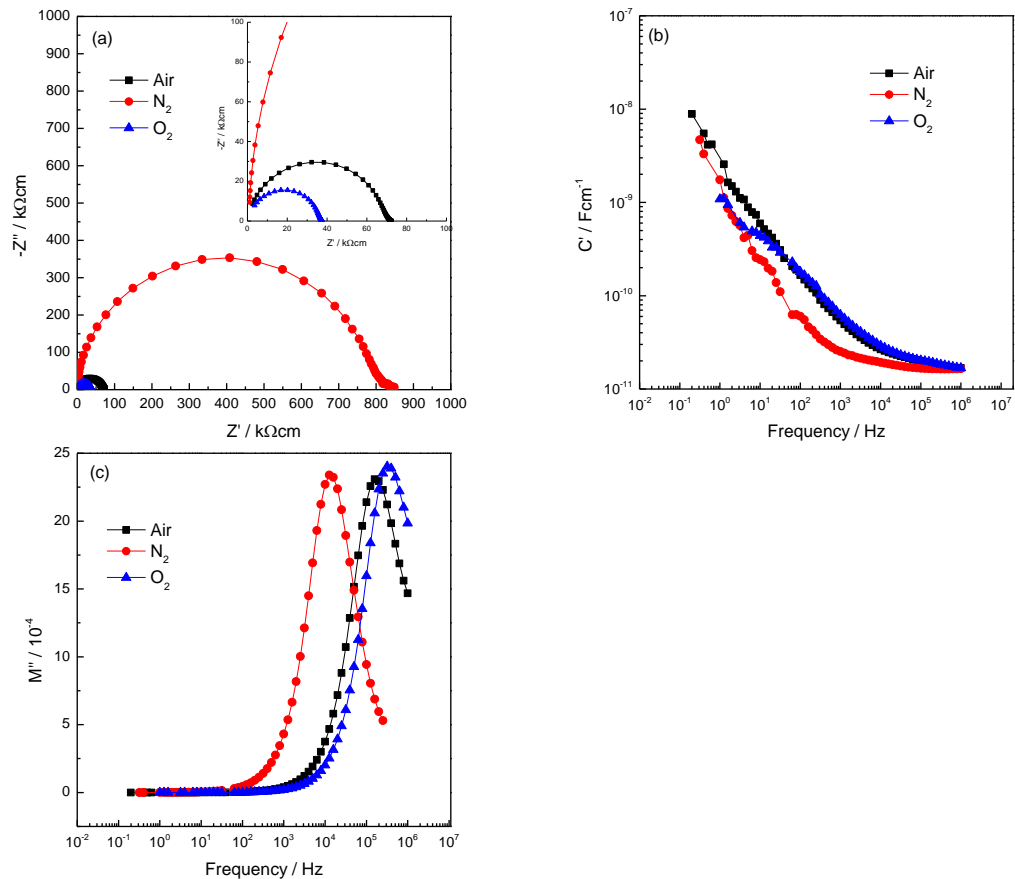


Figure 4-29: 400 °C IS data for $x = 0.05$, slow cooled from 1500 °C, (a) Z^* plot, (b) C' plot and (c) M'' plot in different atmospheres.

(3) Effect of application of a small dc bias voltage

IS was also studied with application of a small dc bias to the sample. Results are shown for $x = 0.05$ in Figure 4-30. R_T decreases gradually with time; eg ~ 43.23 $k\Omega\text{cm}$ after 1 min, decreasing to ~ 12.05 $k\Omega\text{cm}$ after 210 min. Figure 4-30 (c) shows that the capacitance values increase with increasing time. The recovery of R_T after removal of the dc bias is shown in Figure 4-30 (d). A steady state was reached after ~ 2700 min. The decrease in R with dc bias can be attributed to p-type conduction and gives a similar result to the effect of varying pO_2 .

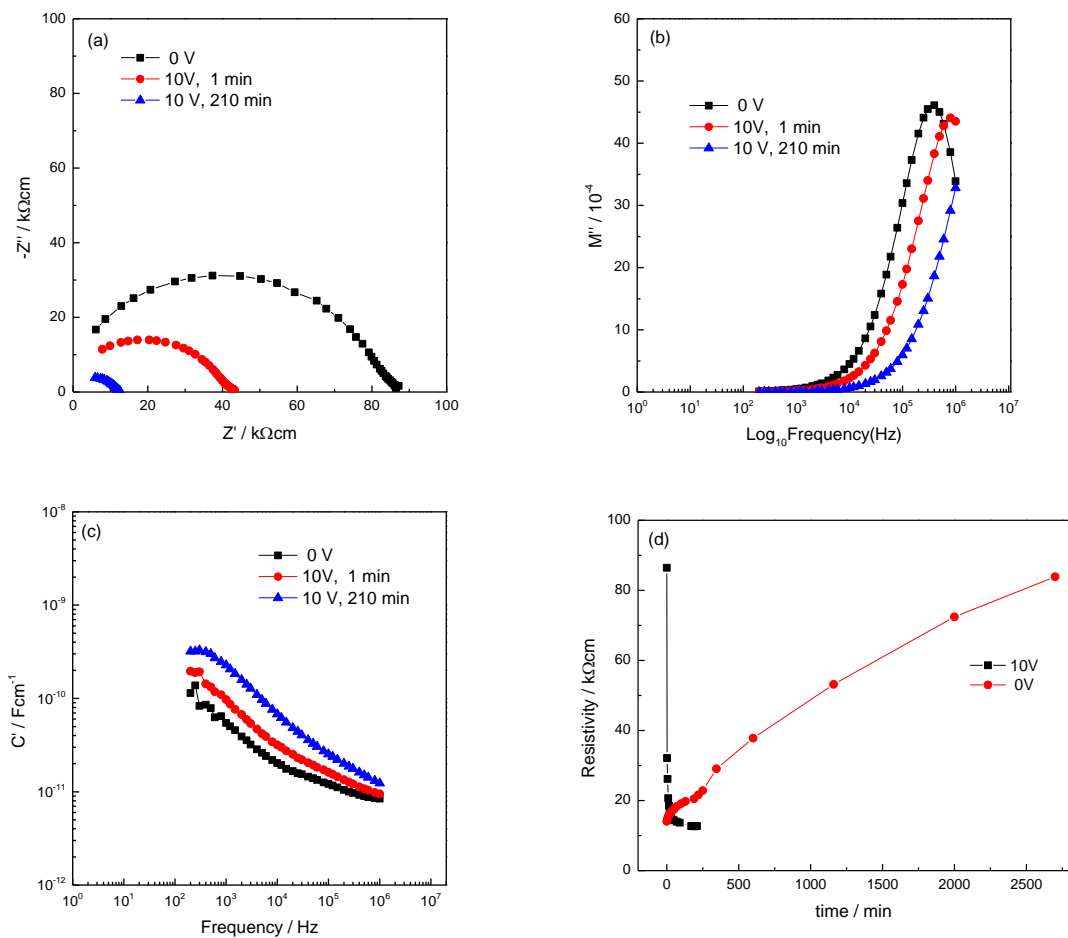


Figure 4-30: (a) Z^* plot (b) M'' plot and (c) C' plot at 400 °C before and after a voltage of 10 V was applied at different measuring times (d) Total resistance at 400 °C with 10V bias and after removing the dc bias at different times in air.

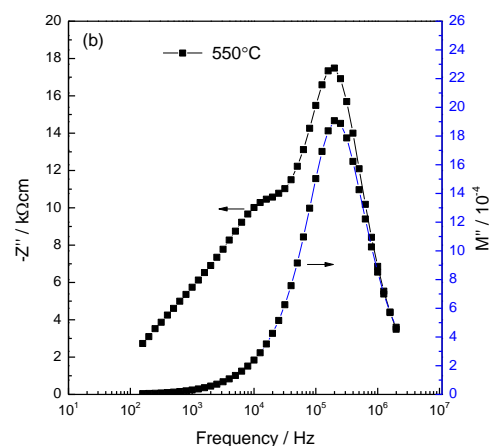
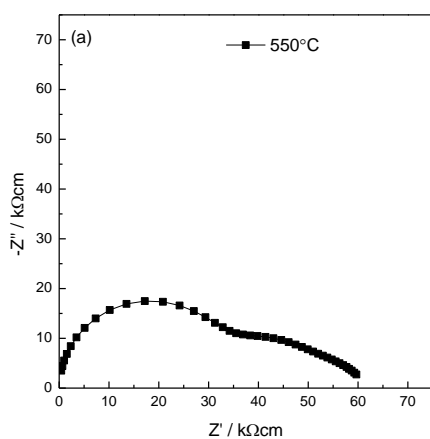
(B) Y-AB samples:

(1) Typical impedance data

Impedance data for Y-AB samples ($0.025 < y < 0.075$) were studied. Generally, all samples were insulating and heterogeneous, containing two components that can be seen in the Z^* plot as two semicircular arcs at high and low frequency which can be assigned to an equivalent circuit composed of two parallel RC elements. Semiconductivity was only observed for the quenched samples whereas, slow cooled samples exhibited much higher resistances.

Z^* plots, Figure 4-31 (a), and combined Z''/M'' spectroscopic plots, Figure 4-31 (b), show two components with similar activation energy since their relative resistances in Z^* plots did not show significant change with temperature. The largest peaks in M'' and Z'' plots are located at high frequency. The bulk capacitance has the smaller value $\sim 2.32 \times 10^{-11} \text{ F cm}^{-1}$ at 550°C whereas, $7.01 \times 10^{-10} \text{ F cm}^{-1}$ was obtained for the low frequency component. Figure 4-31 (b) shows that two different electrical regions can be distinguished similarly from Z''/M'' spectroscopic plots, suggesting that they also belong to bulk and grain boundary components. The capacitance of the high frequency plateau (c) decreases with increasing temperature (not shown).

Arrhenius plots are shown in Figure 4-32. The conductivities are identical with same activation energy values with lower conductivity values of the total.



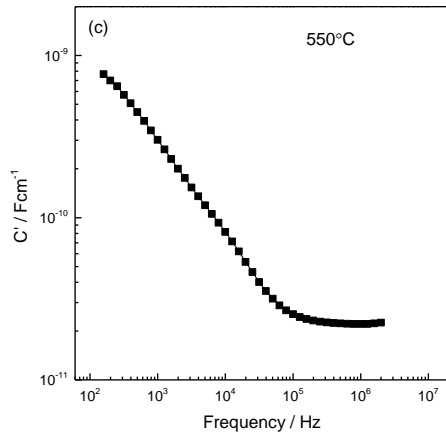


Figure 4-31: 550 °C IS data for $y = 0.075$, slow cooled from 1550 °C, (a) Z^* plot, (b) $-Z''$, M'' plots and (c) C' plot.

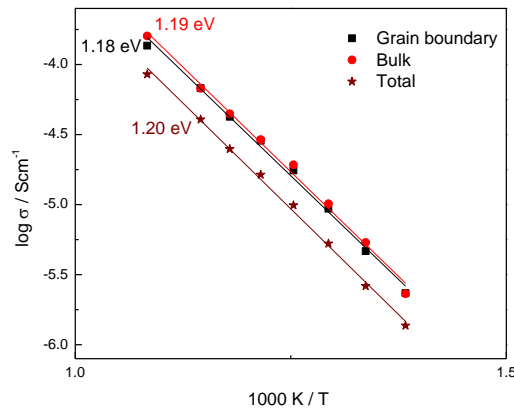


Figure 4-32: Arrhenius plots of the total, bulk and grain boundary conductivity data against reciprocal temperature for $y = 0.075$, slow cooled from 1550 °C.

(2) Effect of cooling rate

The results were very dependent on cooling rate after sintering. Results are presented for three different cooling rates in the following sequence: SC in air, Q in air and Q in liquid N_2 . Partial re-oxidation can occur. A pellet of composition $y = 0.025$ was heated at 1500 °C for 12 hours in air followed by SC in air. IS data are shown in Figure 4-33. The pellet was off-white and insulating. Although the room temperature Z^* plot showed there was no apparent semiconducting component at high frequency and the sample had a total resistance $>10^7 \Omega\text{cm}$, Figure 4-33 (a), the M'' spectra showed an incline at high frequency attributed to a more conducting bulk response, Figure 4-33 (b). The Z'' plot was dominated by a low frequency incline with an associated resistivity $>1 \text{ M}\Omega\text{cm}$.

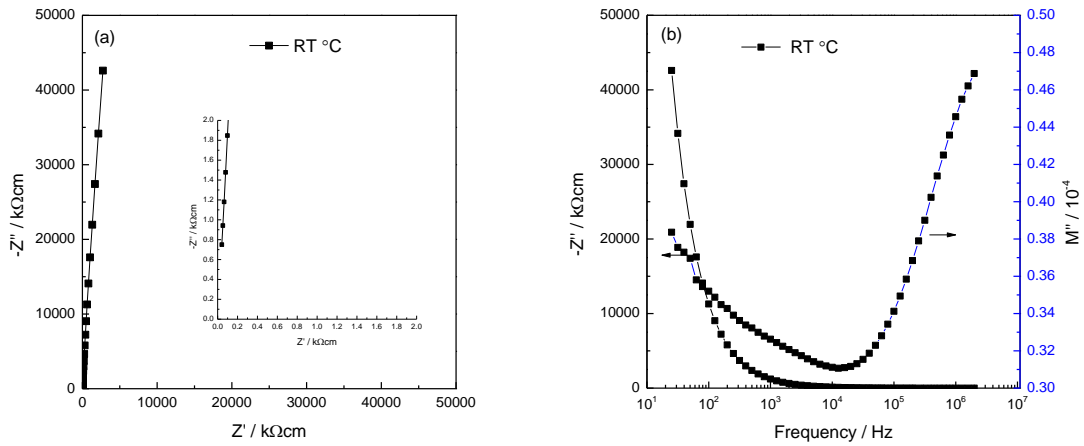


Figure 4-33: Room-temperature (a) Z^* and (b) Z'' , M'' spectroscopic plots for $y = 0.025$ heated at $1500\text{ }^{\circ}\text{C}$ in air, SC, with Pt electrodes.

This sample was then reheated in air at $1500\text{ }^{\circ}\text{C}$ for 12 hours and air-quenched which changed its colour from off-white to dark grey. Room temperature Z^* plot showed a single arc with $R_T \sim 7.43 \times 10^5\ \Omega\text{cm}$, Figure 4-34 (a). M'' plots show two components; a single broad peak which overlapped with the Z peak and a high frequency incline, Figure 4-34 (b), towards another larger peak at $> 10^6$ Hz. It is proposed that this latter peak corresponds to the semiconducting interior of individual grains, with resistivity $< 100\text{ k}\Omega\text{cm}$.

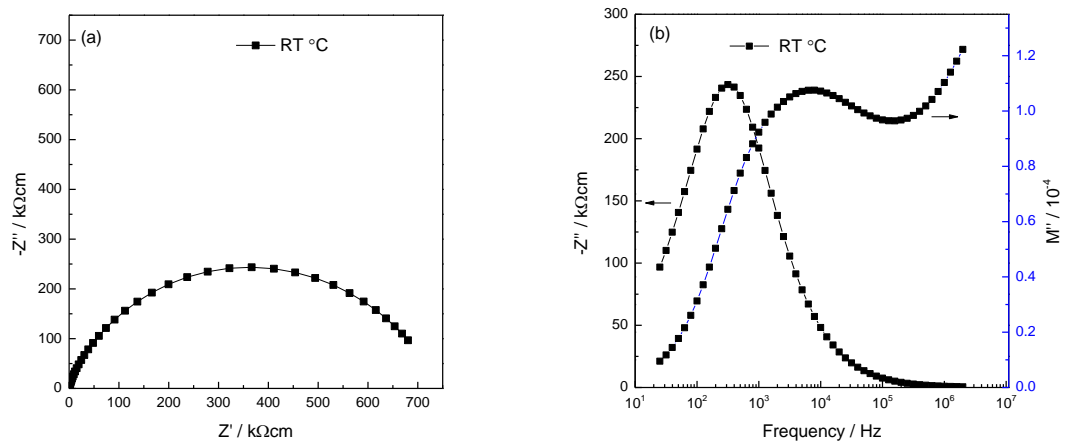


Figure 4-34: Room-temperature (a) Z^* and (b) Z'' , M'' spectroscopic plots for $y = 0.025$ quenched from $1500\text{ }^{\circ}\text{C}$ in air with In-Ga electrodes.

Two different samples prepared under the same conditions (air quenched from $1500\text{ }^{\circ}\text{C}$) were studied at different temperatures from $-263\text{ }^{\circ}\text{C}$ until room temperature, one with In-Ga and one with Ag electrodes. IS data show similar room temperature

behaviour (not shown) to that in Figure 4-34. The M'' incline at high frequency showed broad Debye-like peak maxima for both samples only at low temperatures $\sim \leq -148$ °C as shown in Figure 4-35 for the sample with Ag electrodes. The f_{\max} in M''_1 showed a slight shift to low frequency by ~ 2 times with increasing temperature, whereas the peak M''_2 shifted to higher frequency by ~ 5 times, Figure 4-35.

Capacitance data extracted from M''_1 and M''_2 are plotted against temperature in Figure 4-36. At low temperatures, C_1 and C_2 can be obtained below -150 °C. C_1 and C_2 are shown and have similar values. With increasing temperature, M_1 has a broad maximum at ~ -23 °C. Capacitance data extracted from M''_1 display permittivity maxima, characteristic of bulk BT. The maxima in Figure 4-36 therefore correspond to the transitions; the tetragonal-orthorhombic (2 °C) and cubic-tetragonal (125 °C). The capacitance scale is not accurate due to existence of errors associated with extracting the capacitance data from M'' peaks, in which the peaks are broadened and depressed.

Arrhenius plots show different possible conduction mechanisms, depending on different temperature ranges, Figure 4-37. Both Figures 4-36 and 4-37 show phase transitions at different temperatures.

The sample with Ag electrodes was studied at higher temperatures and showed a PTCR effect as clearly presented in Figure 4-38.

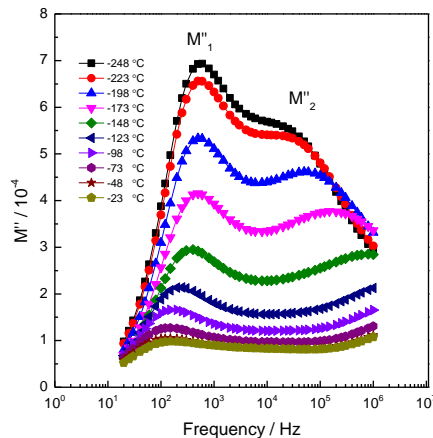


Figure 4-35: Combined modulus, M'' , spectroscopic plots for sample with Ag electrodes at selected temperatures.

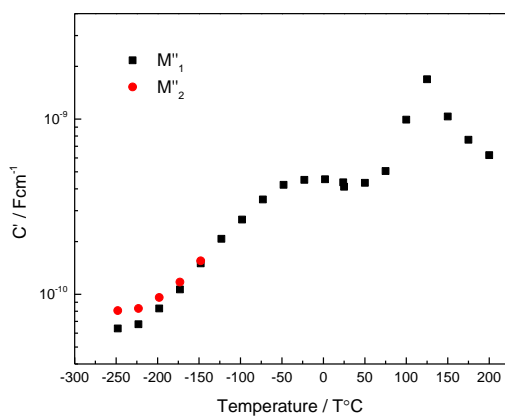


Figure 4-36: Capacitance data (extracted from M'') against temperatures, for sample with Ag electrodes.

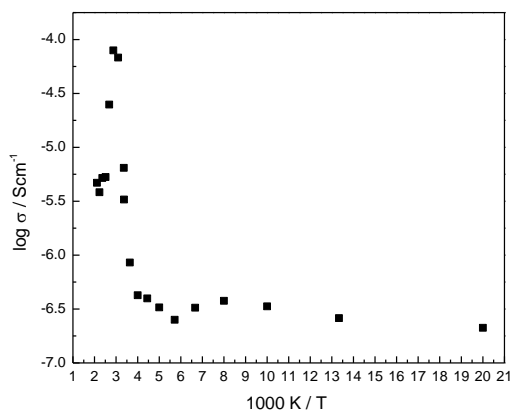


Figure 4-37: Arrhenius plots of the bulk conductivity data (extracted from M''_1) against reciprocal temperature.

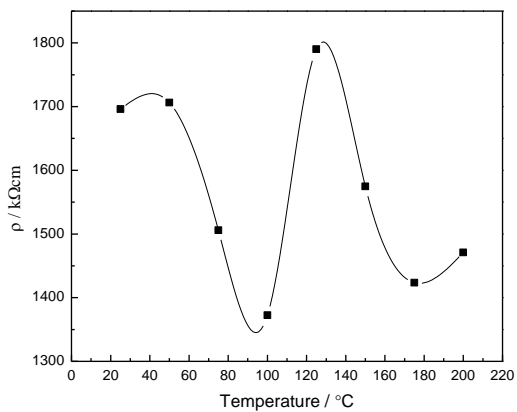


Figure 4-38: Total resistivity as function of temperature.

Further heat treatment was performed on this sample which was reheated to 1500 °C for 12 hours and cooled rapidly in liquid nitrogen. Figure 4-39 is similar to Figure 4-34 but a higher conductivity value was observed with $R_T \sim 65 \text{ k}\Omega\text{cm}$, Figure 4-39 (a). Figure 4-39 (b) shows a more homogeneous sample but with one peak at intermediate frequency and an incline at high frequency which is evidence for a more conductive grain core that can't be quantified, as shown by the increase in M'' data at $> 1 \text{ MHz}$. Capacitance value extracted from the peak in M'' is $\sim 264 \text{ pFcm}^{-1}$.

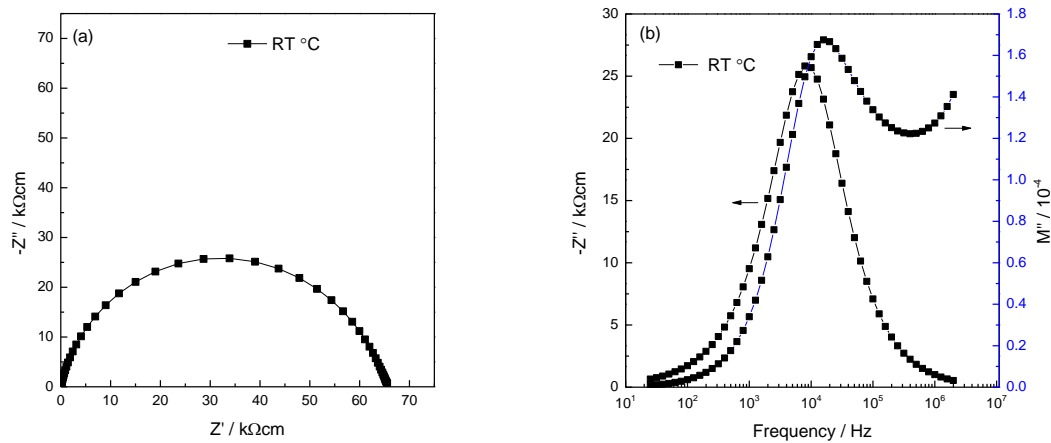


Figure 4-39: Room-temperature (a) Z^* and (b) Z'' , M'' spectroscopic plots for $y = 0.025$ quenched from 1500 °C in liquid nitrogen.

Conductivity data over the composition range $y = 0.025\text{--}0.075$ are shown in Figure 4-40. E_A values are shown in Table 4-12. The conductivity data exhibit a small systematic trend with y , the conductivity of the high frequency component decreases whereas, a very slight decrease was observed for low frequency component.

Table 4-12: Heating temperature, electrode type, cooling rate and E_A for bulk, grain boundary and the total conductivity.

y	Heating temperature	Electrode type	Cooling rate	E_A (b) (eV)	E_A (gb) (eV)	E_A (total) (eV)
0.025 Tetragonal	1500 °C for 12 h in air	Pt	Slow-cooled, 10 °C/min	1.53	1.09	1.32
0.025 Tetragonal	1500 °C for 12 h in air	Ag	Liquid N ₂ -quenched	0.092	0.10	0.104
0.05 Cubic	1550 °C for 96 h in air	Pt	Slow-cooled, 10 °C/min	1.11	1.12	1.16

0.075	1550 °C for 12	Pt	Slow-cooled,	1.19	1.18	1.20
Cubic	h in air		10 °C/min			

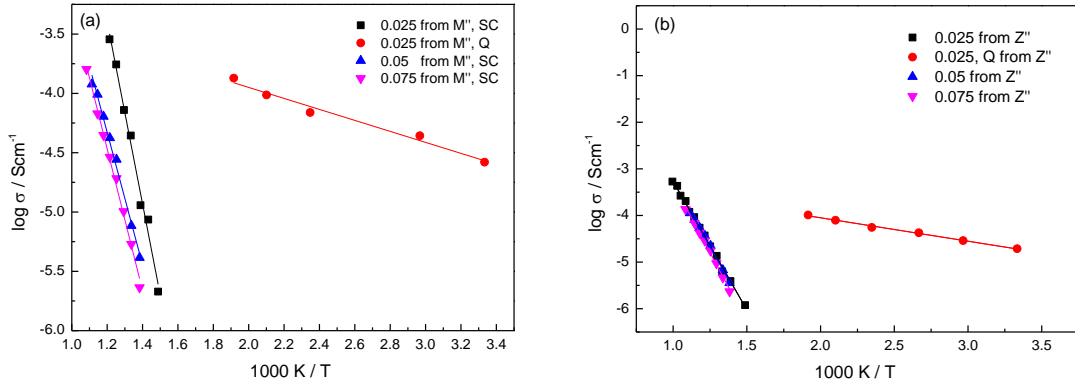
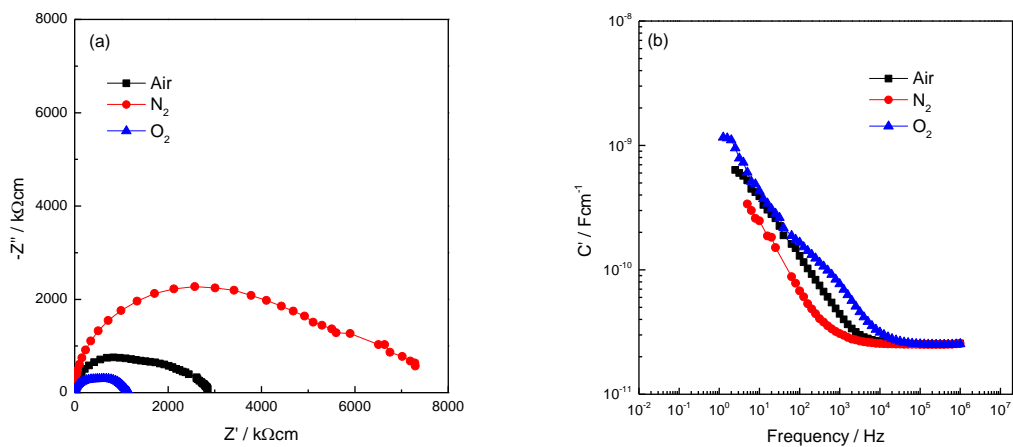


Figure 4-40: Arrhenius plots of conductivity against reciprocal temperature for the high (a) and low (b) frequency components for Y-AB samples.

(3) Effect of oxygen partial pressure

Z^* plots for $y = 0.05$ SC from 1500 °C and measured in O_2 , air and N_2 are shown in Figure 4-41. On changing the atmosphere to N_2 at 400 °C, the conductivity decreased, Figure 4-41 (a), appearing to be p-type. Impedance Z^* complex plane plots, (a), showed two poorly resolved arcs. Figure 4-41 (b) shows that the high frequency capacitance plateau illustrates similar capacitance values $\sim 2.51 \times 10^{-11}$ Fcm^{-1} . The high frequency peak in M'' showed a slight shift to low frequency in N_2 , Figure 4-41 (c). The M'' incline at high frequency was observed for O_2 , air and N_2 .



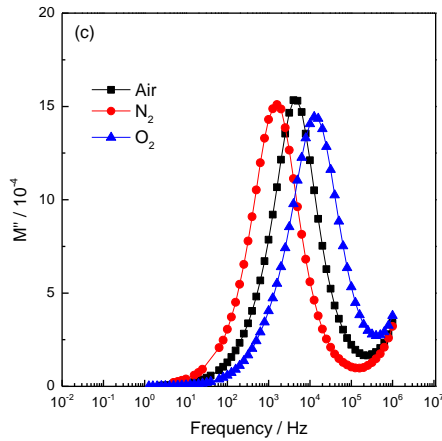


Figure 4-41: 400 °C IS data for $y = 0.05$, slow cooled from 1550 °C, (a) Z^* plot, (b) C' plot and (c) M'' plot in different atmospheres.

Since the Arrhenius plot showed that the Q sample ($y = 0.025$) was n-type, the conduction mechanism was studied in different pO_2 , Figure 4-42.

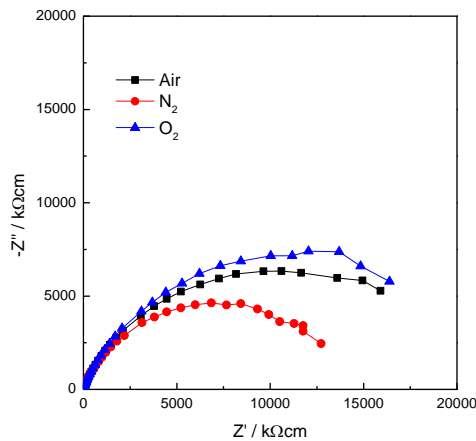


Figure 4-42: RT, Z^* plot for $y = 0.025$ quenched from 1500 °C in liquid nitrogen, measured in air, O_2 and N_2 .

Conductivity (σ_b , σ_{gb} and σ_t) data for $y = 0.025$ quenched from 1500 °C in liquid nitrogen were extracted from M'' , Z'' and Z^* data respectively for N_2 atmosphere are plotted against reciprocal temperature between RT and 200 °C in Arrhenius format, Figure 4-43 (a) which are included for comparison. Similar behaviour was observed for air and O_2 atmospheres (not shown). Bulk and grain boundary conductivity data are compared in Figure 4-43 (b) and (c) to illustrate the change in σ_b and σ_{gb} with temperature in different atmospheres. The change in atmospheres shows a slight

increase in σ_{gb} since N_2 was higher at any presented temperature, Figure 4-43 (c), whereas σ_b did not show a big change under different atmospheres, Figure 4-43 (b).

All Arrhenius format and temperature dependence of resistivity show clearly PTCR behaviour which is presented in Figure 4-44. Similar bulk resistivity data were observed for all atmospheres, Figure 4-44 (a) whereas, grain boundary resistivity data show a weaker PTCR behaviour. Lower conductivity was shown in a nitrogen atmosphere compared to oxygen and air which show similar conductivity.

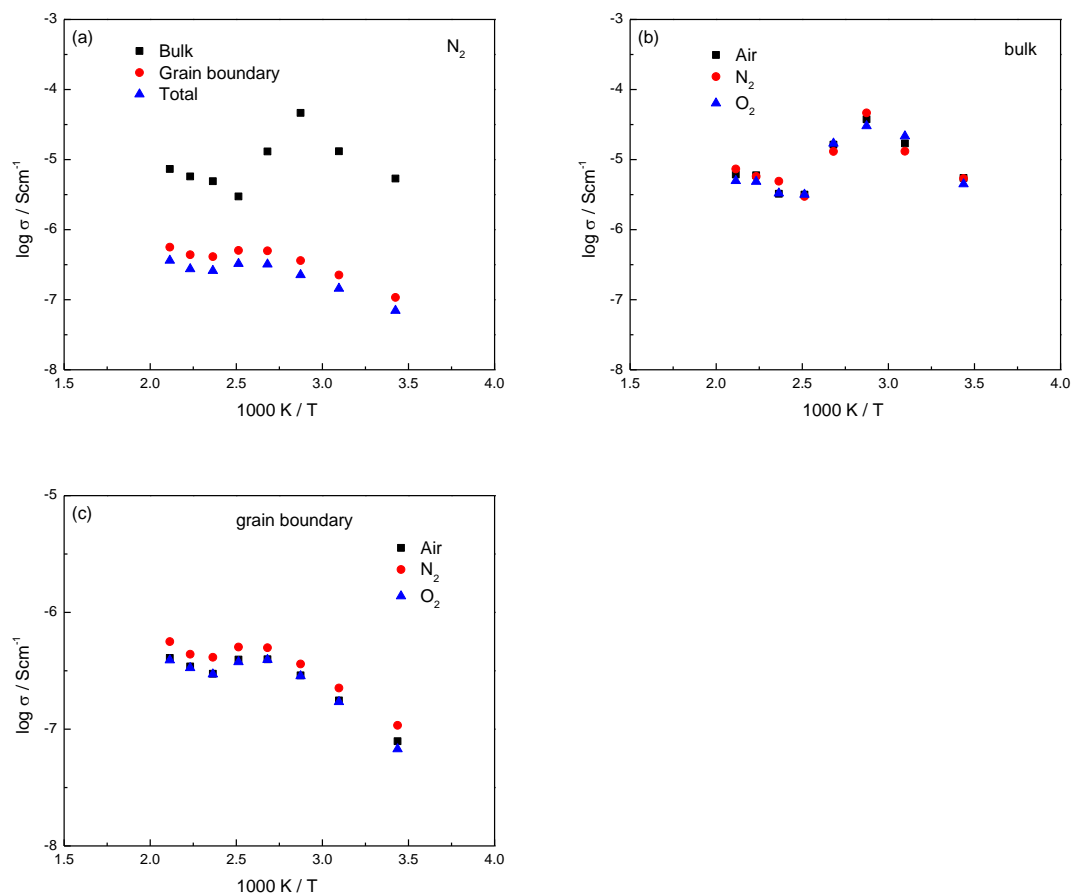


Figure 4-43: Arrhenius plots of σ_b , σ_{gb} and σ_t in N_2 for $y = 0.025$ quenched from $1500 \text{ }^\circ\text{C}$ in liquid nitrogen (a), and of σ_b (b) and σ_{gb} (c) in air, N_2 and O_2 .

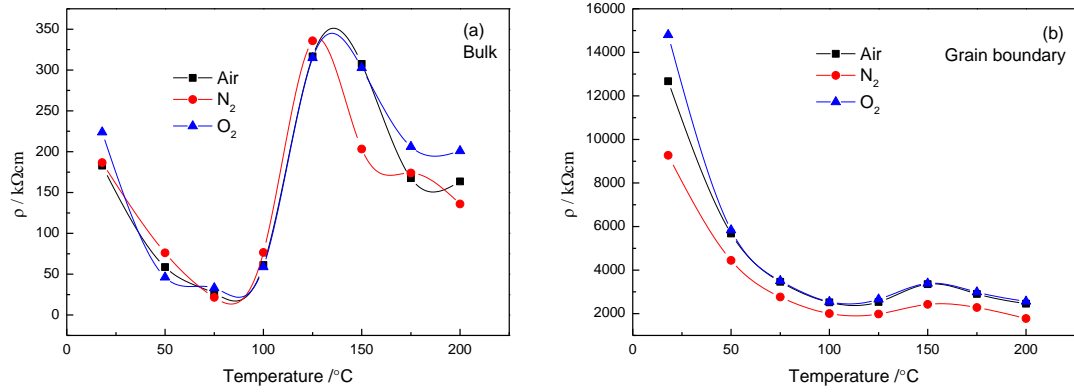
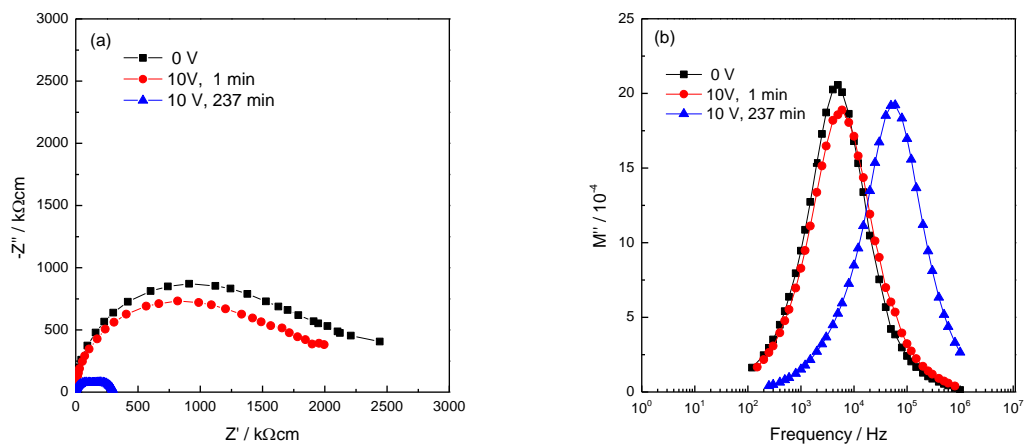


Figure 4-44: Resistivity of bulk (a) and grain boundary (b) as function of temperature in air, N_2 and O_2 for $y = 0.025$ quenched from 1500°C in liquid nitrogen.

(4) Effect of application of a small dc bias voltage

The effect of applying a small dc bias is shown for $y = 0.05$, SC in Figure 4-45. R_T decreases gradually with time and reached a steady-state value after 237 min (a) which confirms that conduction is p-type. Figure 4-45 (c) shows that the high frequency capacitance plateau was unaffected by the dc bias and had a value $\sim 2.00 \times 10^{-11} \text{ Fcm}^{-1}$ whereas, the low frequency capacitance dispersion was affected with dc bias and shifted to higher capacitance. This increase was time-dependent. R_T returned to its original value after removing dc bias after ~ 1820 min, Figure 4-46.



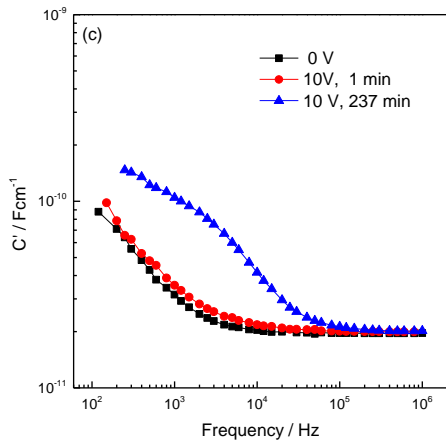


Figure 4-45: (a) Z^* plot (b) M'' plot and (c) C' plot at 400 °C before and after a voltage of 10 V was applied at different measuring times.

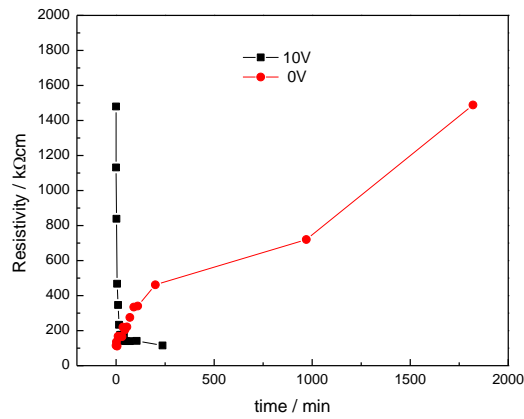


Figure 4-46: Total resistance at 400 °C with 10V bias and after removing the dc bias at different times in air.

(C) Y-A sample:

(1) Typical impedance data

Impedance data for Y-A sample of $\nu = 0.015$, 1350 °C, air, SC was highly insulating at room temperature with $R > 10^8 \Omega\text{cm}$. At high temperatures, two overlapping arcs are present in Z^* plots, Figure 4-47 (a), which correspond to the two Debye peaks in the $-Z''/M''$ spectroscopic plots, Figure 4-47 (b) at 425 °C. Spectroscopic plots of C' , Figure 4-47 (c), also reveal the existence of two plateaux: one at higher frequency with $C' \sim 3.76 \times 10^{-11} \text{ Fcm}^{-1}$ and one at lower frequency with $C' \sim 2.51 \times 10^{-9} \text{ Fcm}^{-1}$.

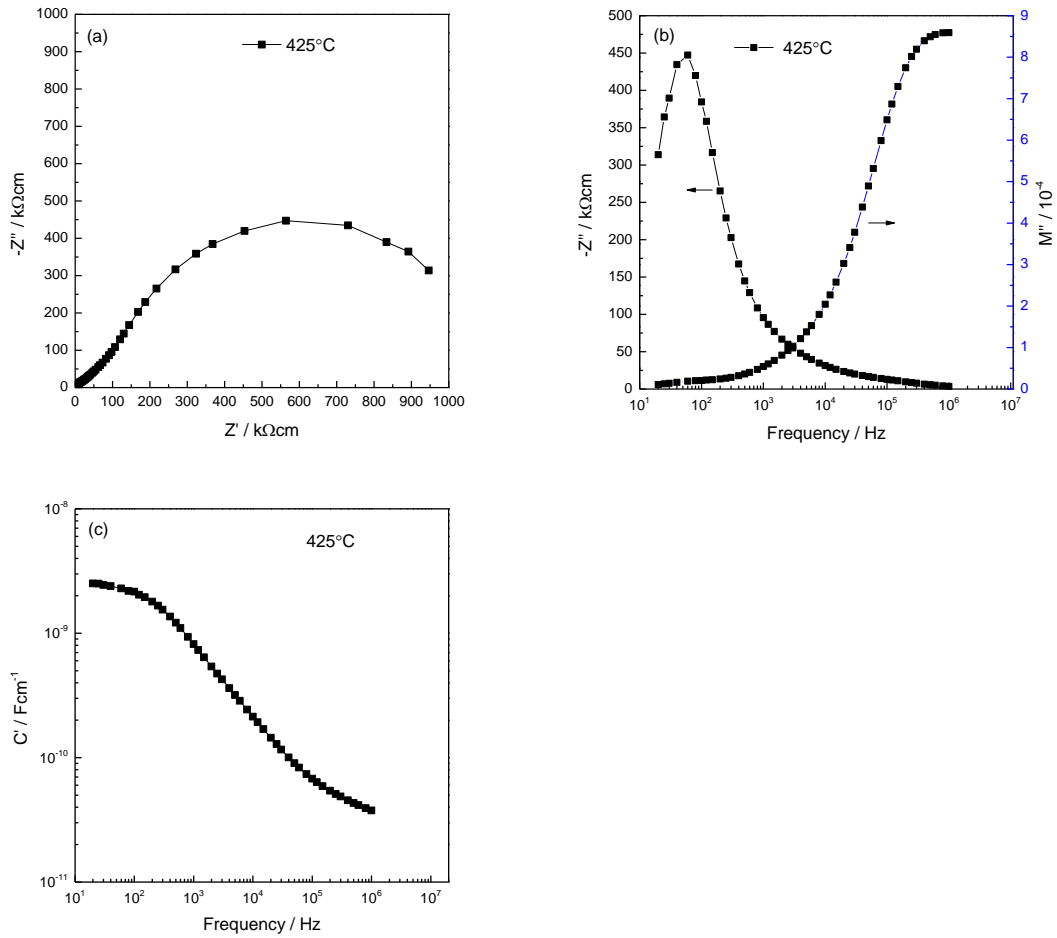


Figure 4-47: 425 °C IS data for $\nu = 0.015$, slow cooled from 1350 °C, (a) Z^* plot, (b) $-Z''$, M'' plots and (c) C' plot.

Resistivity values are shown in conventional Arrhenius format in Figure 4-48. Conductivity data exhibit linear behaviour with an activation 1.49 eV for grain boundary conductivity but with a much reduced activation energy 0.78 eV for bulk conductivity.

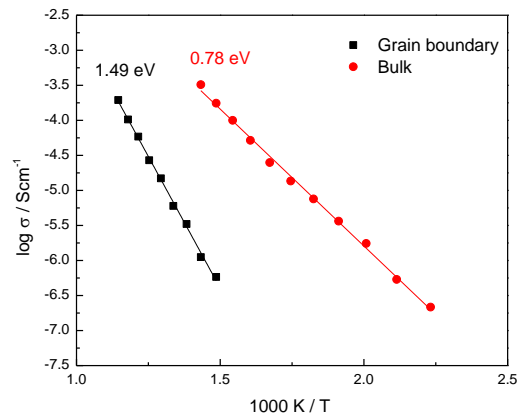


Figure 4-48: Arrhenius plots of the bulk and grain boundary conductivity data against reciprocal temperature for $\nu = 0.015$, SC from 1350 °C.

A different sample, SC in air from 1500 °C was studied but still highly insulating at room temperature, showing slightly higher conductivity than the sample slow cooled in air from 1350 °C (not shown).

(2) Effect of cooling rate

Impedance data for Y-A sample of $\nu = 0.015$, 1350 °C, air, Q at RT with Ag and In-Ga electrodes are shown in Figure 4-49 with electrode-dependent low frequency impedance response.

Room temperature impedance data showed two overlapping arcs with a high frequency intercept. Two arcs were present with Ag electrodes with a high frequency, non-zero intercept on the real axis, Figure 4-49 (a) whereas, the Z^* plots show an incomplete, single high frequency arc with similar resistance value estimated at a nonzero high frequency intercept for sample with In-Ga electrodes. When In-Ga electrodes were used, the low frequency arc disappeared. Figure 4-49 (b) shows one Debye peak in the Z'' spectroscopic plots, associated with the large arc in Z^* for sample with Ag electrodes whereas, the Z'' incline at high frequency was observed for sample with In-Ga electrodes. Both electrodes show that the M'' incline was dominated by the low R , low C response at high frequency, Figure 4-49 (b), indicating the existence of a semiconducting component and extra peak is clearly apparent at $f_{\max} \sim 3-4 \times 10^4$ Hz for Ag sample. Spectroscopic plots of C' , Figure 4-49 (c), also reveal the existence of three components: one at higher frequency, one at the intermediate frequency and one at lower frequency which is associated with electrode-sample interface. PTCR effect was observed for both electrodes with higher conductivity values for In-Ga electrodes as shown in Figure 4-50 and 51.

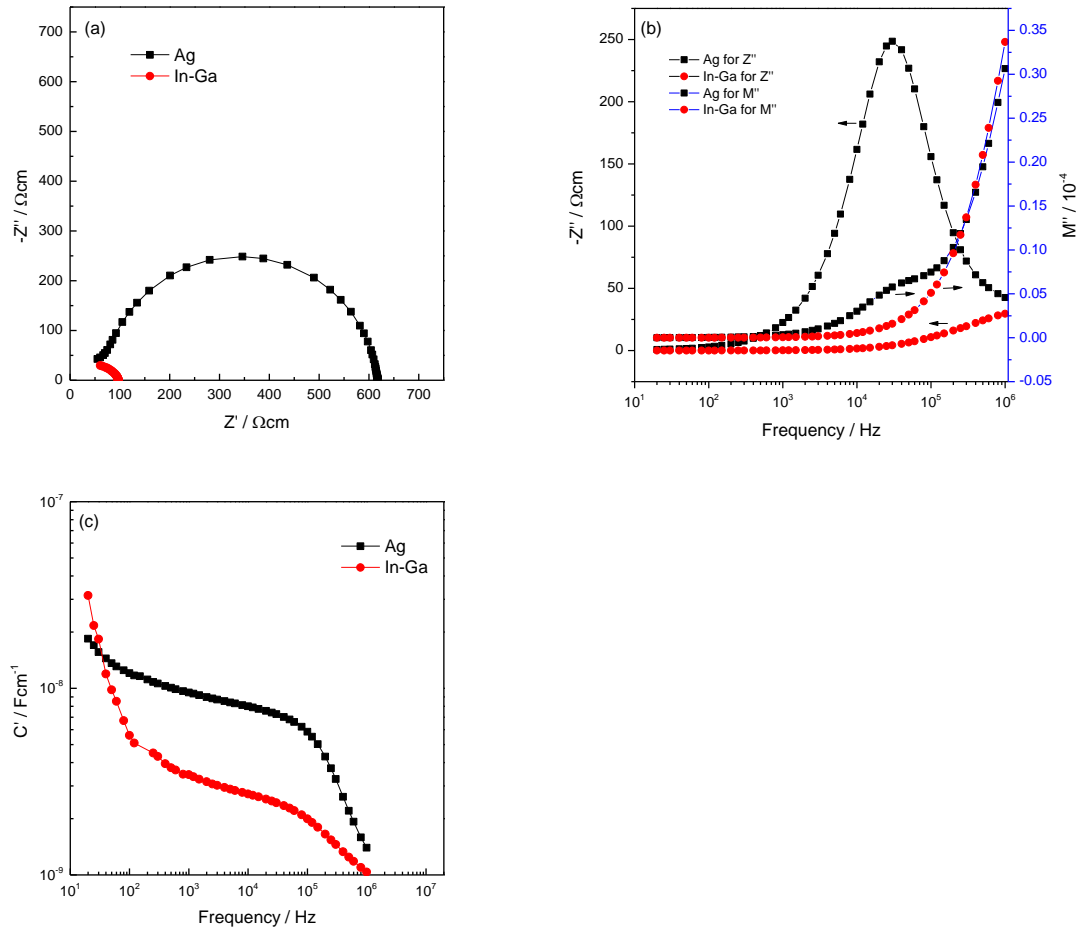


Figure 4-49: RT, IS data for $\nu = 0.015$, quenched from 1350 °C, (a) Z^* plot, (b) $-Z''$, M'' plots and (c) C' plot.

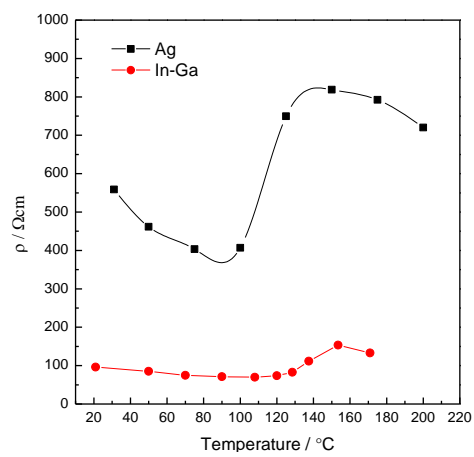


Figure 4-50: Total resistivity as function of temperature.

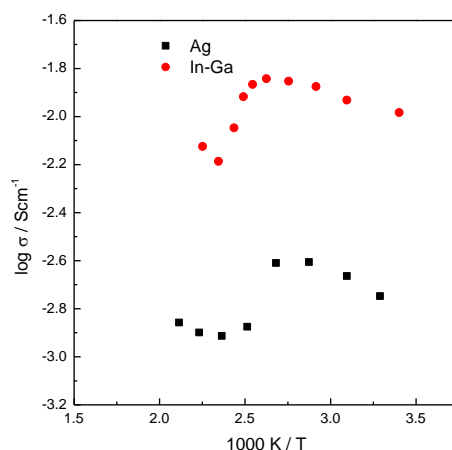
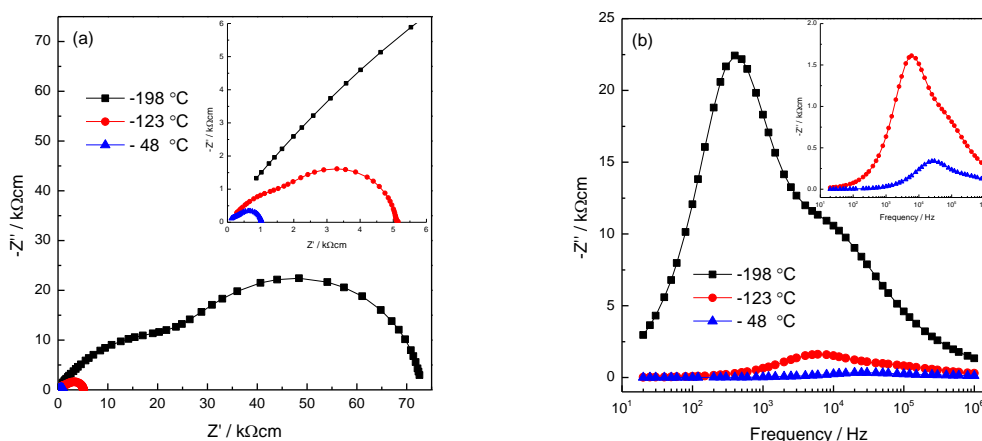


Figure 4-51: Arrhenius plots of the total conductivity data against reciprocal temperature.

To carry out a more thorough investigation of the electrical properties, low temperature impedance data are shown in Figure 4-52. Two semicircular arcs are observed in Z^* plots, Figure 4-52 (a). Resistance values of the non-zero high frequency arc were obtained from intercepts on the real, Z' axis. These two arcs correspond to the two Debye peaks in the Z'' spectroscopic plots, 4-52 (b). The intermediate frequency shoulder peak in Z'' was not well-resolved. The high frequency incline in the M'' data was observed for all measured temperatures which is consistent with a semiconductive region, 4-52 (c). Capacitance, C' data, did not attain a plateau at high frequencies, 4-52 (d) whereas, they are mostly frequency-independent at low frequencies.



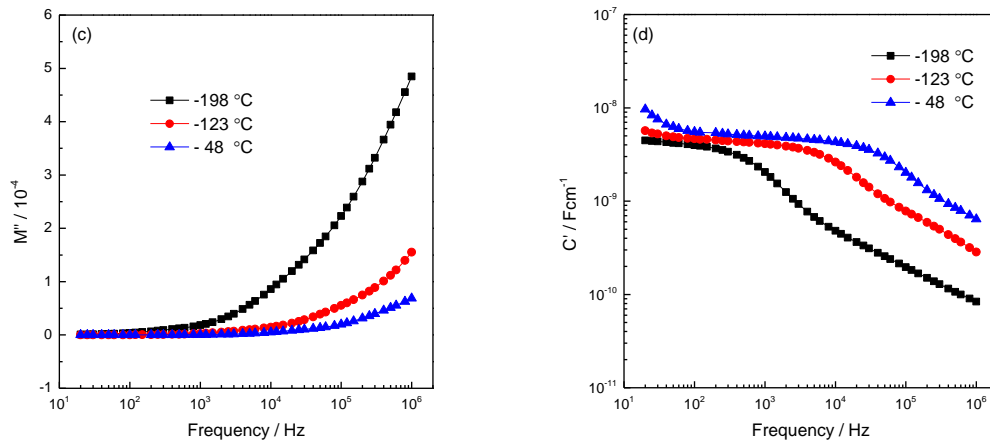


Figure 4-52: Low temperature, IS data for $\nu = 0.015$, quenched from 1350 °C, (a) Z^* plot, (b,c) $-Z''$, M'' plots and (d) C' plot.

Capacitance data were extracted from the high frequency arc in Z^* and plotted against temperature, Figure 4-53. Data illustrate characteristic capacitance maxima corresponding to the rhombohedral-orthorhombic (-110 °C) and the tetragonal-orthorhombic (2 °C) transitions. Arrhenius plots show curved Arrhenius behaviour with different possible conduction mechanisms, depending on different temperature ranges, Figure 4-54.

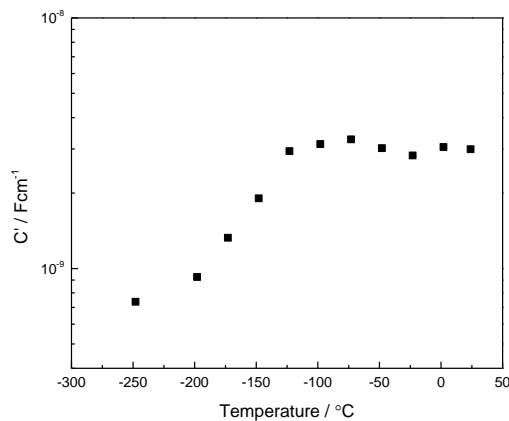


Figure 4-53: Capacitance data (extracted from the high frequency arc in Z^*) against temperatures, for sample with Ag electrodes.

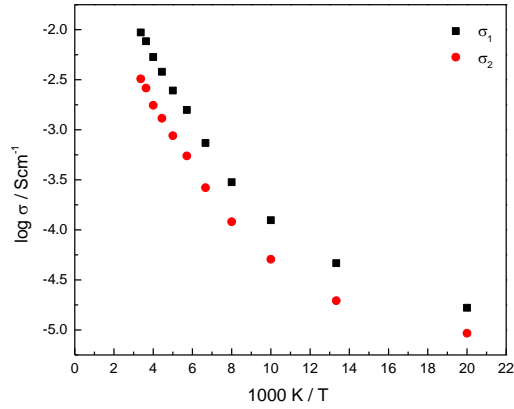


Figure 4-54: Arrhenius plots of conductivity data (extracted from Z^*) against reciprocal temperature.

(3) Effect of oxygen partial pressure

IS measurements were made in different atmospheres at 350 °C for slow cooled sample, Figure 4-55 and RT for quenched sample, Figure 4-56. Figure 4-55 shows that the sample resistance mostly remains unchanged with atmosphere for high frequency arc whereas, the low frequency arc changed with atmosphere. Figure 4-56 shows that the low frequency arc with Ag electrodes disappeared with In–Ga electrodes, indicating it to be associated with an electrode effect. As the measuring atmosphere changed, the sample resistance mostly remains unchanged.

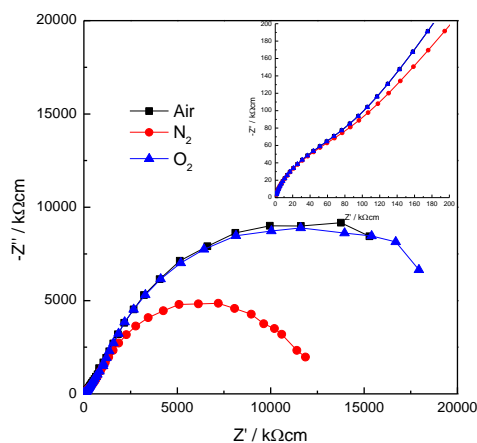


Figure 4-55: 350 °C, Z^* plot for $\nu = 0.015$, slow cooled from 1350 °C in different atmospheres with Pt electrodes.

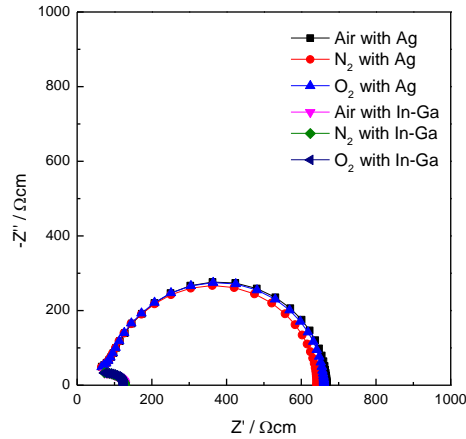
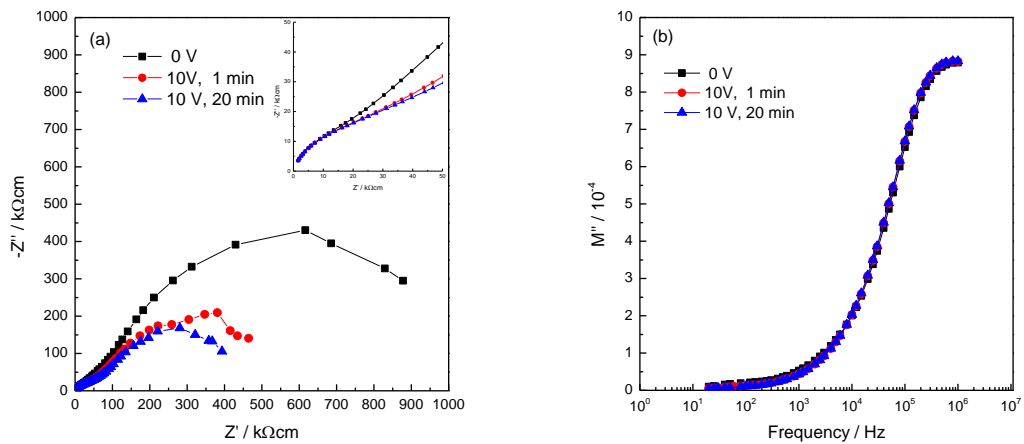


Figure 4-56: RT, Z^* plot for $\nu = 0.015$, quenched from $1350\text{ }^\circ\text{C}$ in different atmospheres with Ag and In-Ga electrodes.

(4) Effect of application of a small dc bias voltage

IS was studied with application of a small dc bias for a sample of composition $\nu = 0.015$, which had been sintered in air at $1350\text{ }^\circ\text{C}$ for 12 h followed by slow cooling to room temperature and measured at $425\text{ }^\circ\text{C}$. The results are shown in Figure 4-57. Z^* and M'' plots show that R_1 was unchanged with dc bias Figure 4-57 (a) and (b) whereas, R_2 was voltage/time-dependent, showing a gradual reduction of R_2 with increasing dc bias. Figure 4-57 (c) shows that the capacitance values were unchanged with dc bias. The recovery of R_2 after removal of the dc bias was observed (not shown). On removal of the dc bias, a steady state was reached within about ~ 60 min.



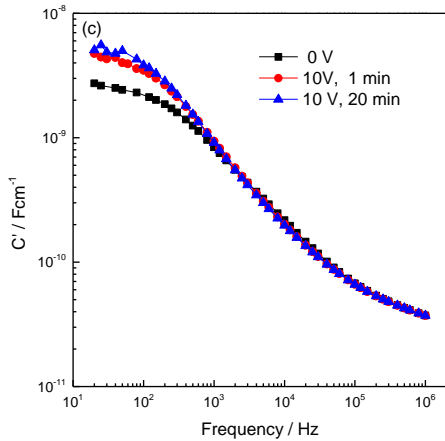
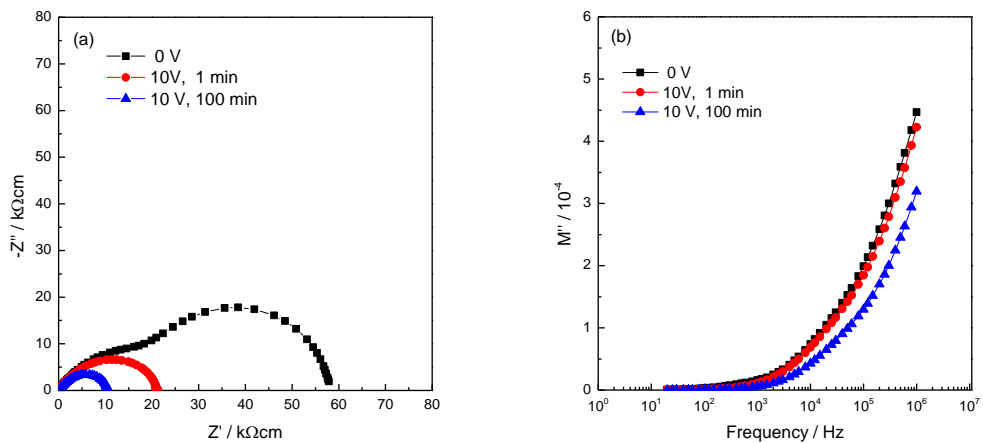


Figure 4-57: (a) Z^* plot (b) M'' plot, (c) Z'' plot and (d) C' plot at 425 °C before and after a voltage of 10 V was applied at different measuring times with Ag electrodes.

The effect of applying a small dc bias to the sample quenched from 1350 °C is shown for $\nu = 0.015$ in Figure 4-(58-61) for two temperatures, -263 °C and RT. Z^* plot shows that at -263 °C, R_T decreases gradually with time and reached a steady-state value after 100 and 325 min, Figure 4-58 (a) and 4-60 (a) respectively and low frequency arc disappeared. The Z'' spectroscopic plots showed two peaks; the low frequency peak disappeared with dc bias and the initial M'' low frequency shoulder peak decreased and the M'' incline shifted towards higher frequency, Figure 4-58 (b,c) and 4-60 (b,c). Figure 4-58 (d) and 4-60 (d) shows that the high and low frequency capacitance data were affected with dc bias. This increase was time-dependent. R_T returned to its original value after removing dc bias after ~ 740 and 150 min, Figure 4-58 and 4-61.



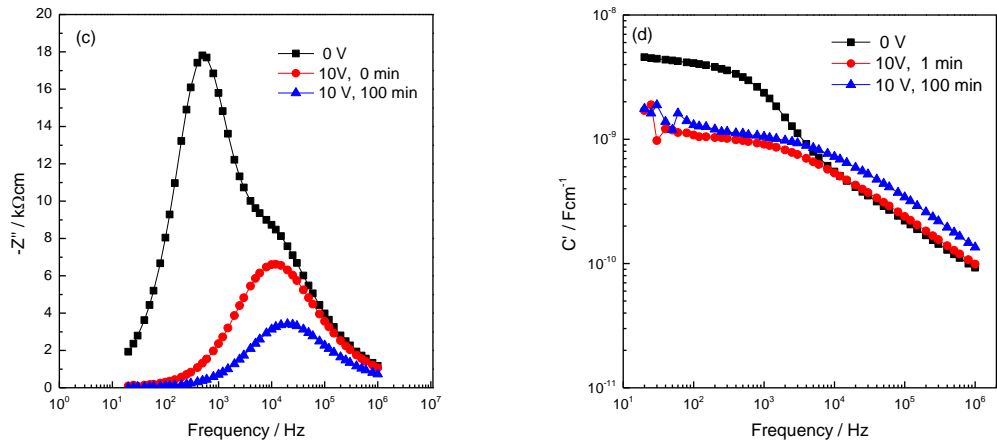


Figure 4-58: (a) Z^* plot (b) M'' plot, (c) Z'' plot and (d) C' plot at $-263\text{ }^\circ\text{C}$ before and after a voltage of 10 V was applied at different measuring times with Ag electrodes.

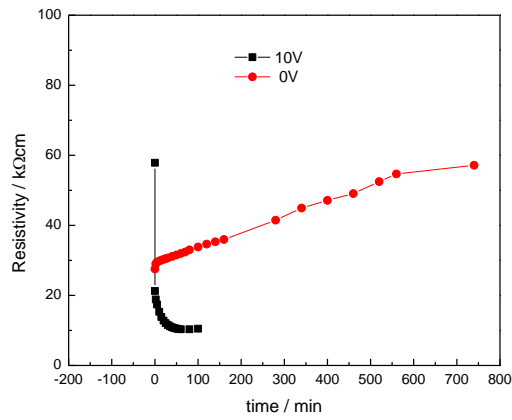
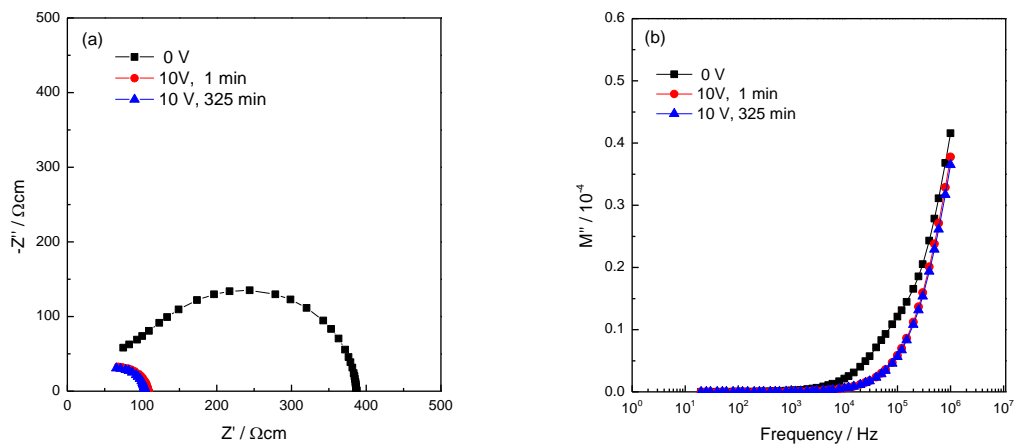


Figure 4-59: Total resistance at $-263\text{ }^\circ\text{C}$ with 10V bias and after removing the dc bias at different times in air with Ag electrodes.



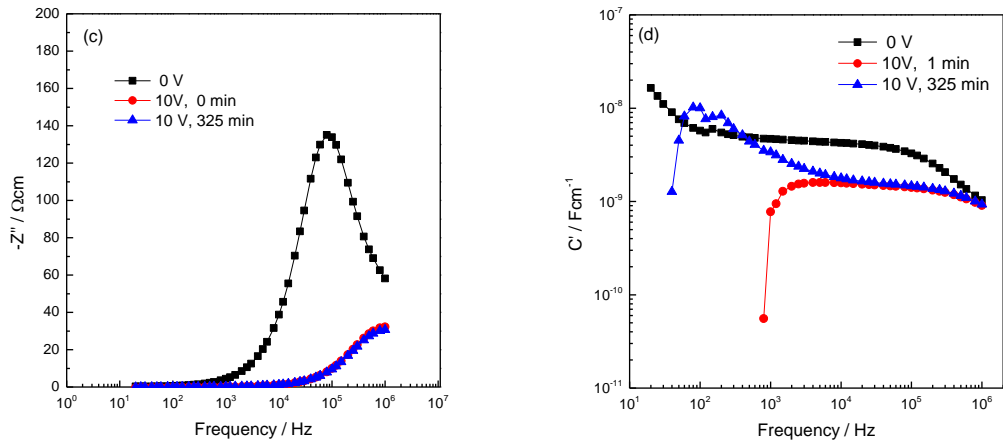


Figure 4-60: (a) Z^* plot (b) M'' plot, (c) Z'' plot and (d) C' plot at RT before and after a voltage of 10 V was applied at different measuring times with Ag electrodes.

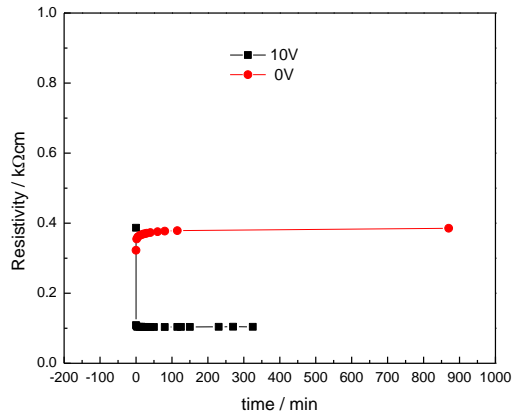


Figure 4-61: Total resistance at RT with 10V bias and after removing the dc bias at different times in air with Ag electrodes.

Similar effect was observed for the same sample but with In-Ga electrodes at -223°C (not shown) as R_T decreases with dc bias.

4.4 Discussion

Phase diagram study of Y-doped BaTiO₃

The composition triangle, BaO–TiO₂–YO_{1.5} is shown in Figure 4-62, on which are superposed loci of the three composition series based on BaTiO₃ with the three possible mechanisms: acceptor, self and donor for substituting Y for Ba and/or Ti. The phase assemblages, according to the ternary phase diagram compositions are listed in Table 4-13. A clear picture of the ternary phase diagram was accurately determined by investigating about 27 different compositions.

Figure 4-63 shows an expanded ternary phase diagram for BaO–TiO₂–YO_{1.5} system based on the presented results in previous sections. The solid solution compositions and the solid solution limits of the three composition mechanisms were determined.

Main features of the diagram are as follows:

First, an extensive range of tetragonal BT solid solutions forms between $x = 0$ to 0.05; with increasing x and y , there is transformation usually to cubic BT polymorph for acceptor and self-compensation joins which has been reported in the literature for acceptor doping [36, 50]. Second, the cubic polymorph was obtained over the range $x = 0.05 - 0.1$ and $y = 0.05 - 0.075$ for acceptor and self-compensation joins respectively. Third, the hexagonal BT polymorph was obtained over the range $x = 0.05 - 0.15$ for only acceptor join. Fourth, donor join shows tetragonal BT polymorph until $v = 0.015$. The solubility limit of Y in Ti-site was to found be at $\sim x = 0.15$ and a small amount of YBa₃Ti₂O_{8.5} as second phase was detected by XRD with increasing x . Smaller solid solution limit of Y in self-compensation join was obtained up to $\sim y = 0.075$ with precipitation of YBa₃Ti₂O_{8.5} or Y₂Ti₂O₇ as secondary phase which is in a good agreement with literature for the minority phase [73]. Two phases that could be indexed as monoclinic Ba₆Ti₁₇O₄₀ and cubic pyrochlore Y₂Ti₂O₇ were identified above the Y solubility on the A-site join at $\sim v = 0.015$. These two phases were widely found in literature [20, 24, 50, 74-76]. The reaction with TiO₂ could form the cubic pyrochlore Y₂Ti₂O₇.

An increase in heating temperature and prolonging the heating period did not show any pure phase at $v > 0.015$.

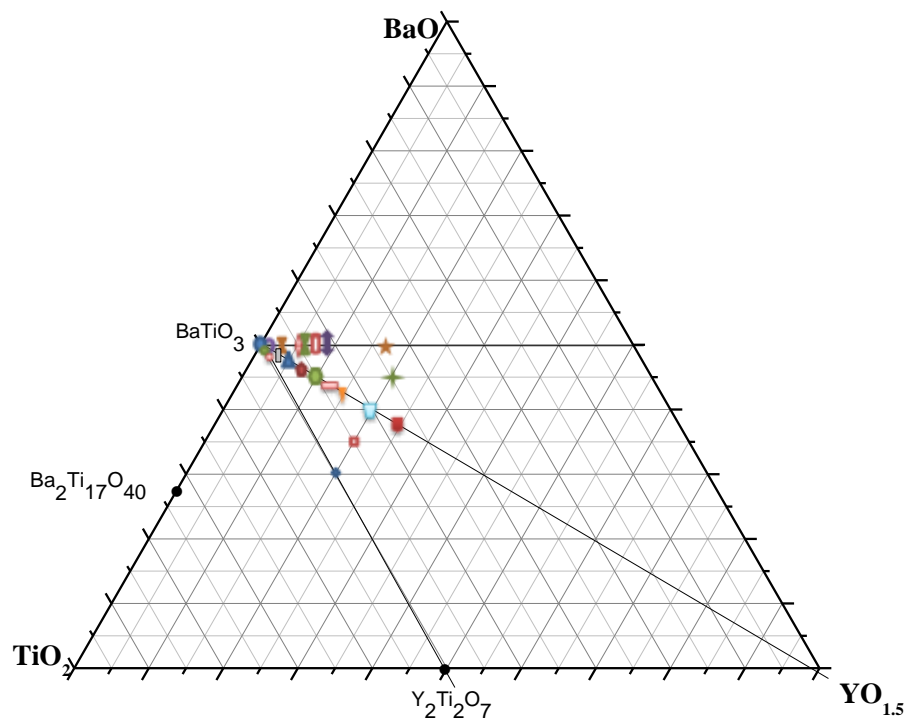


Figure 4-62: Composition triangle BaO–TiO₂–YO_{1.5} showing mostly the compositions studied on acceptor, self and donor joins.

Table 4-13: Phase assemblages of samples labelled in Figure 4-62, h: hexagonal YBa₃Ti₂O_{8.5}, h-BT: hexagonal BaTiO₃, c-BT: cubic BaTiO₃ and t-BT: tetragonal BaTiO₃.

Symbol	Formula	Structure phase
⦿	50BaO 49TiO ₂ 1YO _{1.5} = Ba Ti _{0.98} Y _{0.02} O _{2.99}	t-BT
⊠	50BaO 47.5TiO ₂ 2.5YO _{1.5} = Ba Ti _{0.95} Y _{0.05} O _{2.975}	c-BT
⬠	50BaO 45TiO ₂ 5YO _{1.5} = Ba Ti _{0.90} Y _{0.10} O _{2.95}	c-BT or h-BT
⊞	50BaO 44TiO ₂ 6YO _{1.5} = Ba Ti _{0.88} Y _{0.12} O _{2.94}	h-BT
⬢	50BaO 42.5TiO ₂ 7.5YO _{1.5} = Ba Ti _{0.85} Y _{0.15} O _{2.925}	h-BT
⬆	50BaO 41.25TiO ₂ 8.75YO _{1.5} = Ba Ti _{0.825} Y _{0.175} O _{2.9125}	h-BT + h
★	50BaO 33.3TiO ₂ 16.7YO _{1.5} = BaTi _{0.666} Y _{0.334} O _{2.833}	h
✦	45BaO 35TiO ₂ 20YO _{1.5} = Ba _{0.9} Ti _{0.7} Y _{0.4} O _{2.9}	c-BT + h

□	$48.75\text{BaO } 48.75\text{TiO}_2 \text{ } 2.5\text{YO}_{1.5} = \text{Ba}_{0.975} \text{Ti}_{0.975} \text{Y}_{0.05} \text{O}_3$	t-BT
▲	$47.5\text{BaO } 47.5\text{TiO}_2 \text{ } 5\text{YO}_{1.5} = \text{Ba}_{0.95} \text{Ti}_{0.95} \text{Y}_{0.10} \text{O}_3$	c-BT
◆	$46.25\text{BaO } 46.25\text{TiO}_2 \text{ } 7.5\text{YO}_{1.5} = \text{Ba}_{0.925} \text{Ti}_{0.925} \text{Y}_{0.15} \text{O}_3$	c-BT
◇	$45\text{BaO } 45\text{TiO}_2 \text{ } 10\text{YO}_{1.5} = \text{Ba}_{0.9} \text{Ti}_{0.9} \text{Y}_{0.2} \text{O}_3$	c-BT + $\text{Y}_2\text{Ti}_2\text{O}_7$
▭	$43.75\text{BaO } 43.75\text{TiO}_2 \text{ } 12.5\text{YO}_{1.5} = \text{Ba}_{0.875} \text{Ti}_{0.875} \text{Y}_{0.25} \text{O}_3$	c-BT + $\text{Y}_2\text{Ti}_2\text{O}_7$
▽	$42.5\text{BaO } 42.5\text{TiO}_2 \text{ } 15\text{YO}_{1.5} = \text{Ba}_{0.85} \text{Ti}_{0.85} \text{Y}_{0.3} \text{O}_3$	c-BT + h
▵	$40\text{BaO } 40\text{TiO}_2 \text{ } 20\text{YO}_{1.5} = \text{Ba}_{0.8} \text{Ti}_{0.8} \text{Y}_{0.4} \text{O}_3$	c-BT + h
◆	$37.5\text{BaO } 37.5\text{TiO}_2 \text{ } 25\text{YO}_{1.5} = \text{Ba}_{0.75} \text{Ti}_{0.75} \text{Y}_{0.5} \text{O}_3$	c-BT + h
■	$35\text{BaO } 45\text{TiO}_2 \text{ } 20\text{YO}_{1.5} = \text{Ba}_{0.7} \text{Ti}_{0.9} \text{Y}_{0.4} \text{O}_{3.1}$	c-BT + $\text{Y}_2\text{Ti}_2\text{O}_7$
◆	$30\text{BaO } 50\text{TiO}_2 \text{ } 20\text{YO}_{1.5} = \text{Ba}_{0.6} \text{Ti} \text{Y}_{0.4} \text{O}_{3.2}$	t-BT + $\text{Y}_2\text{Ti}_2\text{O}_7$

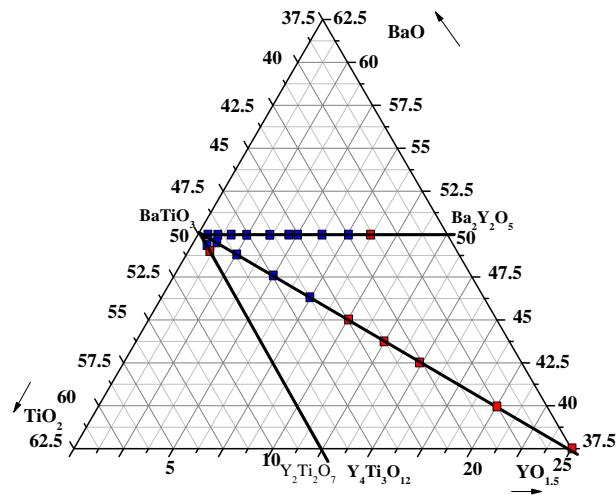
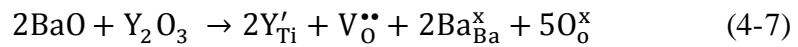


Figure 4-63: Expanded solid solution area of composition triangle BaO–TiO₂–YO_{1.5} showing the single phase (blue symbol) and mixture phase (red symbol) on acceptor, self and donor joins.

Preliminary studies had shown that the doping of BaTiO₃ with Y in the B-site has a solid solubility limit at around 12.2 at.% at 1515 °C [50]. The crystal structure is tetragonal for ($x < 0.059$) and cubic for ($x \geq 0.059$) [36, 41, 53], but another study indicates that the solubility for Y'_{Ti} is close to or less than 3.0 mol% [40]. Ren et al. reported recently that the solubility limit of Ti-site is determined to be $x = 0.02$ [77]. Makovec et al. reported a different behaviour; the solubility of Ti-site is 15 mol. The cubic phase was mainly obtained when samples heating at 1400°C and hexagonal polymorph of BaTiO₃ was exclusively obtained after heating at 1500°C [20]. The

high temperature hexagonal phase of BT appeared to be destabilised by replacing Ti with Y. Therefore, some literature did not obtain this hexagonal polymorph. The destabilisation occurred in this region where the transition from hexagonal to cubic phase was expected. The hexagonal phase was the first product of reaction. High temperatures and prolonged heating was required to transfer to cubic phase. It was mostly kinetically-stable with these conditions.

Oxygen loss can change the phase from tetragonal to hexagonal BT which is commonly obtained in literature [78] which is associated with incorporation of Y^{3+} ions at Ti sites by this reaction:



Results on samples heated at 1420–1600 °C to study the nature of the cubic-hexagonal phase transition, indicated that the equilibrium state was reached only very slowly. Many days sometimes were required to achieve a single phase product. The formation of the thermodynamically-stable product can be observed as the final reaction which may be due to its reaction pathway proceeding through a sequence of stages which involve metastable phases under these reaction conditions as the synthesis is an extremely difficult and slow process. This is an example of Ostwald's rule of successive reactions. The sequence of reactions can be understood in terms of free-energy changes whereby each consecutive phase arrangement has a lower free-energy than the previous one. The gradual reduction in entropy of the phase arrangement may be considered to be the key driving force for the manifestation of a sequence of stages whereby it would begin with high entropy caused by the disordered nature of the starting materials and finish with the low entropy of the final crystalline product [61, 79].

Experiments often yielded a number of different polymorphs or phases, alternating between the hexagonal and tetragonal-cubic phase at different temperatures, independently of whether the method applied involves quenching to room temperature or slowly cooling.

Results in this chapter are in good agreement with some literature [41], indicating that the substitution of Y is more favourable at B-site rather than A-site which disagrees with the simulation study of Lewis and Catlow [34], the experimental

suggestions of Lee and Smyth [80], Xue *et al.* [35] and others [40, 77] as they suggested that Ti-site doping is less favourable, that Ba-site doping is considerably more favourable and either Ba or Ti can be substituted by only very small amounts of yttrium, generally < 1 at.%, or 3 at.% even with excess TiO₂ or BaO [36].

It has been suggested that this investigation indicates that ionic radii are not the only factor for determination the favourable site-occupancy but there are others that can affect the substitution of Y in BT such as the polarizability, characteristics of electronic structure, and bonding character of Y³⁺ ions [41].

The results obtained in this study compared with other published results confirm that there is a divergence with those results which may be explained by several causes. One factor may be the influence of platinum foil during sintering, which led us to the usage of another technique to remove the influence of platinum foil by placing the samples on a small quantity of powder of the same composition as the pellet. This means that there is no direct contact between sample and Pt. Subsequently, this method was used.

It is possible for the samples to lose Ba at high sintering temperatures. Therefore, addition of excess Ba to compensate for loss of Ba may be used to return the composition to the acceptor join.

Graule *et al.* reported that the electronic properties and the microstructure were different between samples sintered with direct contact between the samples and Pt compared to those sintered without direct physical contact between the two [81].

Some samples required high temperatures for complete reaction with longer heating period to obtain the final state.

Lattice parameter values showed the tetragonality of Y-B and Y-AB samples decreased since *a* increases, but *c* decreases with *x,y* and the unit cell volume increased. The change in *V* was linear, reached a plateau and remained unchanged with further increase in *x,y* which suggested that the solid solution limit was achieved, in agreement with the appearance of a secondary phase. Similar behaviour was reported in the literature with Y-A samples which showed that *a*, *c* and *V* all increased with increasing *v*. This behaviour indicated that the Ba²⁺ was replaced by Y³⁺ which was smaller than Ba²⁺ [73, 77].

T_C is dependent on the substitution site and charge compensation mechanism. The substitution of Y at Ti sites shifted the Curie point (T_C) to lower temperatures, which is expected from consideration of Goldschmidt's tolerance factor, in agreement with literature [36, 77].

Ferroelectric domains and T_C can be affected by formation of oxygen vacancy as a result of replacing Ti with Y.

T_C shifted to higher temperatures for Y-A samples, which is in good agreement with some literature [73, 77] but contrary to other studies which showed that T_C shifts to lower temperature [82] and another study showed that no shifting was observed but only reduction of the high permittivity value with increasing ν [76]. Shifting of T_C to higher temperatures was attributed to formation of a core-shell structure and it was suggested that a misfit between the grain core and grain shell may lead to stresses and shift T_C to higher temperatures [73, 83].

The high permittivity value of BT is associated with the displacement of Ti-atom from their its central octahedral position (TiO_6), yielding a noncentrosymmetric tetragonal structure and spontaneous polarisation. A decrease in the peak values of permittivity with an increase in the level of doping was observed as result of the ferroelectricity loss, which lose their polar domain structure.

The height and sharpness of the permittivity maximum peak which reduce at low dopant concentrations are attributed to onset of a diffusion phase transition accompanied by a broadened permittivity peak at high dopant concentrations at $x \geq \sim 0.05$ as result of the coalescence of the individual phase transitions. Similar behaviour was observed in some literature [36] but not in other literature [77]. The transition from normal-ferroelectric to ferroelectric relaxor was observed. A frequency-dependent relaxor character, occurred at high dopant concentrations at $x, y \geq \sim 0.05$ either on B-site or AB site whereas, this behaviour was not observed on the donor join which is attributed to the low solid solubility of Y at the Ba site. The origin of the relaxor phenomenon in Y-doped $BaTiO_3$ is unclear but may a result of Y^{3+} doping, leading to increasing the degree of disorder and may not be associated with compositional fluctuations since normal ferroelectric behaviour with an inhomogeneous distribution of Y-dopant was observed at $x < 0.05$ and ferroelectric

relaxor behaviour with a homogenous distribution of the Y-dopant was observed at $x \geq 0.05$. This behaviour may also be associated with substitution of yttrium onto both Ba and Ti sites, with disruption of the cooperative linking between the ferroelectrically-active TiO_6 octahedra, which was observed with La^{3+} [67], Ho^{3+} [61] or Zr^{4+} [84] doped BT as for example the defects were produced in the form of non-ferroelectric ZrO_6 octahedra with Zr^{4+} or Ti vacancies with La^{3+} .

An excellent Curie–Weiss behaviour was observed for ϵ_r values at temperatures $> T_C$. The Curie–Weiss temperature (T_0) was obtained from linear extrapolation of the inverse ϵ_r , over the high temperature range ($1/\epsilon_r = 0$). These results as well show that the ferroelectric-paraelectric phase transition around the Curie temperature continues to sub-ambient temperatures at high concentrations [85].

The tetragonality decreased with an increase in the level of doping, as evident in both hysteresis loop and Raman spectroscopy results which are consistent with the results obtained from lattice parameter and T_C data.

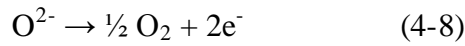
The average grain size of Y-B was greater than Y-A and Y-AB samples which is consistent with literature data [77]. The grain growth of materials is mostly based on diffusion during sintering [77]. Acceptor dopant, Y in place of Ti, is important for involving creation of oxygen vacancies where their mobility can accelerate the diffusion which gives rise to greater grain size in Y-B than Y-A and Y-AB. The EDS result of $x = 0.05$ and 0.10 in Y-B join fits with observations reported in literature [42]. Some samples showed an increase in porosity, which may be attributed to the amount of dopant added as yttria is refractory. The EDS result of $x = 0.175$ in Y-B join showed that the needle-shaped grains have a higher Ba content than the spherical ones. These grains are comparable to those obtained in pure $\text{Ba}_3\text{Ti}_2\text{YO}_{8.5}$ ceramics [48] and is evidence of the secondary phase that may be present in this sample.

Decreasing grain size with an increasing Y content was observed, leading to distortion of the crystalline lattice [38] which is in good agreement with literature data [23, 40, 82, 86, 87]. Therefore, extra grain boundaries were apparent.

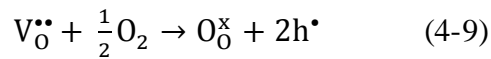
Impedance spectroscopy was used to establish the electrical properties of grain and grain boundary regions of Y-B, Y-AB and Y-A ceramics, showing strong

dependence on the substitution mechanism and in certain cases the dopant concentrations, cation stoichiometry, cooling rate, oxygen partial pressure, dc bias and sintering temperature/time. For Y-B samples, IS showed that samples with $0.09 \leq x \leq 0.15$ were electrically homogenous and showed an insulating bulk response that can be modelled on a single parallel RC element but inclusion of a CPE may be needed for accurate data fitting.

Samples with $0 < x < 0.07$ showed similar electrical conduction behaviour to undoped BT; samples were electrically inhomogeneous and consisted of insulating grains and grain boundaries with room temperature resistivity values $> 10^6 \Omega\text{cm}$ with no evidence of semiconductivity in any of the samples studied whether they were cooled slowly or quenched from high temperatures (1200-1600 °C). All can be modelled approximately using an electrical equivalent circuit with two parallel sets of Resistor-Capacitor (RC) elements connected in series, which represented the grain (bulk) and grain boundary response. Arrhenius plots of bulk and grain boundary conductivity data gave low activation energy values of the bulk component. There may be two reasons for this. It may be associated with loss of oxygen at elevated temperature, consistent with the literature [88], by the idealized reaction:



Alternatively, oxygen vacancies which are the charge compensation mechanism as result of incorporation of Y^{3+} ions at Ti sites may act as acceptors where extra charge is compensated by ionized oxygen vacancies. This is associated with filling of the oxygen vacancies by absorption of oxygen, leaving holes as charge carriers, by the following equation:



Most samples were highly insulating without a notable occurrence of oxygen loss in these samples because the oxygen vacancies were created by Y dopant.

σ_{gb} of BT is lower than σ_{gb} of Y-doped BT whereas E_{A} of BT is higher than E_{A} of Y-doped BT, which may show that a fully-oxidised condition was observed for the grain boundary component. There were no apparent trends and systematic

concentration dependence in the σ and E_A data with increase of Y content for samples processed under similar conditions.

The conduction mechanism in these samples was shown to be p-type by resistance measurements made in different atmospheres and dc bias for $x = 0.05$. The resistance increased reversibly with decreasing pO_2 in the measuring atmosphere and, therefore, holes were the principal charge carriers. This result is in good agreement with literature [22, 27, 40] as the equilibrium electrical conductivity of Y-B ceramics was studied with $x = 0.02, 0.03$ and 0.05 . All of them show p-type characteristic.

The p-type conduction mechanism was also shown by a decrease in the resistance at $400\text{ }^\circ\text{C}$ under the influence of a dc bias voltage of 10 V . The resistance decrease was independent of various kinds of electrode material but was shown by both bulk and grain boundary regions of the sample. On application of a dc bias, the resistance of the sample decreased, rapidly at first, before reaching a steady state. It increased again after removing the dc bias, and finally recovered the original state.

Impedance data for Y-AB samples showed that the electrical properties differed significantly depending on whether the sample was cooled slowly or quenched from $1500\text{ }^\circ\text{C}$. A series of tests was performed for a sample of one composition, $y = 0.025$, which was subjected to a variation of cooling treatments. The bulk resistance decreased for the sample quenched in air compared to the slow cooled sample. Further decrease in resistance was obtained for the sample quenched in liquid nitrogen. The slow-cooled sample had lower conductivity and higher activation energy than the quenched sample. This was attributed to the partial re-oxidation on slow cooling of the ceramics. Electrons were the main charge carriers for the quenched samples and the conduction mechanism was n-type whereas, holes and p-type was found for slow cooled samples.

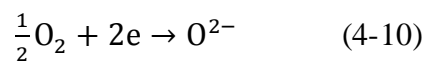
A different characteristic behaviour was observed for the samples quenched rapidly after heating at $1500\text{ }^\circ\text{C}$. M'' spectra show two broad peaks, one was located at higher frequencies, which moved to lower frequencies with increasing temperature, and the other which moved to higher frequencies with increasing temperature.

Resistance data of the low frequency M'' peak showed a (PTCR) effect with an increase in resistance commencing at T_C , which passed through a maximum at some

higher temperature before decreasing to give the thermally activated, negative temperature coefficient resistivity (NTCR) effect. No temperature-dependent data have been obtained for the higher frequency peak as the high frequency M'' peak shifted to even higher frequency (above the upper frequency limit for the impedance analyser, ~ 10 MHz), confirming that this component became more conductive. The observation of PTCR behaviour for the quenched sample is conventionally ascribed to a space-charge effect [89] at the grain surfaces. The electric field associated with the ferroelectric domains in regions below T_C can reduce SB or the barrier height to conduction through the space charge layer [90]. Above T_C , disappearance of domains was observed. A core-shell structure was observed as the semiconducting core was surrounded by the depletion layer [88].

The conduction mechanism was also studied at constant temperature, in which the atmosphere (O_2 , air and N_2) was varied during measurement for a sample of composition $y = 0.05$, sintered in air at 1500 °C for 12 h followed by slow cooling to room temperature.

A similar behaviour was obtained in all three atmospheres for both components, but with different magnitude of the conductivity. The conductivities of both low and high frequency components increased as the measuring atmosphere changed from N_2 to air to O_2 . Absorption of oxygen at the sample surface can be observed with the increase in pO_2 in the measuring atmosphere, according to this reaction:



Since, with increasing pO_2 , electrons are withdrawn from the sample as a direct consequence and the conductivities of the two components increase as a consequence, the conduction mechanism is p-type. The n-type conduction was observed for the quenched sample which was clearly shown by application different atmospheres.

Further insight into the conduction mechanisms for the same sample was obtained, by application of different dc bias voltages over the range 0 V to 10 V during impedance measurements. Both components were very voltage-dependent and in

particular, the associated conductivity increased with increasing dc bias, showing p-type behaviour.

The IS results obtained from slow cooled, Y-A ceramics were substantially different to those obtained from quenched ceramics and were strongly dependent on the cooling rate. The slow cooled sample was insulating for $\nu > 0.01$, in agreement with literature as semiconducting behaviour was observed for donor-doped BT at relatively low doping levels (up to a concentration of around 0.1-0.6 at.%) whereas, with increasing donor contents, insulating behaviour was observed [35, 74, 76, 90-93].

Slow cooled sample showed that the high frequency component was unchanged with dc bias which is related to interfacial effect due to a mismatch in the Fermi level of the interface between both sides or as a result of the existence of space-charge phenomena accompanying by trapped mobile carriers at the interface [94]. This effect is attributed to a grain boundary because the low frequency component was unchanged with different electrodes. The capacitance value of the low-frequency component was $\sim 2.73 \times 10^{-09} \text{ Fcm}^{-1}$ which may confirm that this effect is the Schottky barrier at the grain-grain interfaces.

Y-A sample was very conductive at room temperature for the sample quenched from 1350 °C which is consistent with literature [82] as the sample avoided oxidation during cooling. The resistance was dependent strongly on the electrode material. A Schottky barrier at the electrode-sample interface was observed. The sample was dominated by low frequency arc with Ag electrodes but this effect disappeared with In-Ga electrodes which gave rise to ohmic contact and reduced the effective Schottky barrier impedance. PTCR effect was observed for both electrodes but the sample with In-Ga electrodes showed a weak PTCR effect which is associated with the higher concentration of adsorbed oxygen acceptor states in the barrier region during cooling, as reoxidation occurred.

Conductivity data for Ag sample were generally independent of $p\text{O}_2$ in which the electrode-sample interface was not affected under different atmospheres whereas, strong reduction of resistance was observed with dc bias.

4.5 Conclusions

Y^{3+} is an amphoteric dopant. The solid solubility limit of Y^{3+} in BT is dependent on the substitution mechanism. The solubility limits are determined as when Y^{3+} replaced Ti^{4+} in the BT lattice. The maximum solubility was 15 mol % when Y replaced Ti while when Y^{3+} replaced Ba^{2+} the maximum solubility was 1.5 mol %. When Y^{3+} replaced both Ba^{2+} and Ti^{4+} , the maximum solubility was 7.5 mol %. Therefore, the substitution of Ti^{4+} seems to be favoured as Y^{3+} forms most extensive solid solutions when substituted at Ti-site with charge compensation by creation of oxygen vacancies.

Doping Y^{3+} ions led to the expansion of cell volume, inhibition of the grain growth for the BT materials, reduction of the tetragonality, c/a ratio, of $BaTiO_3$, shifting T_C to lower temperatures for Y-B and Y-AB samples and to higher temperatures for Y-A samples.

The height and sharpness of the permittivity peak maximum were observed at low dopant concentrations whereas there was a diffusion phase transition accompanied by a broadened permittivity peak at high dopant concentrations at $x,y \geq \sim 0.05$.

A relaxor character, frequency-dependent occurred at high dopants concentrations at $x,y \geq \sim 0.05$.

Doping Y^{3+} at the B-site showed insulating behaviour even with quenching since its doping mechanism is dominated by oxide ion vacancy compensation. Doping Y^{3+} at the AB-site and A-site showed semiconductivity for quenched samples.

IS results showed that Y-B samples with $0.09 \leq x \leq 0.15$ were electrically homogenous and samples with $0 < x < 0.07$ and Y-AB and Y-A samples were electrically inhomogeneous.

A PTCR characteristic was obtained for a quenched sample for $y = 0.025$ at Y-AB and $v = 0.015$ at Y-A.

4.6 References

- [1] C.C. Barry, N.M. Grant, Ceramic materials: science and engineering, New York, Springer, (2007) 635-651.
- [2] H. Kishi, N. Kohzu, Y. Mizuno, Y. Iguchi, J. Sugino, H. Ohsato, T. Okuda, Effect of occupational sites of rare-earth elements on the microstructure in BaTiO₃, Japanese journal of applied physics, 38 (1999) 5452.
- [3] H. Kishi, Y. Mizuno, H. Chazono, Base-metal electrode-multilayer ceramic capacitors: past, present and future perspectives, Japanese Journal of Applied Physics, 42 (2003) 1.
- [4] C. Metzmacher, K. Albertsen, Microstructural Investigations of Barium Titanate-Based Material for Base Metal Electrode Ceramic Multilayer Capacitor, Journal of the American Ceramic Society, 84 (2001) 821-826.
- [5] H. Chazono, H. Kishi, DC-electrical degradation of the BT-based material for multilayer ceramic capacitor with Ni internal electrode: impedance analysis and microstructure, Japanese Journal of Applied Physics, 40 (2001) 5624.
- [6] D.M. Smyth, Multilayer ceramic capacitors with base metal electrodes, in, IEEE, pp. 369-373.
- [7] D.F.K. Hennings, Multilayer ceramic capacitors with base metal electrodes, in, IEEE, pp. 135-138.
- [8] A.J. Moulson, J.M. Herbert, Electroceramics Chapman and Hall, New York, 41 (1990).
- [9] M.T. Buscaglia, V. Buscaglia, M. Viviani, P. Nanni, Atomistic simulation of dopant incorporation in barium titanate, Journal of the American Ceramic Society, 84 (2001) 376-384.
- [10] O. Saburi, Properties of semiconductive barium titanates, Journal of the physical Society of Japan, 14 (1959) 1159-1174.
- [11] M. Issa, Electrical properties of polycrystalline PTCR barium titanate, Journal of materials science, 27 (1992) 3685-3692.
- [12] M. Kuwabara, K. Hamamoto, Electric field-induced birefringence in single grain boundaries of PTCR barium titanate ceramics above the Curie point, Ferroelectrics, 290 (2003) 71-81.
- [13] G. Jonker, Halogen treatment of barium titanate semiconductors, Materials Research Bulletin, 2 (1967) 401-407.

- [14] W. Heywang, Semiconducting barium titanate, *Journal of Materials Science*, 6 (1971) 1214-1224.
- [15] A. Feteira, D.C. Sinclair, J. Kreisel, Average and local structure of $(1-x)\text{BaTiO}_3-x\text{LaYO}_3$ ($0 \leq x \leq 0.50$) ceramics, *Journal of the American Ceramic Society*, 93 (2010) 4174-4181.
- [16] Y. Sakabe, Y. Hamaji, H. Sano, N. Wada, Effects of rare-earth oxides on the reliability of X7R dielectrics, *Japanese journal of applied physics*, 41 (2002) 5668.
- [17] H. Saito, H. Chazono, H. Kishi, N. Yamaoka, X 7 R Multilayer Ceramic Capacitors with Nickel Electrodes, *Japanese journal of applied physics*, 30 (1991) 2307-2310.
- [18] K.J. Park, C.H. Kim, Y.J. Yoon, S.M. Song, Y.T. Kim, K.H. Hur, Doping behaviors of dysprosium, yttrium and holmium in BaTiO_3 ceramics, *Journal of the European Ceramic Society*, 29 (2009) 1735-1741.
- [19] M.H. Lin, H.Y. Lu, Site-occupancy of yttrium as a dopant in BaO-excess BaTiO_3 , *Materials Science and Engineering: A*, 335 (2002) 101-108.
- [20] D. Makovec, Z. Samardžija, M. Drofènik, Solid solubility of holmium, yttrium, and dysprosium in BaTiO_3 , *Journal of the American Ceramic Society*, 87 (2004) 1324-1329.
- [21] Y. Nakano, A. Satoh, A. Hitomi, T. Nomura, *Ceramic Transactions*, Vol. 32, Dielectric Ceramics, Processing, Properties, and Application, Am. Ceram. Soc, (1993) 119-128.
- [22] J.H. Jeong, M.G. Park, Y.H. Han, Defect chemistry of Y doped BaTiO_3 , *Journal of Electroceramics*, 13 (2004) 805-809.
- [23] J.H. Kim, Y.H. Han, Effects of Y_2O_3 Addition on the Microstructure and Electrical Property of TiO_2 -excess BaTiO_3 , in, *Trans Tech Publ*, pp. 1025-1028.
- [24] S. Sato, Y. Nakano, A. Sato, T. Nomura, Mechanism of improvement of resistance degradation in Y-doped BaTiO_3 based MLCCs with Ni electrodes under highly accelerated life testing, *Journal of the European Ceramic Society*, 19 (1999) 1061-1065.
- [25] W.-C. Yang, C.-T. Hu, I.N. Lin, Effect of $\text{Y}_2\text{O}_3/\text{MgO}$ co-doping on the electrical properties of base-metal-electroded BaTiO_3 materials, *Journal of the European Ceramic Society*, 24 (2004) 1479-1483.

- [26] M.-H. Lin, H.-Y. Lu, Site-occupancy of yttrium as a dopant in BaO-excess BaTiO₃, *Materials Science and Engineering: A*, 335 (2002) 101-108.
- [27] J.H. Kim, S.H. Yoon, Y.H. Han, Effects of Y₂O₃ addition on electrical conductivity and dielectric properties of Ba-excess BaTiO₃, *Journal of the European Ceramic Society*, 27 (2007) 1113-1116.
- [28] J. Qi, L. Li, Y. Wang, Y. Fan, Z. Gui, Yttrium doping behavior in BaTiO₃ ceramics at different sintered temperature, *Materials Chemistry and Physics*, 82 (2003) 423-427.
- [29] C.-H. Kim, K.-J. Park, Y.-J. Yoon, M.-H. Hong, J.-O. Hong, K.-H. Hur, Role of yttrium and magnesium in the formation of core-shell structure of BaTiO₃ grains in MLCC, *Journal of the European Ceramic Society*, 28 (2008) 1213-1219.
- [30] J.C.C. Lin, W.C.J. Wei, C.Y. Huang, Sintering Behavior and Dielectric Properties of Yttria/Silica-Coated BaTiO₃ Material with Mn-Si-O Glass, *Journal of the American Ceramic Society*, 93 (2010) 4103-4109.
- [31] Y. Tsur, T.D. Dunbar, C.A. Randall, Crystal and defect chemistry of rare earth cations in BaTiO₃, *Journal of Electroceramics*, 7 (2001) 25-34.
- [32] H. Kishi, Y. Mizuno, H. Chazono, Base-metal electrode-multilayer ceramic capacitors: past, present and future perspectives, *Japanese journal of applied physics*, 42 (2003) 1-15.
- [33] H. Kishi, N. Kohzu, J. Sugino, H. Ohsato, Y. Iguchi, T. Okuda, The effect of rare-earth (La, Sm, Dy, Ho and Er) and Mg on the microstructure in BaTiO₃, *Journal of the European Ceramic Society*, 19 (1999) 1043-1046.
- [34] G. Lewis, C. Catlow, Defect studies of doped and undoped barium titanate using computer simulation techniques, *Journal of Physics and Chemistry of Solids*, 47 (1986) 89-97.
- [35] L.A. Xue, Y. Chen, R.J. Brook, The influence of ionic radii on the incorporation of trivalent dopants into BaTiO₃, *Materials Science and Engineering: B*, 1 (1988) 193-201.
- [36] J. Zhi, Z. Yu, C. Ang, Crossover of Ba(Ti,Y)O₃ Solid Solutions to Ba₃Ti₂YO_{8.5}-BaTiO₃ Composites and their Dielectric Properties, *Journal of the American Ceramic Society*, 88 (2005) 2775-2779.
- [37] Y. Tsur, A. Hitomi, I. Scrymgeour, C.A. Randall, Site occupancy of rare-earth cations in BaTiO₃, *Japanese Journal of Applied Physics*, 40 (2001) 255.

- [38] I.A.L.-H. M. Paredes-Olguín, C.Gómez-Yáñez, F.P.Espino-Cortés, Compensation mechanisms a thigh temperature in Y-doped BaTiO₃, *PhysicaB*, 410 (2013) 157-161.
- [39] R. Roseman, T. Armstrong, R. Buchanan, PTCR properties and aging characteristics in Y₂O₃ doped BaTiO₃ ceramics with ZrO₂ additions, in: *Applications of Ferroelectrics, 1990.*, IEEE 7th International Symposium on, IEEE, 1990, pp. 463-467.
- [40] J. Jeong, E.J. Lee, Y.H. Han, J.H. Jeong, J.H. Hwang, Electrical Properties of BaTiO₃ Co-Doped with Rare Earth and Mn, (2005).
- [41] J. Zhi, A. Chen, Y. Zhi, P.M. Vilarinho, J.L. Baptista, Incorporation of yttrium in barium titanate ceramics, *Journal of the American Ceramic Society*, 82 (1999) 1345-1348.
- [42] Z. Samardžija, D. Makovec, M. Čeh, EPMA and Microstructural Characterization of Yttrium Doped BaTiO₃ Ceramics, *Microchimica Acta*, 132 (2000) 383-386.
- [43] G. Lewis, C. Catlow, R. Casselton, PTCR effect in BaTiO₃, *Journal of the American Ceramic Society*, 68 (1985) 555-558.
- [44] D.M. Smyth, *The defect chemistry of metal oxides*, Oxford University Press. ISBN-10: 0195110145. ISBN-13: 9780195110142, 1 (2000) 304.
- [45] P. Blanchart, J.F. Baumard, P. Abelard, Effects of Yttrium Doping on the Grain and Grain-Boundary Resistivities of BaTiO₃ for Positive Temperature Coefficient Thermistors, *Journal of the American Ceramic Society*, 75 (1992) 1068-1072.
- [46] X. Kuang, X. Jing, C.-K. Loong, E.E. Lachowski, J.M.S. Skakle, A.R. West, A New Hexagonal 12-Layer Perovskite-Related Structure: Ba₆R₂Ti₄O₁₇ (R= Nd and Y), *Chemistry of materials*, 14 (2002) 4359-4363.
- [47] W.P.T. Derks, H.A.M. Van Hal, C. Langereis, The formation of YBa₃Ti₂O_{8.5} in the reaction of YBa₂Cu₃O₇ with SrTiO₃, *Physica C: Superconductivity*, 156 (1988) 62-64.
- [48] A. Chena, Z. Yu, V.M. Ferreira, P.M. Vilarinho, J.L. Baptista, Synthesis and characterization of dielectric compositions in the BaO-rich corner of the BaO-Y₂O₃-TiO₂ ternary system, *Journal of the European Ceramic Society*, 16 (1996) 1051-1056.

- [49] M.M.V. Petrović, J.D. Bobić, T. Ramoška, J. Banys, B.D. Stojanović, Antimony doping effect on barium titanate structure and electrical properties, *Ceramics International*, 37 (2011) 2669-2677.
- [50] A.C. Jing Zhi, Yu Zhi, Paula M. Vilarinho, and João L. Baptista, Incorporation of Yttrium in Barium Titanate Ceramics, *J. Am. Ceram. Soc.*, 82 [5] (1999) 1345–1348.
- [51] H.M. Al-Allak, T.V. Parry, G.J. Russell, J. Woods, Effects of aluminium on the electrical and mechanical properties of PTCR BaTiO₃ ceramics as a function of the sintering temperature, *Journal of materials science*, 23 (1988) 1083-1089.
- [52] G. Liu, R.D. Roseman, Effect of BaO and SiO₂ addition on PTCR BaTiO₃ ceramics, *Journal of Materials science*, 34 (1999) 4439-4445.
- [53] Z. Jing, C. Ang, Z. Yu, P.M. Vilarinho, J.L. Baptista, Dielectric properties of Ba(Ti_{1-y}Y_y)O₃ ceramics, *Journal of Applied Physics*, 84 (1998) 983.
- [54] L. Zhang, L. Ben, O.P. Thakur, A. Feteira, A.G. Mould, D.C. Sinclair, A.R. West, Ferroelectric aging and recoverable electrostrain in BaTi_{0.98}Ca_{0.02}O_{2.98} ceramics, *Journal of the American Ceramic Society*, 91 (2008) 3101-3104.
- [55] M.C. Ferrarelli, C.C. Tan, D.C. Sinclair, Ferroelectric, electrical, and structural properties of Dy and Sc co-doped BaTiO₃, *Journal of Materials Chemistry*, 21 (2011) 6292-6299.
- [56] O.P. Thakur, A. Feteira, B. Kundys, D.C. Sinclair, Influence of attrition milling on the electrical properties of undoped-BaTiO₃, *Journal of the European ceramic society*, 27 (2007) 2577-2589.
- [57] B. Jaffe, W.R. Cook, H. Jaffe, *Piezoelectric ceramics*, Academic press London, 1971.
- [58] N. Ma, B.-P. Zhang, W.-G. Yang, D. Guo, Phase structure and nano-domain in high performance of BaTiO₃ piezoelectric ceramics, *Journal of the European Ceramic Society*, 32 (2012) 1059-1066.
- [59] Z.-Y. Shen, J.-F. Li, Enhancement of piezoelectric constant d₃₃ in BaTiO₃ ceramics due to nano-domain structure, *Journal of the Ceramic Society of Japan*, 118 (2010) 940-943.
- [60] L. Ben, *Synthesis and Characterisation of Rare-earth and Calcium Doped BaTiO₃ Ceramics*, PhD thesis, The University of Sheffield, (2009).

- [61] Y. Liu, A.R. West, Ho-doped BaTiO₃: Polymorphism, phase equilibria and dielectric properties of BaTi_{1-x}Ho_xO_{3-x/2}: 0 ≤ x ≤ 0.17, *Journal of the European Ceramic Society*, 29 (2009) 3249-3257.
- [62] J. Pokorný, U.M. Pasha, L. Ben, O.P. Thakur, D.C. Sinclair, I.M. Reaney, Use of Raman spectroscopy to determine the site occupancy of dopants in BaTiO₃, *Journal of Applied Physics*, 109 (2011) 114110.
- [63] A. Feteira, D.C. Sinclair, The influence of nanometric phase separation on the dielectric and magnetic properties of (1-x)BaTiO₃-xLaYbO₃ (0 ≤ x ≤ 0.60) ceramics, *Journal of Materials Chemistry*, 19 (2009) 356-359.
- [64] S. Miao, J. Pokorny, U.M. Pasha, O.P. Thakur, D.C. Sinclair, I.M. Reaney, Polar order and diffuse scatter in Ba(Ti_{1-x}Zr_x)O₃ ceramics, *Journal of Applied Physics*, 106 (2009) 114111.
- [65] I.J. Clark, T. Takeuchi, N. Ohtori, D.C. Sinclair, Hydrothermal synthesis and characterisation of BaTiO₃ fine powders: precursors, polymorphism and properties, *Journal of materials chemistry*, 9 (1999) 83-91.
- [66] P. Ren, N. Masó, A.R. West, Hole conductivity in oxygen-excess BaTi_{1-x}Ca_xO_{3-x+δ}, *Physical Chemistry Chemical Physics*, 15 (2013) 20943-20950.
- [67] F.D. Morrison, D.C. Sinclair, A.R. West, Electrical and structural characteristics of lanthanum-doped barium titanate ceramics, *Journal of Applied Physics*, 86 (1999) 6355-6366.
- [68] T. Nagai, K. Iijima, H.J. Hwang, M. Sando, T. Sekino, K. Niihara, Effect of MgO doping on the phase transformations of BaTiO₃, *Journal of the American Ceramic Society*, 83 (2000) 107-112.
- [69] G. Schileo, A. Feteira, K. Reichmann, M. Li, D.C. Sinclair, Structure–property relationships in (1-x)BaTiO₃-xBiGdO₃ ceramics, *Journal of the European Ceramic Society*, 35 (2015) 2479-2488.
- [70] J. Suchanicz, G. Klimkowski, M. Karpierz, U. Lewczuk, I. Faszczowy, A. Pękala, K. Konieczny, M. Antonova, A. Sternberg, Influence of Compressive Stress on Dielectric and Ferroelectric Properties of the (Na_{0.5}Bi_{0.5})_{0.7} Sr_{0.3}TiO₃ Ceramics, in, IOP Publishing, pp. 012038.
- [71] B.D. Begg, K.S. Finnie, E.R. Vance, Raman Study of the Relationship between Room-Temperature Tetragonality and the Curie Point of Barium Titanate, *Journal of the American Ceramic Society*, 79 (1996) 2666-2672.

- [72] U.M. Pasha, H. Zheng, O.P. Thakur, A. Feteira, K.R. Whittle, D.C. Sinclair, I.M. Reaney, In situ Raman spectroscopy of A-site doped barium titanate, *Applied Physics Letters*, 91 (2007) 2908.
- [73] B. Li, S. Zhang, X. Zhou, Z. Chen, S. Wang, Microstructures and dielectric properties of Y/Zn codoped BaTiO₃ ceramics, *Journal of materials science*, 42 (2007) 5223-5228.
- [74] A. Belous, O. V'yunov, L. Kovalenko, D. Makovec, Redox processes in highly yttrium-doped barium titanate, *Journal of Solid State Chemistry*, 178 (2005) 1367-1375.
- [75] A. Belous, O. V'yunov, M. Glinchuk, V. Laguta, D. Makovez, Redox processes at grain boundaries in barium titanate-based polycrystalline ferroelectrics semiconductors, *Journal of materials science*, 43 (2008) 3320-3326.
- [76] O.I. V'yunov, L.L. Kovalenko, A.G. Belous, V.N. Belyakov, Oxidation of reduced Y-doped semiconducting barium titanate ceramics, *Inorganic materials*, 41 (2005) 87-93.
- [77] P. Ren, Q. Wang, X. Wang, L. Wang, J. Wang, H. Fan, G. Zhao, Effects of doping sites on electrical properties of yttrium doped BaTiO₃, *Materials Letters*, 174 (2016) 197-200.
- [78] M.J. Rampling, SYNTHESIS AND CHARACTERISATION OF UNDOPED AND DOPED HEXAGONAL BARIUM TITANATE, PhD thesis, The University of Sheffield, (2003).
- [79] Y. Liu, E.E. McCabe, D.C. Sinclair, A.R. West, Synthesis, structure and properties of the hexagonal perovskite, h-BaTi_{1-x}Ho_xO_{3-x/2}, *Journal of Materials Chemistry*, 19 (2009) 5201-5206.
- [80] R.Y. Lee, S. Witek, D.M. Smyth, Trivalent impurity behavior in BaTiO₃ and SrTiO₃, in, AMER CERAMIC SOC 735 CERAMIC PLACE, PO BOX 6136, WESTERVILLE, OH 43081-6136, pp. 936-936.
- [81] T. Graule, A. Ulrich, M. Wegmann, Influence of platinum foil impurities on sintering of functional ceramics, *Journal of the European Ceramic Society*, 32 (2012) 3567-3573.
- [82] J.K. Lee, K.S. Hong, J.H. Chung, Revisit to the Origin of Grain Growth Anomaly in Yttria-Doped Barium Titanate, *Journal of the American Ceramic Society*, 84 (2001) 1745-1749.

- [83] S. Sato, Y. Fujikawa, T. Nomura, Rare earth doping on temperature-capacitance characteristics for MLCCs with Ni electrode, *Am Ceram Soc Bull*, 79 (2000) 155.
- [84] R. Farhi, M. El Marssi, A. Simon, J. Ravez, A Raman and dielectric study of ferroelectric ceramics, *The European Physical Journal B-Condensed Matter and Complex Systems*, 9 (1999) 599-604.
- [85] F.D. Morrison, D.C. Sinclair, J. Skakle, A.R. West, Novel Doping Mechanism for Very-High-Permittivity Barium Titanate Ceramics, *Journal of the American Ceramic Society*, 81 (1998) 1957-1960.
- [86] C.-S. Chen, C.-C. Chou, Rietveld refinement on BaTiO₃ materials doped with MgO/Y₂O₃ additives, *Ferroelectrics*, 355 (2007) 159-164.
- [87] Y.H. Song, J.H. Hwang, Y.H. Han, Effects of Y₂O₃ on temperature stability of acceptor-doped BaTiO₃, *Japanese journal of applied physics*, 44 (2005) 1310.
- [88] H. Beltrán, E. Cordoncillo, P. Escribano, D.C. Sinclair, A.R. West, Oxygen loss, semiconductivity, and positive temperature coefficient of resistance behavior in undoped cation-stoichiometric BaTiO₃ ceramics, *Journal of applied physics*, 98 (2005) 4102.
- [89] W. Heywang, Barium titanate as a semiconductor with blocking layers, *Solid State Electron*, 3 (1961) 51-58.
- [90] G.H. Jonker, Some aspects of semiconducting barium titanate, *Solid-State Electronics*, 7 (1964) 895-903.
- [91] R. Wernicke, The influence of kinetic processes on the electrical conductivity of donor-doped BaTiO₃ ceramics, *physica status solidi (a)*, 47 (1978) 139-144.
- [92] T. Murakami, T. Miyashita, M. Nakahara, E. SEKINE, Effect of Rare-Earth Ions on Electrical Conductivity of BaTiO₃ Ceramics, *Journal of the American Ceramic Society*, 56 (1973) 294-297.
- [93] W. Guo, L. Li, X. Wu, H. Wang, Z. Zhang, Effect of Y₂O₃ on dielectric properties of BaTiO₃ ceramics [J], *Journal of Rare Earths*, 22 (2004) 208.
- [94] N. Masó, H. Beltrán, E. Cordoncillo, P. Escribano, A.R. West, Electrical properties of Fe-doped BaTiO₃, *Journal of Materials Chemistry*, 16 (2006) 1626-1633.

Chapter 5: Electrical properties of RE³⁺-doped BaTiO₃ at low concentrations

5.1 Introduction

Modified BT ceramics with different RE³⁺ elements to tailor specific applications are widely used for multilayer capacitors (MLCCs) and PTC resistors since the conductivity and electrical degradation can be controlled by concentration levels. Many authors have previously reported the improvement of the ferroelectric properties of BT-based ceramics by doping with RE³⁺ elements. Gd³⁺, Dy³⁺, Ho³⁺, Y³⁺, and sometimes Er³⁺ are magic dopants. The RE³⁺ elements are indeed incorporated into the BaTiO₃ lattice, and in a manner that depends on their ionic radius [1].

It has been established in the literature that the resistivity minimum behaviour is obtained with small amounts of rare earth dopants such as Y, Ho, La, Nd, Sm and Gd at x values in the range ~ 0.1 – 1 at.% [2-5]. This was attributed to the switching in doping mechanism from electronic compensation to an ionic compensation mechanism. The resistance decreases at low concentrations with electronic compensation since the rare earth ions act as a donor dopant. At high concentrations, the resistance increases with an ionic compensation mechanism [3, 4, 6-9]. This transition from electronic to ionic compensation is accompanied by a rapid decrease of grain size [10]. This transition with increasing RE doping was attributed to the grain size reduction and the insulating layer of barium vacancy formed during cooling [11]. It was proposed that grain growth is inhibited by cation vacancies, leading to the transition into an insulator [12-14]. This behaviour was attributed as well to dopant segregation at grain boundaries which can change the grain boundary energy [15, 16].

Impedance spectroscopy is an important technique to investigate the resistivity minimum. As example for this transition, La-doped BT ceramics showed switching of the charge compensation mechanism from electronic to titanium vacancies. IS data showed that such ceramics were electrically inhomogeneous [3, 17]. It was reported that this behaviour is exclusively obtained with coarse-grained samples for La³⁺-doped BT quenched from ≥ 1350 °C in air [3] whereas, it was observed for

Ho³⁺-doped-BT samples which were fired at 1400 °C in air and slow cooled [2]. This may be associated with a non-equilibrium state which is often observed at high temperatures. During high temperature processing, oxygen loss may occur causing electronic compensation associated with n-type semiconductivity. An increase in the resistance is observed in samples sintered at low temperatures or slow-cooled [3]. In contrast, it has been reported that the atmosphere and cooling rate did not affect the semiconductivity for samples studied at the resistivity minimum. Therefore, the resistivity minimum is not associated with loss of oxygen [2]. Semiconducting behaviour can be imparted to BT by RE doping at the Ba site [18-20].

The effect of RE on electrical resistivity of BT ceramics doped with Ln³⁺ (Dy, Ho, Er and Y) over the range of $x = 0.001 - 0.01$ according to the formula of BaTiO₃ + 1/2yLn₂O₃ + 2%TiO₂ was studied [21]. There were significant decreases in resistivity at $v = 0.3\%$ of La-doped BT. Dy, Ho, Er and Y showed wider range of semiconductivity and extra wide range was observed for Y. A single dopant Y of 0.1–0.8 mol% was introduced in the Ba-site to decrease the resistivity [22]. The substitution of Dy, Ho, Er and Y was in the barium sublattice with electronic compensation at low concentrations and switched to titanium substitution at higher concentrations, showing a U-type curve. The highest resistivity which was associated with PTCR behaviour was obtained for Ho doping at $x = 0.003$. It was reported that the critical dopant concentration of the resistivity minimum for Dy-doped BT was ~ 0.4 mol%, slightly higher than 0.3 mol% for another report [23].

It was reported that donor type behaviour was observed for Ba/Ti < 1 and acceptor type behaviour for Ba/Ti > 1 for Er³⁺ [24] Y³⁺ [25] and Gd³⁺ [26]. Er³⁺ can substitute both Ba²⁺ site and Ti⁴⁺ site simultaneously, bringing about donor-acceptor self-compensation [27].

This chapter concerns BaTiO₃ doped with some rare earth elements (RE³⁺), specifically: Gd, Dy, Ho, Y, Er and Yb in order to study the electrical properties and determine the conditions under which a resistivity minimum occurs with increasing RE content for three joints with three possible charge compensation mechanisms. These are: (RE-A) barium site substitution and electronic compensation, (RE-B) titanium site substitution compensated by oxygen vacancies and (RE-AB) self-compensation.

Specifically, the objective for this chapter was to study the possible occurrence of the resistivity minimum with dilute dopant content on three joins for samples quenched and slow cooled with six rare earths. There are three possible mechanisms for semiconductivity that will be considered for generating Ti^{3+} ions:

1- Direct donor doping using dopants of higher valence than the substituted cation. RE acts as a direct donor dopant under the specific conditions with small concentrations of donor dopants according to the following equation: $Ba^{2+} \rightarrow RE^{3+} + e^-$ and general formula $Ba_{1-\nu}RE_{\nu}e_{\nu}TiO_3$, ($[Ba+RE]/[Ti]=1$); this mechanism is expected on the donor join.

2- Oxygen loss at high temperatures according to $O^{2-} \rightarrow 1/2O_2 + 2e^-$, as oxide ions in the lattice give up electrons to form oxygen gas. In principle, this mechanism occurs in pure BT and can be explained to some extent on the donor join, self-join and acceptor join.

3- Dilute dopant contents as double acceptor doping of BT with two acceptors, Ho^{3+} and Ti^{3+} which was suggested in Ho case [2] and was used to explain the occurrence of the resistivity minimum on the acceptor join as a local charge balance mechanism can be provided by reduction of Ti^{4+} to Ti^{3+} . Oxygen vacancies which are created as result of acceptor doping mechanism can be compensated by this local charge balance mechanism. Ti^{4+} can be substituted by two ions for each oxygen vacancy with one Ho^{3+} and Ti^{3+} . Creation of oxygen vacancy for acceptor mechanism and the occurrence of oxygen loss at high temperatures generate Ti^{3+} [2].

Results will be divided to separate sample-electrode and Schottky barrier effects associated with bulk and for grain boundaries. In addition, there are two types of Schottky barrier which have already been discussed in chapter 3. This is associated with PTCR phenomena.

5.2 Experimental procedure

RE (Gd, Dy, Ho, Y, Er and Yb)-doped BaTiO₃ compositions prepared according to 3 systems: BaTi_{1-x}RE_xO_{3-x/2} acceptor doping join (RE-B), Ba_{1-y}Ti_{1-y}RE_{2y}O₃ , self-compensation doping join (RE-AB) and Ba_{1-v}RE_vTiO₃ donor doping join (RE-A) at several concentrations x, y and $v = 0, 0.0001, 0.001$ and 0.01 were prepared by conventional solid state reaction using an agate mortar and pestle as discussed in chapter 2. Further several additional concentrations were studied for Y doping at x, y and $v = 0.0003, 0.0005, 0.003$ and 0.002 . Compositions were fired at 1350 °C for 12 h in air with cooling rate 10 °C/min, reheated at 1350, 1400 and 1450 °C for 12-24 h then quenched to room temperature by withdrawing them from the furnace and allowing to cool in air.

5.3 Results

5.3.1 XRD Results

The XRD patterns of concentrations $x = 0, 0.0001, 0.001$ and 0.01 for Y, Gd, Dy, Ho, Er and Yb-doped BT are not shown but XRD data demonstrated that all samples were tetragonal and phase-pure.

5.3.2 Electrical properties of Yb-doped BT

IS results indicated that all samples on three joins were electrically insulating and did not show any conductivity at room temperature even with rapid quenching in air. The temperature dependence of ϵ' and $\tan \delta$ for pellets of concentrations x, y and $v = 0, 0.0001, 0.001$ and 0.01 which had been sintered and slow cooled from $1350\text{ }^\circ\text{C}$ for 12 h in air with Pt electrodes measured at 250 kHz are shown in Figure 5-1 (a-i) for acceptor (a-c), self-compensation (d-f) and donor (g-i) joins respectively. ϵ' increases with increase in temperature to reach Curie temperature T_C for all compositions, displaying a dielectric constant maximum in the range ~ 1660 - 6150 , Figure 5-1 (a) for Yb-B, ~ 2900 - 4800 , Figure 5-1 (d) for Yb-AB and ~ 4100 - 7100 , Figure 5-1 (g) for Yb-A.

For Yb-B, the value of the permittivity maximum for $x = 0.0001$ was higher than for other samples where ϵ' showed a sharp peak especially at $x = 0.0001$. At $x = 0.01$ ϵ' demonstrated a pronounced diffuse ferroelectric phase transition.

For Yb-AB, the value of the permittivity maximum decreased with increasing x and then increased at $y = 0.01$.

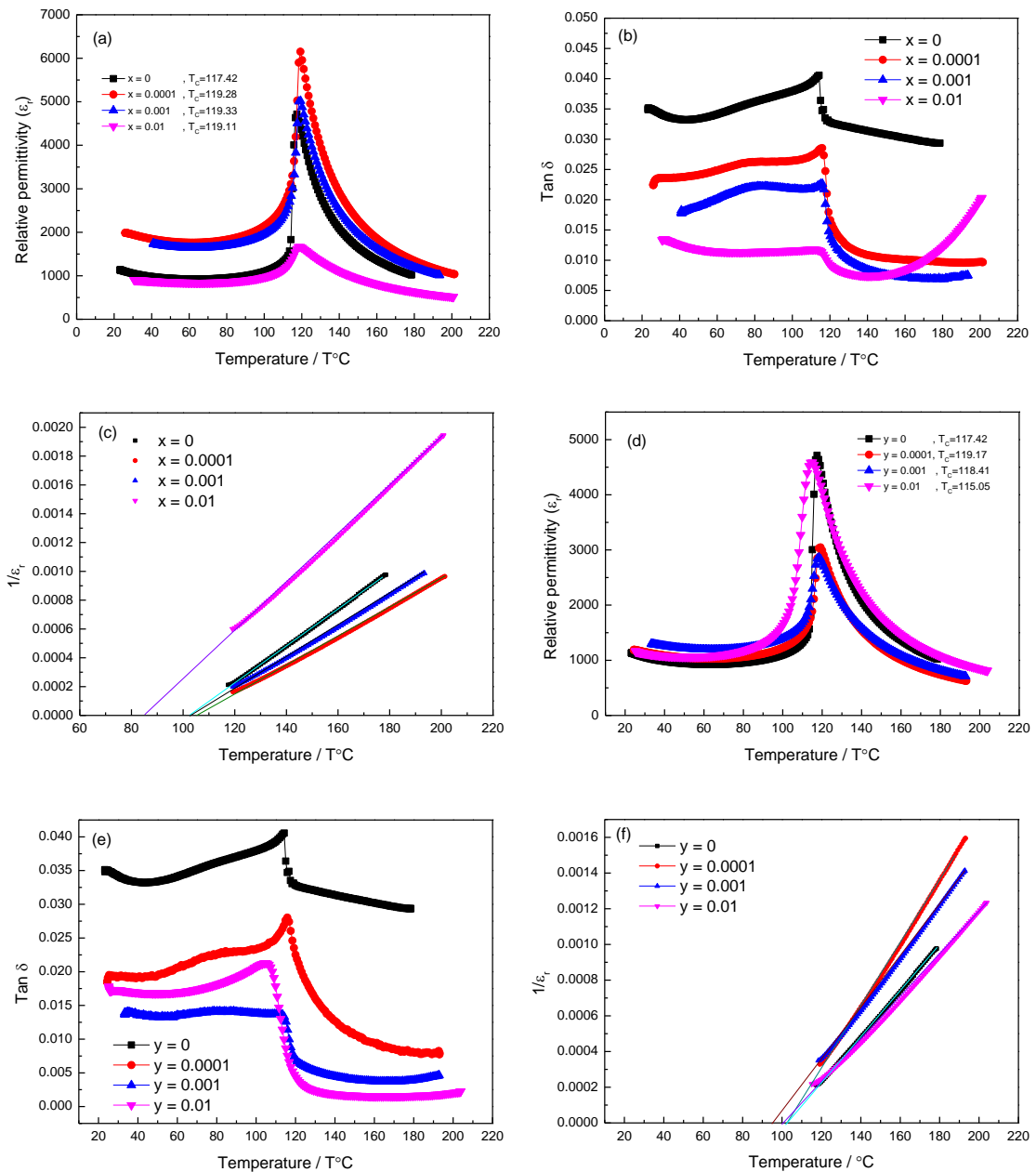
For Yb-A, the value of the permittivity changed with increasing x content from $v = 0$ to 0.0001 , decreased at $v = 0.001$ then reached a maximum at $v = 0.01$.

Generally, all samples showed that normal ferroelectric behaviour was observed. No compositions showed any significant frequency dependence of permittivity and dielectric loss (not shown). Permittivity data are plotted in Curie-Weiss form in Figure 5-1 (c,f,i). Cw data extracted from the Curie-Weiss plots are listed in Table 5-1.

For Yb-B, with increasing x , the dielectric loss decreases. In addition, the composition of $x = 0.01$ had the smallest loss but showed an increase in dielectric loss above ~ 150 °C, Figure 5-1 (b).

For Yb-AB and Yb-A, with increasing y and v , the dielectric loss decreases and then increases at y and $v = 0.01$, Figure 5-1 (e,h).

All compositions showed a non-leaky dielectric behaviour except pure BaTiO_3 which was a leaky dielectric, showing some conductivity with dielectric loss values ~ 0.035 .



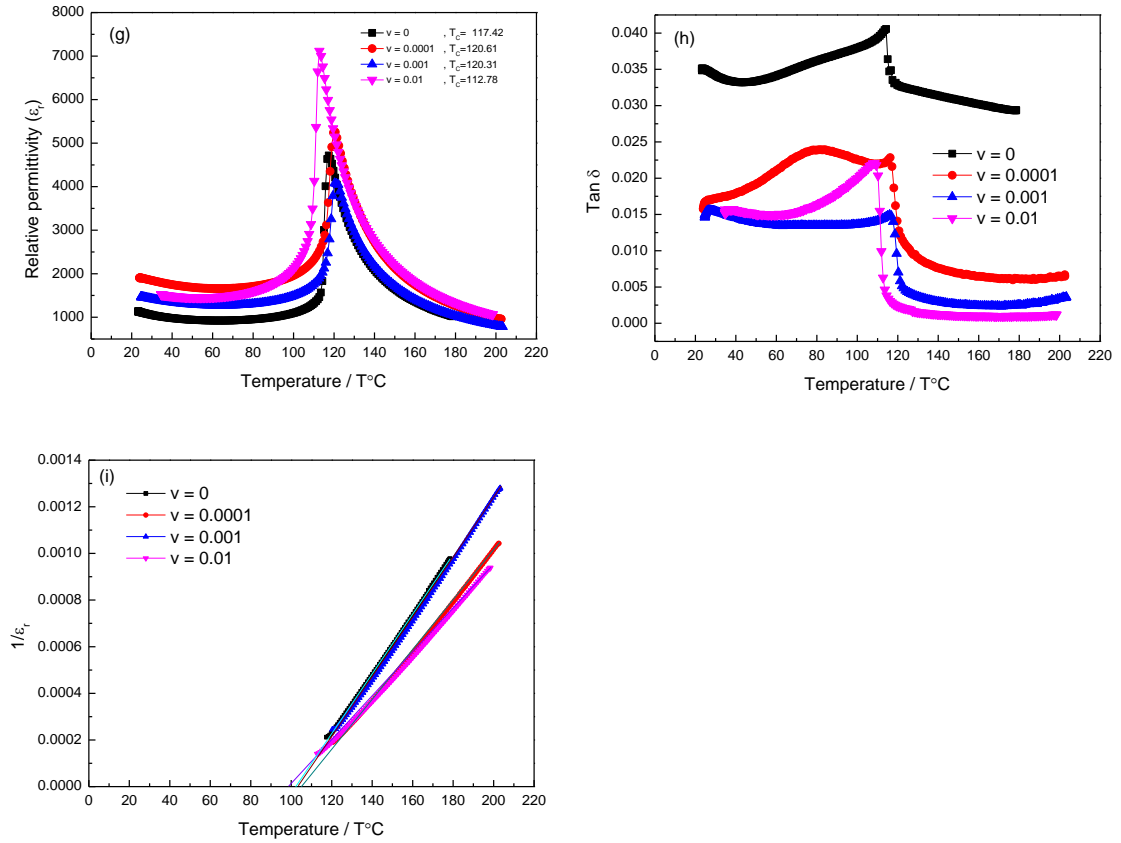


Figure 5-1: Fixed frequency measurements at 250 kHz of (a,d,g) relative permittivity (b,e,h), dielectric loss ($\tan\delta$) versus temperature and Curie-Weiss plots (c,f,i) for Yb-B, Yb-AB and Yb-A at several concentrations (x, y and $v = 0, 0.0001, 0.001$ and 0.01) sintered at $1350\text{ }^\circ\text{C}$ for 12 h in air for samples with Pt electrodes.

Table 5-1: Values of T_C , T_o , $T_C - T_o$ and C_w .

Composition for Yb-B	T_C ($^\circ\text{C}$)	T_o ($^\circ\text{C}$)	$T_C - T_o$ ($^\circ\text{C}$)	C_w (10^5 K)
0	117	103	14	0.78
0.0001	119	106	13	1.01
0.001	119	103	16	0.93
0.01	119	86	33	0.60
Composition for Yb-AB	T_C ($^\circ\text{C}$)	T_o ($^\circ\text{C}$)	$T_C - T_o$ ($^\circ\text{C}$)	C_w (10^5 K)
0	117	103	14	0.78
0.0001	119	103	16	0.57
0.001	118	96	22	0.69
0.01	115	101	14	0.85
Composition for Yb-A	T_C ($^\circ\text{C}$)	T_o ($^\circ\text{C}$)	$T_C - T_o$ ($^\circ\text{C}$)	C_w (10^5 K)
0	117	103	14	0.78

0.0001	121	105	16	0.95
0.001	120	104	16	0.78
0.01	113	99	14	1.05

Samples of $\text{BaTi}_{1-x}\text{Yb}_x\text{O}_{3-x/2}$ at several concentrations $x = 0, 0.0001, 0.001$ and 0.01 sintered at $1350\text{ }^\circ\text{C}$ for 12 h in air were characterised at $450\text{ }^\circ\text{C}$ using an impedance analyser with Pt electrodes which showed all to be electrically heterogeneous. All compositions were insulating at room temperature, whether fired at 1350 or $1450\text{ }^\circ\text{C}$. Impedance complex plane plots, Z^* are shown in Figure 5-2 (a). Two overlapping broad arcs are seen clearly at $x = 0$ and can be attributed to grain and grain boundary impedances. For BaTiO_3 , the grain boundary arc is much greater than the grain arc. The Z''/M'' spectroscopic plots, (b), showed that the Z'' spectrum was dominated by low frequencies and the M'' spectrum was dominated by high frequencies. The f_{max} for Z'' and M'' peaks are separated by three orders of magnitude for $x = 0$ and $1\frac{1}{4}$ orders for $x = 0.0001, 0.001, 0.01$. This indicates an inhomogeneous microstructure. M'' peaks are usually associated with the bulk response of a sample when these occur at higher frequency and are associated with the lowest capacitance in the equivalent circuit. A peak in Z'' is associated with a large resistance, which may be a grain boundary response and is usually observed at lower frequency. If this component has a large capacitance, it is not easily visible in the M'' plot. The Debye-like peaks in Z'' and M'' spectra and arc in Z^* were seen at temperatures $\geq 400, 300, 300, 250\text{ }^\circ\text{C}$ for the above compositions, respectively. For the same data, spectroscopic plots of capacitance, C' against frequency, (c), suggest the presence of two components that correspond to the bulk capacitance C_b at high frequency and the grain boundary capacitance, C_{gb} at low frequency, especially at $x = 0$. The values of the bulk capacitance were around $\sim (2 - 3) \times 10^{-11}\text{ Fcm}^{-1}$, similar to the values extracted from Figure 5-2 (b).

Previous samples of $x = 0.0001, 0.001$ and 0.01 were reheated at $1450\text{ }^\circ\text{C}$ for 24 h in air then air-quenched to room temperature on a brass block. Samples of $x = 0.001$ were reheated at $1350\text{ }^\circ\text{C}$ for 30 min in air then liquid nitrogen-quenched to room temperature. IS results indicated that the samples were electrically insulating and did not show any conductivity at room temperature.

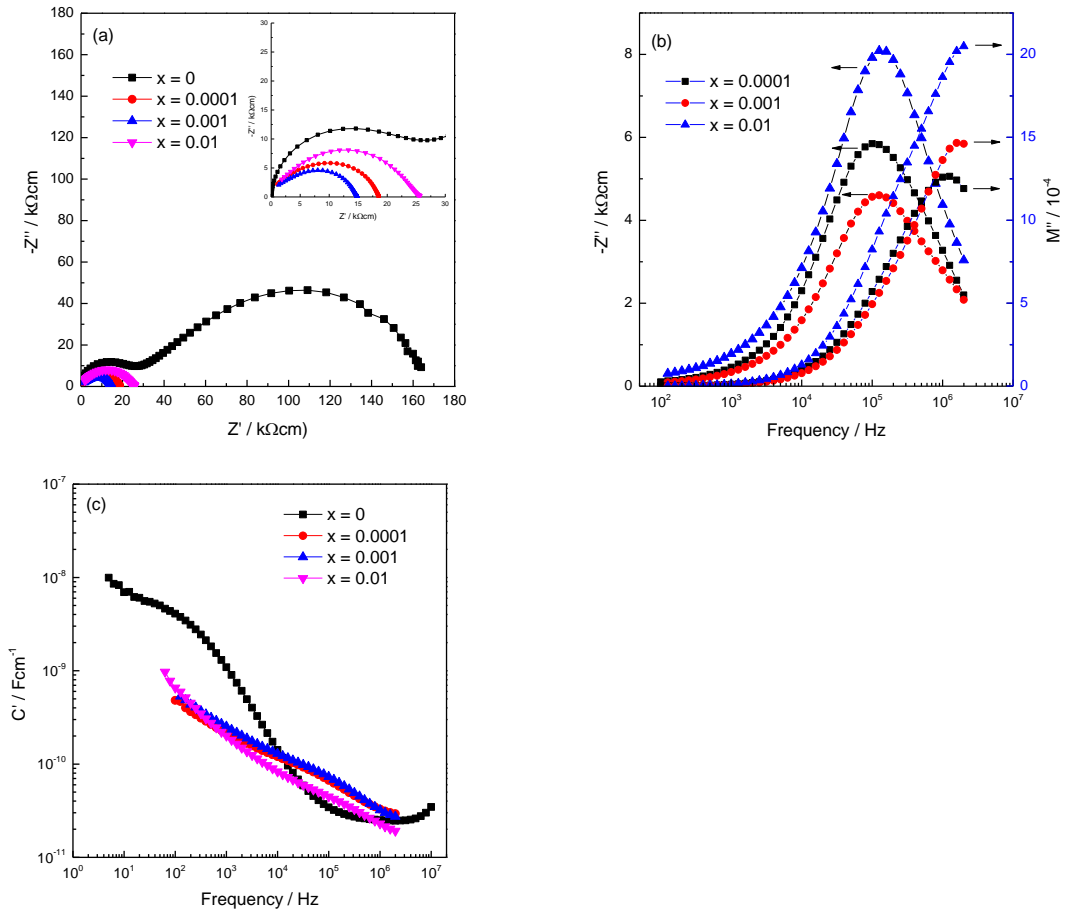
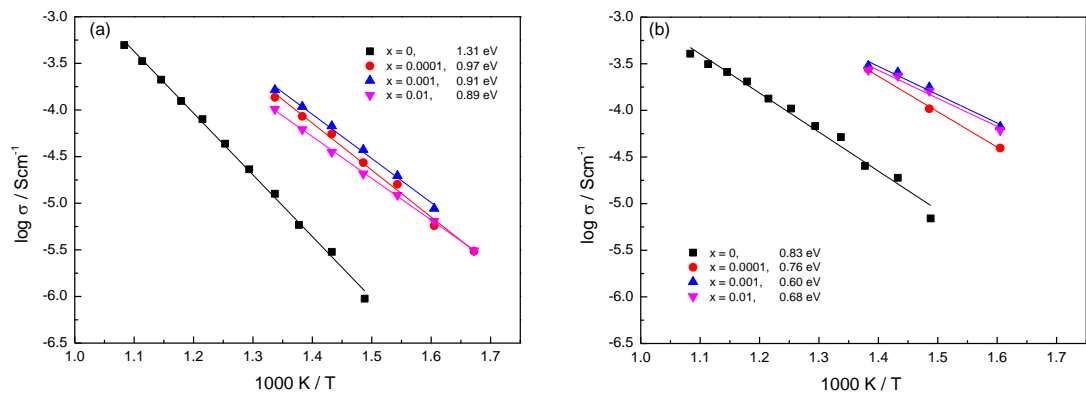


Figure 5-2: 450 °C IS data for BaTi_{1-x}Yb_xO_{3-x/2} at several concentrations ($x = 0, 0.0001, 0.001$ and 0.01), SC, sintered at 1350 °C for 12 h in air, (a) impedance complex plane plots, Z^* (b,c) $-Z''$, M'' spectroscopic plots and (d) C' plots for different frequencies for samples with Pt electrodes.

The conductivity data for the bulk σ_b and grain boundary σ_{gb} with activation energy E_A values are presented in Arrhenius plots, Figure 5-3 (a-f). As is illustrated by the graph, σ_b increases by \sim one order of magnitude on doping, Figure 5-3 (b).



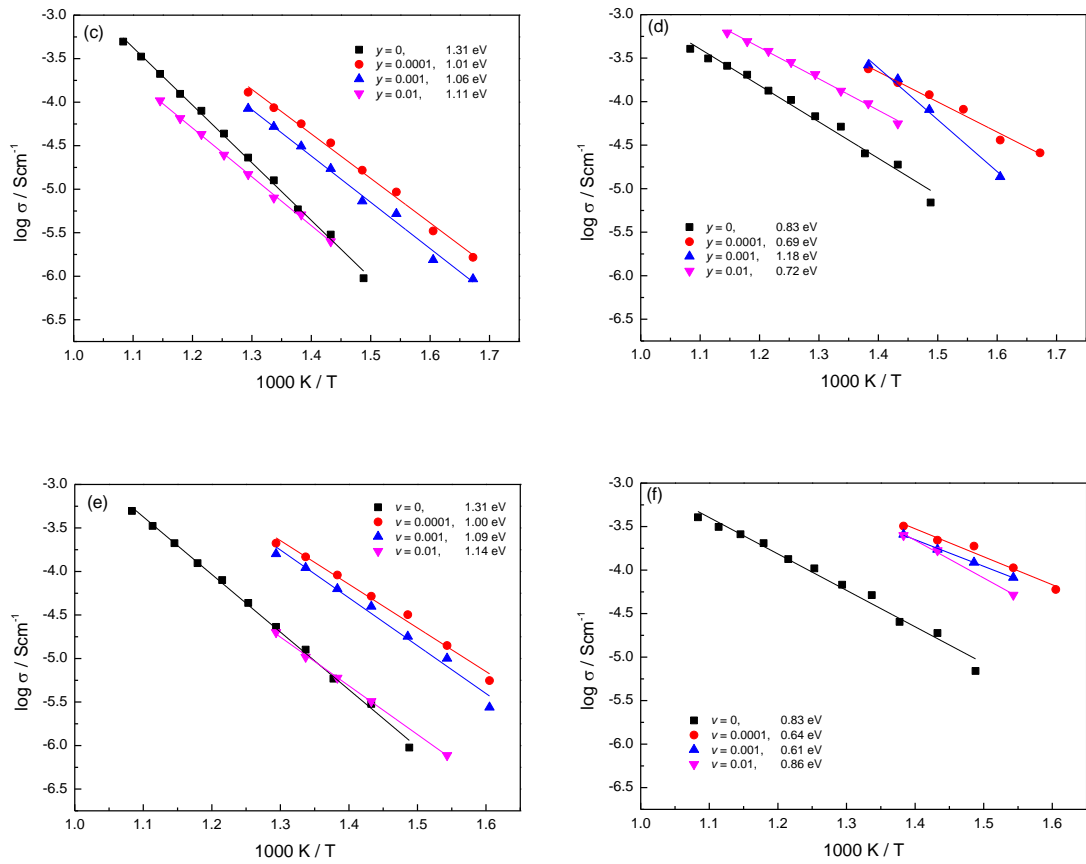


Figure 5-3: Arrhenius plots of conductivity data for Yb-B (a,b), Yb-AB (c,d) and Yb-A (e,f) at several concentrations ($x = 0, 0.0001, 0.001$ and 0.01), SC, sintered at $1350\text{ }^{\circ}\text{C}$ for 12 h in air against reciprocal temperature for samples with Pt electrodes.

(a,c,e) grain boundary conductivity, (b,d,f) bulk conductivity.

The effect of oxygen partial pressure and dc bias was studied for Yb-B, Yb-AB and Yb-A at x, y and $\nu = 0.01$. Similar behaviour was observed. For example for Yb-A, on changing the atmosphere to N_2 at $450\text{ }^{\circ}\text{C}$, the conductivity decreased, Figure 5-4 (a), appearing to be p-type. Figure 5-4 (b) shows that the high frequency capacitance plateau illustrates similar capacitance values $\sim 9.12 \times 10^{-12}\text{ Fcm}^{-1}$. Two peaks in M'' were observed. Both of them showed a slight shift to low frequency in N_2 , (c). Z^* plot with dc bias at $350\text{ }^{\circ}\text{C}$ shows that R_T decreased gradually with time and reached a steady-state value after 25 min, Figure 5-5 (a). This confirms that the conduction mechanism is p-type. The initial M'' peak shifted to higher frequency with increasing time, (b). Figure 5-5 (c) shows that the high frequency capacitance plateau was unaffected by the dc bias and had a value $\sim 3.45 \times 10^{-11}\text{ Fcm}^{-1}$. R_T returned to its original value after removing dc bias after ~ 300 min, (d).

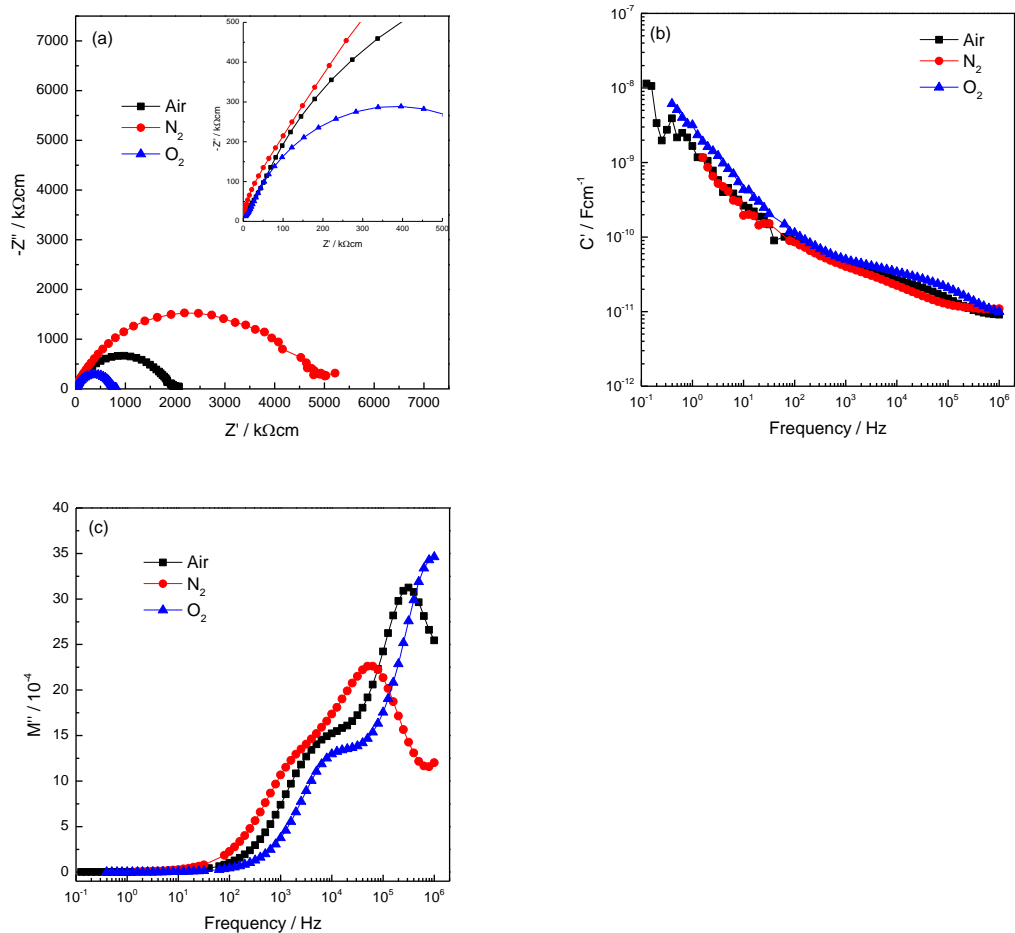
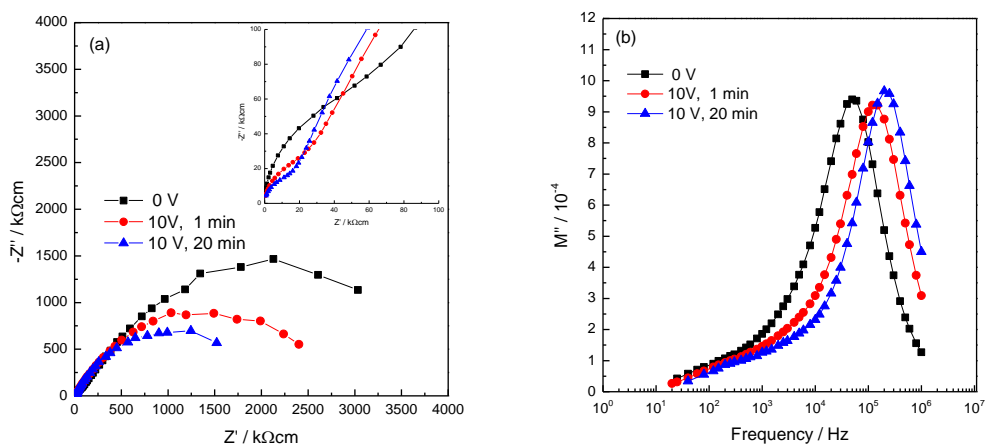


Figure 5-4: 450 °C IS data for Yb-B, $x = 0.01$, Q from 1450 °C, (a) Z^* plot, (b) C' plot and (c) M'' plot in different atmospheres.



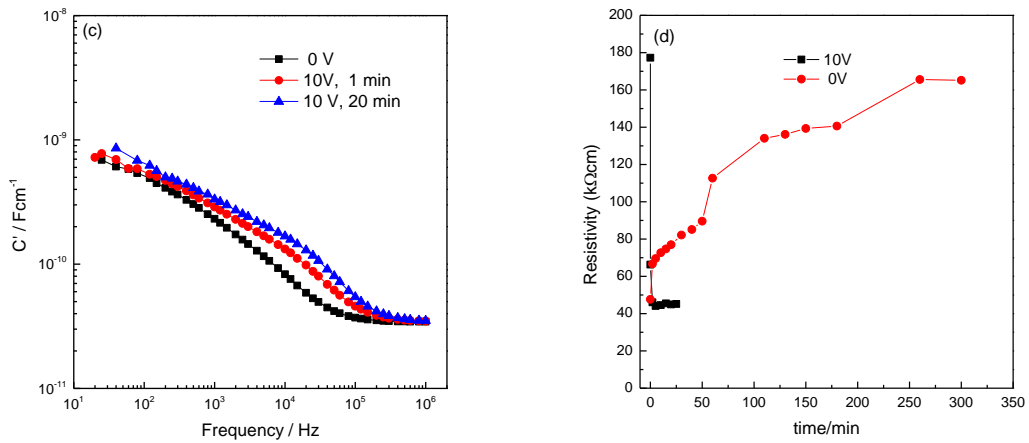


Figure 5-5: 350 °C IS data for Yb-B, $x = 0.01$, Q from 1450 °C, (a) Z^* plot (b) M'' plot, (c) C' plot before and after a voltage of 10 V was applied at different measuring times and (d) Bulk resistance with 10V bias and after removing the dc bias at different times in air.

In summary, Yb-B, Yb-AB and Yb-A samples were very resistive either with SC or Q and p-type behaviour was observed by pO_2 and dc bias.

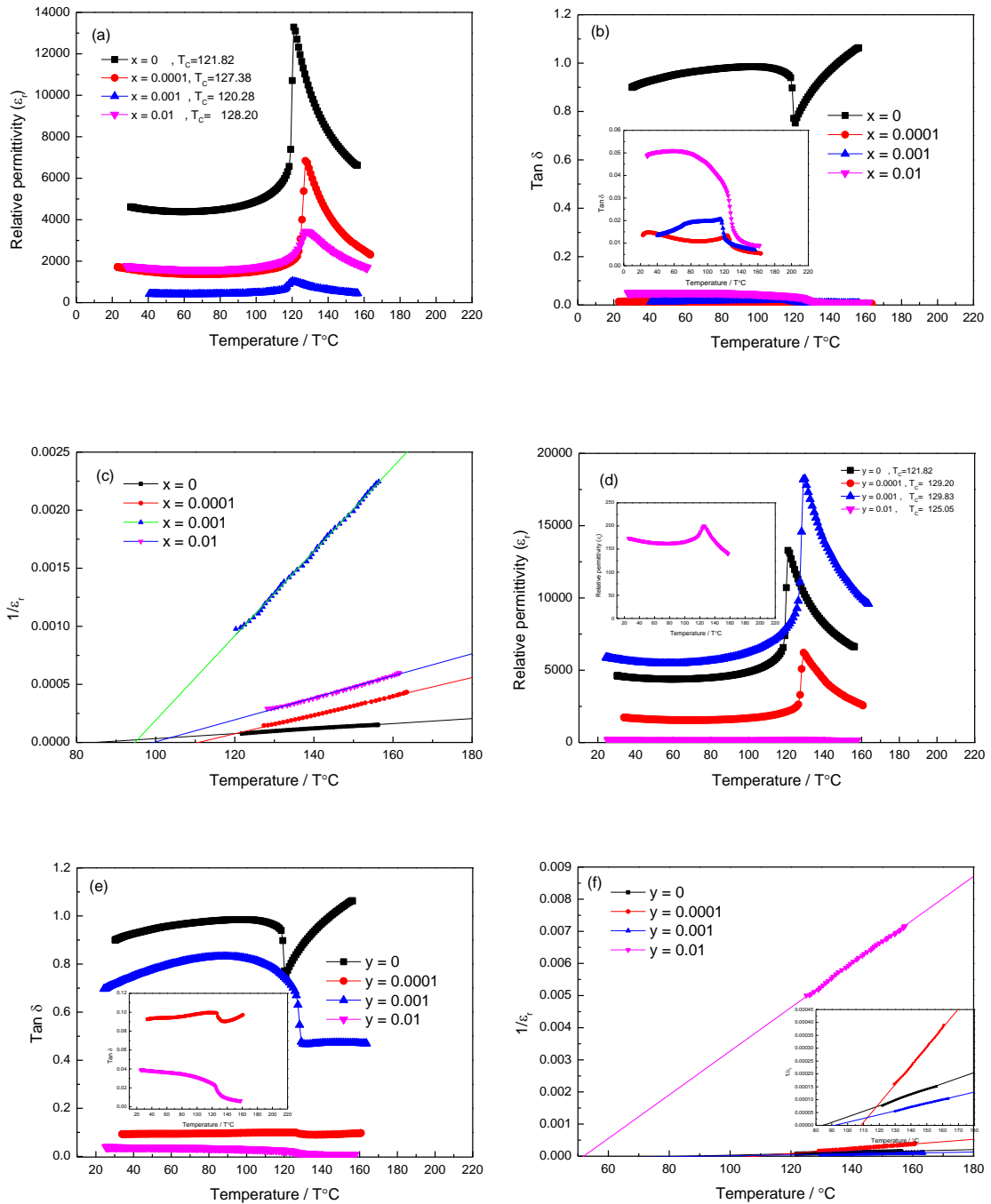
5.3.3 Electrical properties of Er-doped BT

The temperature dependence of ϵ' and $\tan \delta$ for pellets of concentrations x, y and $v = 0, 0.0001, 0.001$ and 0.01 which had been sintered and Q from 1350 °C for 12 h in air with In-Ga electrodes measured at 250 kHz are shown in Figure 5-6 (a-i) for acceptor (a-c), self-compensation (d-f) and donor (g-i) joins, respectively.

In the three joins, at T_C , a clear maximum in permittivity and dielectric loss was observed in the range ~ 1176 - 6932, Figure 5-6 (a) for Er-B, ~ 205 - 18406, Figure 5-6 (d) for Er-AB and ~ 11437 - 18870, Figure 5-6 (g) for Er-A. In general, the transition temperature increases slightly with increasing x, y and v . For Er-B, the magnitude and sharpness of the permittivity maximum decreased substantially with increasing Er content until $x = 0.001$ and then increased at $x = 0.01$, Figure 5-6 (a). For Er-AB, the value of the permittivity maximum for $y = 0.001$ was higher than for other samples. For Er-A, ϵ_{max} has value for $v = 0.001$.

Permittivity data are plotted in Curie-Weiss form in Figure 5-6 (c,f,i). Cw data extracted from the Curie-Weiss plots are listed in Table 5-2.

For Er-B and Er-AB, there was generally a significant decrease in the dielectric loss with Er doping, Figure 5-6 (b,e). A significant increase in the dielectric loss was observed at $v = 0.01$ for Er-A, Figure 5-6 (h).



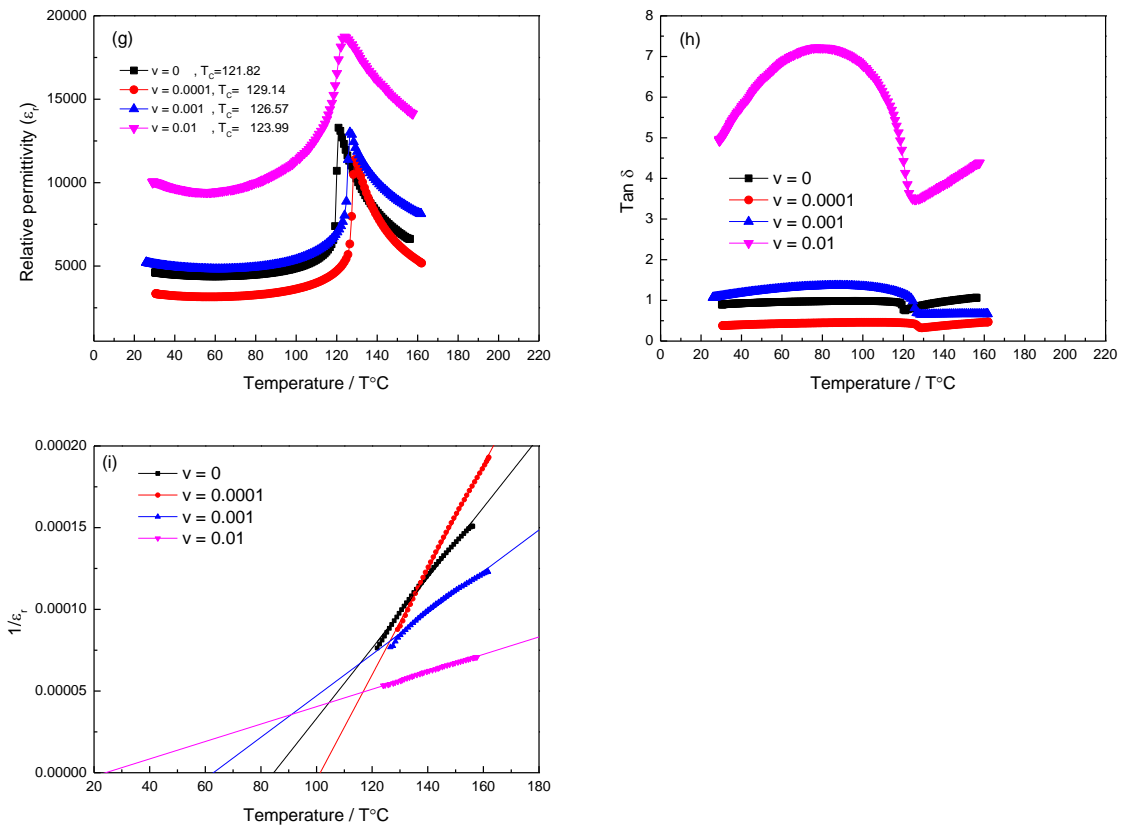


Figure 5-6: Fixed frequency measurements at 250 kHz of (a,d,g) relative permittivity (b,e,h), dielectric loss ($\tan\delta$) versus temperature and Curie-Weiss plots (c,f,i) for Er-B, Er-AB and Er-A at several concentrations (x,y and $v = 0, 0.0001, 0.001$ and 0.01) sintered at $1350\text{ }^\circ\text{C}$ for 12 h in air for samples with In-Ga electrodes.

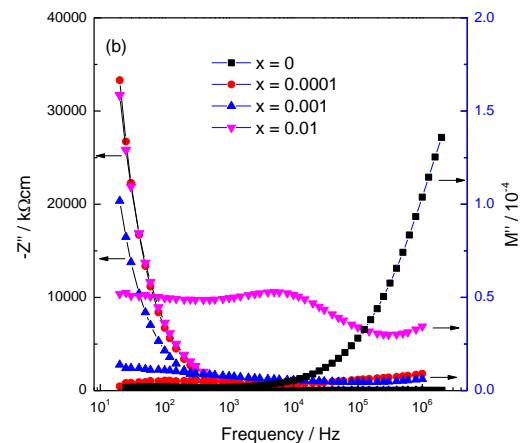
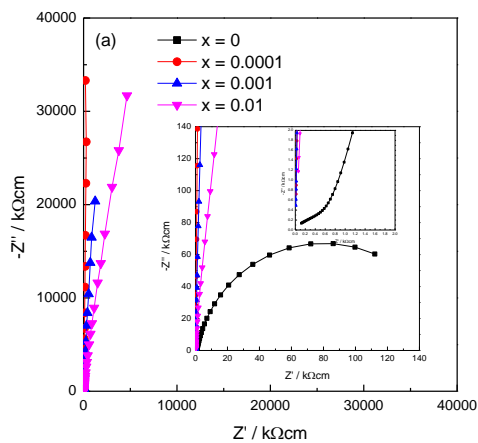
Table 5-2: Values of T_C , T_o , $T_C - T_o$ and C_w .

Composition for Er-B	T_C ($^\circ\text{C}$)	T_o ($^\circ\text{C}$)	$T_C - T_o$ ($^\circ\text{C}$)	C_w (10^5 K)
0	122	85	37	4.64
0.0001	127	110	17	1.24
0.001	120	95	25	0.28
0.01	128	100	28	1.06
Composition for Er-AB	T_C ($^\circ\text{C}$)	T_o ($^\circ\text{C}$)	$T_C - T_o$ ($^\circ\text{C}$)	C_w (10^5 K)
0	122	85	37	4.64
0.0001	129	108	21	1.36
0.001	130	93	37	6.82
0.01	125	52	73	0.15

Composition for Er-A	T_C (°C)	T_0 (°C)	$T_C - T_0$ (°C)	C_w (10^5 K)
0	122	85	37	4.64
0.0001	129	101	28	3.11
0.001	127	63	64	7.88
0.01	124	23	101	18.75

5.3.3.1 IS results for Er-B

Impedance measurements were made for SC and Q pellets in air at $x = 0, 0.0001, 0.001$ and 0.01 with In-Ga electrodes. The data were too resistive to measure at room temperature except Q BT. For Q BT, $x = 0$, a small semicircular core appeared at high frequency in impedance, Z^* , complex plane plot with resistance at RT of $\sim 500 \Omega\text{cm}$ with another much greater semicircular at low frequency, Figure 5-7 (a). Combined Z''/M'' spectroscopic plots are given in (b). M'' also displays evidence of a conductive core for BT but not for Er-B with $x > 0$. Y' against frequency plot of Q BT shows two plateaux at lower and higher frequencies corresponding to the two semicircular in (a), whereas Er-B samples show no evidence of any frequency-independent behaviour at any frequency (c). The spectroscopic plot of the real part of the capacitance, $\log C'$ vs $\log f$ shows a frequency-independent plateau at higher frequencies with associated capacitances, $\sim 221, 324$ and 135 pFcm^{-1} for $x = 0.0001, 0.001$ and 0.01 respectively. These are attributed to the bulk capacitance of the samples with permittivity $\sim 2000-4000$. Data for Q BT (d) show two plateaux attributed to sample bulk (high frequency) and either a grain boundary or a Schottky barrier (low frequency).



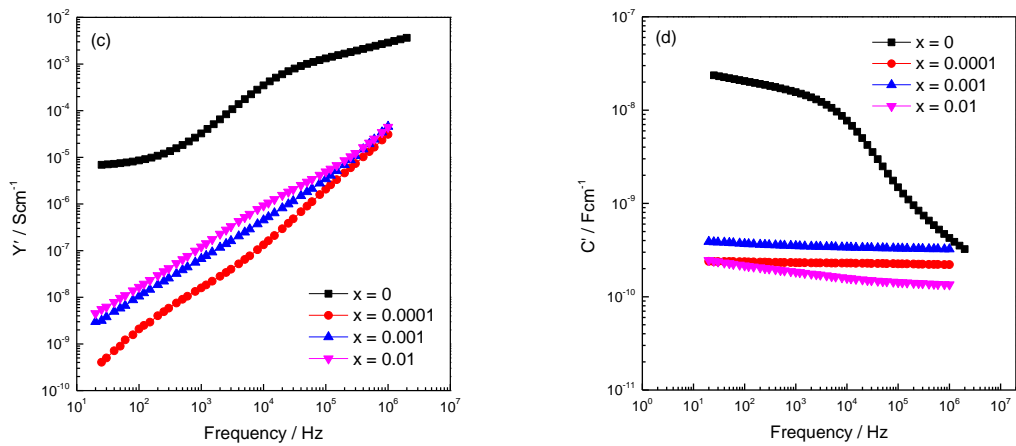


Figure 5-7: RT IS data for Er-B at several concentrations ($x = 0, 0.0001, 0.001$ and 0.01) Q from $1350\text{ }^\circ\text{C}$, (a) impedance complex plane plots, Z^* (b) $-Z''$, M'' spectroscopic plots, (c) Y' plots and (d) C' plots for different frequencies for samples with In-Ga electrodes.

Arrhenius plots are shown in Figure 5-8. The value of the conductivity was lower for $x = 0.0001$ and its activation energy was highest. For these data, total resistance values were obtained from the low frequency intercepts on Z^* plots and are attributed to sample bulk resistances.

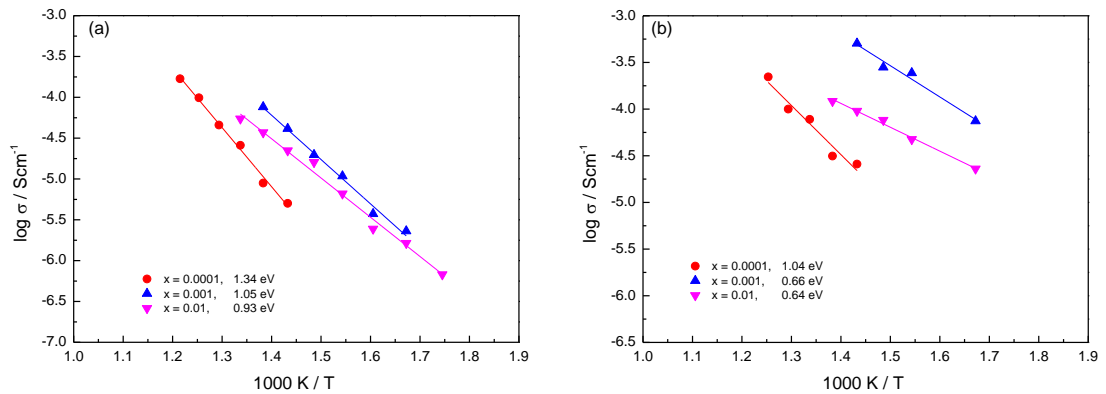


Figure 5-8: Arrhenius plots of (a) grain boundary and (b) bulk conductivity data for Er-B, SC, $x = 0, 0.0001, 0.001$ and 0.01 , sintered at $1350\text{ }^\circ\text{C}$ for 12 h in air with In-Ga electrodes.

IS measurements were made in different atmospheres for $x = 0.01$ with Ag electrodes. The sample was insulating below $350\text{ }^\circ\text{C}$. A clear sensitivity to $p\text{O}_2$ was observed on changing from O_2 to N_2 at $350\text{ }^\circ\text{C}$, Figure 5-9 (a). Z^* plots showed one

broad arc with a small tail at low frequencies and with no evidence of a much smaller, second semicircular arc at high frequencies, compared with Q BT. The C' data showed a frequency-independent plateau at high frequencies, 40 pFcm^{-1} . At low frequency, C' increased to values $\sim 3 \times 10^{-8}$ to $3 \times 10^{-7} \text{ Fcm}^{-1}$, depending on atmosphere, (b). The M'' peak (c) shifted to lower frequencies with decreasing $p\text{O}_2$. The conclusion from these results is that the bulk conductivity is p-type.

Impedance data before and after applying 10V dc bias at $350 \text{ }^\circ\text{C}$ are illustrated in Figure 5-10. RT decreased when a voltage of 10V was applied, (a). The M'' peak shows a small shift to higher frequencies, (b). There is no noticeable effect on C' data, (c). There was no evidence of any significant time dependence of Z^* data on applying/removing the dc bias. The conclusion from the dc bias results is that the conduction is p-type, similar to the conclusion from the $p\text{O}_2$ tests. Similar results were observed for both SC and Q samples.

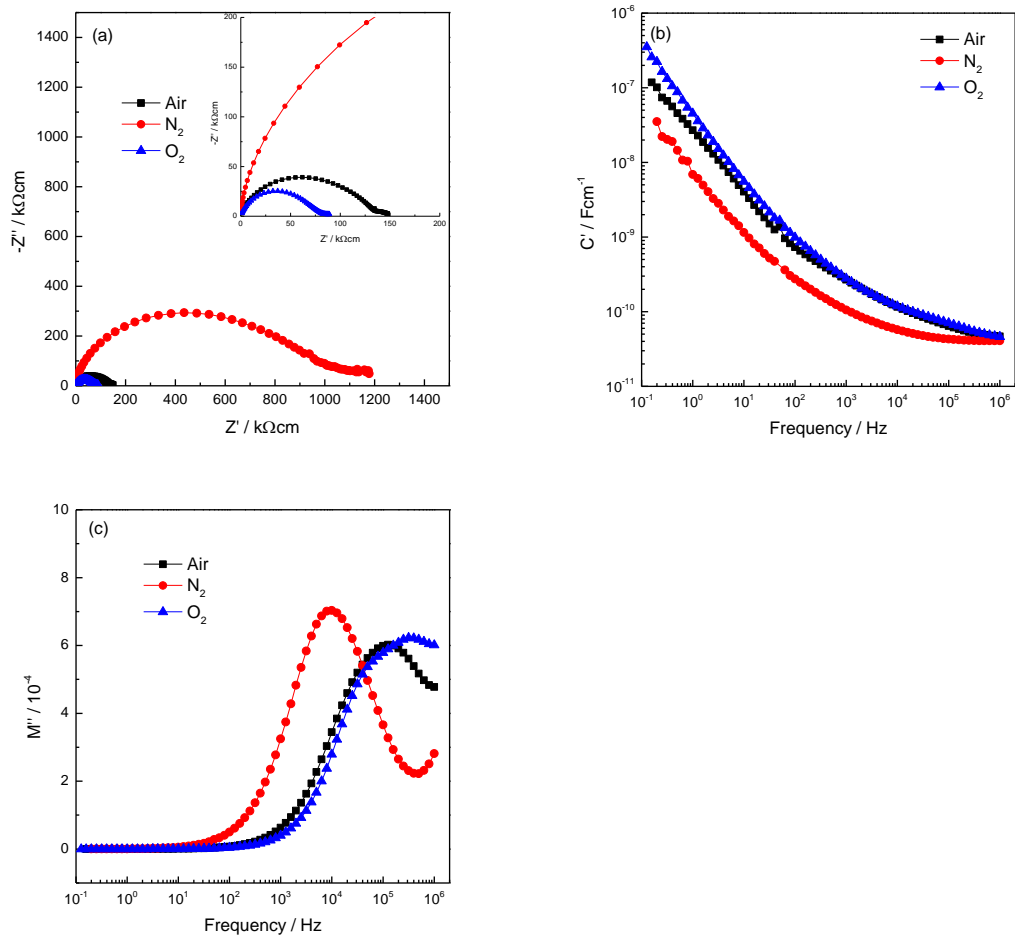


Figure 5-9: 350 °C IS data for Er-B, $x = 0.01$, Q from 1350 °C, (a) Z^* plot, (b) C' plot and (c) M'' plot in different atmospheres with Ag electrodes.

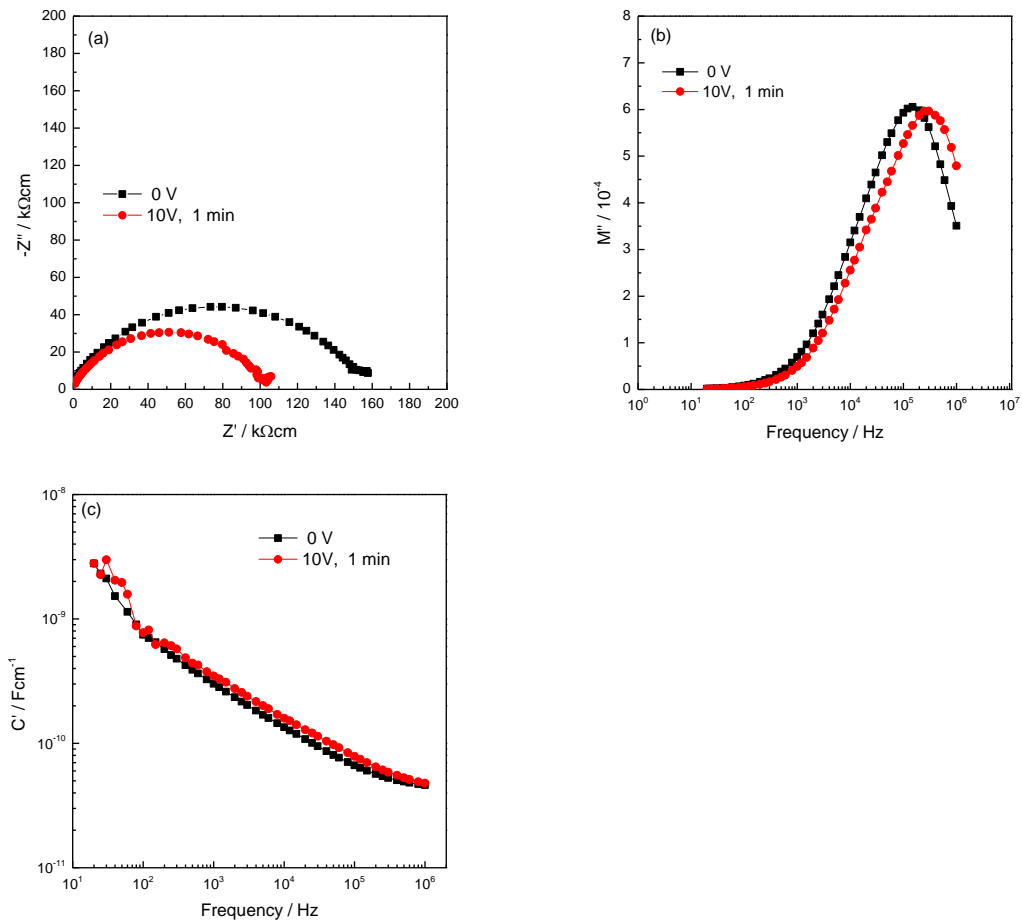


Figure 5-10: 350 °C IS data for Er-B, $x = 0.01$, Q from 1350 °C, (a) Z^* plot (b) M'' plot, (c) C' plot before and after a voltage of 10 V was applied at different measuring times in air with Ag electrodes.

In summary, Er-B samples were very resistive either with SC or Q and p-type behaviour was observed by pO_2 and dc bias.

5.3.3.2 IS results for Er-AB

Impedance measurements were made for SC and Q pellets in air at $y = 0, 0.0001, 0.001$ and 0.01 with In-Ga electrodes. The data for Q samples were very conductive except for $y = 0.01$ which was resistive either with SC or Q although the Q sample was more conductive. Typical Z^* plots showed a single rather distorted arc whose resistance increased dramatically between 21 and 225 °C then decreased slightly, Figure 5-11 (a). Two peaks were clearly apparent in the Z''/M'' spectroscopic plots.

Largest resistance was associated with the low frequency component and low resistance was observed for the high frequency component, which is clearly obvious in the M'' spectrum, (b). Thus, the high frequency incline in the M'' data is consistent with a semiconductive bulk region. At all temperatures, the Y' spectroscopic plot shows a low frequency plateau with a dispersion at higher frequencies, (c), whereas C' spectrum shows a dispersion at higher and a lower frequency plateau, (d).

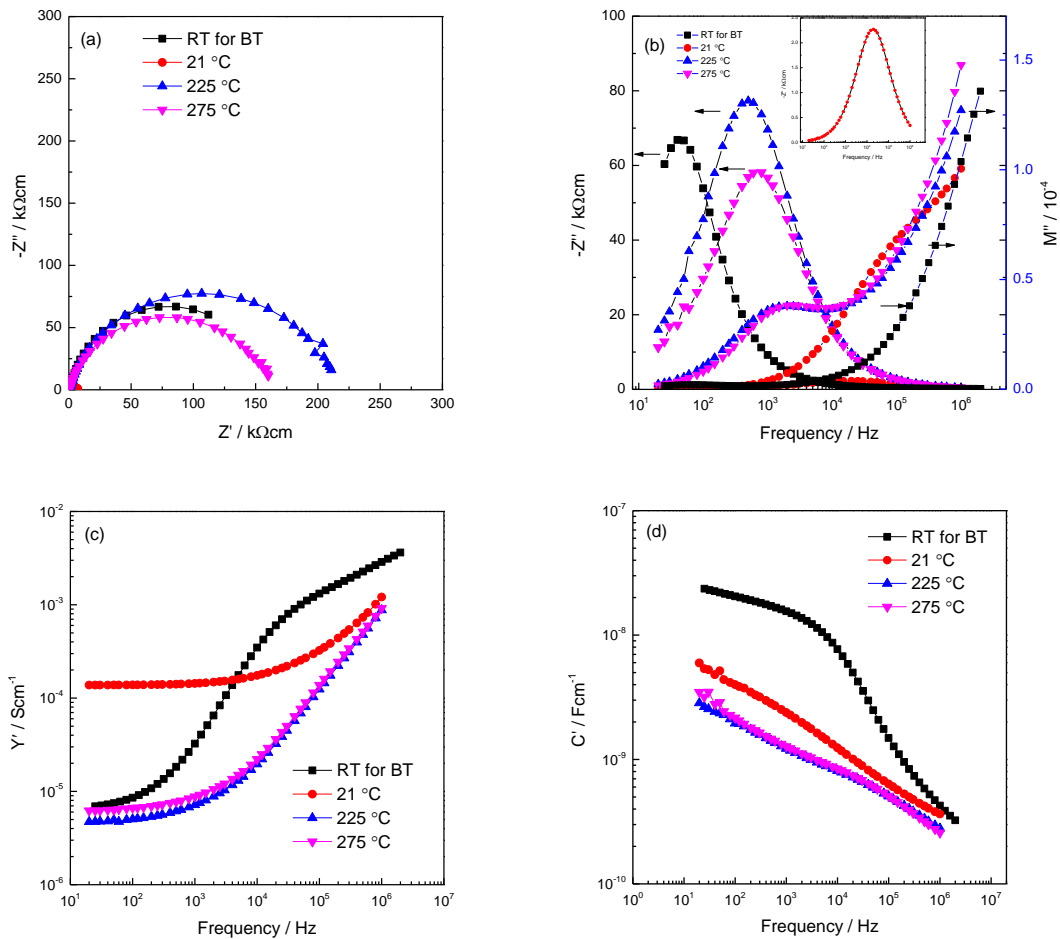


Figure 5-11: RT IS data for Er-AB, $y = 0.001$, Q from 1350 °C, (a) impedance complex plane plots, Z^* (b) $-Z''$, M'' spectroscopic plots, (c) Y' plots and (d) C' plots for different frequencies for samples with In-Ga electrodes.

Figure 5-12 shows a modest PTCR effect for the total resistivity when samples pass through their Curie point.

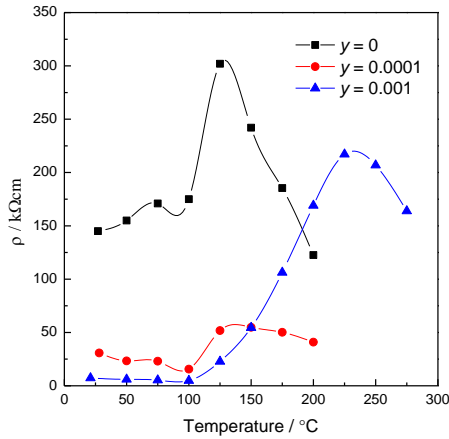
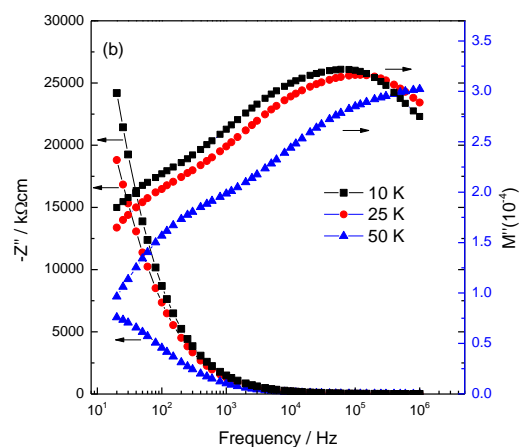
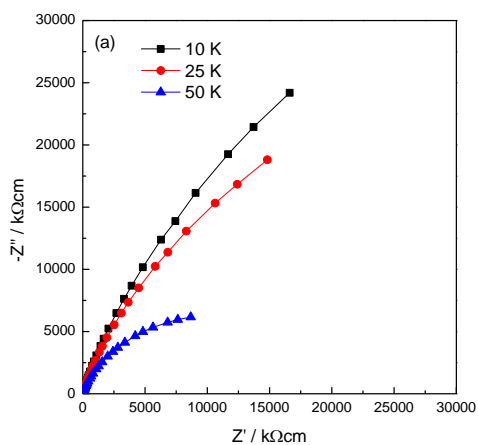


Figure 5-12: Dc resistivity (ρ) as a function of temperature for Er-AB, $y = 0.001$, Q from 1350 °C.

The sample of $y = 0.001$ was studied as well at low temperatures to characterise the bulk response. Z^* plot was dominated by a single, large arc that could not be fully resolved at 10 and 25 K as the total resistance of the sample exceeded 100 MΩcm. At 50 K, a single arc with $R_T \sim 1.86 \times 10^7 \Omega\text{cm}$ is seen, Figure 5-13 (a). M'' spectra show very broad, overlapping peaks, (b). Capacitance data extracted from the M'' peak height values are 1.37×10^{-10} and 1.40×10^{-10} for 10 and 25 K respectively. The Y' data show frequency-dependent conductivity with an approximately linear, power law dependence with the onset of a plateau at low frequency, (c). The C' data show a dispersion tending towards a plateau at high frequency, (d).



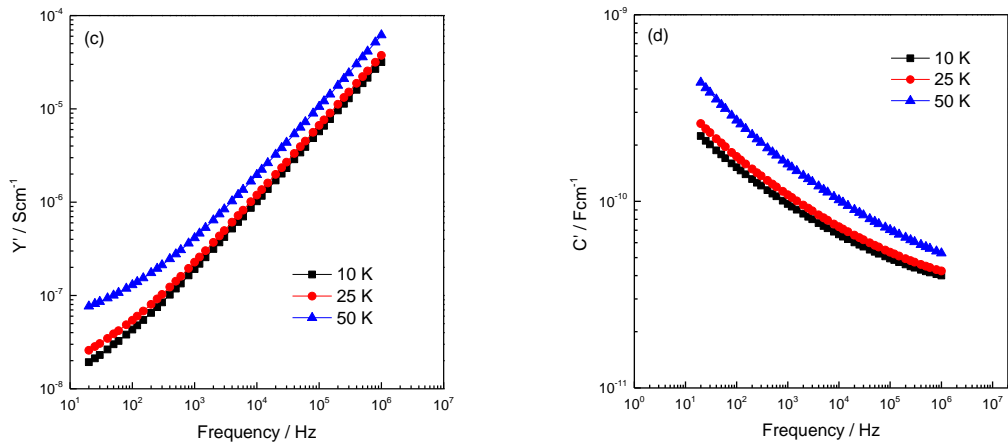


Figure 5-13: IS data for Er-AB, $y = 0.001$ Q from 1350 °C, (a) impedance complex plane plots, Z^* (b) $-Z''$, M'' spectroscopic plots, (c) Y' plots and (d) C' plots for different frequencies for samples with In-Ga electrodes.

The sample of $y = 0.01$ was insulating at room temperature. Two components were observed at high temperatures. σ_b and σ_{gb} values are summarised in Arrhenius format. The activation energies associated with the bulk and grain boundary conductivity are ~ 0.98 and 1.07 eV, respectively, Figure 5-14.

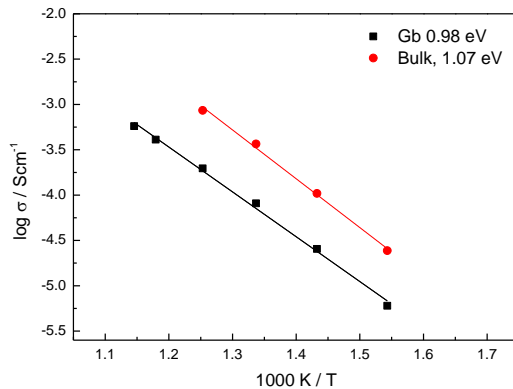


Figure 5-14: Arrhenius plots of conductivity data for Er-AB, $y = 0.01$ Q from 1350 °C against reciprocal temperature for samples with In-Ga electrodes.

The effect of pO_2 was studied for conductive ($y = 0.001$) and insulating ($y = 0.01$) samples. Sample $y = 0.001$ was not sensitive to pO_2 . Z^* data were similar in Air, N_2 and O_2 (not shown). For $y = 0.01$, R_T increased on changing from O_2 to N_2 , Figure 5-15 (a). C' showed a clear decrease at high frequency in N_2 and M_{max} increased and shifted to high frequency, (b,c).

R_T decreased significantly with a dc bias as shown in Z^* at 550 °C. This reduction was time-dependent and a steady-state value was observed after 110 min, Figure 5-16 (a) and indicates that the conduction mechanism is p-type. The M'' peak shifted to higher frequency with increasing time, (b) and (c) shows that the high frequency capacitance plateau was mostly unaffected by the dc bias, with a value $\sim 9.49 \text{ pFcm}^{-1}$. The resistance decrease was fully reversible on removal of the dc bias after ~ 1300 min, (d). The sample of $y = 0.001$, Q also showed similar reduction of resistance with a dc bias, (not shown).

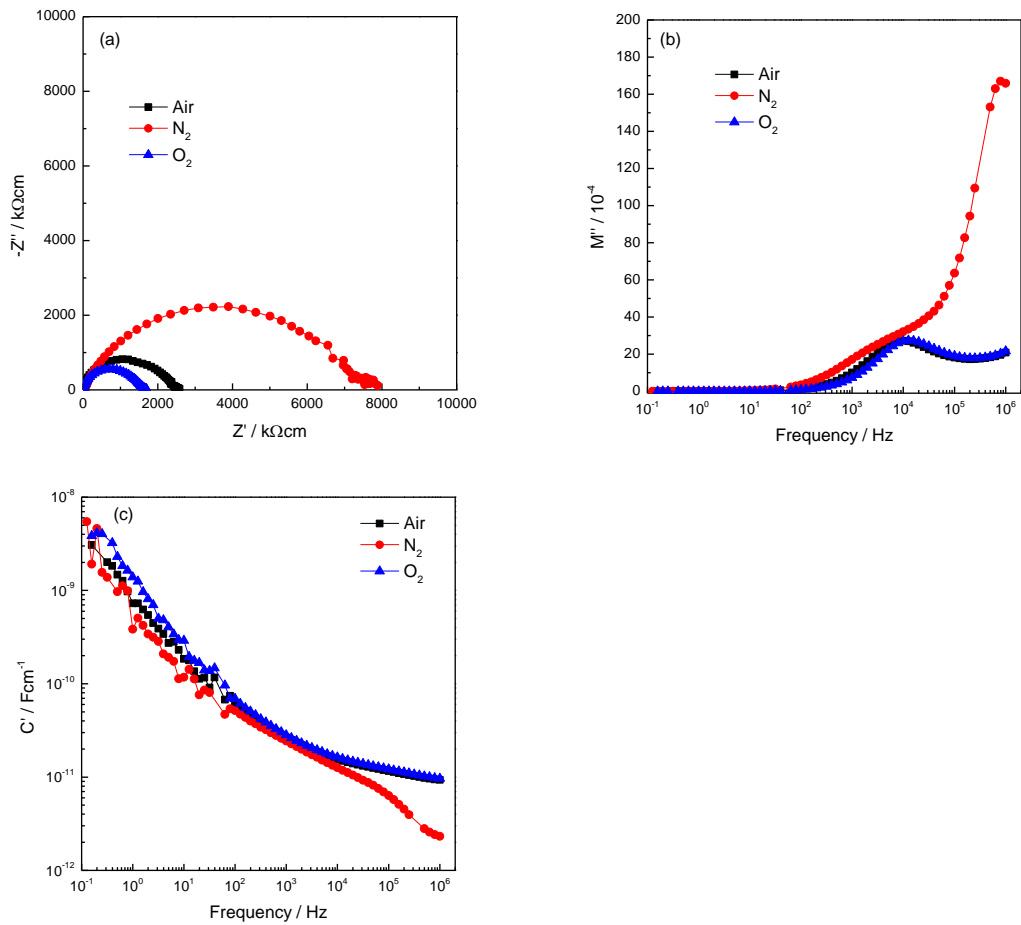


Figure 5-15: 550 °C IS data for Er-AB, $y = 0.01$ Q from 1350 °C, (a) Z^* plot, (b) C' plot and (c) M'' plot in different atmospheres with Ag electrodes.

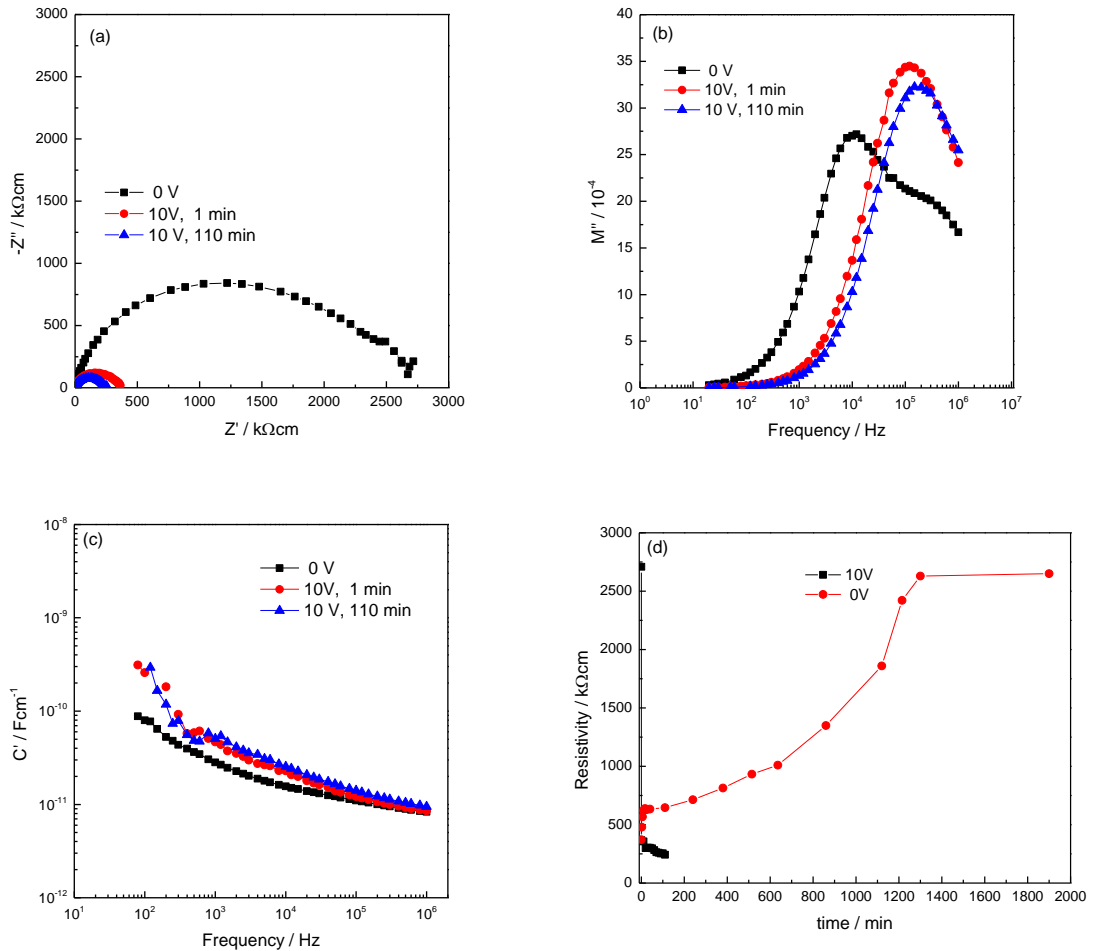


Figure 5-16: 550 °C IS data for Er-AB, $y = 0.01$, Q from 1350 °C, (a) Z^* plot (b) M'' plot, (c) C' plot before and after a voltage of 10 V was applied at different measuring times and (d) Bulk resistance with 10V bias and after removing the dc bias at different times in air.

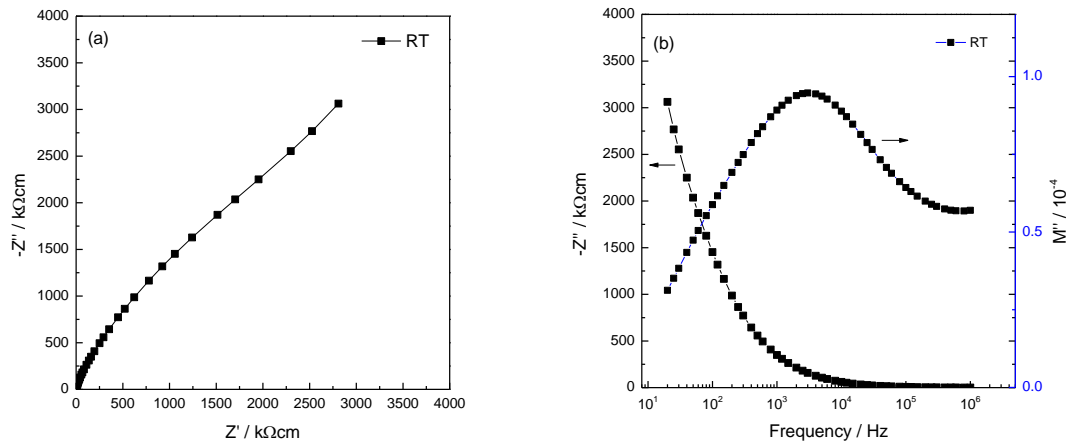
In summary, Er-AB samples were conductive for Q samples and showed a SB effect except for $y = 0.01$ which was resistive either with SC or Q. P-type behaviour was observed by $p\text{O}_2$ and dc bias for insulating sample, 0.01 whereas, conductive sample, 0.001 was not sensitive to $p\text{O}_2$ and the resistance decreased reversibly with dc bias.

5.3.3.3 IS results for Er-A

All Q samples were conductive. A PTCR effect was observed for the total resistance at $v = 0.0001$ and 0.001 (not shown). A clear difference between SC and Q sample was observed for $v = 0.01$, Figure 5-17 and 5-18. They are electrically inhomogeneous.

The SC sample was a dc insulator, with a RT resistance $> 10^6 \Omega\text{cm}$ and Z^* plots indicated there was a zero intersect on the real axis at high frequency, Figure 5-17 (a). The Z'' plot shows a low frequency incline. The M'' data indicate two low resistance components at intermediate and high frequencies, with f_{max} values of $\sim 3 \times 10^3 \text{ Hz}$ with $4.67 \times 10^{-10} \text{ Fcm}^{-1}$ and $> 10^6 \text{ Hz}$ which may be associated with semiconducting region, (b). The Y' data show frequency-dependent values over all range either with low or high frequency regions and there is no evidence for such a dc plateau, (c). The C' data show mostly a high frequency plateau representing the bulk response of the sample with a value $\sim 165 \text{ pFcm}^{-1}$. A clear dispersion region was observed with decreasing frequency, (d).

Q sample shows two components in the Z^* plot, Figure 5-18 (a), as two well-defined semicircular arcs at low and high frequency. The high frequency arc resistance values were changed slightly $\sim 40\text{-}45 \Omega\text{cm}$ over the temperature range from RT-200 °C, whereas a significant change was observed for the low frequency arc. The start of a high frequency peak at $f_{\text{max}} > 10^5 \text{ Hz}$ is seen in M'' data, (b). The maximum is not shown which requires higher frequencies. This component is attributed to the bulk (grain interior) response. Z'' peak changed significantly with an increase in temperature whereas M'' peak did not show considerable change. The Y' plots show two plateaux at high and low frequency separated by dispersion over a range of intermediate frequencies, (c). The C' data are strongly frequency-dependent between $\sim 10^4\text{-}10^6 \text{ Hz}$ as the C' data increasingly show a dispersion to lower values with increasing frequency, (d).



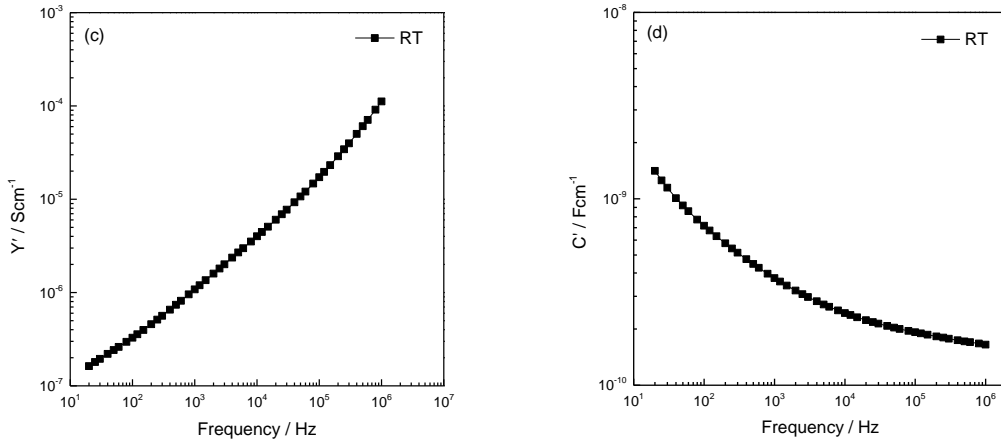


Figure 5-17: IS data for Er-A, SC, $\nu = 0.01$, SC, sintered at 1350 °C, (a) impedance complex plane plots, Z^* (b) $-Z''$, M'' spectroscopic plots, (c) Y' plots and (d) C' plots for different frequencies for samples with Ag electrodes.

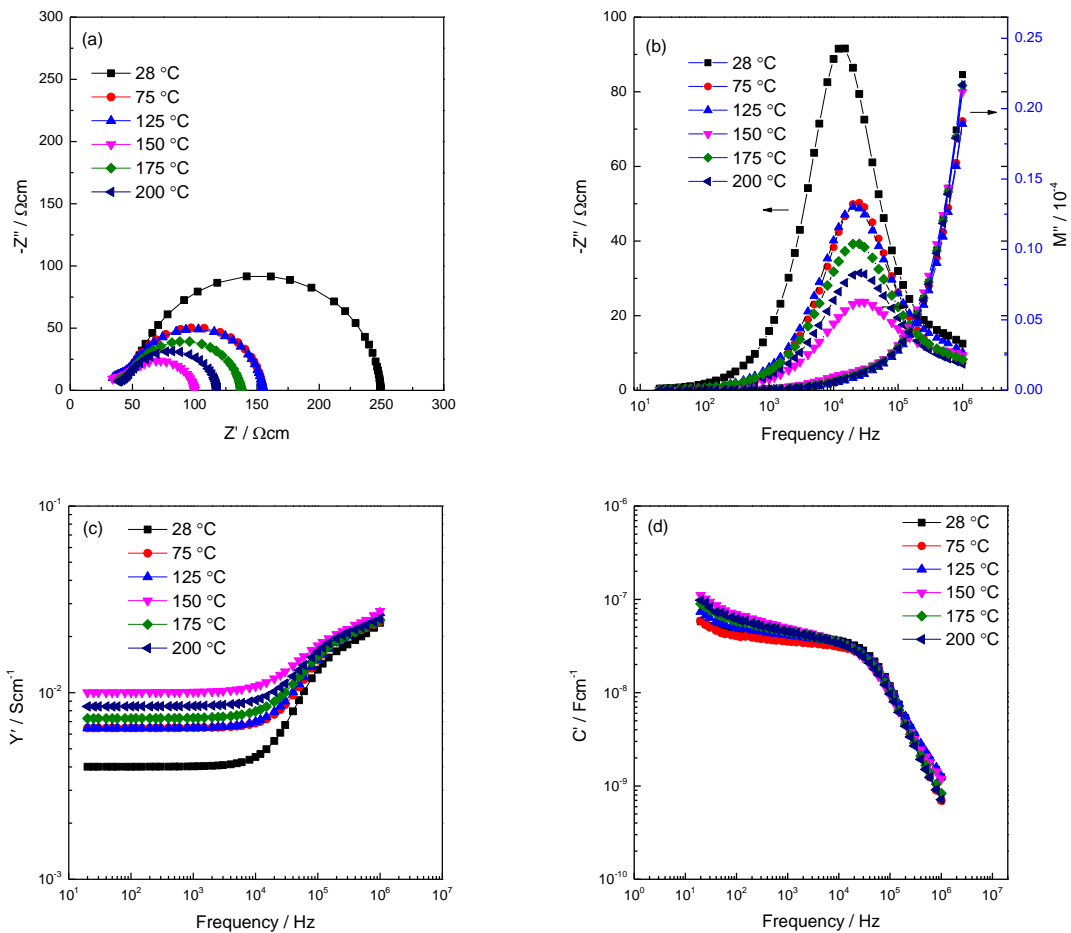


Figure 5-18: IS data for Er-A, $\nu = 0.01$, Q from 1350 °C, (a) impedance complex plane plots, Z^* (b) $-Z''$, M'' spectroscopic plots, (c) Y' plots and (d) C' plots for different frequencies for samples with In-Ga electrodes.

IS data for the same sample with Ag electrodes are presented in Figure 5-19 at low temperatures. A significant change in the high frequency (bulk) response values with temperature was observed. IS data show two semicircles in Z^* at low temperature (25-75 K). The resistance decreases with increasing temperature for both the bulk and grain boundary arcs, Figure 5-19 (a). The low frequency incline in the Z' data with a shoulder on the high frequency side was observed at 25-50 K whereas, the complete peak was seen at ≥ 75 K. The height of the M'' peak decreased and shifted towards higher frequencies with increasing temperature, (b) with $C'_{25} = \sim 8.65 \times 10^{-11}$, $C'_{50} = 9.04 \times 10^{-11}$ and $C'_{75} = 4.67 \times 10^{-10} \text{ Fcm}^{-1}$. The power law dispersion in Y' at higher frequencies, (c) and C' at lower frequencies, (d) was observed.

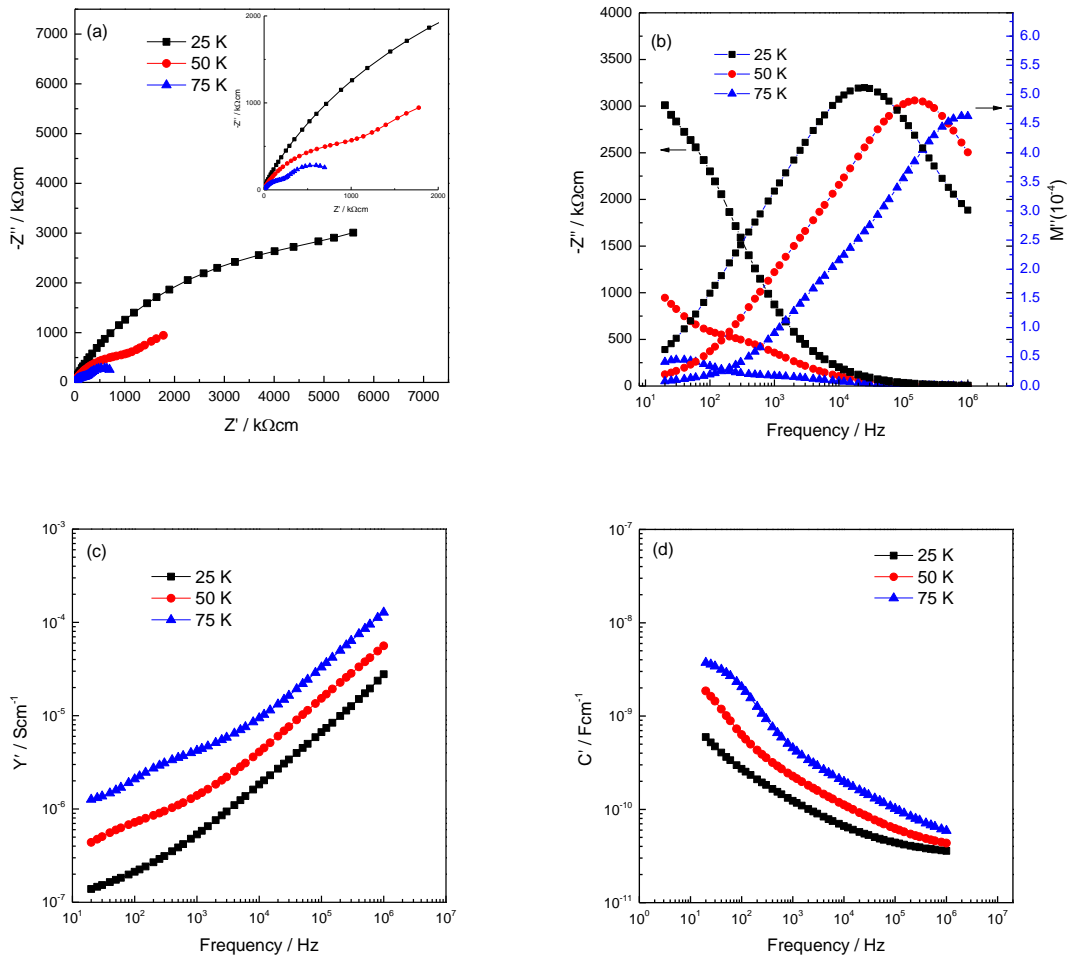


Figure 5-19: IS data for Er-A, $\nu = 0.01$, Q from 1350 °C, (a) impedance complex plane plots, Z^* (b) $-Z''$, M'' spectroscopic plots, (c) Y' plots and (d) C' plots for different frequencies for samples with Ag electrodes.

Different atmospheres and electrode were applied for $\nu = 0.01$, Q. IS data with Ag and In-Ga electrodes in air, N_2 and O_2 gases are shown in Z^* plot, Figure 5-20 (a). There is no change in the impedance data with different gases but a large semicircular arc at low frequency which was observed with Ag electrodes disappeared with In-Ga electrodes. Figure 5-20 (b) shows no considerable effect with changing pO_2 . The C' spectroscopic plots show high capacitance, low frequency plateaus with $C' = \sim 3-7 \times 10^{-9} \text{ Fcm}^{-1}$, followed by a dispersion toward low capacitance at high frequency, Figure 5-20 (c). The sample of $\nu = 0.001$, Q also was independent of pO_2 , (not shown).

Impedance data for $\nu = 0.01$, Q with Ag electrodes, with 10 volt, show no change in the bulk, Figure 5-21 (a) and (b), whereas the low frequency component resistance decreased. This decrease was time-independent. The C' data did not change at high frequency range and as well low frequency region except at $< 10^2$ Hz as a small decrease was observed, 5-21 (c). The sample of $\nu = 0.001$, Q also showed similar behaviour, (not shown).

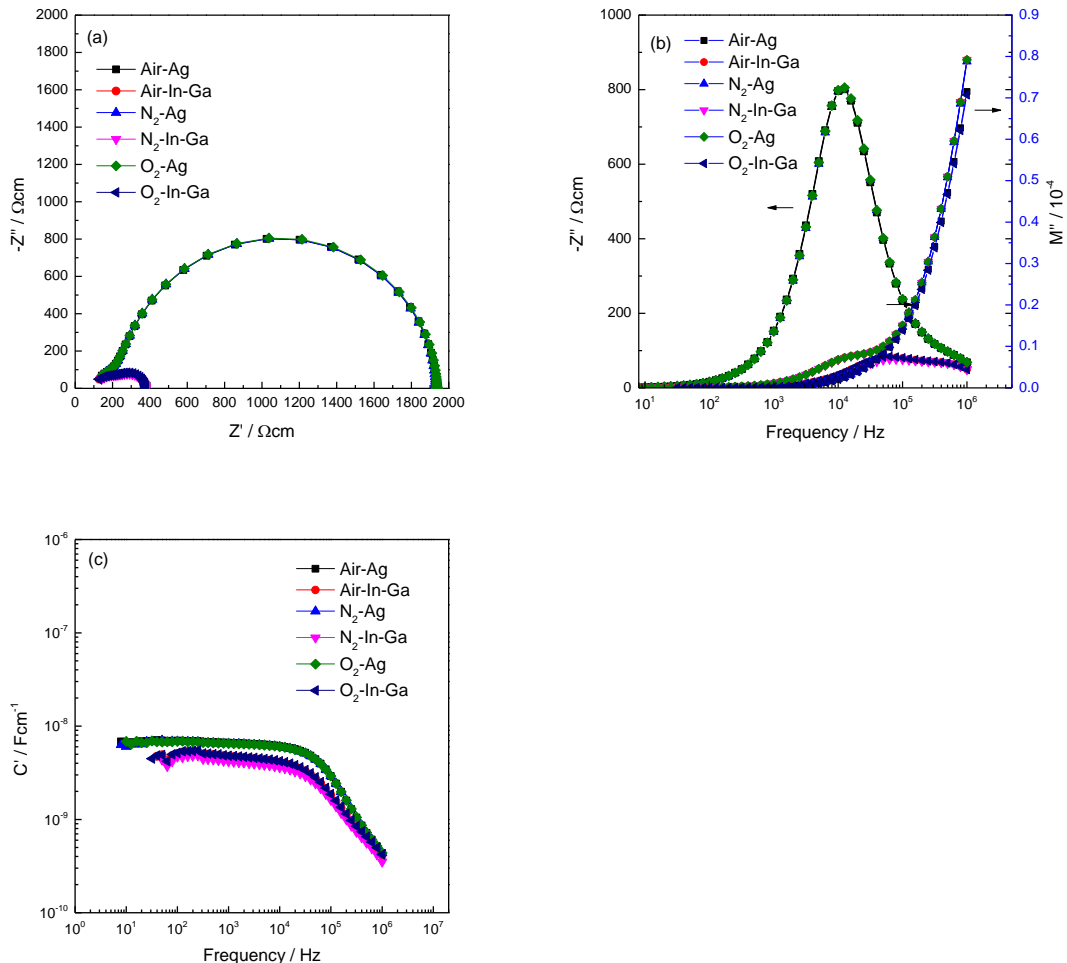


Figure 5-20: RT, IS data for Er-A, $\nu = 0.01$, Q from 1350 °C, (a) Z^* plot, (b) M'' plot and (c) C' plot in different atmospheres with Ag and In-Ga electrodes.

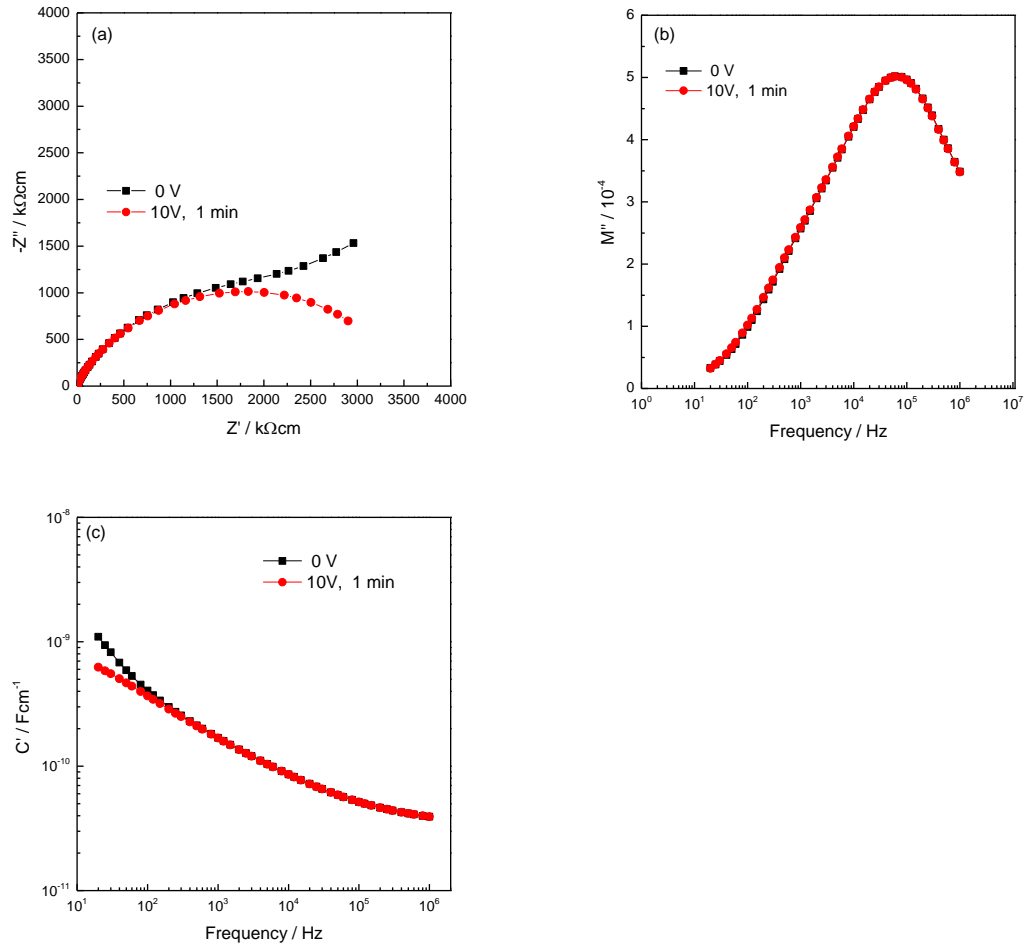


Figure 5-21: RT, IS data for Er-A, $\nu = 0.01$, Q from 1350 °C, (a) Z^* plot (b) C' plot, (c) M'' plot at 10 K before and after a voltage of 10 V was applied at different measuring times.

In summary, Er-A samples were conductive for Q samples and showed a SB effect whereas, SC samples were insulating but not homogenous and probably a conductive core was shown. The high frequency resistance and capacitance of $\nu = 0.01$ and 0.001 samples were insensitive to dc bias whereas, the low frequency component decreased reversibly with dc bias. Low frequency arc in Z^* disappeared on replacing Ag with In-Ga electrodes. Application of different pO_2 did not show any sensitivity to pO_2 . The resistivity minimum was not observed but there was a significant reduction of resistivity with the amount of Er dopant content.

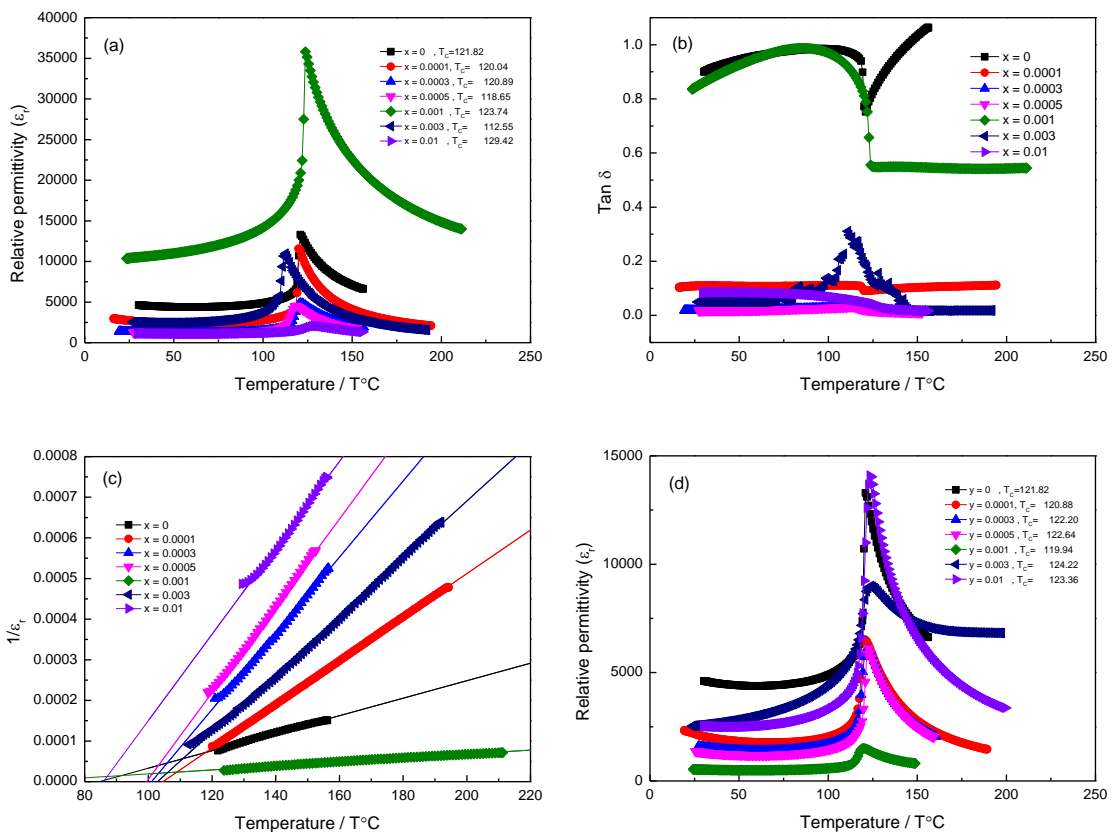
5.3.4 Electrical properties of Y-doped BT

The temperature dependence of ϵ' and $\tan \delta$ for pellets of concentrations x, y and $v = 0 - 0.01$ which had been sintered and Q from 1350 °C for 12 h in air with In-Ga electrodes measured at 250 kHz are shown in Figure 5-22 (a-i) for acceptor (a-c), self-compensation (d-f) and donor (g-i) joins respectively.

In the three joins, at T_C , a clear maximum in permittivity and dielectric loss was observed in the range $\sim 2101- 36141$, Figure 5-22 (a) for Y-B, $\sim 1641- 14215$, Figure 5-22 (d) for Y-AB and $\sim 13385- 1622$, Figure 5-22 (g) for Y-A. In general, the transition temperature of most samples did not show significant change with increasing x, y and v . For Y-B, the magnitude and sharpness of the permittivity maximum decreased substantially with increasing Y content except at $x = 0.001$ which ϵ_{\max} was very high, Figure 5-22 (a). For Y-AB and Y-A, no systematic trend was observed and the value of the permittivity maximum for $y = 0.01$ was higher than for other samples whereas all doping samples were lower than pure BT for Y-A.

Permittivity data are plotted in Curie-Weiss form in Figure 5-22 (c,f,i). Cw data extracted from the Curie-Weiss plots are listed in Table 5-3.

There was a clear decrease in the dielectric loss with all Y doping, Figure 5-6 (b,e,h).



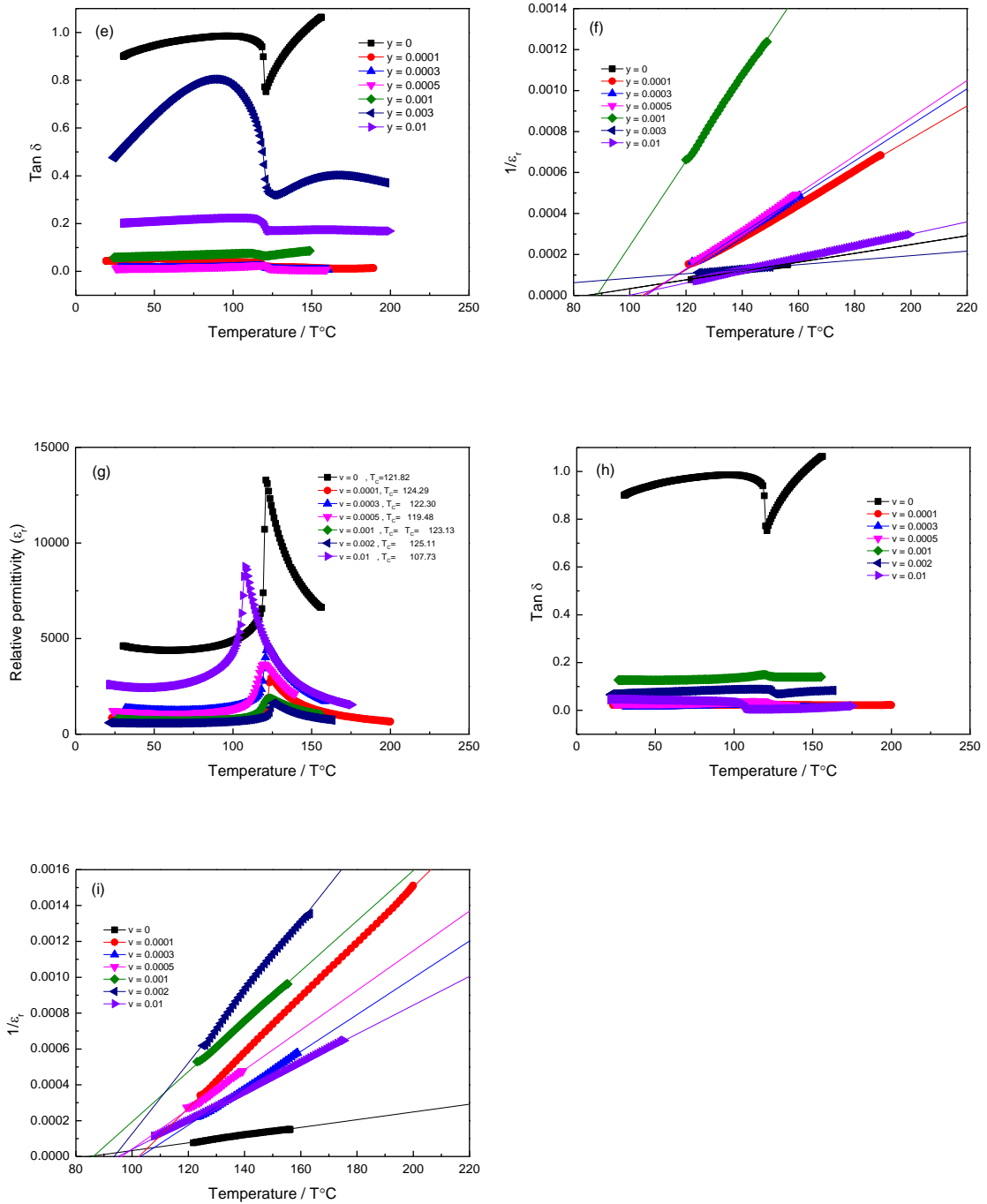


Figure 5-22: Fixed frequency measurements at 250 kHz of (a,d,g) relative permittivity (b,e,h), dielectric loss ($\tan \delta$) versus temperature and Curie-Weiss plots (c,f,i) for Y-B, Y-AB and Y-A at several concentrations (x, y and $v = 0, 0.0001, 0.001$ and 0.01) sintered at 1350 °C for 12 h in air for samples with In-Ga electrodes.

Table 5-3: Values of T_c , T_o , $T_c - T_o$ and C_w .

Composition for Y-B	T_c (°C)	T_o (°C)	$T_c - T_o$ (°C)	C_w (10^5 K)
0	122	85	37	4.64

0.0001	120	104	16	1.86
0.0003	121	101	20	1.07
0.0005	119	99	20	0.94
0.001	124	61	63	20.49
0.003	113	102	11	1.41
0.01	129	86	43	0.94
Composition for Y-AB	T_C (°C)	T_o (°C)	$T_C - T_o$ (°C)	C_w (10^5 K)
0	122	85	37	4.64
0.0001	121	105	16	1.25
0.0003	122	105	17	1.14
0.0005	123	106	17	1.09
0.001	120	88	32	0.48
0.003	124	24	100	9.10
0.01	123	100	23	3.35
Composition for Y-A	T_C (°C)	T_o (°C)	$T_C - T_o$ (°C)	C_w (10^5 K)
0	122	85	37	4.64
0.0001	124	103	21	0.65
0.0003	122	103	19	0.97
0.0005	120	96	24	0.90
0.001	123	86	37	0.71
0.002	125	93	32	0.50
0.01	108	95	13	1.24

5.3.4.1 IS results for Y-B

Sample 0.001 behaved differently to those with lower and higher Y contents. Impedance measurements were made for SC and Q pellets in air at $x = 0, 0.0001, 0.0003, 0.0005$ and 0.01 . The data for SC and Q samples were too resistive at RT without showing any evidence of a conductive core. C' and Y' data showed a CPE. At high temperature, two components were observed. Two plateaux in C' were seen, indicating gb and b. Bulk and grain boundary conductivity data for SC sample at $x = 0.0001$ and 0.01 are plotted in Arrhenius format, Figure 5-23. Different pellet with same condition for $x = 0.01$ showed a poor semiconductive behaviour with $R_T \sim 7.5 \times 10^5 \Omega\text{cm}$. This sample was reheated and Q from 1400 and 1500 °C but was still too resistive to measure.

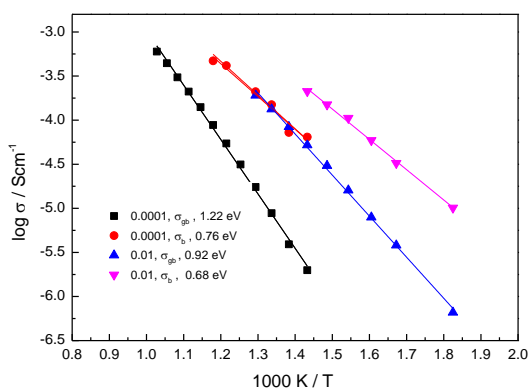
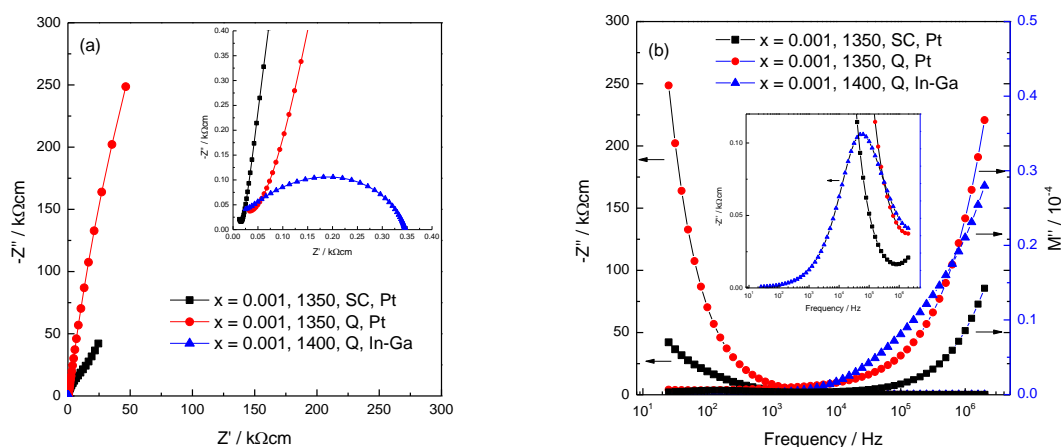


Figure 5-23: Arrhenius plot of conductivity data for Y-B at $x = 0, 0.0001$ and 0.01 , SC, sintered at $1350\text{ }^{\circ}\text{C}$ for 12 h in air against reciprocal temperatures for samples with Pt electrodes.

The sample of $x = 0.001$ was studied to characterise its bulk response. Impedance measurements were made for SC and Q pellets in air with different electrodes. In Z^* , a semicircular arc with resistance of ~ 20 and $50\ \Omega\text{cm}$ with another resistive component at low frequency was clearly seen for both SC and Q respectively at same conditions; $1350\text{ }^{\circ}\text{C}$ for 12 h in air with Pt electrodes at RT whereas, two overlapping broad arcs are seen for sample Q from 1400 with In-Ga electrodes, Figure 5-24 (a). Combined Z''/M'' spectroscopic plots are given in (b). M'' also displays evidence of a conductive core. The C' data are strongly frequency-dependent between $\sim 10^5$ - 10^6 Hz as the C' data increasingly show dispersion to lower values with increasing frequency. Data at low frequency show a general plateau attributed to a Schottky barrier effect, (c).



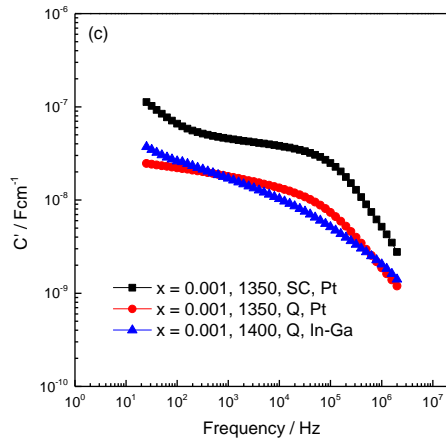
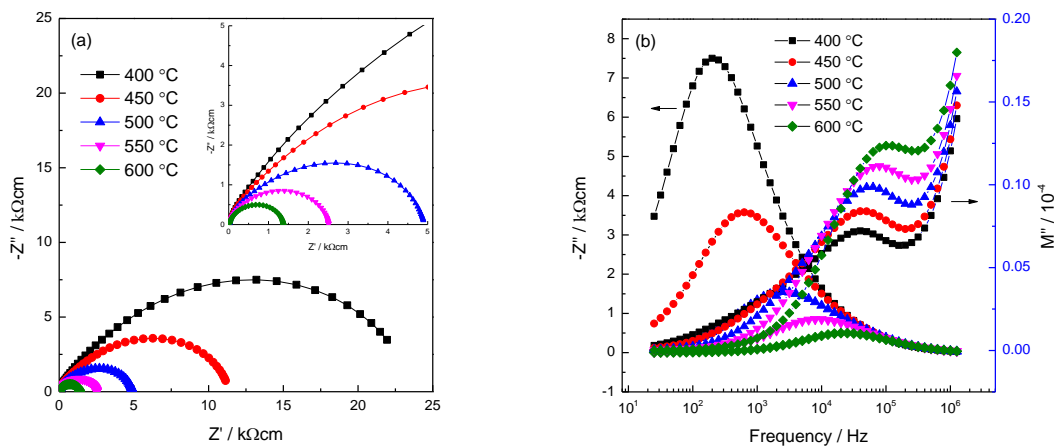


Figure 5-24: RT IS data for Y-B, SC and Q samples at $x = 0.001$, (a) impedance complex plane plots, Z^* (b) $-Z''$, M'' spectroscopic plots and (c) C' plots for different frequencies.

SC sample at higher temperatures shows three regions. Broad semicircular arcs were seen in the Z^* plot, Figure 5-25 (a). The M'' data indicate two components; peaks between $\sim 10^4$ - 10^6 Hz and the start of a high frequency peak at $f_{\max} > 10^6$ Hz, (b). Z'' peak decreased significantly and shifted to high frequency with an increase in temperature. The Y' plots show a clear plateau at low frequency separated by dispersion over a range of intermediate frequencies, (c). The C' data are strongly frequency-dependent and low frequency data show that SB is dominant, (d). At low frequency, Y' increases with temperature but C' decreases. Resistance decreases but the region becomes thicker. At intermediate frequency, Y' data and C' change less with temperature in the low frequency region.

A modest PTCR effect for the total resistivity was observed for sample Q from 1400 °C with In-Ga electrodes (not shown).



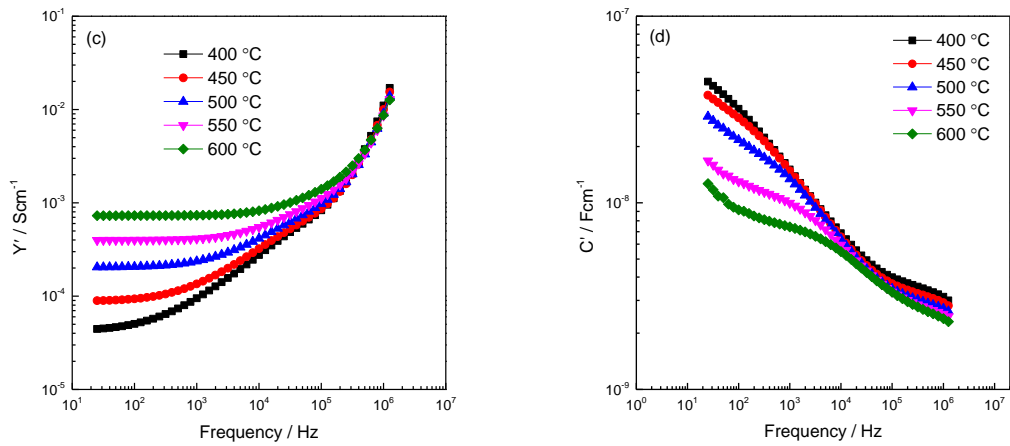
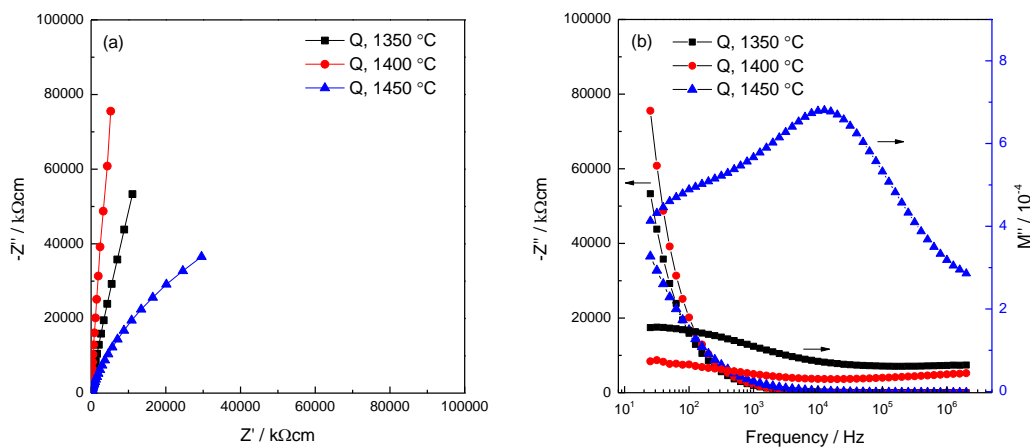


Figure 5-25: IS data for Y-B, SC, $x = 0.001$, sintered at $1350\text{ }^{\circ}\text{C}$ for 12 h in air, (a) impedance complex plane plots, Z^* (b) $-Z''$, M'' spectroscopic plots, (c) Y' plots and (d) C' plots for different frequencies for samples with Pt electrodes.

A sample prepared by *PBM* shows similar behaviour to *HM* sample: a conductive core was observed for $x = 0.001$, Q from $1350\text{ }^{\circ}\text{C}$ and 0.003 , Q from $1400\text{ }^{\circ}\text{C}$ with $R_1 \sim 3000$ and $250\text{ }\Omega\text{cm}$ (not shown) whereas, *BM* sample at $x = 0.001$ did not show any evidence of a conductive core even with Q from different temperatures in Z^* . Figure 5-26 (a) shows that the data of Z^* were too resistive to measure at room temperature. The Z'' plot shows a low frequency incline. The M'' data did not indicate the bulk response, (b). The admittance, Y' data show no evidence of any dc conductivity either with low or high frequency regions, (c). C' data show frequency-independent plateaux at higher frequencies with associated capacitances, ~ 64 , 67 and 21 pFcm^{-1} for sample Q from 1350 , 1400 and $1450\text{ }^{\circ}\text{C}$ respectively. These are attributed to the bulk capacitance of the samples.



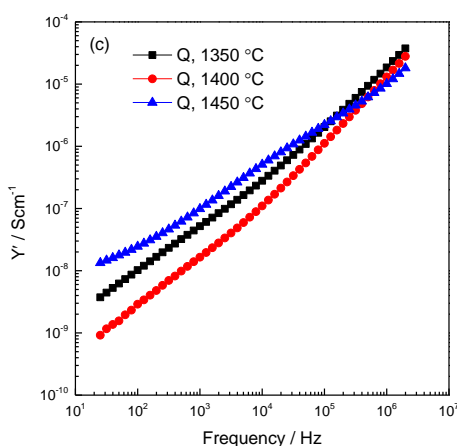


Figure 5-26: RT IS data for Y-B, *BM*, $x = 0.001$, (a) impedance complex plane plots, Z^* (b) $-Z''$, M'' spectroscopic plots (c) Y' plots and (d) C' plots for different frequencies with In-Ga electrodes.

Different atmospheres were applied for $x = 0.01$ with Ag electrodes. The sample start showed clear semicircular arcs at 350 °C. The data showed a decrease in conductivity with decreasing pO_2 at 350 °C, Figure 5-27 (a). Z^* plots showed one broad arc with a small tail at low frequencies. The C' data showed a frequency-independent plateau at high frequencies, 51 pFcm^{-1} , (b). The M'' peak (c) shifted to lower frequencies with decreasing pO_2 . The conclusion from these results is that the bulk conductivity is p-type. The sample of $x = 0.001$, Q also was independent of pO_2 , (not shown).

Effect of applying 10V dc bias at 350 °C is shown in Figure 5-28. R_T decreased when a voltage of 10V was applied, (a). The M'' broad peak shows that the peak height reduced and became two separate peaks, (b). All C' data increased slightly after applying 10V dc bias, (c). There was a significant time dependence of Z^* data on removing the dc bias. The conclusion from the dc bias results is that the conduction is p-type, similar to the conclusion from the pO_2 tests. Similar results were observed for both SC and Q samples. The sample of $x = 0.001$, Q showed that, R_T decreased with dc bias (not shown).

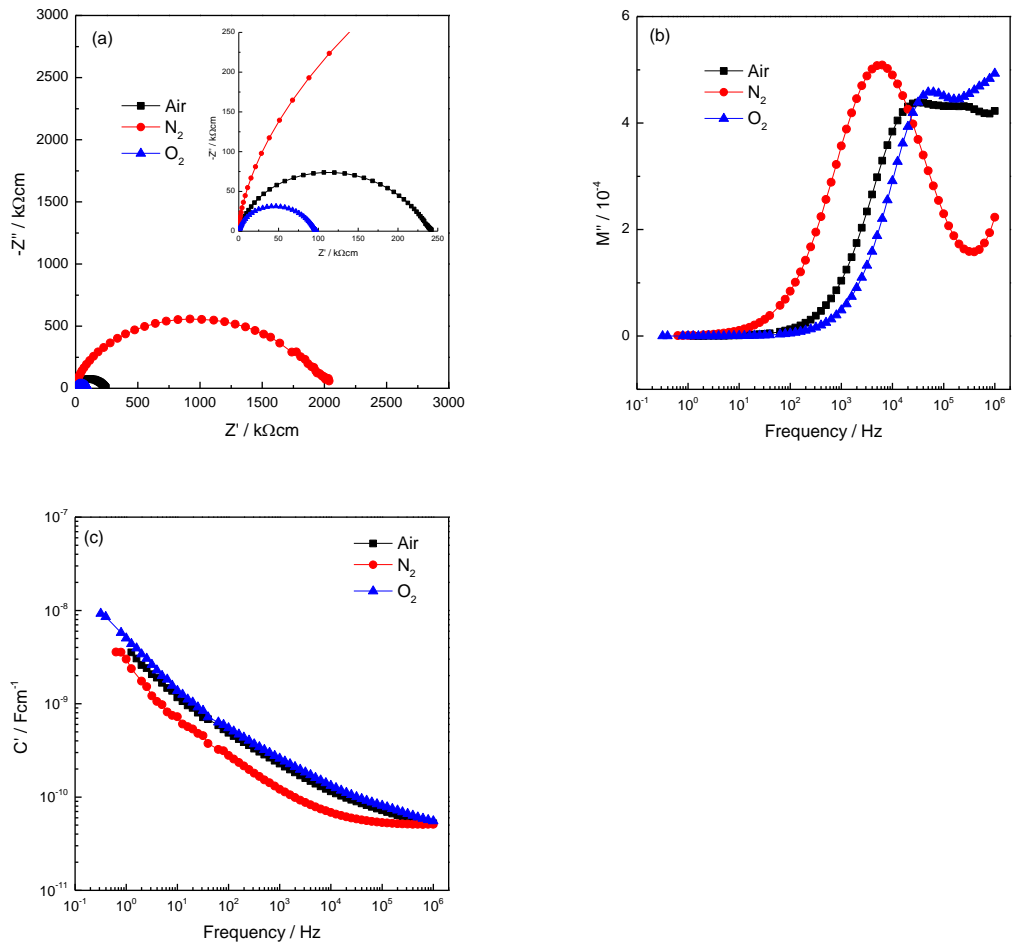
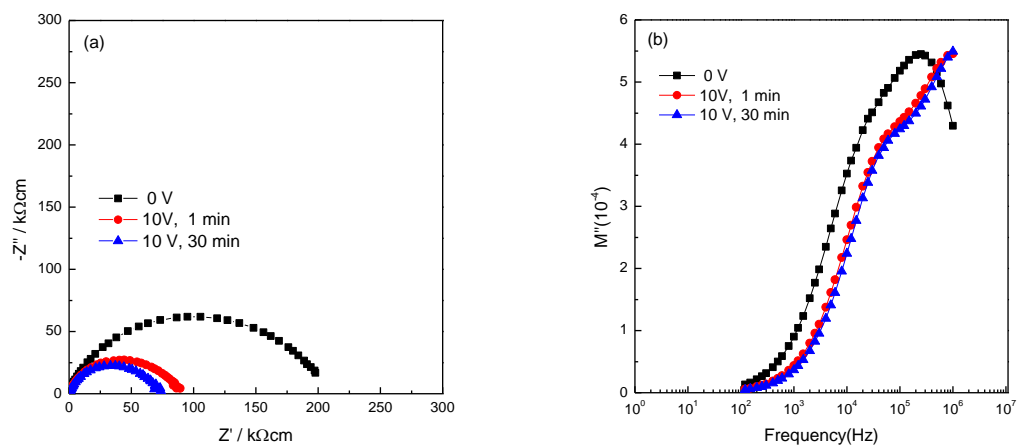


Figure 5-27: 350 °C IS data for Y-B, $x = 0.01$, Q from 1400 °C, (a) Z^* plot, (b) M'' plot and (c) C' plot in different atmospheres with Ag electrodes.



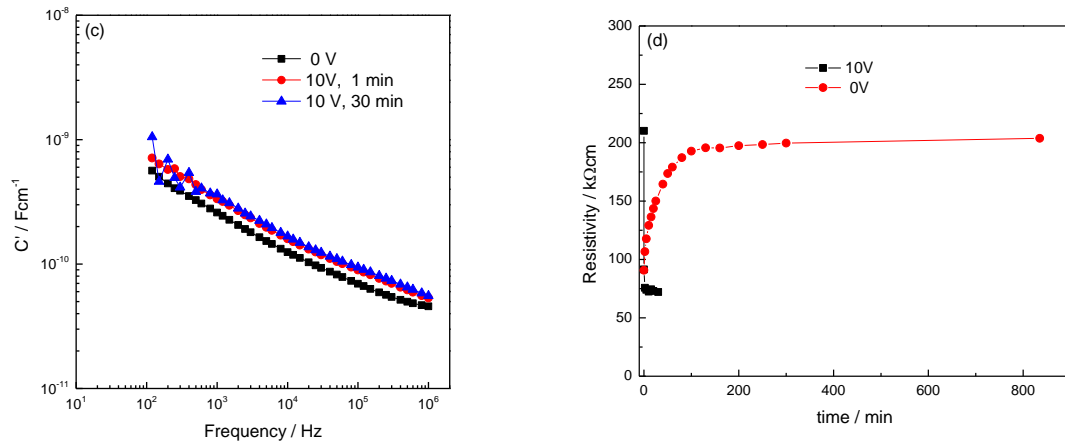


Figure 5-28: 350 °C IS data for Y-B, $x = 0.01$, Q from 1400 °C, (a) Z^* plot (b) M'' plot, (c) C' plot before and after a voltage of 10 V was applied at different measuring times and (d) Total resistance with 10V bias and after removing the dc bias at different times in air with Ag electrodes.

In summary, Y-B samples were resistive for both SC and Q samples at $x = 0, 0.0001, 0.0003, 0.0005$ and 0.01 and no conductive core was observed. A conductive core for both SC and Q samples was observed for $x = (0.001, HM)$ and $(0.001$ and $0.003 PBM)$ and showed a SB effect whereas, $0.001, BM$ sample showed that R_T was too high to measure with little evidence of conductive core for sample Q only from 1450 °C. P-type behaviour was observed by pO_2 and dc bias for insulating sample, 0.01 whereas, conductive sample, 0.001 was not sensitive to pO_2 and the resistance decreased reversibly with dc bias.

5.3.4.2 IS results for Y-AB

Too resistive data were observed either with SC or Q pellets in air at $y = 0, 0.0001, 0.0003,$ and 0.0005 at RT and showed a weak conductive core. The increase of temperature showed two components. Bulk and grain boundary conductivity data for SC sample at $y = 0.0001$ are plotted in Arrhenius format, Figure 5-29. $\sigma_b > \sigma_{gb}$ by half order of magnitude at low temperatures, ~ 250 °C, therefore, σ is dominated by σ_{gb} . With increasing temperature, the difference between σ_b and σ_{gb} values reduced gradually.

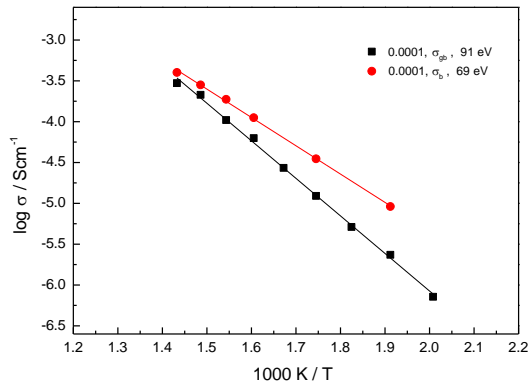


Figure 5-29: Arrhenius plot of conductivity data for Y-AB, $y = 0.0001$, SC, sintered at $1350\text{ }^{\circ}\text{C}$ for 12 h in air against reciprocal temperature for samples with Pt. electrodes

A conductive core component at high frequency with resistance at RT of ~ 200 and $2000\ \Omega\text{cm}$ in Z^* were observed for SC and Q pellets respectively in air with Pt electrodes for $y = 0.001$. A semicircular arc was shown for sample Q from 1400 with In-Ga electrodes, Figure 5-30 (a). Generally, the C' data showed lower values compared to the same composition on Y-B, (b).

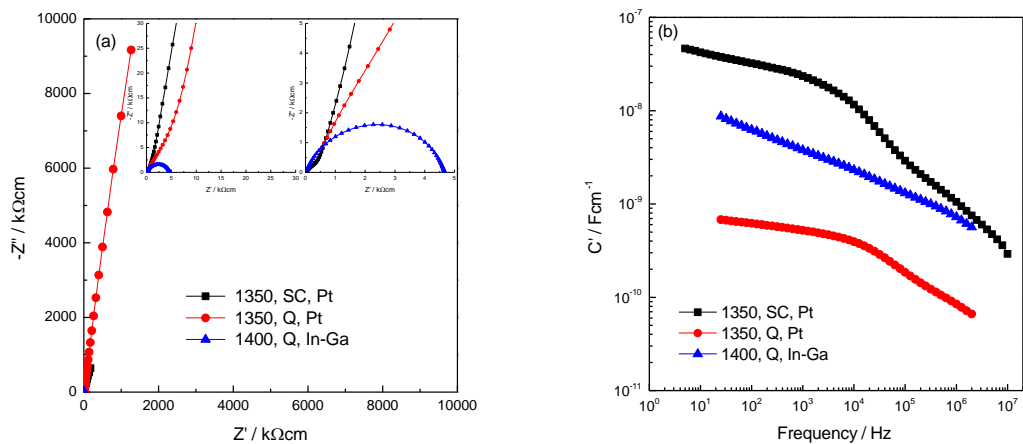


Figure 5-30: IS data for Y-AB, SC and Q, $y = 0.001$, (a) impedance complex plane plots, Z^* and (b) C' plots for different frequencies.

Sample Q from $1400\text{ }^{\circ}\text{C}$ with In-Ga electrodes showed a modest PTCR effect for the total resistivity (not shown).

PBM samples show a conductive core for $y = 0.001$, Q from $1350\text{ }^{\circ}\text{C}$ and 0.003 , Q from $1400\text{ }^{\circ}\text{C}$ with $R_1 \sim 150$ and $22000\ \Omega\text{cm}$ respectively (not shown) whereas, *BM* sample at $y = 0.001$ showed a poor semiconductive behaviour for sample Q from

1350 °C with two overlapping arcs with $R_T \sim 8.85 \times 10^5 \Omega\text{cm}$. Sample Q from 1400 and 1450 °C were too resistive to measure at room temperature, Figure 5-31 (a).

The Z'' / M'' plots data for a sample Q from 1450 °C, (b), show that the sample was too resistive to measure at RT as f_{max} of any Debye-type peaks in Z'' and M'' plots must occur below the lower measuring frequency limit of the instrumentation (<20 Hz). The Z'' plot of sample Q from 1400 °C showed similar behaviour. The M'' peak was clearly shown for sample Q from 1350 °C, (b). The total conductivity could be measured only for sample Q from 1350 °C at low frequency, (c). C' data is frequency-independent for all Q temperatures at high frequency with $C_b \sim 65, 53$ and 47 pFcm^{-1} for sample Q from 1350, 1400 and 1450 °C respectively, (d).

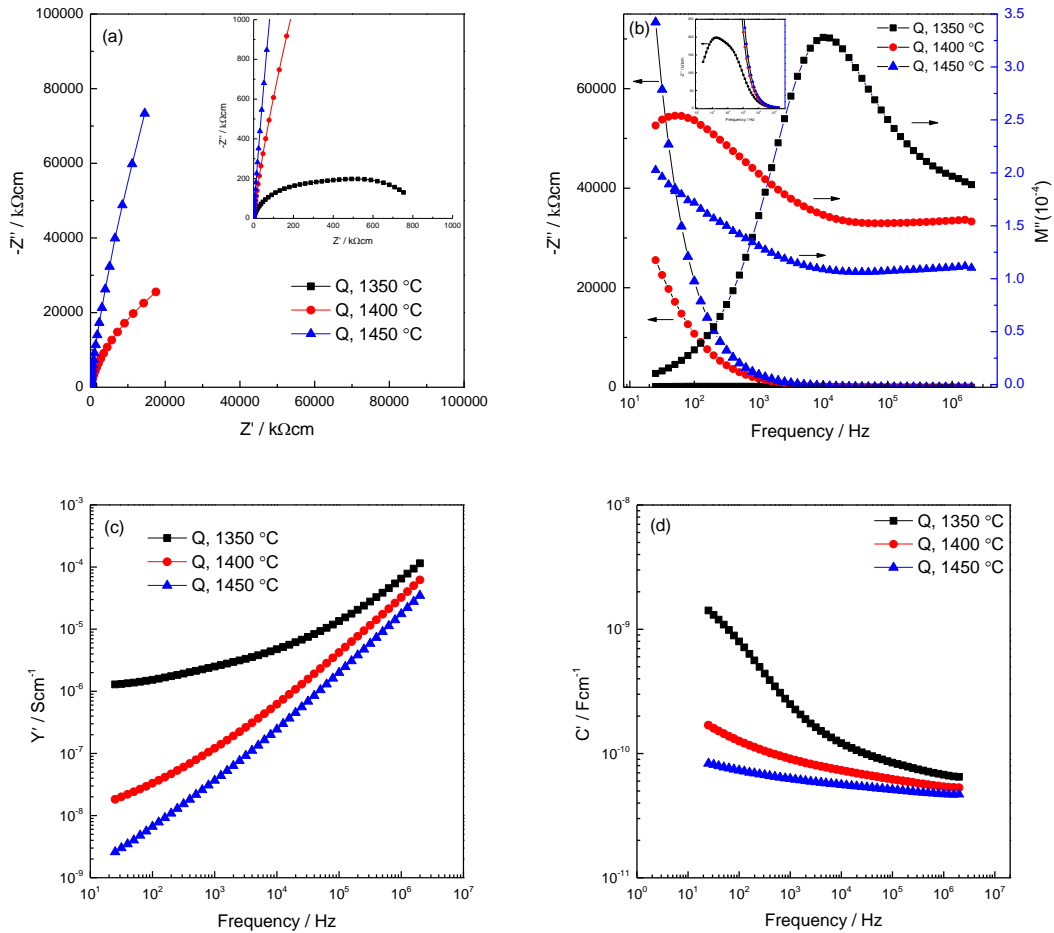


Figure 5-31: IS data for Y-AB, BM, Q sample at $y = 0.001$, (a) impedance complex plane plots, Z^* (b) $-Z''$, M'' spectroscopic plots (c) Y' plots and (d) C' plots for different frequencies with In-Ga electrodes.

The effect of cooling rate for $y = 0.01$, sintered at $1400\text{ }^\circ\text{C}$ for 12 hours in air was studied. Results are shown for three different cooling rates in the following sequence: SC in air, Q in air and Q in liquid N_2 . The room temperature Z^* plot showed there was an apparent semiconducting component at high frequency for SC and Q in air and the low frequency component was very resistive whereas, a semicircular arc was observed for sample Q into liquid nitrogen with $R_T \sim 1.91 \times 10^5\ \Omega\text{cm}$, Figure 5-32 (a). The M'' spectra showed a broad peak between 10^3 - 10^5 Hz and another incline at $> 10^6$, indicating the presence of a conductive component in this ceramic, (b). The Z'' peak and low frequency plateau in Y' was only shown for sample Q into liquid N_2 , (b) and (c). C' data are typically associated with the bulk and grain boundary components, (d).

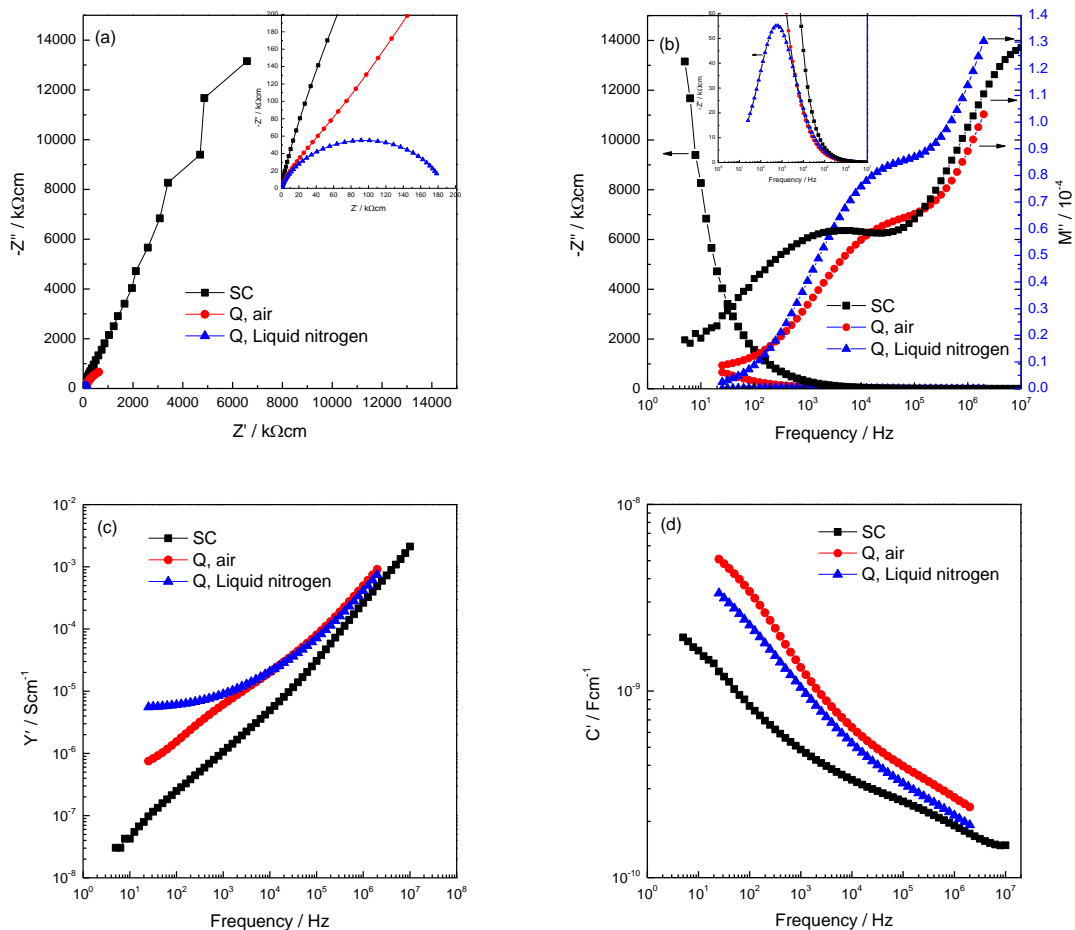
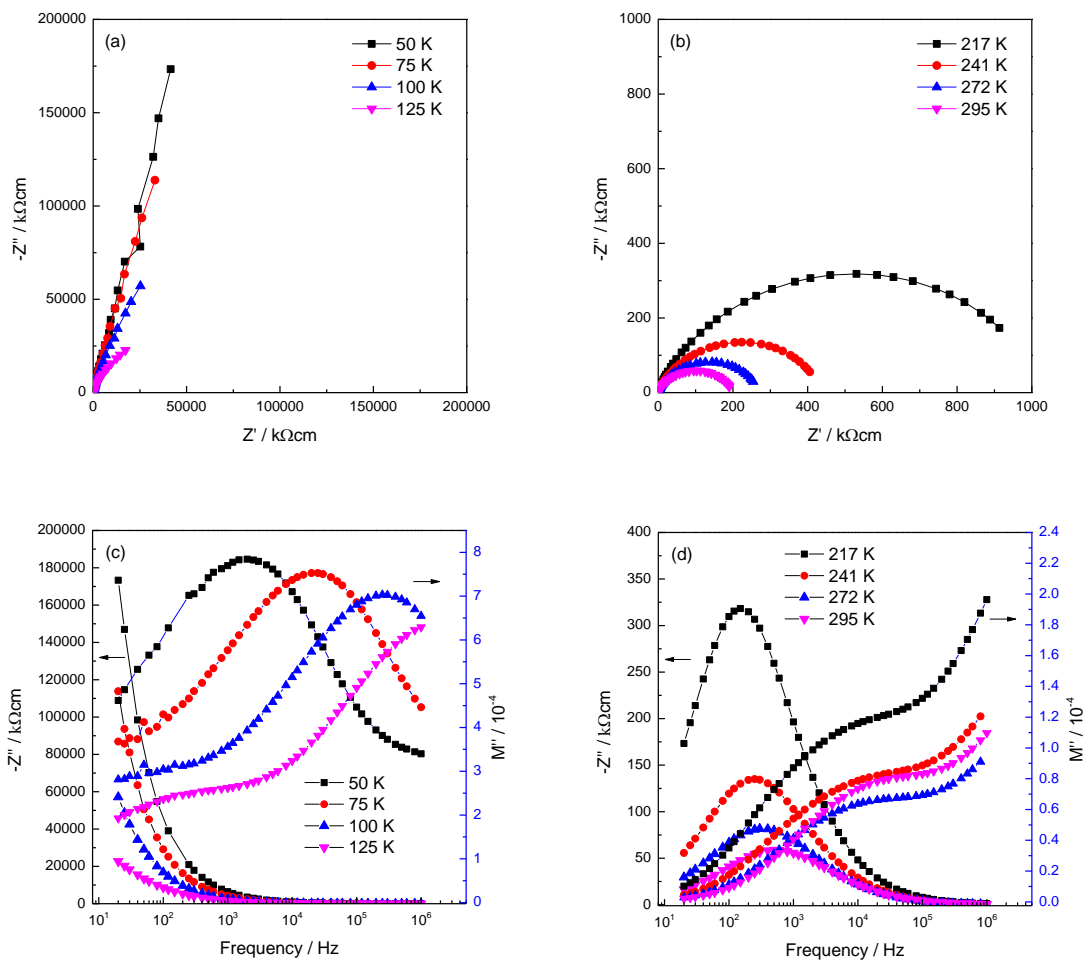


Figure 5-32: RT IS data for Y-AB, $y = 0.01$, SC and Q form $1400\text{ }^\circ\text{C}$, (a) impedance complex plane plots, Z^* (b) $-Z''$, M'' spectroscopic plots (c) Y' plots and (d) C' plots for different frequencies with In-Ga electrodes.

For sample Q from 1400 °C into liquid N₂, IS data were obtained at low temperature. The total resistivity was too resistive to measure between 50-125K whereas it can be measured between 217-295K as a semicircular arc was observed, Figure 5-32 (a) and (b). The M'' peaks represented the bulk response with $C_b \sim 56, 59$ and 63 pFcm^{-1} for 50, 75 and 100K respectively. The M'' plot between 217-295K shows evidence for a more conductive grain core that can not be measured, which is clearly seen by the increase in M'' data at $> 10^6 \text{ Hz}$, (c) and (d). The total conductivity and low frequency peak can not be measured for 50-125K, (c,e). The Z'' peak and low frequency plateau in Y' was only shown for 217-295K, (d,f). C_b and C_{gb} data for 50-125K were lower than 217-295K, (g,h). The σ_b , σ_{gb} and σ_T data were calculated from the M'' , Z'' and Z^* plots respectively, Figure 5-33. The activation energy for σ_b , σ_{gb} and σ_T is very low.



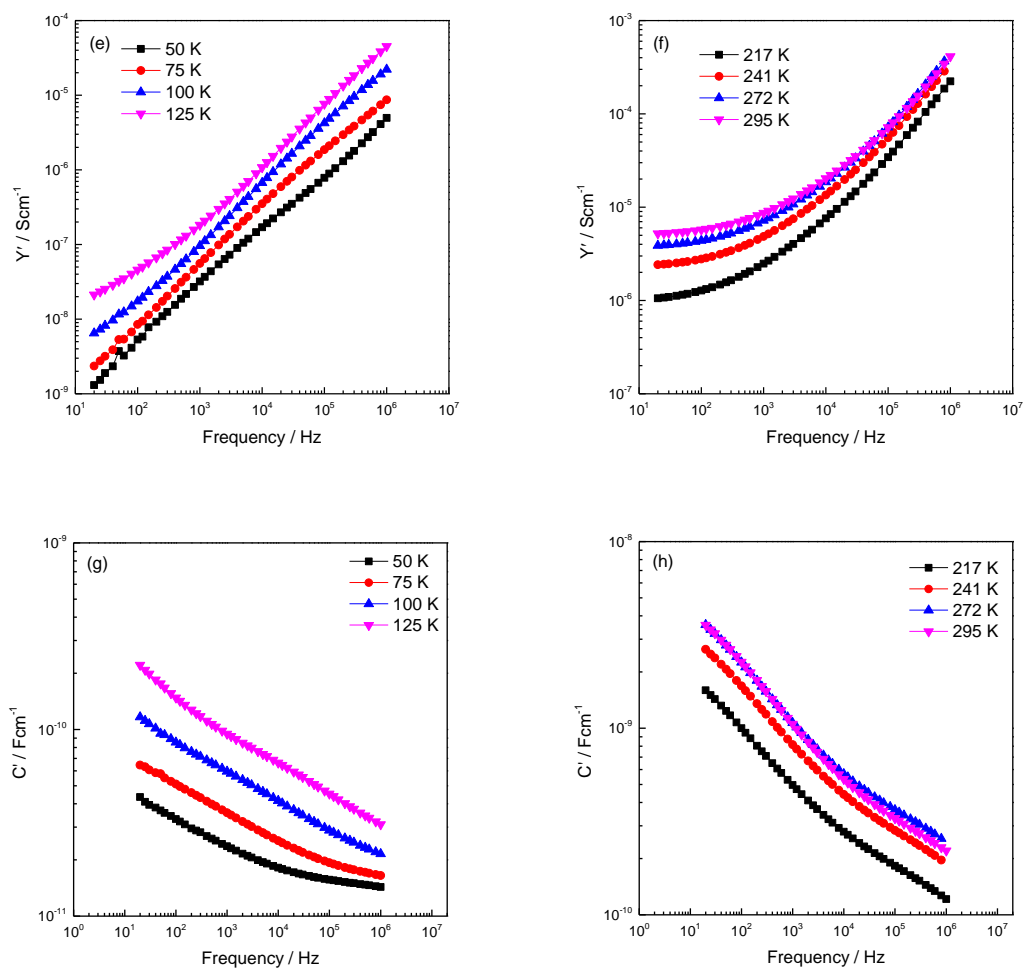


Figure 5-33: IS data for Y-AB, Q from 1400 °C into liquid N₂ for y = 0.01, (a,b) impedance complex plane plots, Z* (c,d) -Z'', M'' spectroscopic plots (e,f) Y' plots and (g,h) C' plots for different frequencies with In-Ga electrodes.

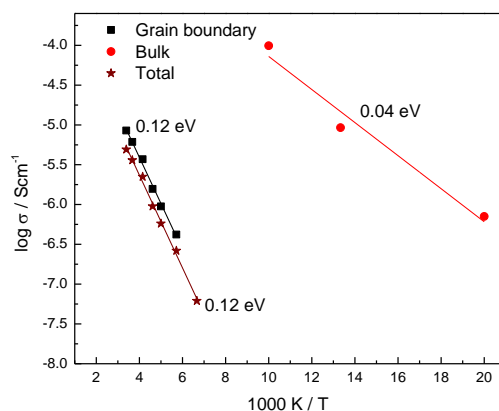


Figure 5-34: Arrhenius plot of σ_b , σ_{gb} and σ_T data for Y-AB, y = 0.01, Q from 1400 °C into liquid N₂ against reciprocal temperature for samples with In-Ga electrodes.

Q sample from 1500 °C in air for $y = 0.01$ showed no apparent sensitivity was shown to the change of pO_2 at RT. $R_T \sim 7 \times 10^4 \Omega\text{cm}$, Figure 5-35 (a). M'' and C' data were same for different atmospheres, (b,c). The sample of $y = 0.001$, Q also was independent of pO_2 , (not shown).

The effect of a dc bias of 10 V on the impedance response of Q sample from 1500 °C in air for $y = 0.01$ was studied at 50K, Figure 5-36. There are two components in Z^* , attributed to the bulk and grain boundary. R_b was essentially unchanged as shown in high frequency region either in Z^* or M'' peaks, (a,b) whereas, R_{gb} showed a small decrease which is clearly seen in the total resistance in Z^* and low frequency M'' peaks. C' data were unchanged either with low or high frequency regions, (c). On removal of the dc bias, R_{gb} increased and regained its original state with very little time-dependent ~ 10 min, (not shown). The sample of $y = 0.001$, Q showed that, R_T decreased with dc bias (not shown).

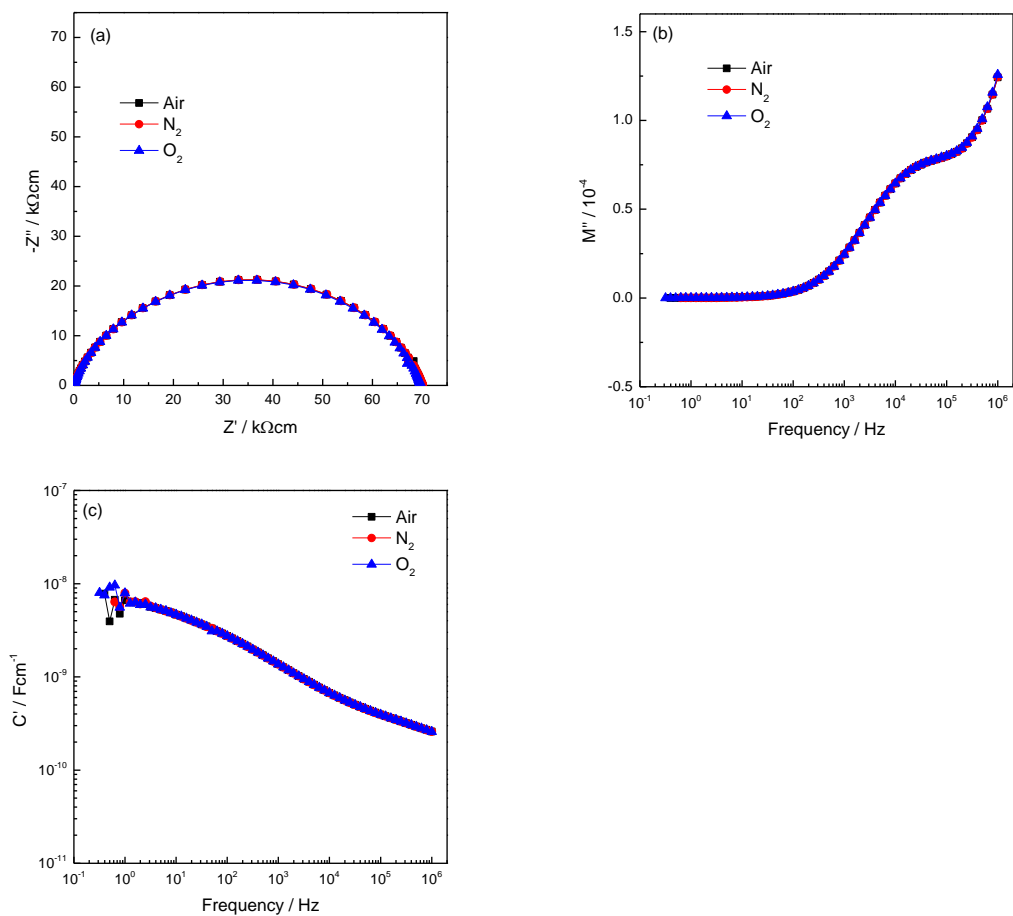


Figure 5-35: RT, IS data for Y-AB, $y = 0.01$, Q form 1500 °C, (a) Z^* plot, (b) M'' plot and (c) C' plot in different atmospheres with Ag electrodes.

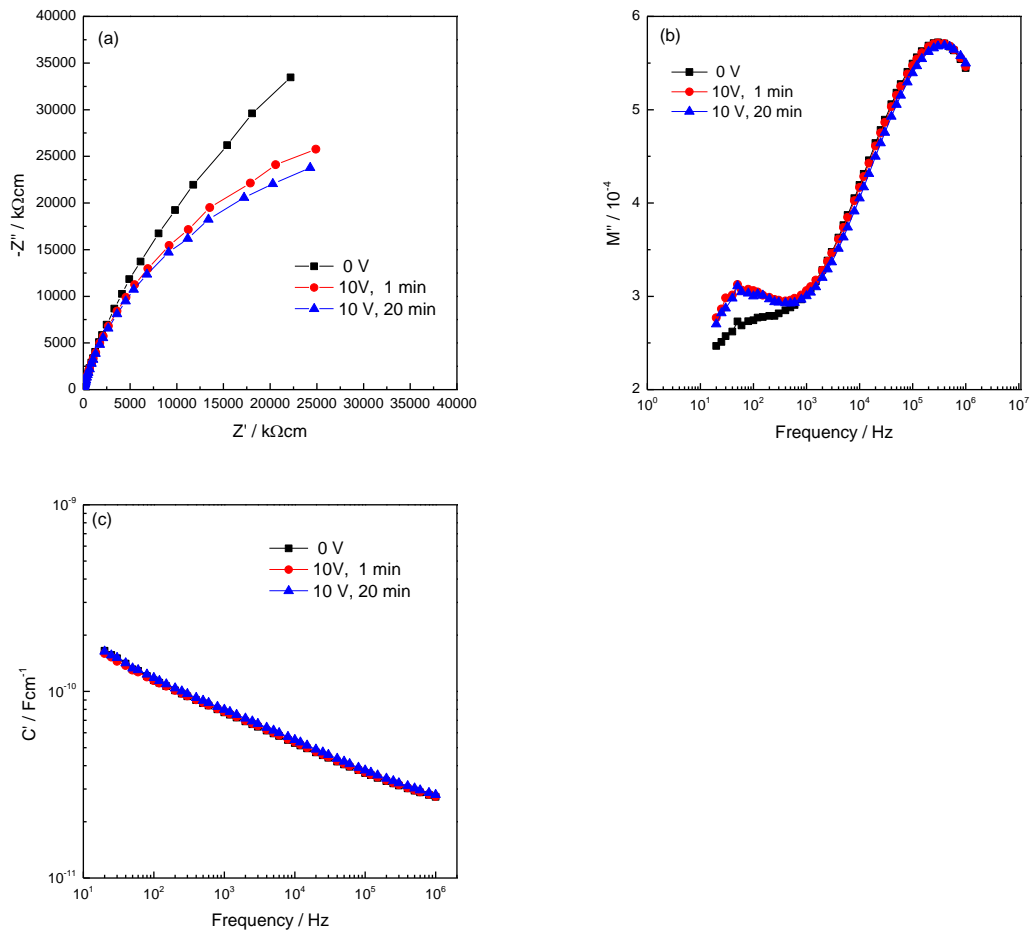


Figure 5-36: 50K IS data for Y-AB, $y = 0.01$, Q form 1500 °C, (a) Z^* plot (b) M'' plot and (c) C' plot at 50K before and after a voltage of 10 V was applied at different measuring times with Ag electrodes.

In summary, Y-AB samples showed a weak conductive core for $y = 0.0001$, SC. SC and Q samples showed a clear conductive core component for $x = 0.001$ and showed a SB effect. Conductivity was affected by cooling rate. The difference between *HM*, *PBM* and *BM* was different to Y-B behaviour as the semicircular arc was seen for *BM*, 0.001, Q from 1350 °C. No apparent sensitivity was shown to the change of pO_2 at RT for $y = 0.01$, Q from 1500 °C. Dc bias showed that R_b at 50K was independent of dc bias whereas, R_{gb} showed a reversible decrease in grain boundary resistance.

5.3.4.3 IS results for Y-A

Pellets of $\nu = 0, 0.0001, 0.0003, \text{ and } 0.0005$ were heated at different temperatures, 1350, 1350, and 1400 °C for about 12 hours; this was followed by SC and air quenching. For $\nu = 0.0001$, a clear conductive core was seen for SC, Figure 5-37

(a,b) and weak one was shown for Q. The material was very resistive for $\nu = 0.0003$ and 0.0005 and no data could be collected (not shown).

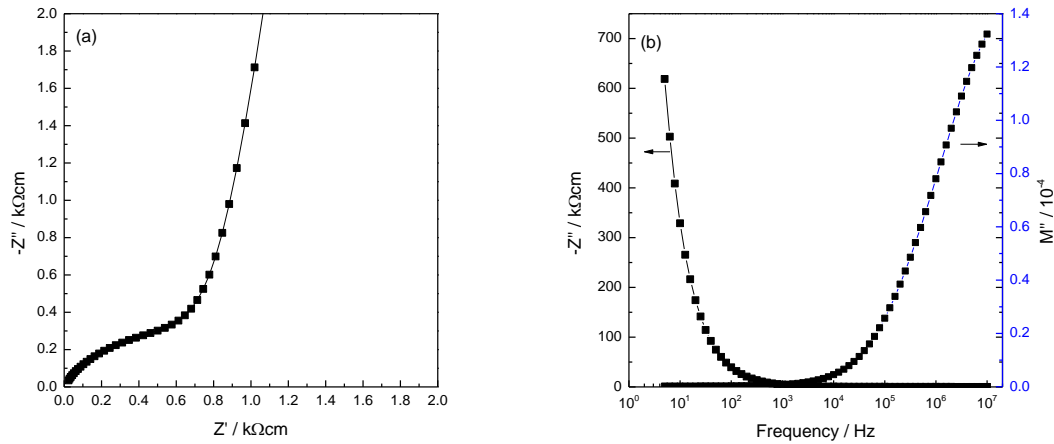


Figure 5-37: IS data for Y-A, SC, sintered at 1350 °C in air at $\nu = 0.0001$, (a) impedance complex plane plots, Z^* and (b) $-Z''$, M'' spectroscopic plots for different frequencies with Pt electrodes.

The effect of SC and Q with Pt electrodes on $\nu = 0.001$ was shown in Figure 5-38. The SC and Q, 1350 °C samples show non-zero intercept at RT of $\sim 10 \Omega\text{cm}$ at high frequencies in impedance complex plane plots, which suggests that this sample is electrical inhomogeneous. There is good evidence for a conductive grain core of $\sim 25 \Omega\text{cm}$, whereas at low frequency the total sample was resistive, (a). Impedance patterns appear to be not resolved: overlapping of two semicircular arcs are presented for sample Q from 1400 °C with In-Ga electrodes. A high frequency incline is observed in the M'' which represents the bulk component, (b). A frequency-independent plateau at low frequency is followed by a cross-over region to a high frequency with dispersion for SC and Q from 1400 °C samples whereas no plateau was seen for Q from 1350 °C, (c). The C' data show that a Schottky barrier is dominant at low frequency, following by a dispersion at high frequency (d).

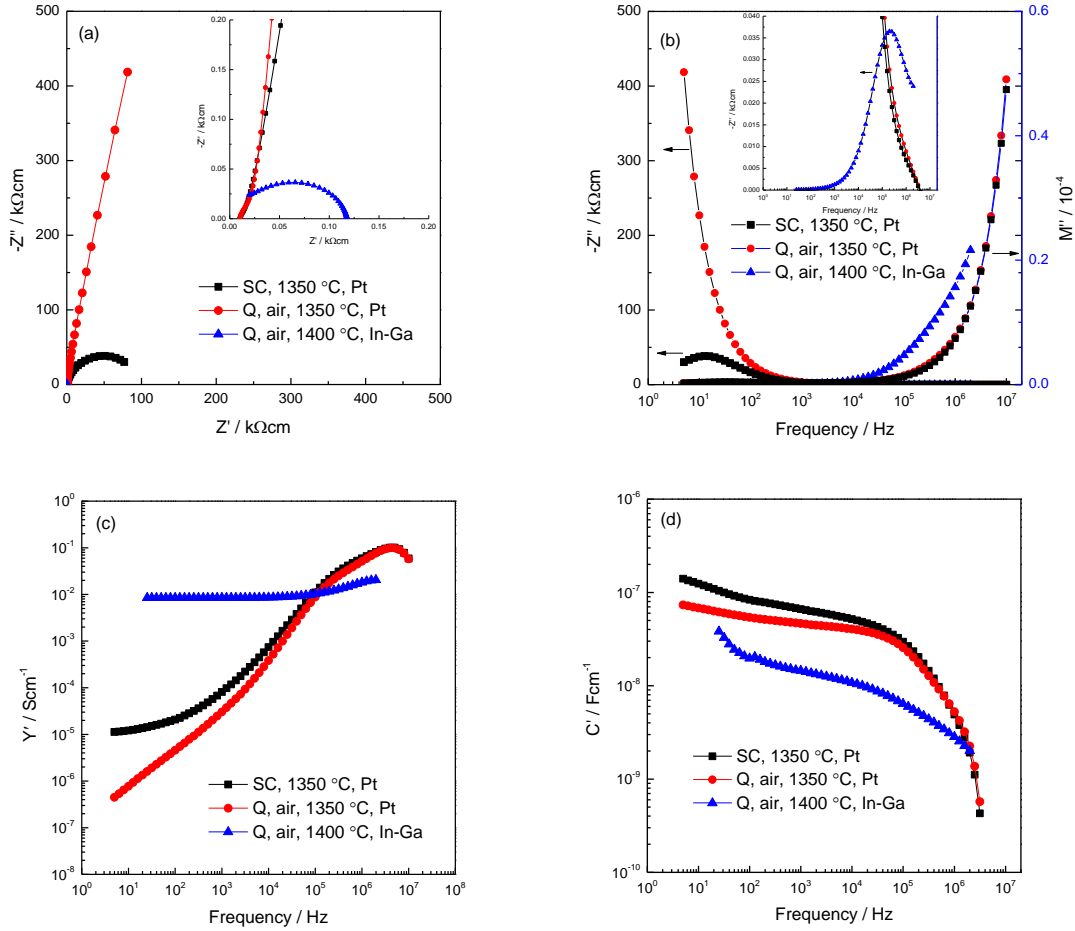


Figure 5-38: RT IS data for Y-A, SC and Q sample at $\nu = 0.001$, (a) impedance complex plane plots, Z^* (b) $-Z''$, M'' spectroscopic plots (c) Y' plots and (d) C' plots for different frequencies.

For sample Q from 1350 and 1400 °C in air, IS data were obtained at low temperature. The σ_T data were calculated from the low frequency plateau in Y' , Figure 5-39. Sample Q from 1350 was studied from 50 K to RT and sample Q from 1400 was studied from RT to 200 °C. Arrhenius plot exhibits three ferroelectric phase transitions from cubic to tetragonal ~ 125 °C and from tetragonal to orthorhombic at ~ 2 °C and from orthorhombic to rhombohedral at ~ 98 °C.

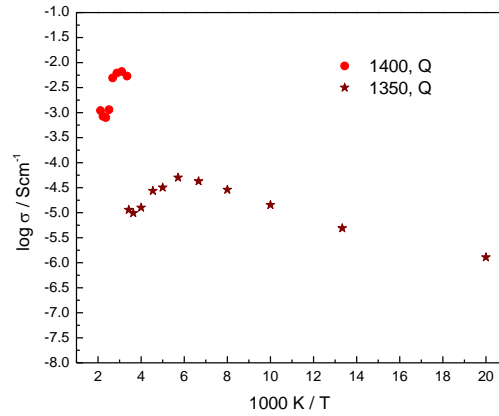


Figure 5-39: Arrhenius plot of σ_T data for Y-A at $\nu = 0.001$, Q from 1350 °C and 1400 °C against reciprocal temperature.

Sample of $\nu = 0.002$, *HM* showed a poor semiconductive behaviour with $R_T \sim 1.75 \times 10^5 \Omega\text{cm}$ (not shown).

PBM samples show a conductive core for $y = 0.001$, Q from 1350 °C and 0.003, Q from 1400 °C with $R_l \sim 16700$ and $250 \Omega\text{cm}$ respectively (not shown) whereas, *BM* sample at $\nu = 0.001$ showed a single arc, but somewhat distorted from the ideal semicircular shape for sample Q from 1350 and 1400 °C with $R_T \sim 1.26 \times 10^5$ and $2.18 \times 10^5 \Omega\text{cm}$. For $\nu = 0.001$, sample Q from 1450 °C were too resistive to measure at room temperature, Figure 5-40 (a). M'' spectra are dominated by low C_b effects, (b). The data indicate that both Z''/M'' peaks were mostly overlapping as single peaks with some broadening and a small difference in peak maxima frequencies were observed with starting another high frequency component. The Y' data show no evidence of any frequency-independent behaviour for sample Q from 1450 °C, whereas the total conductivity can be obtained from the low frequency plateau for sample Q from 1350 and 1400 °C, (c). C' data showed a frequency-independent plateau at high frequencies for sample Q from 1350 and 1400 °C, whereas a mostly frequency-independent plateau for low and high frequency regions was obtained for sample Q from 1450 °C, (d).

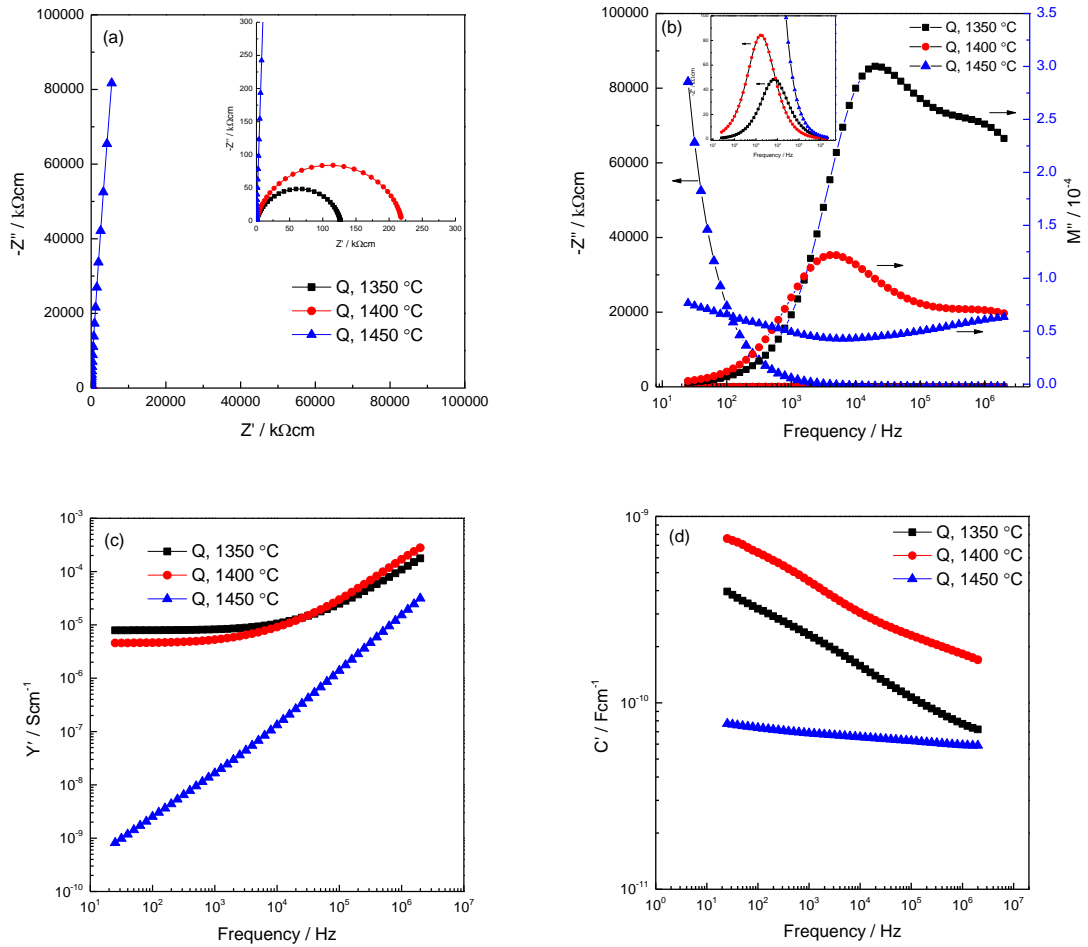


Figure 5-40: RT IS data for Y-A, *BM*, Q, $\nu = 0.001$, (a) impedance complex plane plots, Z^* (b) $-Z''$, M'' spectroscopic plots (c) Y' plots and (d) C' plots for different frequencies with In-Ga electrodes.

For $\nu = 0.01$, samples of 1350 SC, 1350 Q and 1400 °C Q in air are shown in Figure 5-41. The samples of 1350 SC, 1350 Q are too resistive to measure, but the sample of 1350 Q shows a clear semiconducting grain core at higher frequency with $R_b \sim 5900 \Omega\text{cm}$ and $C_b \sim 847 \text{ pFcm}^{-1}$ whereas the sample of 1400 Q has two semicircles, the small one is probably with a non-zero high frequency intercept with $R_b \sim 36 \Omega\text{cm}$ and $R_{gb} \sim 325 \Omega\text{cm}$ and $C_{gb} \sim 0.98 \text{ nFcm}^{-1}$. The larger semicircular at low frequency is dominated by Schottky barrier effect with $R_{SB} \sim 806 \Omega\text{cm}$ and $C_{SB} \sim 0.16 \text{ nFcm}^{-1}$, (a).

M'' plots, (b) show a marked variation in the shape of the plots. A single broad peak is seen for 1350 Q at high frequency whereas the peak can not be measured for 1400 Q as its peak always occurs at $f_{\text{max}} > 1 \text{ MHz}$. Little evidence of a conductive core

was seen for 1350 SC. Capacitance data (c) for 1350 Q and 1400 °C Q, show that a high capacitance, low frequency plateau is observed followed by, a dispersion region with increasing frequency. The capacitance data for 1350 SC are mostly independent of frequency with a slight increase at low frequency. With increasing temperature, a PTCR effect with a dramatic resistance increase at T_C was observed (not shown).

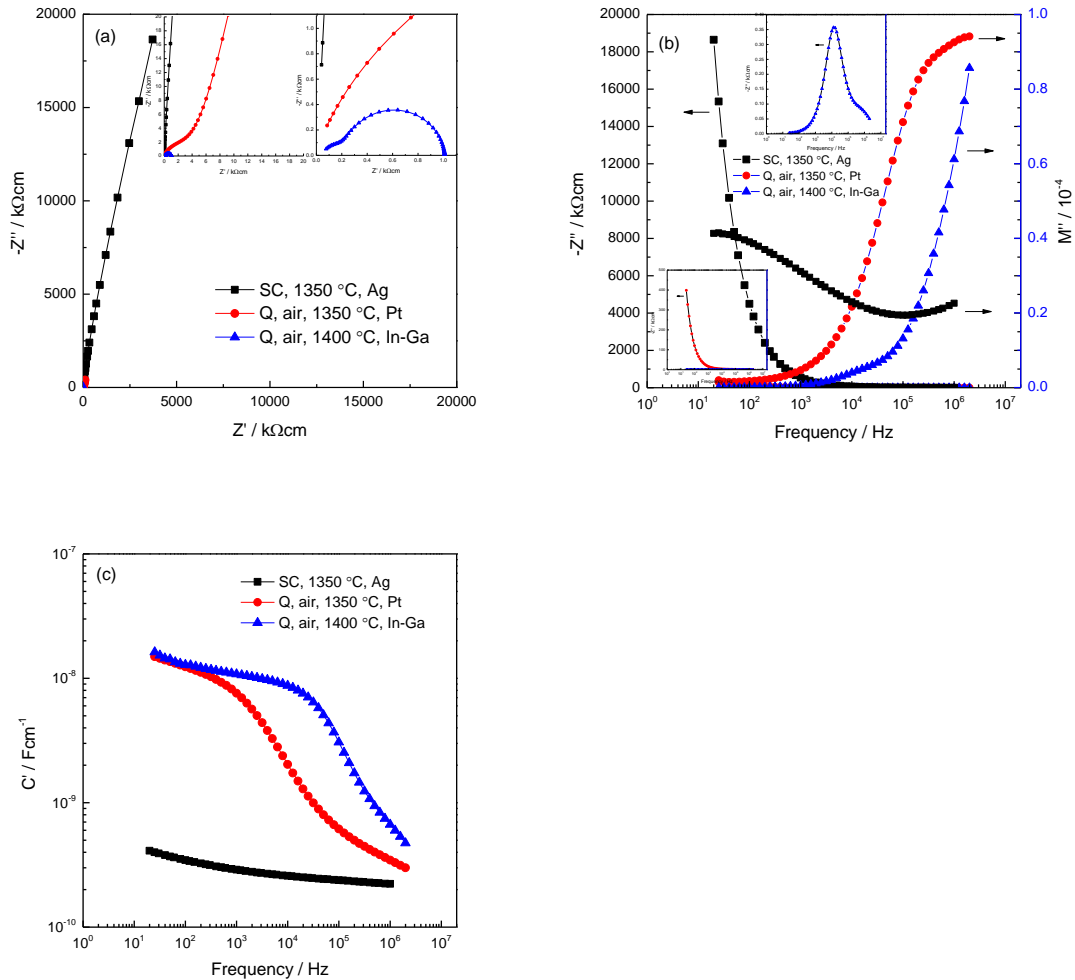


Figure 5-41: IS data for Y-A, SC and Q sample at $\nu = 0.01$, (a) impedance complex plane plots, Z^* (b) $-Z''$, M'' spectroscopic plots and (c) C' plots for different frequencies.

The surface oxygen exchange reaction of at $\nu = 0.01$, Q from 1250 °C, measured at 100 °C is shown by noticeable and reversible changes in resistivity in different atmospheres, Figure 5-42. The low frequency resistivity decreased with decreasing pO_2 . Sensitivity to atmosphere was observed only for low frequency component, R_2 and C_2 (a,c). For the high frequency component, no changes with changing

atmosphere were observed for R_1 , C_1 and M'' peak (a,b,c). The impedance sample of $\nu = 0.001$, Q also was independent of pO_2 , (not shown).

Similar behaviour was observed with dc bias, Figure 5-43. R_1 , C_1 and M'' peak were unaffected by the dc bias (a,b,c) whereas, the low frequency component; R_2 and C_2 (a,c) show a clear decrease. The decrease of the low frequency component is reversible on removal of the dc bias with very little time dependence after ~ 20 min. The sample of $\nu = 0.001$, Q showed that, R_T decreased with dc bias (not shown).

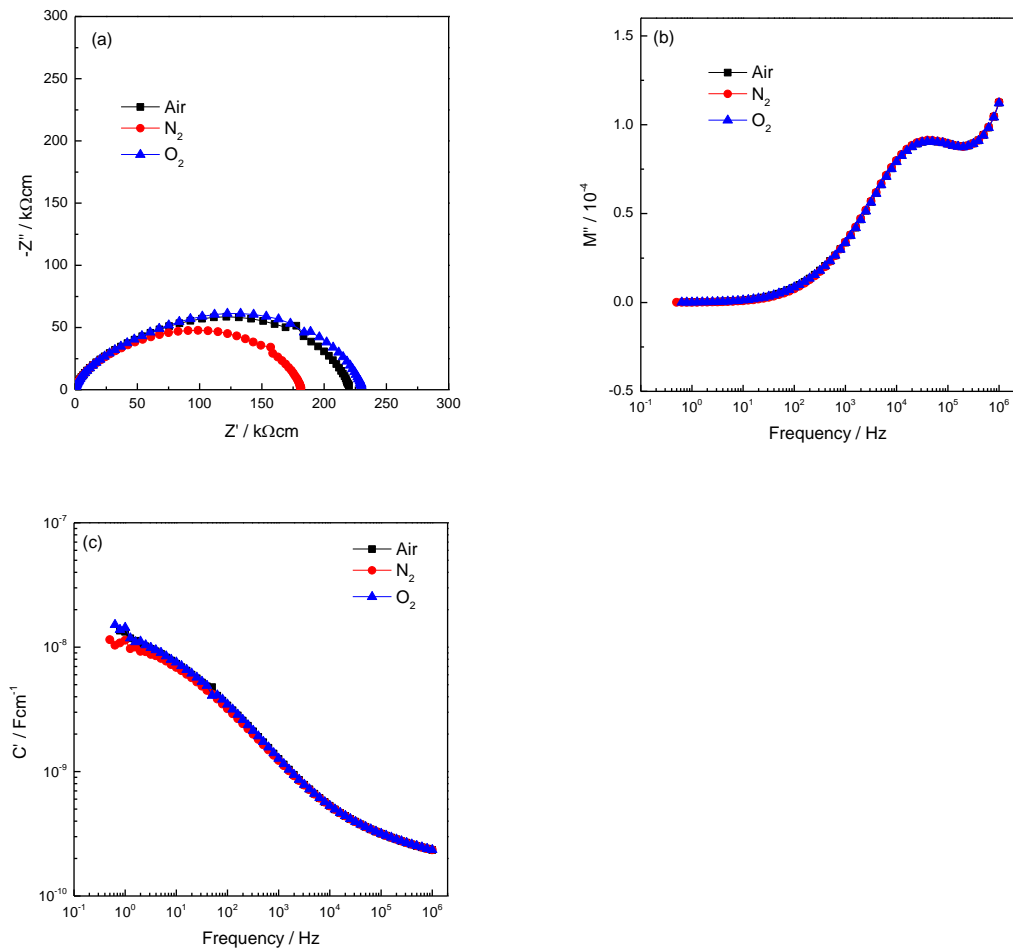


Figure 5-42: 100 °C IS data for Y-A, Q from 1250 °C, $\nu = 0.01$, (a) Z^* plot, (b) M'' plot and (c) C' plot in different atmospheres with In-Ga electrodes.

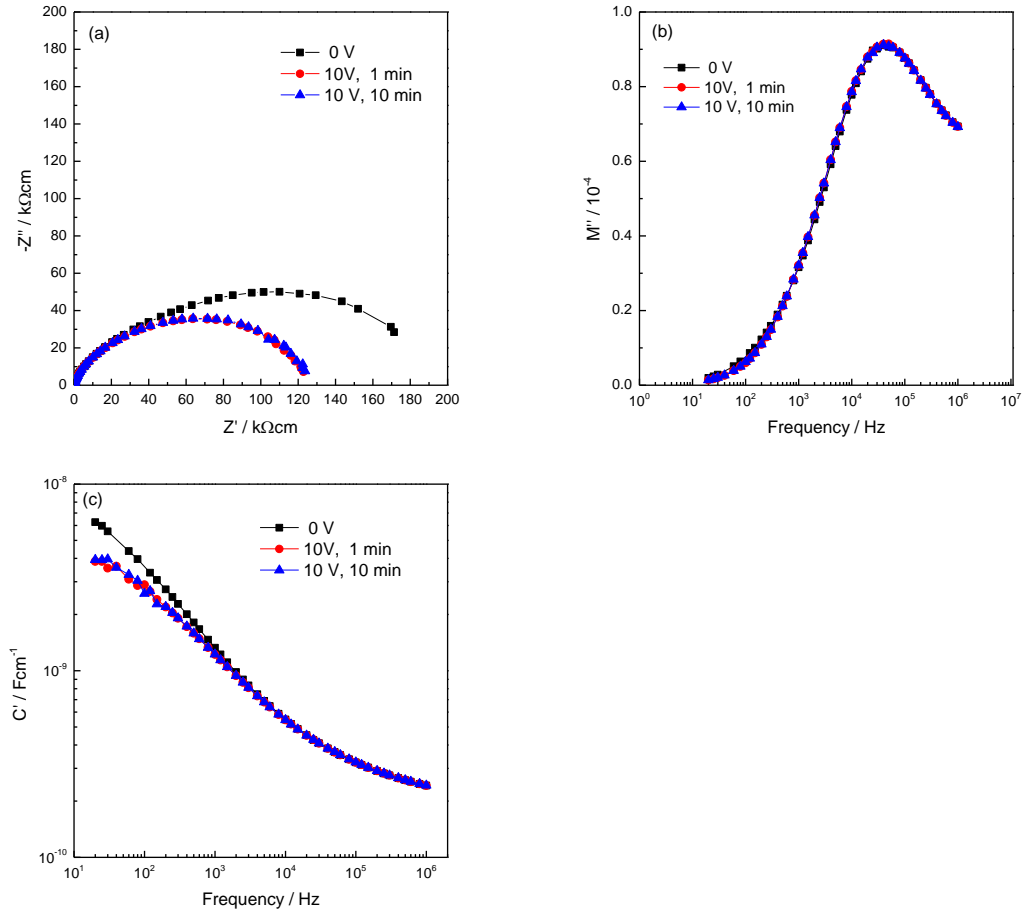


Figure 5-43: 100 °C IS data for Y-A, Q from 1250 °C, $\nu = 0.01$, (a) Z^* plot (b) M'' plot and (c) C' plot before and after a voltage of 10 V was applied at different measuring times with In-Ga electrodes.

In summary, Y-A samples showed a conductive core was observed for both SC and Q samples for $\nu = 0.0001$. More conductive data were shown for $\nu = 0.001$ and 0.01. The difference between *HM*, *PBM* and *BM* was different to Y-B behaviour as the semicircular arc was seen for *BM*, 0.001, Q from 1350 and 1400 °C. No apparent sensitivity was shown to the change of pO_2 at RT for $y = 0.01$, Q from 1500 °C. Dc bias showed that R_b at 50K was independent of dc bias whereas, R_{gb} showed a reversible decrease in grain boundary resistance. The bulk component for $\nu = 0.01$ at 100 °C was independent of both dc bias and pO_2 whereas, the low frequency resistance decreased on application of a small dc bias voltage and was reversible on removal of the dc bias.

5.4 Discussion

The electrical properties of RE³⁺ (Gd, Dy, Ho, Y, Er and Yb)-doped BaTiO₃ compositions prepared according to 3 doping mechanisms: (RE-B), (RE-AB) and (RE-A) at several concentrations x,y and $v = 0, 0.0001, 0.001$ and 0.01 were characterised using IS and LCR measurements.

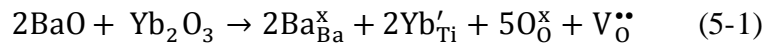
The XRD result indicates that all samples are tetragonal pure single phase and all observed reflections can be indexed.

The temperature dependence of ϵ' and $\tan \delta$ was studied. Generally, all samples showed that a normal ferroelectric behaviour was observed and no systematic trend was observed with RE³⁺. Some samples were leaky dielectrics as shown by the very high permittivity maximum and high dielectric loss.

IS data obviously clearly showed that the electrical properties of RE-doped BT are strongly dependent on pO₂, dc bias, cooling rate, type of electrodes, sintering temperature and RE³⁺ concentration. In some cases, the method for mixing reagents by *HM*, *PBM* or *BM* was also a variable.

For Yb-doped BT:

IS results indicated that all samples on the three joins were electrically insulating and did not show any conductivity at room temperature even with rapid quenching in air. Yb³⁺ substituted mainly at the Ti-site with charge compensation via oxygen vacancies:



At high temperatures, most samples show bulk and grain boundary conductivities with $E_a \sim 0.6-0.9$ eV and 1 eV.

P-type behaviour was indicated for x,y and $v = 0.01$ by both pO₂ and dc bias measurements at 400 °C. No evidence of n-type behaviour for SC and Q samples at different temperatures was seen, even with rapid Q into liquid N₂. P-type behaviour may be associated with O₂ absorption on cooling. Effect of SC and air Q was studied.

In some cases, C' is lower for SC samples due to oxidation on cooling.

No resistivity minimum was observed for Yb-BT for all three joins, Figure 5-44.

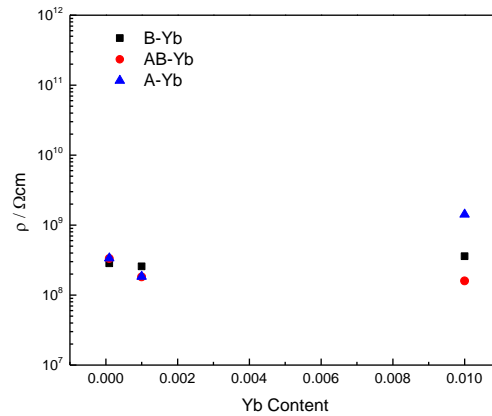


Figure 5-44: Total resistivity at RT in Yb-doped BT.

For Er-doped BT:

All samples are insulating on the Er-B join whether Q or SC especially at $x = 0.01$, as $R \sim 10^{10} \Omega\text{cm}$ was observed at RT for a Q sample. This shows that a very small amount of Er-B completely prevents O_2 loss. This could be very relevant to avoiding loss in capacitor BT materials. dc bias and $p\text{O}_2$ show that the conduction is p-type.

Er-A data show that all Q samples were conductive whereas, SC samples were insulating but not homogenous and probably a conductive core was shown. This means that the semiconductivity of Q samples on the donor join is due to oxygen loss and not to direct donor doping. Q samples show a clear Schottky barrier (SB) with In-Ga or Ag electrodes with a sample resistance of $\sim 40 \Omega\text{cm}$. Low temperature data show the high frequency C' plateau at $\sim 40 \text{ pFcm}^{-1}$ and a temperature-dependent R_b of $1.17 \times 10^4 \Omega\text{cm}$. There is also evidence at 75-175K of a second plateau in Y' and an intermediate semicircle in Z^* which could be R_{gb} . The R_{SB} can also be measured over a wide temperature range below RT. Low temperature data show the bulk response over the range of 25-75K.

The high frequency resistance and capacitance of $v = 0.01$ sample was insensitive to the application of a small dc bias. By contrast, the low frequency component changed with a dc bias. $R_b \ll R_{SB}$ and R_b is independent of dc bias.

Application of different $p\text{O}_2$ did not show any sensitivity to $p\text{O}_2$.

Replacing Ag with In–Ga electrodes resulted in significant difference in the electrical properties. Low frequency arc in Z^* disappeared with In-Ga electrodes as Ag with a high electron work function produced non-ohmic contacts whereas, In-Ga alloy gave ohmic contacts. This second semicircle is indicative of a Schottky barrier present at the electrode interface.

On the self-compensation join, Er-AB, very conductive data were shown for Q samples except for $y = 0.01$ which was resistive either with SC or Q although the Q sample was more conductive. SB was observed for $y = 0.0001$, Q sample with $C' \sim 3 \times 10^8 \text{ Fcm}^{-1}$ and a small PTCR effect with resistance increase of 3-4 times at 100-125 °C. Similar data for 0.001 with a conductive core clearly present in M'' data. Low temperature data show the bulk response over the range of 10-50K.

Both pO_2 and dc bias was applied for two different Q samples; conductive sample which was dominated by SB for $y = 0.001$ and insulating sample for $y = 0.01$. Conductive sample of $y = 0.001$ was not sensitive to pO_2 . Z^* data were similar in Air, N_2 and O_2 whereas p-type behaviour was observed for insulating sample of $y = 0.01$. Both samples showed that the resistance decreased reversibly on application of a small dc bias which is associated with a SB effect and p-type behaviour. For SB at the sample–electrode interface, there is a decrease in the height of potential barrier in the forward bias direction with increasing the width of the depletion region [28].

No resistivity minimum was observed for Er-BT for all three joins, Figure 5-45. There is a clear reduction on Er-AB and Er-A joins but the solid solution limit is ≤ 0.01 . Therefore, any increase of resistivity at higher dopant content can not be observed.

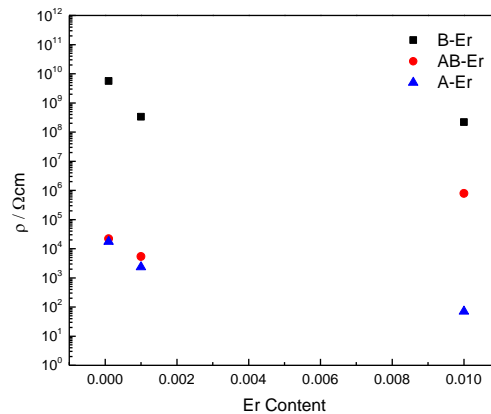


Figure 5-45: Total resistivity at RT in Er-doped BT.

For Y-doped BT:

For Y-B, too resistive data and no conductive core was observed for SC and Q pellets in air at $x = 0, 0.0001, 0.0003, 0.0005$ and 0.01 . For example, the $x = 0.0001$, $1350\text{ }^{\circ}\text{C}$, SC in air showed two components in Z^* with very insulating total resistance value with $E_a \sim 1.17\text{ eV}$ at higher temperatures. Two plateaux were seen in C' , indicating the bulk and grain boundary. A conductive core for both SC and Q samples was observed for $x = 0.001$, $1350\text{ }^{\circ}\text{C}$. C' plateau was observed at 50 nFcm^{-1} which is probably associated with a SB effect whereas, two overlapping broad arcs were seen for sample Q from $1400\text{ }^{\circ}\text{C}$. The sample still shows a SB, but it is much smaller, consistent with a more ohmic contact with In-Ga. R_T showed a maximum at $175\text{ }^{\circ}\text{C}$, which looks like a PTCR effect even though the R value is for the SB.

The *BM* samples showed different behaviour. R_T was too high to measure with little evidence of conductive core. C' data were much less. The *PBM* samples showed a conductive core with very high R_T values. This behaviour was also observed for *BM* and *PBM* samples on Y-AB and Y-A joins. It is probably that the sample was more homogenous after *BM* as *BM* increased the homogeneity and removed local donor-doped region.

Effect of Q was shown for $x = 0.01$ samples Q from different temperatures $1350, 1400$ and $1450\text{ }^{\circ}\text{C}$. $1350\text{ }^{\circ}\text{C}$, Q sample has higher σ_T as oxygen-deficient samples on B join pick up some O_2 at lower temperature to become p-type. Dc bias data on $1350\text{ }^{\circ}\text{C}$ sample showed p-type. Similar results with $p\text{O}_2$ change were seen in two samples.

For Y-AB, a weak conductive core was seen for $y = 0.0001$, $1350\text{ }^{\circ}\text{C}$, SC. R_T was very high to measure. SC and Q samples showed a clear conductive core component for $x = 0.001$, $1350\text{ }^{\circ}\text{C}$, SC and Q. These results were dominated by SB effect that depended on electrode: Pt, Au and In-Ga. Effect of cooling rate was clearly observed for $y = 0.0001$, $1400\text{ }^{\circ}\text{C}$ with SC in air, Q in air and Q into liquid N_2 . SC was insulating and R_T was too high to measure and showed conductive core. Q in air showed similar behaviour but with more conductive data whereas, Q into liquid N_2 showed a semicircular arc with $R_T \sim 1.91 \times 10^5\ \Omega\text{cm}$. Low temperature data were

collected for sample Q into liquid N₂. The bulk component was clearly seen in the M'' peaks with C_b ~ 56, 59 and 63 pFcm⁻¹ for 50, 75 and 100K respectively.

Dc bias and pO₂ were applied for Q sample from 1500 in air for y = 0.01. No apparent sensitivity was shown to the change of pO₂ at RT which is probably associated with a SB effect. Therefore, dc bias was studied at low temperature to characterise the bulk response at 50K. R_b was independent of dc bias whereas, R_{gb} showed a reversible decrease in grain boundary resistance.

For Y-A, a conductive core was observed for both SC and Q samples for ν = 0.0001 whereas, R_T can not be measured. More conductive data were shown for ν = 0.001 and 0.01. Similar to x and y =0.001 results as conductive core was observed for SC and Q with resistive R_T and semiconductive semicircular arc for 1400 °C, Q.

The oxygen exchange reaction at ν = 0.01 at 100 °C was indicated by dc bias and pO₂. The bulk component was independent of both dc bias and pO₂ whereas, the low frequency resistance decreased on application of a small dc bias voltage and was reversible on removal of the dc bias.

The total resistivity passed through a minimum at 0.001 then increased at 0.01, Figure 5-46.

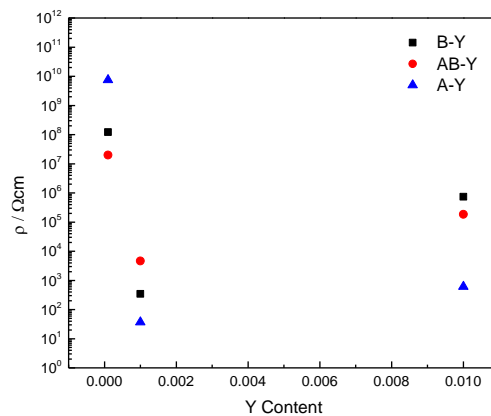


Figure 5-46: Total resistivity at RT in Y-doped BT.

In this chapter, results of Ho, Dy and Gd were not presented. Summary results only are presented here.

For Ho-B, Dy-B and Gd-B, a conductive semicircular arc with a SB effect was observed for 1350 °C, Q samples, at $x = 0.0001$ and 0.001 with $R_T \sim 1800$ and $48 \Omega\text{cm}$ for Ho-B, 650 and $180 \Omega\text{cm}$ for Dy-B, 25000 and $1200 \Omega\text{cm}$ for Gd-B at RT with PTCR effect whereas, 0.01 and *PBM*, 0.001 for Ho-B were very insulating without showing any conductive core for Ho-B, Dy-B. The *PBM*, 0.001 showed semicircular arc with $R_T \sim 1800 \Omega\text{cm}$ for Gd-B. The 0.01 sample showed two components at high temperatures for the bulk and grain boundary with E_a of b and gb ~ 0.79 and 0.91 for Ho-B, 0.75 and 1.05 for Dy-B, 0.77 and 0.91 eV for Gd-B. The 0.01 sample at 350 °C for Ho-B and Gd-B and 300 °C for Dy-B was p-type as indicated by dc bias and $p\text{O}_2$.

For Ho-AB and Dy-AB, similar behaviour to Ho-B was observed for all compositions with $R_T \sim 33000$ and $15 \Omega\text{cm}$ for Ho-AB and 440 and $160 \Omega\text{cm}$ for Dy-AB at RT for $y = 0.0001$ and 0.001 but *PBM*, 0.001 for Ho-AB showed a conductive core of $\sim 2500 \Omega\text{cm}$. The 0.01 sample showed two components at high temperatures for the bulk and grain boundary with E_a of b and gb ~ 1.09 and 1.03 eV for Ho-AB, 1.09 and 1.01 for Dy-AB. For Gd-AB, $y = 0.0001$, 0.001 *PBM* and 0.01 were insulating with little conductive core. At higher temperatures, E_a of b and gb was ~ 1.17 and 1.51 eV for 0.0001 , 1.03 and 1.15 eV for 0.001 . The Q sample 0.001 , for Gd-AB showed conductive data for the bulk and grain boundary components at RT with $C_b \sim 4.01 \times 10^{-10} \text{ Fcm}^{-1}$ and $C_{gb} \sim 4.82 \times 10^{-9} \text{ Fcm}^{-1}$. A p-type behaviour was shown for 0.01 sample at 400 °C for Ho-AB, 425 °C for Dy-AB, 450 °C for Gd-AB with dc bias and $p\text{O}_2$.

For Ho-A and Dy-A, a weak conductive core was seen for $v = 0.0001$ at RT with E_a of b and gb ~ 1.16 and 1.29 eV for Ho-A and total E_a 0.95 eV for Dy-A for higher temperatures. A conductive semicircular arc was shown for $v = 0.001$ and 0.01 with $R_T \sim 3$ and $9000 \Omega\text{cm}$ for Ho-A and ~ 70 and $1350 \Omega\text{cm}$ for Dy-A at RT whereas, *PBM*, 0.001 sample for Ho-A showed a conductive core of $\sim 500 \Omega\text{cm}$ and an insulating low frequency component. The sample 0.01 , SC showed a weak conductive core for Ho-A, Dy-A and Gd-A whereas, Q sample for Ho-A and Gd-A showed a conductive data for the bulk and grain boundary components at RT with $C_b \sim 2.5 \times 10^{-10}$, $1.30 \times 10^{-10} \text{ Fcm}^{-1}$ and $C_{gb} \sim 3.5 \times 10^{-9}$, $1.26 \times 10^{-9} \text{ Fcm}^{-1}$. A

semicircular arc was seen for Q samples of 0.0001, 0.001, 0.001 *PBM*, 0.01 with $R_T \sim 5000, 47, 8440$ and $5066 \Omega\text{cm}$. SB were dominated for all samples except 0.01. Dc bias was studied for $v = 0.01$ at 25K. Bulk resistance was independent of dc bias and grain boundary showed p-type behaviour for Ho-A, Dy-A and Gd-A. All of them also were independent of pO_2 and low frequency arc with Ag electrodes disappeared with In-Ga electrodes for Ho-A and Gd-A.

Figure 5-(47-49) shows the resistivity vs composition dependencies for Ho-, Dy- and Gd-BT. A minimum of resistivity was seen at 0.001.

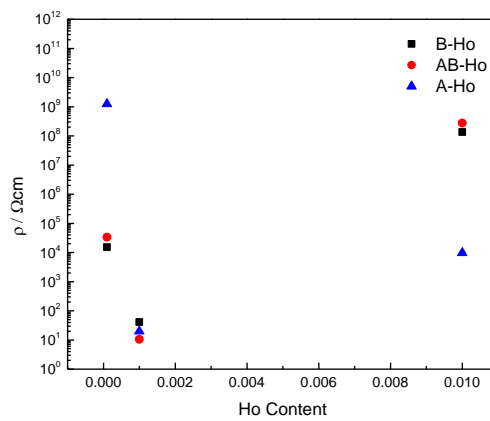


Figure 5-47: Total resistivity at RT in Ho-doped BT.

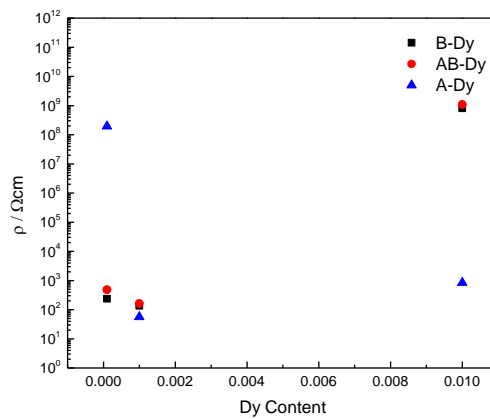


Figure 5-48: Total resistivity at RT in Dy-doped BT.

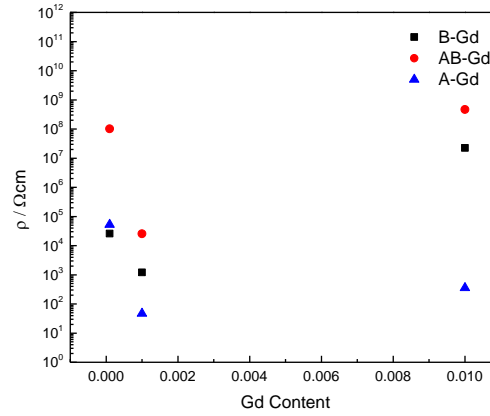
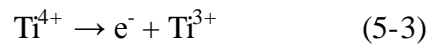
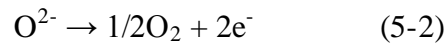


Figure 5-49: Total resistivity at RT in Gd-doped BT.

Many data show that loss of oxygen occurred. Inhomogeneous materials were produced showing sometimes a semiconducting grain core region with oxidation of resistive grain boundary and/or sample surface region.

The electrons liberated due to oxygen loss are the source of semiconductivity with reduction of Ti^{4+} to Ti^{3+} :



SC, annealing at lower temperatures or in O_2 , prevented loss of oxygen.

Resistivity minimum behaviour can occur by loss of oxygen or direct doping. Most results indicate that the resistivity minimum is a result of oxygen loss. With increasing RE^{3+} , the increase of resistivity is attributed to the immobility of cation vacancies [29] which is associated with reoxidation on cooling or switching of the compensating mechanism from electronic to ionic [30].

The difference between Q and SC samples are consistent with literature of Y-doped BT [31] as only Q samples in air from 1350 °C showed blue colour, indicating semiconductive behaviour whereas, SC ones are yellowish to brownish-buff with insulating behaviour. Another study [10] showed that the sample remained semiconducting due to Q from the sintering temperature which is associated with avoiding oxidation during cooling.

The resistivity minimum was observed for Y-doped BT which is in good agreement with literature [32] as U-shape curve of bulk and grain boundary was shown and semiconductive data were observed over the range of 0.001-0.004. Another report showed this reduction between 0.003-0.006 [33]. It was between 0.001-0.003 for Dy-A [34]. The range of 0.002-0.006 was studied for Y-A [35]. The semiconductivity was observed for all compositions but a minimum in resistivity was observed at Y concentration at $\nu = 0.004$.

Generally, composition 0.001 showed semiconductive behaviour for many samples on different joins. This behaviour for the same composition was reported for some RE^{3+} elements. In contrast, the study of Y, Dy, Ho, Er and La doped BT showed that the sample was insulating for all elements at 0.001 and the semiconductivity and associated minimum RT resistivity were observed at a dopant concentration of around 0.003-0.005 [21], 0.002-0.005 [36] or 0.002-0.01 [37] for Y-AB with a shift from n-type to p-type semiconducting properties with increasing Y^{3+} content.

It was reported [38] that both Er-AB and Y-AB were insulating but in contrast, another [27] report for that Er-B and Er-AB showed predominantly self-compensating behaviour whereas, [25, 39] reported that Y-AB acts as donor-type behaviour at low Y contents especially at $y = 0.001$ and is insulating, similar to BT behaviour at higher Y contents which is in good agreement with Y-AB results in this study but Y-B shows acceptor behaviour. Their pO_2 study show p-type behaviour for Y-B at $x = 0.02$ and n-type for Y-A [16] at $\nu = 0.01$ which are consistent with results obtained in this chapter.

The conductivity of Y-B [40, 41] and Y-A [42] was studied. Semiconducting data with resistivity minimum were observed at low level of x and $\nu \sim \leq 0.01$ with donor-doped behaviour whereas acceptor-doped behaviour was observed at higher levels at $\sim > 0.01$. These results were consistent with those obtained in this chapter.

The resistivity of Er-doped BT on three joins was presented in literature [43] for x, y and $\nu = 0.01$. ER-AB and ER-A behave as donor impurities whereas, ER-B was insulating. These results are in good agreement with the present results. No resistivity minimum was seen for Er-A. There was a reduction of resistivity at $\nu =$

0.001 and 0.01 but no results were obtained at higher concentrations due to the lower solid solution limit, < 0.01 [27].

Some studies [27] showed that Er-B did not show resistivity minimum and the conduction mechanism was p-type behaviour, in good agreement with this chapter results.

It was reported [26] that Gd-A samples of $0 < v < 0.05$ are electrically inhomogeneous, containing a high frequency semiconducting region and a low frequency insulating region. This behaviour was obtained here for same compositions.

Gd-AB was studied [44] with different conditions. Electrical resistivity exhibited a minimum at a specific content. The semiconductivity was observed only at Gd contents from $y = 0.0005$ to 0.003 which are close to the data presented here but another report [45] for three joins showed the resistivity minimum even on the acceptor join as the resistivity minimum was located at $x \sim 0.01$ for most samples.

The resistivity minimum was observed for Ho-B [2] for samples, heated > 1400 °C. A new compensation mechanism was proposed for two Ti^{4+} as Ho^{3+} ion occupies first Ti^{4+} ion and second Ti^{4+} reduced to Ti^{3+} for each oxygen vacancy. Samples of $x = 0.001$ and 0.01 showed similar bulk resistivity values for SC and Q. This result is partially consistent with the obtained results as the resistivity minimum was shown but with different resistivity values between SC and Q due to oxygen loss which accompanied partial reduction of Ti^{4+} to Ti^{3+} . Similar to this difference between SC and Q was presented in literature [46, 47] for other reports for Gd-A.

It was shown that Dy-B showed p-type behaviour for $x = 0.01$ which is consistent with literature [48] but they did not observe semiconducting data at low concentrations which is inconsistent with presented results here. For DY-A, the resistivity minimum which is associated with semiconductivity was shown at $v = 0.001$, consistent with the presented results here.

Resistivity minimum was not shown for Yb-doped BT which was not observed also in literature for Yb-B [49]. It is probably because that Yb^{3+} is relatively small and therefore substitutes mainly the B-site [24].

5.5 Conclusions

The semiconductivity with resistivity minimum was studied for RE³⁺ (Gd, Dy, Ho, Y, Er and Yb)-doped BaTiO₃ at low concentrations.

From the XRD analysis, all samples seem to be single phase and can be indexed as tetragonal structure.

No semiconductivity was observed for Yb-B, Yb-AB, Yb-A and Er-B, even with rapid Q into liquid N₂; samples showed p-type behaviour by dc bias and pO₂.

Er-A data show that all Q samples were conductive whereas, SC samples were insulating, showing a conductive core. Resistivity minimum could not be studied perhaps as a result of low solubility.

Other joins and RE³⁺ showed semiconductivity with a resistivity minimum at 0.001.

Most samples depended strongly on cooling rate. Loss of oxygen was generally dominant.

SB behaviour was shown in some Q samples with PTCR characteristic using IS measurements under dc bias which characterised the electrode effect. The high frequency resistance and capacitance was insensitive to the application of a small dc bias. By contrast, the low frequency component changed with a dc bias. As expected, since $R_b \ll R_{SB}$, R_b is independent of dc bias. Application of different pO₂ did not show any sensitivity to pO₂.

5.6 References

- [1] Y. Mizuno, H. Kishi, K. Ohnuma, T. Ishikawa, H. Ohsato, Effect of site occupancies of rare earth ions on electrical properties in Ni-MLCC based on BaTiO₃, *Journal of the European Ceramic Society*, 27 (2007) 4017-4020.
- [2] Y. Liu, A.R. West, Semiconductivity in Acceptor-Doped BaTi_{1-x}Ho_xO_{3- x/2- δ/2}, *Journal of the American Ceramic Society*, 96 (2013) 1512-1520.
- [3] F.D. Morrison, A.M. Coats, D.C. Sinclair, A.R. West, Charge compensation mechanisms in La-doped BaTiO₃, *Journal of Electroceramics*, 6 (2001) 219-232.
- [4] J. Nowotny, M. Rekas, Defect chemistry of BaTiO₃, *Solid State Ionics*, 49 (1991) 135-154.
- [5] O. Saburi, Properties of semiconductive barium titanates, *Journal of the Physical Society of Japan*, 14 (1959) 1159-1174.
- [6] N.H. CHAN, D.M. Smyth, Defect Chemistry of Donor-Doped BaTiO₃, *Journal of the American Ceramic Society*, 67 (1984) 285-288.
- [7] J. Daniels, K. Hardtl, D. Hennings, R. Wernicke, Defect Chemistry And Electrical-Conductivity of Doped Barium-Titanate Ceramics, in, PHILIPS RESEARCH LABORATORIES BUILDING WBP ROOM NO. 42, EINDHOVEN, NETHERLANDS, 1976, pp. 487-488.
- [8] C.J. Peng, H.Y. Lu, Compensation effect in semiconducting barium titanate, *Journal of the American Ceramic Society*, 71 (1988) C-44-C-46.
- [9] T.B. Wu, J.N. Lin, Transition of Compensating Defect Mode in Niobium-Doped Barium Titanate, *Journal of the American Ceramic Society*, 77 (1994) 759-764.
- [10] J.K. Lee, K.S. Hong, J.H. Chung, Revisit to the Origin of Grain Growth Anomaly in Yttria-Doped Barium Titanate, *Journal of the American Ceramic Society*, 84 (2001) 1745-1749.
- [11] J. Daniels, K.H. Hardtl, D. Hennings, R. Wernicke, Defect Chemistry And Electrical-Conductivity of Doped Barium-Titanate Ceramics, in, PHILIPS RESEARCH LABORATORIES BUILDING WBP ROOM NO. 42, EINDHOVEN, NETHERLANDS, 1976.
- [12] G.H. Jonker, E.E. Havinga, The influence of foreign ions on the crystal lattice of barium titanate, *Materials Research Bulletin*, 17 (1982) 345-350.

- [13] H.M. Chan, M.R. Harmer, D.M. Smyth, Compensating Defects in Highly Donor-Doped BaTiO₃, *Journal of the American Ceramic Society*, 69 (1986) 507-510.
- [14] L.A. Xue, Y. Chen, R.J. Brook, The effect of lanthanide contraction on grain growth in lanthanide-doped BaTiO₃, *Journal of materials science letters*, 7 (1988) 1163-1165.
- [15] S.B. Desu, D.A. Payne, Interfacial segregation in perovskites: III, microstructure and electrical properties, *Journal of the American Ceramic Society*, 73 (1990) 3407-3415.
- [16] S.H. Hur, J.K. Lee, K.-S. Hong, S.J. Park, Incorporation phenomena of donor dopant in BaTiO₃ systems, *Solid state ionics*, 108 (1998) 81-84.
- [17] F.D. Morrison, D.C. Sinclair, J. Skakle, A.R. West, Novel Doping Mechanism for Very-High-Permittivity Barium Titanate Ceramics, *Journal of the American Ceramic Society*, 81 (1998) 1957-1960.
- [18] O.I. V'yunov, L.L. Kovalenko, A.G. Belous, V.N. Belyakov, Oxidation of reduced Y-doped semiconducting barium titanate ceramics, *Inorganic materials*, 41 (2005) 87-93.
- [19] O. Saburi, Semiconducting bodies in the family of barium titanates, *Journal of the American Ceramic Society*, 44 (1961) 54-63.
- [20] V.J. Tennery, R.L. Cook, Investigation of Rare-Earth Doped Barium Titanate, *Journal of the American Ceramic Society*, 44 (1961) 187-193.
- [21] P. Yongping, Y. Wenhui, C. Shoutian, Influence of rare earths on electric properties and microstructure of barium titanate ceramics, *Journal of Rare Earths*, 25 (2007) 154-157.
- [22] S.W. Ding, G. Jia, J. Wang, Z.Y. He, Electrical properties of Y- and Mn-doped BaTiO₃-based PTC ceramics, *Ceramics International*, 34 (2008) 2007-2010.
- [23] M. Drofenik, Oxygen Partial Pressure and Grain Growth in Donor-Doped BaTiO₃, *Journal of the American Ceramic Society*, 70 (1987) 311-314.
- [24] Y. Tsur, T.D. Dunbar, C.A. Randall, Crystal and defect chemistry of rare earth cations in BaTiO₃, *Journal of Electroceramics*, 7 (2001) 25-34.
- [25] J.H. Jeong, M.G. Park, Y.H. Han, Defect chemistry of Y doped BaTiO₃, *Journal of Electroceramics*, 13 (2004) 805-809.

- [26] L. Ben, Synthesis and Characterisation of Rare-earth and Calcium Doped BaTiO₃ Ceramics, PhD thesis, The University of Sheffield, (2009).
- [27] J.H. Hwang, Y.H. Han, Defect chemistry of Er-doped BaTiO₃, *Solid State Ionics*, 140 (2001) 181-186.
- [28] T.B. Adams, D.C. Sinclair, A.R. West, Characterization of grain boundary impedances in fine-and coarse-grained CaCu₃Ti₄O₁₂ ceramics, *Physical review B*, 73 (2006) 094124.
- [29] Y.L. Chen, S.F. Yang, PTCR effect in donor doped barium titanate: review of compositions, microstructures, processing and properties, *Advances in Applied Ceramics*, 110 (2011) 257-269.
- [30] A.R. West, T.B. Adams, F.D. Morrison, D.C. Sinclair, Novel high capacitance materials:-BaTiO₃: La and CaCu₃Ti₄O₁₂, *Journal of the European Ceramic Society*, 24 (2004) 1439-1448.
- [31] H.-Y. Lu, M.-H. Lin, Charge compensation mechanism in yttria-doped barium titanate, *Ceramics international*, 31 (2005) 989-997.
- [32] P. Blanchart, J.F. Baumard, P. Abelard, Effects of Yttrium Doping on the Grain and Grain-Boundary Resistivities of BaTiO₃ for Positive Temperature Coefficient Thermistors, *Journal of the American Ceramic Society*, 75 (1992) 1068-1072.
- [33] V.N. Tsygankov, V.V. Safonov, Doping effects on the properties of BaTiO₃-based solid solutions, *Inorganic materials*, 38 (2002) 397-399.
- [34] M.D. Glinchuk, I.P. Bykov, S.M. Kornienko, V.V. Laguta, A.M. Slipenyuk, A.G. Bilous, O.I. V'Yunov, O.Z. Yanchevskii, Influence of impurities on the properties of rare-earth-doped barium-titanate ceramics, *Journal of Materials Chemistry*, 10 (2000) 941-947.
- [35] A.M. Slipenyuk, M.D. Glinchuk, I.P. Bykov, V.V. Laguta, S.N. Nokhrin, A.G. Belous, O.I. V'Yunov, L.L. Kovalenko, L. Jastrabik, ESR study of BaTiO₃ ceramics doped by Y and Ca, *Ferroelectrics*, 254 (2001) 349-357.
- [36] A. Belous, O. V'yunov, M. Glinchuk, V. Laguta, D. Makovez, Redox processes at grain boundaries in barium titanate-based polycrystalline ferroelectrics semiconductors, *Journal of materials science*, 43 (2008) 3320-3326.
- [37] C.M. Huang, C.Y. Lin, J. Shieh, Relationship between the evolutions of the microstructure and semiconductor properties of yttrium-doped barium titanate ceramics, *Journal of Physics D: Applied Physics*, 44 (2011) 345403.

- [38] K. Takada, E. Chang, D.M. Smyth, Rare earth additions to BaTiO₃, *Advances in Ceramics*, 19 (1987) 147-152.
- [39] L.A. Xue, Y. Chen, R.J. Brook, The influence of ionic radii on the incorporation of trivalent dopants into BaTiO₃, *Materials Science and Engineering: B*, 1 (1988) 193-201.
- [40] J.H. Kim, S.H. Yoon, Y.H. Han, Effects of Y₂O₃ addition on electrical conductivity and dielectric properties of Ba-excess BaTiO₃, *Journal of the European Ceramic Society*, 27 (2007) 1113-1116.
- [41] M.-H. Lin, H.-Y. Lu, Site-occupancy of yttrium as a dopant in BaO-excess BaTiO₃, *Materials Science and Engineering: A*, 335 (2002) 101-108.
- [42] J.H. Kim, Y.H. Han, Effects of Y₂O₃ Addition on the Microstructure and Electrical Property of TiO₂-excess BaTiO₃, in, *Trans Tech Publ*, pp. 1025-1028.
- [43] K. Takada, H. Ichimura, D.M. Smyth, Equilibrium Conductivity for Er Doped BaTiO₃, *Japanese Journal of Applied Physics*, 26 (1987) 42.
- [44] T. Murakami, T. Miyashita, M. Nakahara, E. SEKINE, Effect of Rare-Earth Ions on Electrical Conductivity of BaTiO₃ Ceramics, *Journal of the American Ceramic Society*, 56 (1973) 294-297.
- [45] M.T. Buscaglia, M. Viviani, V. Buscaglia, C. Bottino, P. Nanni, Incorporation of Er³⁺ into BaTiO₃, *Journal of the American Ceramic Society*, 85 (2002) 1569-1575.
- [46] J. Nowotny, M. Rekas, Defect chemistry of BaTiO₃, *Solid State Ionics*, 49 (1991) 135-154.
- [47] I. Ueda, S. Ikegami, Oxidation phenomena in semiconducting BaTiO₃, *Journal of the Physical Society of Japan*, 20 (1965) 546-552.
- [48] E.J. Lee, J. Jeong, Y.H. Han, Electrical properties of Dy₂O₃-doped BaTiO₃, *Japanese journal of applied physics*, 43 (2004) 8126.
- [49] D.W. Hahn, Y.H. Han, Electrical properties of Yb-doped BaTiO₃, *Japanese journal of applied physics*, 48 (2009) 111406.

Chapter 6: Conclusions and Further Work

6.1 Conclusions

Generally, IS data of *HM*, *BM* and *PBM* samples were studied for two kinds of sample: (i) slow-cooled and (ii) quenched. The results were interpreted using the following schemes:

For bulk/grain boundary impedances:

- 1- n-type behaviour was shown by decreasing conductivity with increasing pO_2 and increasing dc bias.
- 2- For intrinsic conductivity there was no effect of pO_2 or dc bias.
- 3- p-type behaviour was shown by increasing conductivity with increasing pO_2 and increasing dc bias.

For Schottky Barrier (SB) impedances:

Two types of Schottky barrier were observed:

- 1- For metal-sample interfaces, there was no effect of pO_2 and R_{SB} decreased with increasing dc bias.
- 2- For SB produced to partial oxidation of surface or grain boundary, R_{SB} decreases with decreasing pO_2 and decreases with increasing dc bias.

6.1.1 Electrical properties of BT

6.1.1.1 Electrical properties of SC BT

SC BT samples were insulating and electrically inhomogeneous. The bulk and grain boundary impedance was observed apparent clearly at temperatures ≥ 400 °C.

The grain boundary resistance was usually higher than the bulk resistance at lower temperatures but also had higher activation energy.

p-type conduction was generally observed by dc bias. The resistance changes with dc bias were time-dependent and reversible to their original value after removal of the dc bias.

The change in resistance of grain boundary was greater than the bulk resistance with dc bias.

Increasing pO_2 also showed that both bulk and grain boundary resistances decreased, indicating p-type behaviour. The resistance decrease is reversible on reducing pO_2 .

In summary, SC BT is insulating with p-type behaviour. This may be associated with a slight departure from a Ba:Ti ratio of 1:1, caused by possible Ba loss during sintering. The holes may be associated with underbonded oxide ions or unavoidable impurities such as Fe^{3+} .

6.1.1.2 Electrical properties of Q BT

Q samples made by *HM*, *BM* and *PBM* showed similar behaviour to SC samples, there were usually electrically insulating. Some Q samples however showed a much higher σ with lower density, as a consequence of loss of oxygen at high temperatures which was preserved during quenching.

For some Q samples, a Schottky barrier impedance was observed and the Schottky barrier height was rather different for In-Ga, Ag and Pt electrodes.

Total conductivity (σ_T) data for samples quenched from 1400 °C with In-Ga and Ag electrodes show a PTCR effect on heating through T_C .

The similar results with all three electrodes may show that a grain boundary-related Schottky barrier may be dominant at low frequency, especially since In-Ga electrodes are considered to yield ohmic contacts when used on samples with semiconducting $BaTiO_3$ that does not form a Schottky barrier at the ceramic-electrode interface [1].

A sample-electrode Schottky barrier effect was apparently not observed as no difference was observed using different types of electrodes such as In-Ga and Ag. Since this result is not associated with an interface, as is commonly observed with a Schottky barrier at a sample-electrode contact, it is sample-related and probably related to oxidation of sample surfaces, either at the pellet outer surface or internal grain boundaries.

For the Q sample, R_T appears to demonstrate predominantly n-type behaviour but, the Schottky barrier height may also be sensitive to pO_2 , depending on the mechanism of Schottky barrier formation.

There was a clear difference in behaviour between dc bias and pO_2 results for the sample quenched from 1380 and a slow-cooled sample. For the Q sample, R_t decreased with increasing dc bias whereas it decreased in a reducing atmosphere. By contrast, the resistance of SC samples decreased with increasing dc bias but increased in a reducing atmosphere. n-type materials show a decrease in conductivity with either increasing pO_2 or dc bias; p-type materials show the opposite effect with an increase in conductivity with either increasing pO_2 or dc bias; intrinsic materials appear to show little or no effect. For Schottky barriers, the barrier height and therefore the resistance decreases with dc bias; the effect of pO_2 on Schottky barriers is less clear and depends on whether O_2 adsorption/desorption affects the barrier height.

The sample quenched from 1400 °C showed a high conductivity and apparent n-type behaviour. On reheating and quenching from lower temperature (1380 °C), it still gave n-type behaviour but with lower conductivity. p-type conductivity was observed for samples quenched from $\sim < 1380$ °C. The oxygen loss that occurs increasingly at high temperature appears to be a change from p- to n-type behavior at 1380 °C.

The change of the conduction type from p-type to n-type or the appearance of a Schottky barrier effect was observed for some samples above 1380 °C. Dc bias data show that the resistance decreased with increasing the voltage which is probably as result of Schottky barrier effect. In the p-type region, O_2 molecules are adsorbed onto the sample surface with creation of O^- species that are considered to be the principal source of holes. The adsorbed oxygen is observed either with slow cooled samples or on annealing samples at lower temperatures. An increased conductivity was observed with a decrease in annealing temperature and is attributed to an increase in hole concentration; this increase is less than that observed for samples of BT that were acceptor-doped on the Ti site.

6.1.2 Phase diagram study and crystal chemistry of Y-doped BT

The solubility limit of Y in Ti-site was found to be at $\sim x = 0.15$ and a small amount of $\text{YBa}_3\text{Ti}_2\text{O}_{8.5}$ as second phase was detected by XRD with increasing x . Smaller solid solution limit of Y on self-compensation join was obtained up to $\sim y = 0.075$ with precipitation of $\text{YBa}_3\text{Ti}_2\text{O}_{8.5}$ or $\text{Y}_2\text{Ti}_2\text{O}_7$ as secondary phase. Two phases that could be indexed as monoclinic $\text{Ba}_6\text{Ti}_{17}\text{O}_{40}$ and cubic pyrochlore $\text{Y}_2\text{Ti}_2\text{O}_7$ were identified above the Y solubility on the A-site join at $\sim v = 0.015$. Results therefore indicated that the substitution of Y is more favourable at the B-site rather than the A-site.

An extensive range of tetragonal BT solid solutions forms between $x = 0$ to 0.05 ; with increasing x and y , there is transformation usually to cubic BT polymorph for acceptor and self-compensation joins. The cubic polymorph was obtained over the range $x = 0.05 - 0.1$ and $y = 0.05 - 0.075$ for acceptor and self-compensation joins, respectively. The hexagonal BT polymorph was obtained over the range $v = 0.05 - 0.15$ for the acceptor join only. The donor join shows a tetragonal BT polymorph until $v = 0.015$.

The high temperature hexagonal phase of BT appeared to be destabilised by replacing Ti with Y. The destabilisation occurred in this region where the transition from hexagonal to cubic phase was expected. The hexagonal phase was the first product of reaction. High temperatures and prolonged heating was required to transfer to the cubic phase. It was mostly kinetically-stable with these conditions. Results on samples heated at $1420-1600\text{ }^\circ\text{C}$ to study the nature of the cubic-hexagonal phase transition, indicated that the equilibrium state was reached only very slowly. Many days sometimes were required to achieve a single phase product. Experiments often yielded a number of different polymorphs or phases, alternating between the hexagonal and tetragonal-cubic phase at different temperatures, independently of whether the method applied involves quenching to room temperature or slowly cooling.

A frequency-dependent relaxor character occurred at high dopant concentrations at $x, y \geq \sim 0.05$ either on the B-site or AB sites whereas, this behaviour was not observed on the donor join.

A normal ferroelectric behaviour with an inhomogeneous distribution of Y-dopant was observed at $x < 0.05$ and BT as the permittivity exhibits a sharp increase of the dielectric constant at the ferroelectric-paraelectric transition whereas, ferroelectric relaxor behaviour with a homogenous distribution of the Y-dopant at was observed $x \geq 0.05$. Some low concentration samples were leaky dielectrics as shown by the very high permittivity maximum and high dielectric loss. Excellent Curie–Weiss behaviour was observed for ϵ_r values at temperatures $> T_C$.

6.1.3 Electrical properties of Y-doped BT at high concentrations

For Y-B samples, IS showed that samples with $0.09 \leq x \leq 0.15$ were electrically homogenous and showed an insulating bulk response.

Samples with $0 < x < 0.07$ showed similar electrical conduction behaviour to undoped BT; samples were electrically inhomogeneous with no evidence of semiconductivity in any of the samples studied whether they were cooled slowly or quenched from high temperatures (1200-1600 °C).

Most samples were highly insulating in these samples because the oxygen vacancies were created by Y dopant.

σ_{gb} of BT is lower than σ_{gb} of Y-doped BT whereas E_A of BT is higher than E_A of Y-doped BT, which may shows that a fully-oxidised condition was observed for the grain boundary component of BT. The conduction mechanism in these samples was shown to be p-type by measurements made in different atmospheres and dc bias.

Impedance data for Y-AB samples showed that the electrical properties differed significantly depending on whether the sample was cooled slowly or quenched from 1500 °C. A series of tests was performed for a sample of one composition, $y = 0.025$, which was subjected to a variation of cooling treatments. The bulk resistance decreased for the sample quenched in air compared to the slow cooled sample. Further decrease in resistance was obtained for the sample quenched in liquid nitrogen. The slow-cooled sample had lower conductivity and higher activation energy than the quenched sample.

Conductivity data showed, from the Arrhenius plots and pO_2 dependence of composition $y = 0.05$, SC, sintered in air at 1500 °C and $y = 0.025$, Q from 1500 °C

into liquid nitrogen, that the conduction mechanism was p-type and n-type, respectively.

The IS results obtained from slow cooled, Y-A ceramics were substantially different to those obtained from quenched ceramics and were strongly dependent on the cooling rate. The slow cooled sample was insulating for $\nu > 0.01$ and the high frequency component was unchanged with dc bias.

Y-A sample was very conductive at room temperature for the sample quenched from 1350 °C. The resistance was dependent strongly on the electrode material. A Schottky barrier at the electrode-sample interface was observed. The impedance was dominated by low frequency arc with Ag electrodes but this effect disappeared with In-Ga electrodes which gave rise to ohmic contact and reduced the effective Schottky barrier impedance. PTCR effect was observed for both electrodes but the sample with In-Ga electrodes showed a weak PTCR effect.

Conductivity data for Ag sample were generally independent of pO_2 in which the electrode-sample interface was not affected under different atmospheres whereas, strong reduction of resistance was observed with dc bias.

6.1.4 Electrical properties of RE-doped BT with low dopant concentrations

Electrical properties of RE^{3+} (Gd, Dy, Ho, Y, Er and Yb)-doped $BaTiO_3$ compositions prepared according to 3 systems: (RE-B), (RE-AB) and (RE-A) at several concentrations x,y and $\nu = 0, 0.0001, 0.001$ and 0.01 were characterised.

IS data exhibit clearly that the electrical properties are strongly dependent on pO_2 , dc bias, cooling rate, type of electrodes, sintering temperature and RE^{3+} concentration.

For Yb-doped BT:

IS results indicated that samples on all three joins were electrically insulating and did not show any conductivity at room temperature even with rapid Q into liquid N_2 . p-type behaviour was indicated for x,y and $\nu = 0.01$ by both pO_2 and dc bias.

For Er-doped BT:

All samples were insulating on Er-B join whether Q or SC especially at $x = 0.01$. Dc bias and pO_2 showed that the conduction is p-type.

Er-A data show that all Q samples were conductive whereas, SC samples were insulating and probably a conductive core was shown which is supportive evidence for loss oxygen mechanism. Q samples show a clear Schottky barrier (SB) with In-Ga or Ag electrodes. The high frequency resistance and capacitance was insensitive to the application of a small dc bias. By contrast, the low frequency component changed with a dc bias. Application of different pO_2 did not show any sensitivity to pO_2 . Replacing Ag with In-Ga electrodes resulted in significant difference in the electrical properties. The low frequency arc in Z^* disappeared with In-Ga electrodes.

On the self-compensation join ER-AB, very conductive data were shown for Q samples except for $y = 0.01$ which was resistive either with SC or Q although the Q sample was more conductive. This result is supportive evidence for the oxygen loss mechanism for $y < 0.01$. SB was observed for $y = 0.0001$, Q sample with a small PTCR effect. Similar data for 0.001 with a conductive core was clearly present in the M'' data. Both pO_2 and dc bias tests were used for two different Q samples; a conductive sample which was dominated by SB for $y = 0.001$ and an insulating sample for $y = 0.01$. The conductive sample of $y = 0.001$ was not sensitive to pO_2 . Z^* data were similar in Air, N_2 and O_2 whereas p-type behaviour was observed for an insulating sample of $y = 0.01$. Both samples showed that the resistance decreased reversibly on application of a small dc bias which is associated with SB effect and p-type behaviour.

For Y-doped BT:

For Y-B, too resistive data and no conductive core was observed for SC and Q pellets in air at $x = 0, 0.0001, 0.0003, 0.0005$ and 0.01 . A conductive core for both SC and Q samples was observed for $x = 0.001, 1350\text{ }^\circ\text{C}$ which is supportive evidence for direct donor doping mechanism.

Effect of Q was shown for $x = 0.01$ samples Q from different temperatures $1350, 1400$ and $1450\text{ }^\circ\text{C}$. $1350\text{ }^\circ\text{C}$, Q sample has higher σ_T . Dc bias data on $1350\text{ }^\circ\text{C}$ sample showed p-type. Similar results with pO_2 change were seen in two samples.

For Y-AB, a weak conductive core was seen for $y = 0.0001, 1350\text{ }^\circ\text{C}$, SC which is supportive evidence for the direct donor doping mechanism. R_T was too high to measure. SC and Q samples showed a clear conductive core component for $x =$

0.001, 1350 °C, SC and Q. These results were dominated by an SB effect that depended on the electrode: Pt, Au and In-Ga. Effect of cooling rate was clearly observed for $y = 0.0001$, 1400 °C with SC in air, Q in air and Q into liquid N₂. SC was insulating and R_T was too high to measure but showed conductive core. Q in air showed similar behaviour but with more conductive data whereas, Q into liquid N₂ showed a semicircular arc.

Dc bias and pO₂ were applied to a Q sample from 1500 in air for $y = 0, 0.01$. No apparent sensitivity was shown to the change of pO₂ at RT which is probably associated with the SB effect. Therefore, dc bias was studied at low temperature to characterise the bulk response at 50 K. R_b was independent of dc bias whereas, R_{gb} showed a reversible decrease in grain boundary resistance.

For Y-A, a conductive core was observed for both SC and Q samples for $\nu = 0.0001$ which is supportive evidence for direct donor doping mechanism whereas, R_T could not be measured. More conductive data were shown for $\nu = 0.001$ and 0.01. Similar to x and $y = 0.001$ results as conductive core was observed for SC and Q with resistive R_T and semiconductive semicircular arc for 1400 °C, Q.

The oxygen exchange reaction at $\nu = 0.01$ at 100 °C was indicated by dc bias and pO₂. The bulk component was independent of both dc bias and pO₂ whereas, low frequency component showed that the low frequency resistance decreased on application of a small dc bias voltage and the resistance decrease is reversible on removal of the dc bias.

For Ho-, Dy-, and Gd-doped BT:

For Ho-B, Dy-B and Gd-B, a conductive semicircular arc with SB effect was observed for 1350 °C, Q samples, at $x = 0.0001$ and 0.001 with PTCR effect whereas, 0.01 and *PBM*, 0.001 for Ho-B were very insulating without showing any conductive core for Ho-B, Dy-B.

For Ho-AB and Dy-AB, similar behaviour to Ho-B was observed for all compositions but *PBM*, 0.001 for Ho-AB showed a conductive core. For Gd-AB, $y = 0.0001$, 0.001 *PBM* and 0.01 were insulating with little conductive core. The Q

sample 0.001, for Gd-AB showed conductive data for the bulk and grain boundary components at RT.

For Ho-A and Dy-A, a weak conductive core was seen for $\nu = 0.0001$ at RT. A conductive semicircular arc was shown for $\nu = 0.001$ and 0.01 whereas, PBM, 0.001 sample for Ho-A showed a conductive core and an insulating low frequency component. The sample 0.01, SC showed a weak conductive core for Ho-A, Dy-A and Gd-A whereas, Q sample for Ho-A and Gd-A showed a conductive data for the bulk and grain boundary components at RT. A semicircular arc was seen for Q samples of 0.0001, 0.001, 0.001 *PBM*, 0.01. SB were dominated for all samples except 0.01.

6.1.5 Resistivity minimum of RE-doped BT

No resistivity minimum was observed for Yb-BT and Er-BT for all three joins whereas, the total resistivity passed through a minimum at 0.001 then increased generally at ≥ 0.01 for Y-, Ho-, Dy- and Gd-BT on all three joins. Loss of oxygen seems the most dominant mechanism and responsible for resistivity minimum with little evidence of direct donor doping in some cases.

6.1.6 Effect of preparation routes

The bulk conductivity data of the three different milling routes, *HM*, *BM*, and *PBM* for undoped BT, slow cooled samples showed no significant differences but sometimes there is clear differences for example, Y-B samples showed that a conductive core for both SC and Q samples was observed for $x = (0.001, HM)$ and $(0.001$ and $0.003 PBM)$ and showed a SB effect whereas, 0.001, *BM* sample showed that R_T was too high to measure with little evidence of conductive core for sample Q only from 1450 °C. For Y-AB and Y-A samples, the difference between *HM*, *PBM* and *BM* was different to Y-B behaviour as the semicircular arc was seen for *BM*, 0.001, Q from 1350 °C for Y-AB and from 1350 °C and 1400 °C for Y-A .

6.2 Further Work

- Literature data reported that the difference between conventional solid state and sol-gel methods under small amount of dc bias was unknown. This phenomenon could not be explained entirely. Therefore, It is desirable to study the effect of dc bias on BT prepared by different methods.

- It is possible that samples lose Ba at high sintering temperatures. Therefore, addition of excess Ba to compensate for loss of Ba may be used to return the Y-doped compositions to the acceptor join which may require addition of excess Ba to some samples that are not single phase.
- It was reported in the literature that the solubility limit of some RE³⁺ dopants is dependent on the atmosphere, such as N₂. Thus, electrical properties in this case should be studied as electrical properties can be understood and controlled by application of different atmosphere.
- The mechanism of the stabilization of the hexagonal phase for Y-doped requires investigation.
- Since the need to include a CPE in data analysis was shown for many samples, a study of equivalent electrical circuit fitting is required to determine the electrical response of inhomogeneous materials and to extract resistance and capacitance values of low and high frequency components which could not be observed by normal IS experiments.
- Further low concentration dopants between 0.001 and 0.01 such as 0.002, 0.003, 0.004, 0.005, 0.006, 0.007, 0.008 and 0.009 for RE³⁺-doped BT on all three joins with different cooling rates and preparation methods are important to observe precisely the resistivity minimum.
- The influence of oxygen content on electrical properties needs further investigation by annealing some conductive samples in different conditions as this behaviour needs to be properly and accurately identified.
- To fully determine the optimum conditions to achieve complete reaction for *BM/HM/PBM*. i.e. determine the effect of T, t after milling.

6.3 References

- [1] D.P. Cann, C.A. Randall, Electrode effects in positive temperature coefficient and negative temperature coefficient devices measured by complex-plane impedance analysis, *Journal of applied physics*, 80 (1996) 1628-1632.